

**School of Chemical and Petroleum Engineering  
Department of Chemical Engineering**

**Engineering Carbon-Semiconductor Hybrid Materials for  
Photocatalysis and Solar Cells**

**Zhangfeng Shen**

**This thesis is presented for the Degree of  
Doctoral of Philosophy  
of  
Curtin University**

**November 2017**

## Declaration

To the best of my knowledge and belief this thesis contains no material previously published by any other person except where due acknowledgement has been made. This thesis contains no material which has been accepted for the award of any other degree or diploma in any university.

Signature: zhangfeng shen

(Zhangfeng Shen)

Date: 08/11/2017

## Acknowledgement

First of all, I would like to take this opportunity to express my sincere gratitude to my principle supervisor, Prof. Shaomin Liu, for his invaluable advice and instructive guidance both in research and life. His understanding and support really help me get through tough times during this period. I'm always encouraged by his wisdom and humor to laugh at the setbacks in life.

Equally, I am deeply grateful to my co-supervisor, Dr Lihong Liu, for her encouragement and assistance on my research. Her dedication and commitment to work have had influence on both my career and my life. I would also like to thank Prof. Shaobin Wang for the support of using the equipment for my experiment. Special thanks are given to Dr. Jaka Sunarso, for his advice in paper writing and his help on revising my manuscripts. I also express my great thanks to Prof. Guiqiang Wang who taught me to make the first solar cell and Prof. Degang Li for his teaching relevant electrochemistry knowledge.

Subsequently, I owe special thanks to my colleagues and friends, Chi Zhang, Ping Liang, Meiwen Wang, Tingting Li, Xiaochen Guo, Huayang Zhang, Wenjie Tian, Hao Tain, Xiaoguang Duan, Wei Wang, Jian Kang, Kun Zhang, Ning Han and many others. They are all nice people and gave me great help not only on my research but also on the oversea life.

Here, I would also express my appreciations to Curtin Chemical Engineering laboratory technician team members for their full support in purchasing chemicals and training for analytic instruments. I am also grateful to technical staffs from UWA CMCA microscopy centre for their training and assistance in SEM and TEM. Besides, I'm very much obliged to Prof. Huagui Yang's group for giving me a chance to learn the fabrication of perovskite solar cells.

I also sincerely acknowledge the financial support for my PhD study from Australian Research Council via its Future Fellow Program (FT12100178) and the Curtin International Postgraduate Research Scholarship.

Last but not least, I express my deepest gratitude to my family — my parents and my brother, for their continuous support, tolerance and love. Home is the harbor for ever. Love you all.

## Abstract

Nowadays, the development of clean and sustainable energy sources has become a hot spot of research due to the global rising demand for energy along with associated environmental issues. As a clean and abundant energy source, solar light is a promising candidate to comply with long-term energy demand. Carbon-semiconductor hybrid materials (CSHMs) combining both advantages of carbon and semiconductor are believed to play more and more important roles on solar energy conversion. The enhanced light harvesting ability, high degree of charge carrier separation and photochemical stability have made CSHMs receiving immense scientific interests in the photocatalytic and photovoltaic areas. An overview of recent development of CSHMs, including their synthesis methods and applications for photocatalysis/photoelectron-catalysis and various solar cells, are summarized to gain the principle understanding of these nanocomposites. To design the facile synthesis routes for CSHMs, yeast mold broth is used as carbon source and structure-directing agent for the growth of carbon-enwrapped ZnO superstructure. This microbe-free strategy offers superior ease-of-preparation with minimal negative environmental impact and various particle morphologies from solid microrod to mesocrystals of porous microcylinder, nanodisk, nanocone, nanoflower, and microhamburger could be obtained by adjusting the zinc precursor concentration, broth pH value, and broth content. Meanwhile, silver nanoparticles can be facilely deposited onto the hybrid by photo-reduction in the broth. The resultant ZnO@C-Ag composite exhibits a significant improvement in the solar light-irradiated photo-degradation of methylene blue solution. Carbon-doped TiO<sub>2</sub> beads are also prepared through a hydrothermal treatment of the hexadecylamine (HDA) directed TiO<sub>2</sub> bead precursor in the presence of 10 wt.% HCl. The obtained micro-sized TiO<sub>2</sub> have hierarchical structure consisting of rutile nanorods, and rutile/brookite nanoparticles, where the carbon is derived from HDA after calcination. The C-TiO<sub>2</sub> beads with another anatase TiO<sub>2</sub> beads with small particle size (500 nm) are used as the anode for dye-sensitized solar cell (DSSC), where the C-TiO<sub>2</sub> bead layer is coated on the top of anatase bead layer. Due to the larger particle size and the presence of one-dimensional (1D) rutile nanorods with the carbon doping, the C-TiO<sub>2</sub> bead layer is advantageous in terms of fast electron transport, while the anatase layer provides large surface area for dye loading. The DSSC based on such structure arrangement achieved a power conversion efficiency (PCE) of 7.24%, which is much higher than cell based on P25 (5.41%). Then, a dye and carbon dots (CDs) complex obtained through a

single-step hydrothermal treatment of the celery leaf extract is used to sensitize  $\text{TiO}_2$  film as the photoanode in DSSCs. It has been found the hydrothermal temperature exerts great influence on the physical properties of CDs and the survival rate of the natural dyes. The DSSC based on low temperature ( $120^\circ\text{C}$ ) obtained complex gives higher efficiency, which is 1.7 times higher than the one based on the original extract. Besides functioning as a light sensitizer, CDs with a lower amount of trap states can work as an effective electron-transfer intermediate to improve the interaction between the dye and  $\text{TiO}_2$  and suppress the photogenerated carrier recombination, thus improving solar-cell performance. Moreover, a novel counter electrode (CE) composed of  $\text{WO}_x@WS_2$ @carbon core-shell film is also developed by a sulfurization treatment of a mesoporous  $\text{WO}_x$ /carbon film coated on FTO glass. The well-interconnected three-dimensional (3D)  $WS_2$  structure with coated carbon film provides high electrocatalytic activity and fast reaction kinetics for the reduction of triiodide to iodide due to its sufficient active sites on 3D  $WS_2$  framework containing surface edge-oriented nanosheets and the facile electron transfer and electrolyte diffusion via the continuously carbon layer. The DSSC device with the CE of  $\text{WO}_x@WS_2$ @carbon achieved the PCE of 7.71% compared favourably with 7.34% from conventional Pt CE. The thesis presents and discusses several cost-effective methods to fabricate CSHMs, which enhance the performance in photocatalytic degradation of environmental contaminants and electricity generation from solar cells.

## Publications by the Author

1. **Shen Z**, Liang P, Wang S, Liu L, Liu S. Green synthesis of carbon- and silver-modified hierarchical ZnO with excellent solar light driven photocatalytic performance. *ACS Sustainable Chemistry & Engineering*. 2015; 3(5):1010-6.
2. **Shen Z**, Liu B, Pareek V, Wang S, Li X, Liu L, et al. Sustainable synthesis of highly efficient sunlight-driven Ag embedded AgCl photocatalysts. *RSC Advances*. 2015; 5(98):80488-95.
3. **Shen Z**, Wang G, Tian H, Sunarso J, Liu L, Liu J, et al. Bi-layer photoanode films of hierarchical carbon-doped brookite-rutile TiO<sub>2</sub> composite and anatase TiO<sub>2</sub> beads for efficient dye-sensitized solar cells. *Electrochim Acta*. 2016; 216:429-37.
4. **Shen Z**, Guo X, Liu L, Sunarso J, Wang G, Wang S, et al. Carbon-dot/natural-dye sensitizer for TiO<sub>2</sub> solar cells prepared by a one-step treatment of celery leaf extract. *ChemPhotoChem*. 2017; 1(10):470-8.
5. **Shen Z**, Wang M, Liu L, Sofianos M, Yang H, Wang S, et al. Carbon-coated three-dimensional WS<sub>2</sub> film consisting of WO<sub>3</sub>@WS<sub>2</sub> core-shell blocks and layered WS<sub>2</sub> nanostructures as counter electrodes for efficient dye-sensitized solar cells. *Journal of Power Sources*, under review.
6. Zhou C, **Shen Z**, Liu L, Liu S. Preparation and functionality of clay-containing films. *J Mater Chem*. 2011; 21(39):15132-53.

## Manuscripts in Preparation

1. **Shen Z**, Liu L, Liu S. Carbon-semiconductor hybrid materials and their applications in photo-/photoelectro-catalysis and solar cells-A review.

# Table of Contents

<b>Acknowledgement</b> .....	<b>i</b>
<b>Abstract</b> .....	<b>ii</b>
<b>Publications by the Author</b> .....	<b>iv</b>
<b>Chapter 1: Introduction</b> .....	<b>1</b>
1.1 Background .....	1
1.2 Research objectives.....	2
1.3 Thesis organization.....	3
Reference .....	4
<b>Chapter 2: Literature Review</b> .....	<b>6</b>
Abstract.....	6
2.1 Introduction .....	6
2.2 Synthesis of carbon-semiconductor hybrid materials (CSHMs).....	8
2.2.1 Amorphous carbon .....	8
2.2.2 Carbon nanotubes.....	13
2.2.3 Graphene.....	17
2.2.4 Fullerene .....	30
2.2.5 Carbon dots .....	31
2.3 Photo-degradation of pollutants .....	33
2.3.1 Amorphous carbon .....	34
2.3.2 Carbon nanotubes.....	35
2.3.3 Graphene.....	37
2.3.4 Fullerene .....	48
2.3.5 Carbon dots .....	52
2.4 Photocatalytic hydrogen or oxygen generation .....	56
2.4.1 Carbon nanotubes.....	58
2.4.2 Graphene.....	59
2.4.3 Fullerene .....	61
2.4.4 Carbon dots .....	62
2.5 Photocatalytic carbon dioxide (CO <sub>2</sub> ) reduction.....	63
2.6 Photocatalytic reduction of nitro organics to amino organics.....	65
2.7 Photocatalytic selective oxidation .....	66
2.8 Dye-sensitized solar cells (DSSCs) .....	67

2.8.1 Photoanode.....	68
2.8.2 Counter electrodes.....	77
2.9 Quantum dots sensitized solar cells (QDSSCs) .....	93
2.9.1 Photoanodes .....	93
2.9.2 Counter electrodes.....	94
2.10 Carbon dots sensitized solar cells (CDSSCs).....	97
2.11 Perovskite solar cells (PSCs).....	102
2.12 Conclusions and outlook.....	109
References.....	110
<b>Chapter 3: Green synthesis of carbon and silver modified hierarchical ZnO with excellent solar light driven photocatalytic performance.....</b>	<b>134</b>
Abstract.....	134
3.1 Introduction .....	134
3.2 Experimental section.....	136
3.2.1 Sample preparation.....	136
3.2.2 Characterization .....	137
3.2.3 Photocatalytic test .....	137
3.3 Results and discussion .....	138
3.3.1 Morphology and structure characterization of ZnO particles.....	138
3.3.2 Silver modified ZnO@C samples .....	144
3.4 Conclusions .....	148
References.....	148
<b>Chapter 4: Bi-layer photoanode films of hierarchical carbon-doped brookite-rutile TiO<sub>2</sub> composite and anatase TiO<sub>2</sub> beads for efficient dye-sensitized solar cells .....</b>	<b>151</b>
Abstract.....	151
4.1 Introduction .....	152
4.2 Experimental .....	154
4.2.1. Materials and syntheses .....	154
4.2.1.2. Synthesis of Bead-A .....	155
4.2.1.3. Synthesis of Bead-B .....	155
4.2.2. Preparation of TiO <sub>2</sub> working electrode.....	155
4.2.3. Fabrication of dye-sensitized solar cell .....	156
4.2.4. Characterization .....	156
4.3 Results and discussion .....	158

4.3.1. Structure and morphology .....	158
4.3.2. Formation mechanism of TiO <sub>2</sub> beads .....	166
4.3.3. Solar cells performances.....	167
4.4 Conclusions .....	174
References.....	175
<b>Chapter 5: Carbon-dot/natural-dye sensitizer for TiO<sub>2</sub> solar cells prepared by a one-step treatment of celery leaf extract .....</b>	<b>179</b>
Abstract.....	179
5.1 Introduction .....	180
5.2 Experimental Section.....	182
5.2.1 Materials .....	182
5.2.2 Dye extraction and Carbon Dots synthesis .....	182
5.2.3 Solar cell fabrication .....	183
5.2.4 Characterization and Measurement.....	183
5.3 Results and Discussion .....	184
5.3.1 Structure and morphology .....	184
5.3.2 Optical properties .....	189
5.3.3 Solar cells performances.....	196
5.4 Conclusions .....	200
References.....	200
<b>Chapter 6: Carbon-coated three-dimensional WS<sub>2</sub> film consisting of WO<sub>3</sub>@WS<sub>2</sub> core-shell blocks and layered WS<sub>2</sub> nanostructures as counter electrodes for efficient dye-sensitized solar cells.....</b>	<b>204</b>
Abstract.....	204
6.1 Introduction .....	204
6.2 Experimental section.....	206
6.2.1 Materials .....	206
6.2.2 Synthesis of WO <sub>x</sub> green powder .....	207
6.2.3 Preparation of counter electrodes.....	207
6.2.4 Fabrication of dye-sensitized solar cell .....	208
6.2.5 Characterization .....	209
6.3 Results and discussion .....	210
6.3.1. Morphology and compositions.....	210
6.3.2. Electrochemical properties .....	221

6.3.3. Photovoltaic performance .....	224
6.4. Conclusions .....	226
References .....	227
<b>Chapter 7: Conclusions and Perspectives .....</b>	<b>230</b>
7.1 Conclusions .....	230
7.1.1 Green synthesis of carbon- and silver-modified hierarchical ZnO with excellent solar light driven photocatalytic performance .....	230
7.1.2 Bi-layer photoanode films of hierarchical carbon-doped brookite-rutile TiO <sub>2</sub> composite and anatase TiO <sub>2</sub> beads for efficient dye-sensitized solar cells .....	231
7.1.3 Carbon-dot/natural-dye sensitizer for TiO <sub>2</sub> solar cells prepared by a one-step treatment of celery leaf extract .....	231
7.1.4 Carbon-coated three-dimensional WS <sub>2</sub> film consisting of WO <sub>3</sub> @WS <sub>2</sub> core-shell blocks and layered WS <sub>2</sub> nanostructures as counter electrodes for efficient dye-sensitized solar cells .....	232
7.2 Perspectives .....	232
<b>Appendix: Permission of Reproduction from the Copyright Owner .....</b>	<b>234</b>

## Chapter 1: Introduction

### 1.1 Background

Two major problems challenging the contemporary society are energy depletion and environmental pollution caused by continuous consumption of non-renewable fossil fuels, which is resulting in irreparable damage to the natural world and human society. This situation has inspired researchers to search other energy alternatives-renewable energy sources for the future.[1, 2] Solar energy, being a clean, abundant and easily available energy resource, can be efficiently harnessed by photocatalytic and photovoltaic processes to aid in environmental remediation and green energy generation.[3]

Among the solar photoreactions, photocatalysis is a hot topic attracting worldwide attention.[4] The use of solar energy in chemical synthesis started from the end of the 19th century when Ciamician and Silber studied the chemical behaviour of organic compounds under solar irradiation.[5] During the 1970s, Fujishima and Honda demonstrated the market potential of heterogeneous photocatalysis, which promoted the exploitation of photocatalysts.[6] With the development of nanotechnology in recent years, it becomes possible to greatly enhance the photocatalytic efficiency through the synthesis and manufacture of new photocatalysts.[7] The solar energy can be stored of new chemical bonds that in the form as fuel through photocatalysis process, such as water splitting for H<sub>2</sub> and CO<sub>2</sub> photoreduction.[8] Mover, photocatalysis also allows the utilization of solar light to efficiently degrade pollutants using semiconductors as photocatalysts.[9]

In addition, sun energy can also be directly converted into electricity through the process of photovoltaics. The development of solar cell technology begun from 1839 when Alexandre Edmond Becquerel observed the photovoltaic effect via an electrode in a conductive solution exposed to light.[10] Since Bell Lab's announced the first silicon solar cell in 1954,[11] the development of solar cell has gone through three generations. First generation solar cells are mainly based on silicon wafers which still are dominating the solar cell market.[12] The second generation solar cells include amorphous Si-based thin films solar cells, cadmium telluride/cadmium sulfide (CdTe/CdS) solar cells and copper indium gallium selenide (CIGS) solar cells.[13] The third-generation solar cells are solution processable and more cost-effective with excellent potential for large-scale solar electricity generation, including dye-

sensitized solar cells, quantum dots sensitized solar cells, polymer solar cells and recently emerging perovskite solar cells.[14, 15]

In both photocatalysis and photovoltaics, semiconductor materials play important roles for solar energy utilisation or conversion because they have capability to generate photoexcited electron-hole pairs that can be used to generate electricity or induce chemical reactions.[16] However, the application of semiconductor materials still faces big challenges. For instance, some semiconductors with the wide band gap (e.g.  $\text{TiO}_2$  and  $\text{ZnO}$ ) have limited light-harvesting capability and the high electron-hole pair recombination rate also results in low quantum efficiency. Some semiconductors (e.g.  $\text{CdS}$ ) suffer from photocorrosion leading to poor stability. Thus, hybrid nanomaterials are developed to overcome these drawbacks.[17] Among them, carbon materials are one of the most promising candidates to decorate semiconductor materials not only because they are cheap and environment friendly but also have excellent electrical conductivity and photochemical stability. The carbon-semiconductor hybrid materials are expected to enhance light harvesting, charge carrier separation and stability, facilitating to realise the full potentials of these semiconductor in both photocatalysis and solar cells.

## **1.2 Research objectives**

The major objective of the research is to develop green, economical and convenient synthesis methods to construct carbon-semiconductor hybrid materials and improve their photocatalytic and photovoltaic performance by combining both advantages of the carbon and semiconductor materials. To this end, following studies have been included:

1. Summarizing the current research status of carbon-semiconductor hybrid materials including their preparation methods and their structure-related applications in solar energy conversion.
2. Synthesizing carbon- and silver-modified  $\text{ZnO}$  superstructures through a microbe-free biogenic approach and using them as the photocatalyst for dye degradation under solar light.
3. Fabricating carbon-doped hierarchical  $\text{TiO}_2$  via in-situ precursor transformation and employing them as photoanode materials to improve the solar efficiency of DSSCs.

4. Developing a cheap approach to obtain nature dye-carbon dot complexes as sensitizers for TiO<sub>2</sub> based solar cells and studying the functions of carbon dots in light harvesting and converting.
5. Using sulfurization to fabricate carbon-coated three-dimensional WS<sub>2</sub> film as counter electrode in DSSCs and examining the possibility in replacing noble platinum electrode.

### **1.3 Thesis organization**

This thesis consists of seven chapters: introduction, literature review, experimental results and discussions, and conclusions and perspectives

#### **Chapter 1: Introduction**

The background and history of the development of photocatalysis and solar cells is briefly introduced. The research objectives and thesis organization are also listed in this chapter.

#### **Chapter 2: Literature review**

This chapter presents an overall review of the reported fabrication methods of carbon-semiconductor hybrid materials. The applications of these hybrids in solar energy conversion including photo-/photoelectro-catalysis and solar cells are also introduced and discussed with up-to-date research examples. An outlook for the future development of carbon-semiconductor hybrid materials is featured at the last part of this chapter.

#### **Chapter 3: Green synthesis of carbon- and silver-modified hierarchical ZnO with excellent solar light driven photocatalytic performance**

Yeast mold broth is used as the carbon source and the directing agent for the green growth of carbon-coated ZnO supercrystals. The reaction parameters are varied to study the effects on morphology and structure of ZnO particles. Ag nanoparticles are also used to decorate ZnO@C hybrid for improving the photocatalytic activity towards organic dye degradation.

#### **Chapter 4: Bi-layer photoanode films of hierarchical carbon-doped brookite-rutile TiO<sub>2</sub> composite and anatase TiO<sub>2</sub> beads for efficient dye-sensitized solar cells**

Two TiO<sub>2</sub> beads with different structures and compositions were synthesized from the same precursor. The hierarchical carbon-doped brookite-rutile TiO<sub>2</sub> beads and anatase TiO<sub>2</sub> beads

with different size are applied in assembling the photoanode of DSSCs. Their functions to the enhanced DSSC performance were characterized and discussed.

### **Chapter 5: Carbon-dot/natural-dye sensitizer for TiO<sub>2</sub> solar cells prepared by a one-step treatment of celery leaf extract**

This chapter presents a low-cost hydrothermal approach to obtain natural dye-carbon dots (CDs) complexes, which were used as light sensitizers for TiO<sub>2</sub> based solar cells. The influence of hydrothermal temperatures on the structure and optical property of CDs as well as dye surviving are studied. The roles that CDs played in solar cell are discussed.

### **Chapter 6: Carbon-coated three-dimensional WS<sub>2</sub> film consisting of WO<sub>3</sub>@WS<sub>2</sub> core-shell blocks and layered WS<sub>2</sub> nanostructures as counter electrodes for efficient dye-sensitized solar cells**

A carbon-coated three-dimensional WS<sub>2</sub> catalytic network is fabricated through a simple sulfurization of a mesoporous WO<sub>x</sub>/carbon film and applied as counter electrode for DSSCs. This WS<sub>2</sub> based electrode shows better catalytic activity toward I<sub>3</sub><sup>-</sup> reduction than conventional Pt electrode. The structural evolutions of different nanoparticles during sulfurization are carefully investigated.

### **Chapter 7: Conclusions and Perspectives**

The chapter summarizes the major findings of this thesis and gives suggestions for further research in this field.

## **Reference**

1. Holdren, J.P., *Science and Technology for Sustainable Well-Being*. Science, 2008. **319**(5862): p. 424-434.
2. Lior, N., *Sustainable energy development: The present (2009) situation and possible paths to the future*. Energy, 2010. **35**(10): p. 3976-3994.
3. Liu, X., et al., *Noble metal-metal oxide nanohybrids with tailored nanostructures for efficient solar energy conversion, photocatalysis and environmental remediation*. Energy & Environmental Science, 2017. **10**(2): p. 402-434.
4. Spasiano, D., et al., *Solar photocatalysis: Materials, reactors, some commercial, and pre-industrialized applications. A comprehensive approach*. Applied Catalysis B: Environmental, 2015. **170-171**(Supplement C): p. 90-123.
5. Roth, H.D., *The Beginnings of Organic Photochemistry*. Angewandte Chemie International Edition in English, 1989. **28**(9): p. 1193-1207.
6. Fujishima, A. and K. Honda, *Electrochemical Photolysis of Water at a Semiconductor Electrode*. 1972. **238**: p. 37.

7. Tong, H., et al., *Nano-photocatalytic Materials: Possibilities and Challenges*. Advanced Materials, 2012. **24**(2): p. 229-251.
8. Zecchina, A. and S. Califano, *Photocatalysis*, in *The Development of Catalysis*. 2017, John Wiley & Sons, Inc. p. 243-268.
9. Dong, H.R., et al., *An overview on limitations of TiO<sub>2</sub>-based particles for photocatalytic degradation of organic pollutants and the corresponding countermeasures*. Water Research, 2015. **79**: p. 128-146.
10. Fraas, L.M., *History of Solar Cell Development*, in *Low-Cost Solar Electric Power*. 2014, Springer International Publishing: Cham. p. 1-12.
11. Chapin, D.M., C.S. Fuller, and G.L. Pearson, *A New Silicon p-n Junction Photocell for Converting Solar Radiation into Electrical Power*. Journal of Applied Physics, 1954. **25**(5): p. 676-677.
12. Sharma, S., K.K. Jain, and A. Sharma, *Solar Cells: In Research and Applications: A Review*. Materials Sciences and Applications, 2015. **Vol.06No.12**: p. 12.
13. Fthenakis, V., *Sustainability of photovoltaics: The case for thin-film solar cells*. Renewable and Sustainable Energy Reviews, 2009. **13**(9): p. 2746-2750.
14. Yan, J. and B.R. Saunders, *Third-generation solar cells: a review and comparison of polymer:fullerene, hybrid polymer and perovskite solar cells*. RSC Advances, 2014. **4**(82): p. 43286-43314.
15. Sharma, D., R. Jha, and S. Kumar, *Quantum dot sensitized solar cell: Recent advances and future perspectives in photoanode*. Solar Energy Materials and Solar Cells, 2016. **155**: p. 294-322.
16. Rajeshwar, K., N.R. de Tacconi, and C.R. Chenthamarakshan, *Semiconductor-based composite materials: Preparation, properties, and performance*. Chemistry of Materials, 2001. **13**(9): p. 2765-2782.
17. Li, J.H. and J.Z. Zhang, *Optical properties and applications of hybrid semiconductor nanomaterials*. Coordination Chemistry Reviews, 2009. **253**(23-24): p. 3015-3041.

*Every reasonable effort has been made to acknowledge the owners of copyright material. I would be pleased to hear from any copyright owner who has been omitted or incorrectly acknowledged.*

## **Chapter 2: Literature Review**

### **Abstract**

Solar energy is one of the potential alternatives for fossil-fuel-based energy sources meeting the clean and renewable requirement. Carbon-semiconductor hybrid materials are promising materials for solar energy conversion because of their enhanced light harvesting ability and high degree of charge carrier separation. In this review, we summarized recent developments of carbon-semiconductor hybrids based on five different carbon structures, including amorphous carbon, carbon nanotube, graphene, fullerene and carbon dots. The various preparation methods related to different nanostructures of both carbon and semiconductor are addressed. In the regard of solar energy conversion, the applications of these hybrid materials in photocatalytic degradation of environmental contaminants, water splitting into H<sub>2</sub> or O<sub>2</sub>, photocatalytic reduction of CO<sub>2</sub>, other selective redox reaction, dye-sensitized solar cells, quantum dots sensitized solar cells, carbon dots sensitized solar cells and perovskite solar cells are provided. Facing the emerging challenges in photocatalytic and photovoltaic areas, we hope this review will serve as a useful guide in the design of advanced carbon-semiconductor hybrids, which make the use solar energy more effective and economical.

### **2.1 Introduction**

The demand for energy will keep increasing tremendously due to the rapid population and economic growth. Nowadays, humans still rely heavily on fossil fuels, including coal, petroleum and nature gas, which have limited resource reserves and their combustion has caused a series of environmental issues, such as air pollution, global warming and climate change.[1] Thus, the development of alternative renewable energy is the urgent affairs for human society. As a clean and abundant energy source, solar light is widely recognized as one of the most promising alternatives to traditional fossil fuel, which can be harnessed by photocatalytic and photovoltaic processes to convert into chemical energy and electricity.[2, 3] With the sunlight irradiation, photocatalysts could generate positive and negative charge carries, which can be used for fuel production, chemical synthesis and environmental remediation.[4, 5] Based on photovoltaic devises, these charge carries can be transported into external circuit to produce electricity.[6]

Advanced materials are the key to effectively convert solar light through above approaches. Solar energy conversion mainly depends on semiconductor materials, which have been extensively investigated due to their capability of generating photoexcited electrons that can be used to generate electricity or induce chemical reactions. For example, as a recent research hotspot, solar cells based on perovskite have achieved high conversion efficiency over 20% with small laboratory-level cells and 11–13% with small module-level cells.[7] However, the single use of these materials still suffer from low quantum efficiency and/or poor stability.[8] For instance, TiO<sub>2</sub> and ZnO with wide band gap can only harvest UV region, which is only 5% of the solar of the spectrum, while CdS, a visible-light-driven photocatalyst, suffer from photocorrosion obstructing its practical application.[9, 10] Thus, hybrid nanomaterials have been developed to combine different advantages, such as optical, electronic and magnetic properties, for the wide-ranging applications in environment remediation and solar energy conversion.[11-13] As one of the most abundant elements in earth, carbon materials play a major role in electrodes, electrocatalysis, photocatalysis, biofuels, water purification and gas separation/storage. [14] Due to the excellent electrical conductivity, controllable porosity, chemical stability, low cost and environmental kindness of carbon materials, the nanohybrids of carbon and semiconductor are expected to overcome the major problems of applied materials in the photocatalytic and photovoltaic areas, such as high price, low surface area, narrow photo-response range, rapid photo-generated electron-hole recombination and instability in chemical conditions. For example, the photo-induced electrons on the conduction band of TiO<sub>2</sub> could transfer into to carbon nanotubes or graphene and transport in their network due to the high electrical conductivity and electron affinity, which promote the charge carrier separation and result large photocurrent.[15] After coupling with carbon materials, the light absorption range of wide band gap semiconductor could also be extended, which means more photoexcited electrons will be produced.[16]

The successful application of carbon-semiconductor hybrid materials (CSHMs) is depended on their morphology, structure, composition, particle size, and other parameters. To integrate these dissimilar materials together with uniform dispersion and strong interfacial contact resulting multifunctional nanocomposites is still a big challenge. Based on different carbon structures, the CSHMs can be divided into five categories, including amorphous carbon-, carbon nanotube-, graphene-, fullerene-, carbon dots- semiconductor nanohybrids. A number of review articles have been published on the synthesis, properties and applications of carbon or semiconductor materials solely.[14, 17-24] There are only a few reviews focusing on

CSHMs. For example, the preparation and application of semiconductor/graphene composite photocatalysts have been summarized by Chen et al.[25] and Xie et al.[26], severally. Han et al. have reviewed the photoactivity and photostability of ZnO coupled by versatile carbon materials.[27] However, none of the previous reviews have systematically concentrated on the dependence of preparation and applications of CSHMs on the different carbon structures and various semiconductor materials.

In this review, we focus on recent developments (mainly since the year of 2010) of different nanostructures of carbon-semiconductor nanocomposites including their preparation and applications related to solar energy conversion in photocatalysis/photoelectrocatalysis and photovoltaic cells. The preparation methods, design and construction different structured CSHMs based on five types of carbon materials are firstly presented. Moreover, the enhanced photocatalytic and photovoltaic performance and corresponding mechanisms of these different nanohybrids are demonstrated by comparison to pure semiconductor or carbon. As great challenges still remain, we hope this review can be applied as a background source for the design of highly efficient and economic nanocomposites for solar-to-energy conversion.

## **2.2 Synthesis of carbon-semiconductor hybrid materials (CSHMs)**

Mechanical blending including mortar grinding, ball milling, mechanical stirring, magnetic stirring and ultrasonic dispersion, is widely used and an easy way to prepare CSHMs by directly mixing carbon and semiconductor components in some organic solvents (usually ethanol) with or without dispersant (such as terpineol and Triton X 100) and binder under the assistance of physical forces. Amorphous carbon,[28, 29] carbon nanotube,[30, 31] graphene naosheet[32-37] and fullerene [38-40] have been applied to construct CSHMs by one or two of these methods. However, CSHMs prepared by mechanical mixing or dispersing usually suffer from low uniform distribution degree and poor interfacial contact between semiconductor and carbon materials, which are not conducive to their photocatalytic and photovoltaic applications. In this section we summarize the other fabrication techniques, and the pros and cons of different CSHMs.

### **2.2.1 Amorphous carbon**

Amorphous carbon is nontoxic with good thermal, chemical stability, electron conductivity and absorption ability. Except for the direct mixing of semiconductor materials with the

existing amorphous carbon such as coal, petroleum coke, pitch coke, active carbon (Ac) and carbon black (Cb), various kinds of carbonaceous sources can also be transformed into amorphous carbon during the synthesis process of semiconductor materials after a suitable heat treatment.

Wet chemical synthesis method is widely used to synthesize size and shape controlled nano or sub-micro particles with multicomponent phases, using liquid phase at one of the process stages. This method allows lower temperature and shorter duration of phase formation, including sol-gel process, hydrothermal synthesis, spray drying, Pechini method etc. Kalpana and Selvaraj reported a ZnS-enwrapped amine-functionalized fly ash nanocomposite (ZnS/A-FA) through the wet chemical synthesis method (dried at 80°C without further heat treatment), which has a higher surface area of 153.5 m<sup>2</sup> g<sup>-1</sup> than that of bare ZnS (68.5 m<sup>2</sup> g<sup>-1</sup>).[41]

Sol-gel combustion synthesis is a simple and reliable method to prepare highly porous materials due to large amounts of gases release during the reaction and avoidance of calcination at high temperature, which has been applied in the synthesis of visible-light-active semiconductor photocatalysts, including TiO<sub>2</sub> [42] and ZnO[43]. In the synthesis of TiO<sub>2</sub>, the process normally involves three steps: (a) the hydrolysis of the alkoxide, (b) the nitration reaction to form Ti(NO<sub>3</sub>)<sub>2</sub> and (c) the combustion reaction of the titanyl nitrate (oxidizer) with a suitable fuel (glycine, oxalic acid, urea and others) to formulate TiO<sub>2</sub> nanoparticles with N<sub>2</sub>, CO<sub>2</sub> and H<sub>2</sub>O as the reaction by-products. Thus, the combustion synthesis can result in the carbon(C)-modified TiO<sub>2</sub> (C@TiO<sub>2</sub>) at appropriate conditions.[44, 45] The urea to titanyl nitrate ratio was found to determine the maximum combustion temperature, which in turn affects the specific surface area, crystallite size and fraction of the anatase phase in the synthesized titania particles.[42] Moustakas et al. found the optimal synthesis conditions for the C-modified TiO<sub>2</sub> (C@TiO<sub>2</sub>) were determined to 11.4 of urea to titanyl nitrate ratio and 400 °C calcination temperature, as the temperature (350~450°C) should make the urea combustion reaction fully completed but remain the carbon formed on the TiO<sub>2</sub> surface and the fuel to oxidizer ratio should stand on the flameless combustion range. [44] The resulted C-modified TiO<sub>2</sub> have response in the visible range (2.19 eV) and high values of BET surface area (175.2 m<sup>2</sup>/g) and porosity (75.6%). An activated carbon (Ac) supported Zn<sup>2+</sup>-TiO<sub>2</sub> photocatalyst was prepared by adding granular Ac into a sol containing Zn(NO<sub>3</sub>)<sub>2</sub> and titanium tetrapropoxide (Ti(OC<sub>4</sub>H<sub>9</sub>)<sub>4</sub>), followed by dry and calcination.[46] Chen et al. also fabricated amorphous carbon-coated tungsten oxide (C@WO<sub>3</sub>) by the similar method using glycine and glucose as fuel, where the contents of carbon can be controlled by the glucose

adding.[47] A certain content of amorphous carbon can improve absorption ability of the CSHMs, refine and separate the particles and affect the phase of powders, playing a positive influence to their photocatalysis. However, the excessive carbon will reduce the photocatalytic activity as the carbon is black and can weaken the light arriving on the catalysis surface by scattering and absorption.

Spray pyrolysis have been reported to fabricate  $\alpha$ -MoO<sub>3</sub>/C composite film at 400 °C in air, where the spraying solution was prepared in distilled water by using molybdenum salt and cane sugar as carbon source.[48] Impregnation and followed carbonization was applied to prepare carbon-coated WS<sub>2</sub> (C@WS<sub>2</sub>), where glucose was used as carbon source to be absorbed onto the surface of WS<sub>2</sub> particles.[49] Pechini method consisting in the formation of a polymeric resin produced by polyesterification between a metal chelate complex from hydroxycarboxylic acid and a polyhydroxyalcohol also have been applied to prepare C-containing K<sub>2</sub>Sr<sub>2</sub>(Ni<sub>0.75</sub>Nb<sub>4.25</sub>)O<sub>15- $\delta$</sub>  composite.[50]

Hydrothermal synthesis is another wet chemical synthesis method to prepare amorphous carbon-semiconductor composites in a closed liquid system. Glucose is widely used as the carbon source to form amorphous carbon during the hydrothermal process. [51-53] For instance, Maletić et al. synthesized TiO<sub>2</sub>/C composites by hydrothermal carbonization, using titanium isopropoxide and glucose precursor solution.[51] Zhang et al. fabricated TiO<sub>2</sub>/C hybrids through a hydrothermal treatment of the solution containing tetrabutyl titanate (Ti(OBu)<sub>4</sub>) and glucose at acid condition, and the content of carbon in the composites can be adjusted by etching in air at high temperature.[52] This TiO<sub>2</sub>/C composite can further turn into TiO<sub>2</sub>/carbon@TiO<sub>2</sub> core-shell nanocomposite when applied with another hydrothermal step, as shown in Figure 2.1a.[54] Sha et al. used TiCl<sub>3</sub> and glucose to prepare reduced TiO<sub>2</sub> (containing Ti<sup>3+</sup> or oxygen vacancy)/C (r-TiO<sub>2</sub>/C) nanocomposites, which has good response to visible light region (low band gap 1.30 eV) and high BET surface area (240 m<sup>2</sup>/g).[53] Peng et al. synthesized a peapod-like TiO<sub>2</sub>/carbon nanocomposite by adhering glucose molecules onto the surface of H<sub>2</sub>Ti<sub>3</sub>O<sub>7</sub> (HTO) nanotubes via hydrogen bonding during the hydrothermal process, where TiO<sub>2</sub> nanoparticles were encapsulated inside by the carbon fibers (Figure 2.1b).[55] The mesoporous structure and thin carbon shells cannot only prevent the encapsulated TiO<sub>2</sub> nanoparticles from aggregation, but also allow light penetration to improve the photocatalytic activity. Zhang et al. reported the hydrothermal synthesis of TiO<sub>2</sub>/C hollow composite spheres (Figure 2.1c), where SiO<sub>2</sub>@TiO<sub>2</sub> core-shell spheres were employed as the hard template and the SiO<sub>2</sub> core gradually could be dissolved with the

hydrothermal treatment time.[56] The thickness of carbon layer could be easily controlled by tuning the glucose concentration.

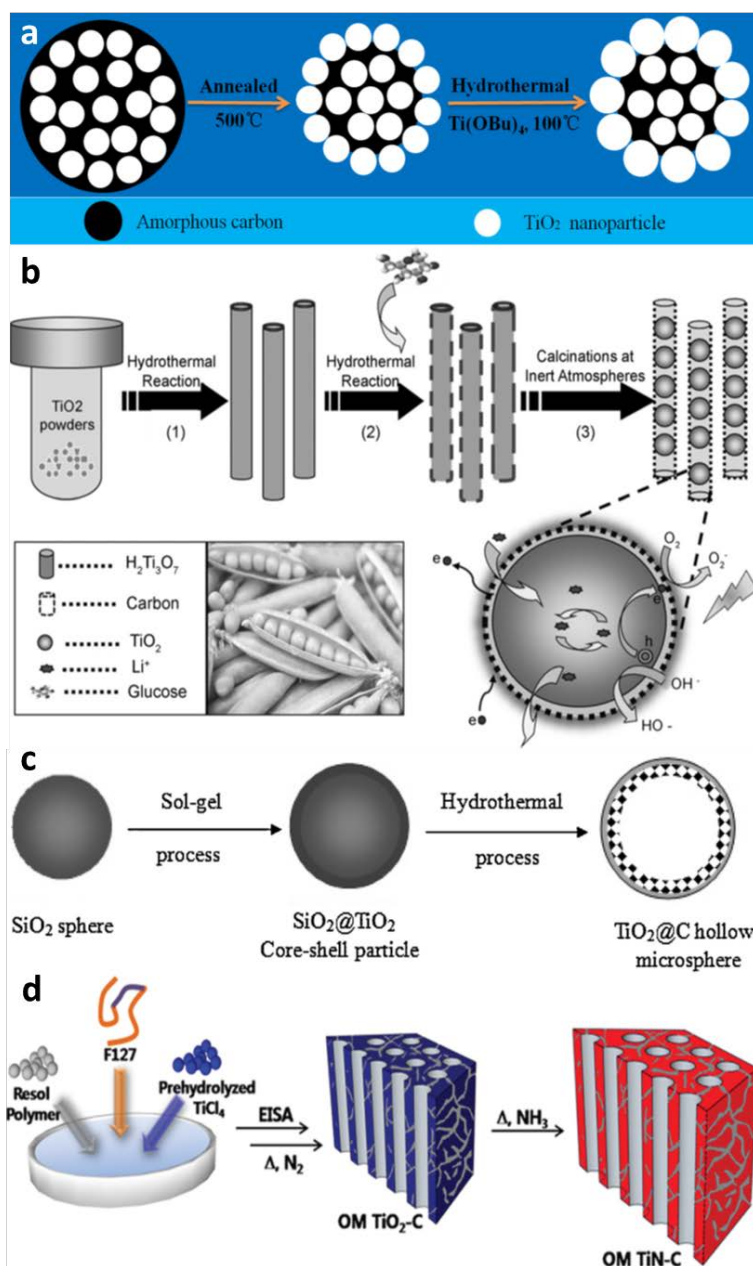


**Figure 2.1.** Schematic illustration of (a) the formation of  $\text{TiO}_2/\text{C}@\text{TiO}_2$  nanoparticles, (b) the synthesis route of the peapod-like  $\text{TiO}_2/\text{C}$ , (c) the synthetic procedure used for fabrication of  $\text{TiO}_2@\text{C}$  hollow composite structures and (d) the synthesis of ordered mesoporous  $\text{TiN-C}$  nanocomposites. Reprinted with permission from ref.[54-57] Copyright 2014 Elsevier, 2015 Wiley-VCH, 2013 Elsevier and 2012 American Chemical Society.

Activated carbon (Ac) was also used as carbon source during hydrothermal process. For example, Bagheri et al. prepared Ac-supported mesoporous  $\text{TiO}_2$  via a polyethylene glycol (PEG)-assisted hydrothermal method.[58] In fact, some surfactants with long alkyl chains,

which are widely used as structure-directing agent for the synthesis of semiconductor materials, can also be converted into amorphous carbon in situ during heat treatment to achieve homogeneous CSHMs. We have prepared micro-sized carbon doped TiO<sub>2</sub> beads consisting of rutile nanorods, and rutile and brookite nanoparticles through a hydrothermal treatment of the hexadecylamine (HDA) directed TiO<sub>2</sub> bead precursor in the presence of 10 wt.% HCl, followed by a calcination process.[59] We also have presented a green method for rapid growth of high-quality and carbon enwrapped ZnO nanomicrostructures (C@ZnO) through a hydrothermal process with yeast mold broth powder as both the carbon precursor and directing agent of ZnO nucleation.[60] The sizes and shapes of C@ZnO can be adjusted by changing the zinc precursor concentration, broth pH value, and broth content. Chen et al. reported a compositional material, TiOPC, containing titanium, oxygen, phosphorus, and carbon, prepared by from carbon thermal transformation of hydrothermal synthesized TiP<sub>2</sub>O<sub>7</sub> with sucrose in an atmosphere of nitrogen at high temperature.[61] Besides, urea also can be used as carbon source to form CSHMs after thermal treatment by controlling the molar ratio of urea to metal chloride.[62]

The use of surfactant, polymer, biopolymer, etc. as directing agent for the synthesis of nanomaterials is also called soft-template method.[63] After thermal treatment, those template can be transfer to amorphous carbon and the resulted CSHMs have hierarchical structure. Xu et al. used cetyltrimethylammonium bromide (CTAB) as a soft template to synthesized FeC<sub>2</sub>O<sub>4</sub> nanowire, which could be transformed to nanocomposites of iron carbide encaged in nitrogen-doped carbon (Fe<sub>3</sub>C@N-C) after a simple carbothermal reduction in the presence of cyanamide (NH<sub>2</sub>CN) at 600 °C.[64] Hao et al. also reported the synthesis of core-shell, yolk-shell and hollow Fe<sub>3</sub>O<sub>4</sub>@carbon microboxes by carbonizing Fe<sub>2</sub>O<sub>3</sub>@polymer precursor.[65] Tungsten dioxide imbedded in mesoporous carbon (WO<sub>2</sub>/MC) structure[66] and Co<sub>3</sub>O<sub>4</sub>/MC composites[67] have been fabricated by carbonizing the polyethylene polypropylene glycol (F127, a triblock copolymer)/metal cation/resorcinol-formaldehyde resols. Jang et al. prepared TiO<sub>2</sub>/C coated SiO<sub>2</sub> beads by coated a triblock copolymer, Pluronic P123, containing TiO<sub>2</sub> precursors onto SiO<sub>2</sub> nanospheres and converted into carbon after thermal treatment.[68] Ramasamy et al. reported the synthesis of an ordered mesoporous titanium nitride-carbon (TiN-C) nanocomposite with high surface area (389 m<sup>2</sup> g<sup>-1</sup>) and uniform hexagonal mesopores (ca. 5.5 nm) via the soft-template method (Figure 2.1d), where Pluronic F127 triblock copolymer formed an ordered structure with inorganic precursors,

resol polymer, and prehydrolyzed  $\text{TiCl}_4$ , followed by a successive heating at  $700^\circ\text{C}$  under nitrogen and ammonia flow.[57]

Recently, metal-organic frameworks (MOFs) have gained particular attention as a novel class of nanoporous materials, which can also as template to fabricate CSHMs as their designable framework structures modularly built from transition-metal clusters as nodes and organic ligands as struts.[69, 70] Different structured metal oxide with highly nanoporous carbon can be achieved by direct carbonization of MOFs without the need for any additional carbon precursors due to the large carbon content in MOFs. For example, MOF derived porous C- $\text{Fe}_3\text{O}_4$ ,[71] C-coated ZnO quantum dots[72, 73] and porous ZnO/Zn $\text{Fe}_2\text{O}_4$ /C octahedra with hollow interiors[74] have been reported.

Electrochemical deposition has been reported to prepare metal sulfide/C hybrid films. There are two different approaches: one is direct deposition of carbon material and metal sulfide onto conductive substrates;[75] the other is coating a carbon film on the substrate first and then deposition metal sulfide into the carbon film.[76] Various kinds of conductive carbon (like acetylene black, etc.) and soluble metal salt (such as  $\text{FeCl}_2$  and  $\text{NiCl}_2$ ) can be applied for electrochemical deposition, while thiourea and  $\text{Na}_2\text{S}_2\text{O}_3$  can be used as the sulfur source. The electrochemically deposited structure can be controlled by varying the operating conditions. In addition to electrochemical deposition, Geng et al. recently reported a reproducible and printable method to construct iron sulfide ( $\text{FeS}$ )/carbon material, where conductive carbon paste and iron powder was firstly doctor-bladed onto substrate and then the dried film was immersed into polysulfide electrolyte for the iron particles transform into iron sulfides.[77] Besides, amorphous carbon have also be deposited onto  $\text{TiO}_2$  nanotube (NT) arrays by chemical vapor deposition (CVD) method,[78] and the  $\text{Sb}_2\text{S}_3$ /carbon hybrid film was obtained via an atmospheric pressure thermal evaporation method to deposit  $\text{Sb}_2\text{S}_3$  onto carbon film.[79]

### **2.2.2 Carbon nanotubes**

The increasing application of carbon nanotubes (CNTs) can be attributed to the excellent properties of CNTs such as unique structure, high electrochemical stability, exceptional electrical conductivity and high specific surface area. There are two types of CNTs: single-walled carbon nanotubes (SWCNTs) and multi-walled carbon nanotubes (MWCNTs). Both of them have different structures which depend on the metallic band structure and their states density.

Impregnation is a facile method to prepared supported nanohybrids.  $\text{TiO}_2/\text{MWCNT}$  nanocomposite have been prepared by this method (Figure 2.2a).[80, 81] Before impregnation, the MWCNTs are usually purified by refluxing in concentrated nitric acid or sulfuric and nitric acid mixture to introduce oxygenated functionalities onto the nanotube surface, which can improve the interaction with the titanium precursor, such as titanium tetrakisopropoxide (TTIP), during impregnation. The final  $\text{TiO}_2/\text{MWCNT}$  composites are formed after a dry and calcination process. The obtained composites have better interfacial contact between  $\text{TiO}_2$  and MWCNTs compared with the samples prepared by a mechanical mixing process.[80] Yi et al. applied a similar aqueous chemical solution method using polyethylenimine as an assistant to combine the  $\text{Ti}^{4+}$  with CNTs, which could be further subjected spin-coating to fabricate uniform, transparent, and superhydrophilic  $\text{TiO}_2@\text{CNTs}$  thin film.[82]  $\text{TiN-CNTs}$  hybrids have been prepared by thermal hydrolysis of  $\text{TiOSO}_4$  on CNTs in a aqueous solution and subsequent nitridation in an ammonia atmosphere, where the CNTs were underwent hydrothermally treatment in  $\text{NaOH}$  solution before use.[83] Sol-gel method also have been applied to prepare  $\text{TiO}_2/\text{MWCNT}$  with the assistance of nitric acid [84, 85] and  $\text{ZnO}/\text{CNTs}$  with triethanolamine (TEA) as stabilizer.[86, 87] The entire process is similar to the impregnation method, where the mixture solution is heated to form a gel before dry or calcination.

Hydrothermal method is widely used to fabricate MWCNTs decorated transition metal sulfides, such as cobalt sulfides,[88, 89] nickel sulfides,[90] molybdenum disulfides ( $\text{MoS}_2$ ),[91] and tungsten disulfide ( $\text{WS}_2$ ).[92, 93] Similarly, the MWCNTs were underwent acid treatment to functionalize the graphitic  $\text{sp}^2$  carbon into  $-\text{COOH}$  functional group on their sidewalls before use. The hydrothermal temperature and time are normally controlled at  $180\sim 240$  °C and 12 h, respectively. For the synthesis of cobalt sulfide/MWCNT, two-step heating process ( $110$  °C for 4 h, followed by at  $240$  °C for 12 h) was applied, [88, 89] and for  $\text{WS}_2$  longer time (24h) was needed. [92, 93] Thiourea was commonly used as the sulfur source for the hydrothermal synthesis. It was also found that the adding of glucose during hydrothermal process could introduce amorphous carbon into the hybrids, which offered a large surface area and improved the conductivity of nanocomposite.[93] Not only the nanoparticles, but also some substrates can be subjected to hydrothermal treatment to prepare nanohybrids. For example,  $\text{TiO}_2/\text{MWCNT}$  hybrids have been fabricated by coating  $\text{TiO}_2$  nanoparticles onto the vertically aligned MWCNT arrays grown on tantalum foils[94] and FTO substrates[95] via a hydrothermal process, respectively.

Electrophoresis deposition also can be used to prepare CNTs/semiconductor hybrid films on conductive substrates as the surface of CNTs can be charged after acid treatment or further cation adsorption. Zhang et al. prepared a TiO<sub>2</sub>/CNTs composite by electrophoresis depositing positively (Al<sup>3+</sup>) charged CNTs into porous nanocrystalline TiO<sub>2</sub> film.[96] Xiao et al. first deposited MWCNTs on Ti foil substrates by using electrophoresis, and then further deposited NiS[97] or CoS[98] layer on the MWCNTs by using a pulse potentiostatic method to form the hybrid films, which can be used as the counter electrode for DSSCs. Moreover, electrospinning, another method using electric force, was also reported to fabricate TiO<sub>2</sub>/MWCNTs composites, in which uniformly distributed single-crystalline rice grain-shaped TiO<sub>2</sub> were obtained.[99, 100]

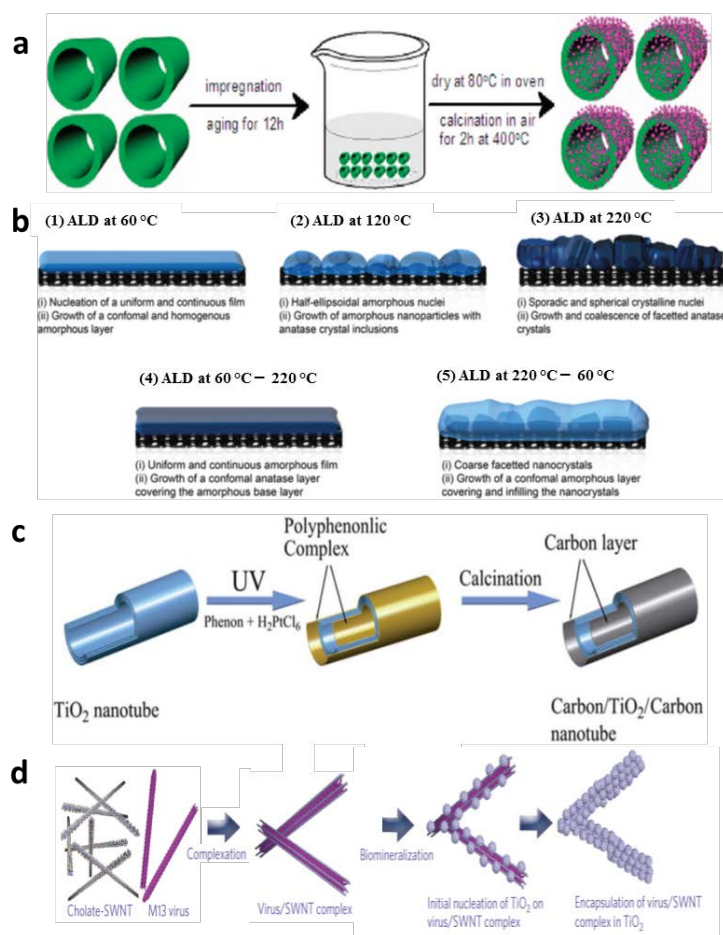


**Figure 2.2.** Schematic illustration of (a) the preparation of CNT/TiO<sub>2</sub> nanocomposite photocatalyst using a wet impregnation method followed by calcination in air, (b) evolution of the nucleation (i) and growth (ii) of ALD TiO<sub>2</sub> on MWCNTs using TTIP and H<sub>2</sub>O at different temperature courses, (c) the preparation of the CTCNT composites, and (d) process of virus/SWNT complexation, and biomimneralization of TiO<sub>2</sub> on the surface of the virus/SWNT complex. Reprinted with permission from ref.[80, 101-103] Copyright 2010 American Chemical Society, 2015 The Royal Society of Chemistry, 2014 Royal Society of Chemistry and 2011 Nature Publishing Group.

The laser pyrolysis and chemical vapor deposition (CVD) methods have already been described for the synthesis of TiO<sub>2</sub> nanoparticles[104] and CNTs[105], respectively, which also can be used for synthesis CNTs/semiconductor composites. The laser pyrolysis is a flow method based on the resonance between the emission of a CO<sub>2</sub> laser and the absorption of a chemical precursor. Wang et al. have synthesized a homogeneous distribution TiO<sub>2</sub>/MWCNT composite by single-step laser pyrolysis of the toluene dispersion of TTIP and MWCNTs, which could achieve high coverage and intimate interface between the TiO<sub>2</sub> particles and MWCNTs.[106] Zeng et al. reported two step CVD synthesis of ZnO/CNT hybrid films, where vertically aligned CNTs were firstly growth on stainless steel sheets using C<sub>2</sub>H<sub>2</sub> gas as carbon source and then ZnO nanostructures were attach to CNTs using zinc acetate as zinc source.[107]

Guerra-Nuñez et al. report a new strategy to obtain ultrathin TiO<sub>2</sub> coatings deposited by “Temperature-step” Atomic Layer Deposition (TS-ALD) with complete surface coverage of non-functionalized MWCNTs.[101] As shown in Figure 2.2b, the morphology and crystallinity of the TiO<sub>2</sub> film can be controlled by the ALD temperature. Complete coverage of MWCNTs with conformal anatase layers was obtained by using a low temperature of 60 °C during the nucleation stage followed by an increase to 220 °C during the growth stage, which resulted in a continuous and amorphous TiO<sub>2</sub> layer, covered with a conformal anatase coating (Figure 2.2b(4)). On the other hand, starting with the deposition at 220 °C and reducing to 60 °C resulted insporadic crystal grains at the CNT/TiO<sub>2</sub> interface covered with an amorphous TiO<sub>2</sub> layer(Figure 2.2b(5)).

Other methods were also reported to fabricate TiO<sub>2</sub>/CNT composites. Zhao et al. reported a hitherto carbon/TiO<sub>2</sub>/carbon nanotube (CTCNT) composite featuring a TiO<sub>2</sub> nanotube sandwiched between two thin tubes of carbon with about 1nm thick graphitic carbon layers.[102] The carbon layers were formed on two surfaces of TiO<sub>2</sub> tubes through a UV photo-polymerization of phenol with H<sub>2</sub>PtCl<sub>6</sub> in aqueous solution and followed by calcination in an argon atmosphere (Figure 2.2c). Tettey et al. fabricated TiO<sub>2</sub>@CNTs thin film by oppositely charged species of layer-by-layer (LbL) assembly approach, where an amphiphilic surfactant, aerosol OT (AOT), was used to impart opposite surface charge onto MWCNTs and TiO<sub>2</sub> in toluene. [108] In this LbL approach, oxidation of MWCNTs is not necessary and the film composition and conductivity can be adjusted by controlling the concentration of AOT and LbL circles.

In addition, biological templates also have been reported to use for the fabrication of TiO<sub>2</sub>/SWNTs nano composite. For example, Dang et al. prepared SWNTs/TiO<sub>2</sub> nanocrystal core-shell nanocomposites using a genetically engineered M13 virus as a template, where virus and sodium cholate-dispersed SWNTs were firstly bound together by pH control and then went through a TiO<sub>2</sub> biomineralization process at low temperature (Figure 2.2d).[103] Some DNA molecules are also able to self-assemble into sophisticated nanostructures and wrap around SWNTs to aid their dispersion. Zhang et al. reported the use of plasmid DNA from Bacillus cells as a biological scaffold to fabricate SWNTs/TiO<sub>2</sub> and d SWNTs/TiO<sub>2</sub>/Ag nanocomposites, where DNA bound and wrapped around the SWNTs became the anchored sites for Ag<sup>+</sup> and TiO<sub>2</sub> NPs clusters growth.[109]

### 2.2.3 Graphene

The unique and outstanding properties of graphene, including excellent electron conductivity and high transparency, have spurred increasing interest to synthesize the graphene (GR)-semiconductor nanocomposites for the photocatalytic and photovoltaic applications. The graphene layers with excellent electron conductivity could realize the quick transport of electrons via its extended  $\pi$ -conjugation structure, consequently benefiting the separation of photo-generated carriers on semiconductor materials. However, the large-scale production of graphene nanosheets remains a huge challenge. The techniques for the synthesis of graphene can be divided into “bottom up” and “top down” approaches. In the former method, graphene is synthesized from atoms or molecules via chemical reactions, such as epitaxial growth of graphene on substrates[110] or CVD[111], where the cost of using precious metal as substrate is expensive and scalable production is restricted to surface area of the substrate. Chemical exfoliation of graphite, electrostatic deposition and thermal exfoliation are some representative examples of top down methods. Among them, the chemical exfoliation of graphite oxide (GO), commonly Hummers method,[112] is efficient and results in high yields of single-layered graphene oxide, which can then be deposited on any substrate over large areas using solution based methods. Besides, the presence of oxygen functionalities at GO surface provides many reactive sites for chemical modification using well-known carbon surface chemistry. Thus, GO is normally used as the start material to prepare graphene-based nanocomposites. Although GO/semiconductor hybrids can be obtained simply by blending[113], thermal treatment[114], impregnation method[115] or two-phase self-assembly approach[116], the reduction of GO to reduced graphene oxide (rGO) is always involved in

the preparation to recover the conjugated network and electrical conductivity. Various graphene-semiconductor hybrids have been prepared by mechanical blending, UV-light assisted photoreduction, thermal reduction, sol-gel, hydrothermal, electrospinning, and atomic layer deposition, etc.

UV-assisted photocatalytic reduction, a room-temperature and environmentally friendly protocol, has been applied to prepare GR-TiO<sub>2</sub> nanocomposites, in which the GO suspended in ethanol or methanol accepts electrons from UV irradiated TiO<sub>2</sub> suspensions and is reduced to RGO (Figure 2.3a).[117-120] The advantage of photocatalytic reduction is the direct interaction between TiO<sub>2</sub> nanoparticles and individual GO sheets, which facilitates delamination of rGO sheets after reduction as the attached TiO<sub>2</sub> particles keep them separated and the solution can be easily transferred or film-cast to a wide range of substrates.[118] The degree of reduction can be adjusted by changing the TiO<sub>2</sub> content and UV irradiation time. Lu et al. found that the maximum reduction degree of GO can be achieved by controlling the weight ratio (TiO<sub>2</sub>/GO) of 10 under 15 min UV irradiation.[120] Besides TiO<sub>2</sub>, ZnO/rGO nanocomposites also have been synthesized by UV-assisted photocatalytic reduction as the band structure of ZnO is close to TiO<sub>2</sub>. [121, 122] Moreover, the hybridization of rGO with immobilized ZnO nanorods can be achieved by this process as well.[123]

GO can be reduced solely by heat treatment in inert or reducing atmospheres,[124, 125] while the preparation of semiconductor materials always involves the annealing process. Thus, the GR- semiconductor hybrids can be obtained through a simple heat treatment. For example, the P25/GR composite was prepared was calcined the mixture of P25 and GO at 300 °C for 2 h under argon atmosphere with the heating rate 100 °C min<sup>-1</sup>. [126] Zhang et al. synthesized TiO<sub>2</sub>/GR composites using the tetrabutyl titanate and GO as the starting materials, then the obtained precursors were calcined at 450°C for 2 h. [127] They compared the products calcined under air and nitrogen atmospheres, and the formation of oxygen vacancies was observed in the sample annealed in nitrogen atmosphere, leading to higher photocatalytic activity. Zhang et al. obtained Zn<sub>0.5</sub>Cd<sub>0.5</sub>S/rGO nanocomposite simply through a heat treatment of their co-precipitation product with GO at 400°C for 3 h in Ar atmosphere.[128] This method was also used to prepare TiO<sub>2</sub>/GR [129]and ZnO/GR[130] photoanodes, by simple thermal treatment of the composite paste of GO and metal oxide coated on FTO glasses.

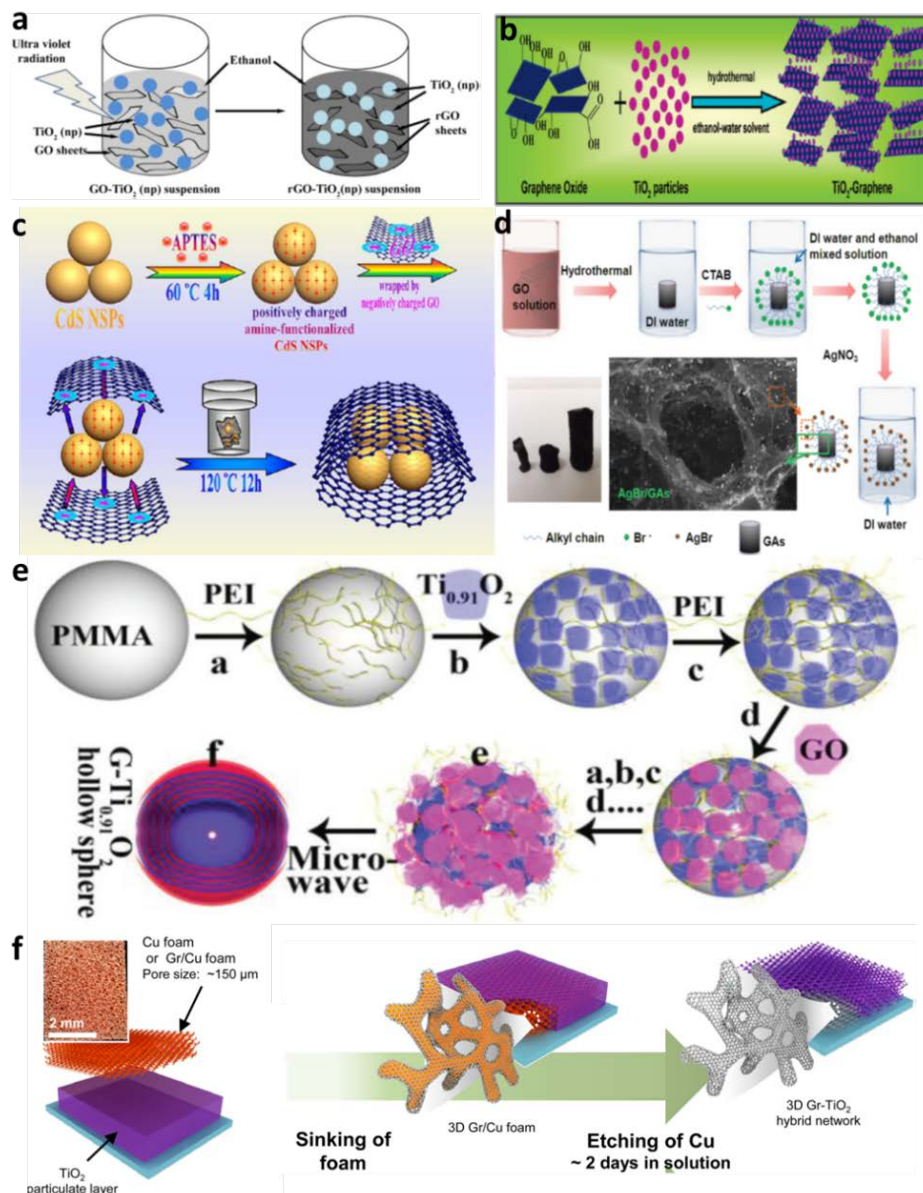


**Figure 2.3.** Schematic illustration of (a) preparation of graphene-TiO<sub>2</sub> nanocomposites through the photocatalytic reduction by the ultraviolet radiation of GO-TiO<sub>2</sub> nanoparticle suspension; (b) preparation of P25-GR nanocomposites by a hydrothermal treatment in the solvent of ethanol-water; (c) electrostatic self-assembly of uniform CdS/GR nanocomposites, followed by GO reduction via a hydrothermal treatment, (d) fabrication of the AgBr/GAs 3D photocatalytic composite materials and the different sizes adjusted by the volumes of the reaction vessels, (e) procedure for preparing the LBL-assembled multilayer-coated spheres consisting of titania nanosheets and GO nanosheets, followed by microwave reduction of GO into GR, and (d) the synthesis procedure of 3D GR-TiO<sub>2</sub> frameworks including transfer and subsequent sinking of 3D Gr/Cu foam completely into TiO<sub>2</sub> particulate layer followed by Cu etching process and subsequent annealing process. Reprinted with permission from ref.[119, 142-146] Copyright 2014 Elsevier Ltd., 2010 American Chemical Society, 2013 American Chemical Society, 2015 WILEY-VCH, 2012 WILEY-VCH, and 2015 American Chemical Society.

Chemical reduction is another approach to convert GO to rGO in the fabrication of GR-semiconductor nanohybrids. There are three ways for fabrication of GR based hybrid materials: (1) the reduction of GO is carried out firstly and then rGO is subjected to synthesis of GR-semiconductor nanocomposites; (2) the reduction of GO and the hybridization with semiconductor materials are accomplished simultaneously; (3) the hybridization of GO and semiconductor goes first and then the GO reduction is performed. Hydrazine [131-139] or sodium borohydride[127] is commonly employed as the reducing agents in the approaches (1) and (3). For example, TiO<sub>2</sub>/GR composites have been prepared using P25[131] or tetrabutyl titanate (TBOT) [127] and reduced GO as start materials at acidic condition. The ZnO/GR[132] and SiO<sub>2</sub>/GR composite were obtained through in situ chemical reduction of ZnO/GO and SiO<sub>2</sub>/GR hybrid with hydrazine, respectively. For these approaches, ultrasonic waves[133] and microwave [134] were also applied to control the particle size of crystalline TiO<sub>2</sub> and its homogeneous dispersion on the graphene sheets. Some green reductants, such as ascorbic acid (vitamin C)[140] and thiourea[141], can also be used to reduce GO for the preparation of GR based nanohybrids.

For approach (2), some chemicals consist of the building block of semiconductor materials also have the reduction capability to GO simultaneously. For example, it was found GO can be rapidly reduced at room temperature by TiCl<sub>3</sub>, which is also a precursor for the synthesis of TiO<sub>2</sub>. Zhu et al. reported a one-pot method for water-phase synthesis TiO<sub>2</sub>/rGO composites using TiCl<sub>3</sub> as both a reducing agent and a precursor.[147] During the synthesis, poly(N-vinyl-2-pyrrolidone)(PVP) was used to stabilize the as-prepared nanocomposite by the strong interaction between the negatively charged GO and Ti<sup>3+</sup>. Chen et al. also prepared TiO<sub>2</sub>/GO composites by using TiCl<sub>3</sub> and GO as reactants and sodium dodecyl sulfate (SDS) as disperser. [148] They found the concentration of GO in the starting solution have great effect on the crystalline quality and chemical states of carbon elements from GO in TiO<sub>2</sub>/GO composites, where GO could form as either a p-type or n-type semiconductor in the composites. Besides Ti<sup>3+</sup>, the redox reaction between the GO and the reactive cations Sn<sup>2+</sup> was also used to form SnO<sub>2</sub>/rGO composites.[149]

In addition, GO also can be reduce to GR through a hydrothermal route, which is also widely applied for the synthesis of semiconductor materials. The hydrothermal conversion method has several advantages over the common chemical reduction processes[150]: (1) it avoids the use of hazardous and strong reductant, like hydrazine, which inevitably introduces noncarbon impurities into the treated GO; (2) the closed system at relatively high temperature and

internal pressure promotes the recovery of  $\pi$ -conjugation after dehydration, which is favorable for minimizing defects; and (3) engineering the parameters of temperature and pressure affords a facile method to control the degree of reduction of the GO and the growth of semiconductor materials. Fan et al. have studied different techniques including UV-assisted photocatalytic reduction, hydrazine reduction, and hydrothermal method to prepare P25/GR nanocomposites and found the sample prepared by the hydrothermal method exhibited the best photocatalytic activity due to the strong interaction between P25 and RGO.[151] The hydrothermal temperature and time for the preparation of P25/GR nanocomposites (Figure 2.3b) are differently controlled from 120~180 °C and 3~24 h, respectively, and water and ethanol are normally chosen as the solvent.[142, 152-154]

Besides P25, titanium sources, such as TTIP,[155] TBOT,[156-158]  $\text{TiF}_4$ [15] and  $\text{TiCl}_4$ , [159, 160] can also be used for hydrothermal synthesis of  $\text{TiO}_2$ /GR to improve the interfacial contact between  $\text{TiO}_2$  and the GR surface. Different to P25, the mixture of these titanium sources and GO normally undergoes a sol-gel process to form  $\text{TiO}_2$ /GO precursor before the hydrothermal treatment. To control the hydrolysis of these titanium sources is critical for the property of  $\text{TiO}_2$ /GR products, because  $\text{TiO}_2$  oligomers generated by the rapid hydrolysis tend to aggregate into larger  $\text{TiO}_2$  nanoparticles, which will greatly decrease the surface-volume ratio of  $\text{TiO}_2$  and increase the diffusion length of photo-generated carriers. Thus, acidic condition,[155-157] organic solvents with small amount of water,[156, 158] or low temperature[157, 160] were applied to reduce their hydrolysis rate. The hydrothermal temperature are controlled at 180~220 °C, which is higher than the case of P25, and the time is maintained from 6~20h. Pure anatase  $\text{TiO}_2$  is formed in the  $\text{TiO}_2$ /GR composites when use TTIP or TBOT as titanium source, while anatase and rutile mixed phase is obtained when use  $\text{TiCl}_4$  because of the existence of Cl<sup>-</sup>. It was found the content of rGO in the composite would affect the ratio of anatase to rutile phase. [159, 160]

The precursors used in aforementioned works were unstable in water phase or sensitive to air which limited the  $\text{TiO}_2$  loading amount. To make  $\text{TiO}_2$  nanoparticles highly-distributed grow on the graphene sheets, some green chemical assistants can also be used during hydrothermal process to increase the use of active sites in GR. For example, Shen et al. prepared  $\text{TiO}_2$ /rGO composite by a one-step hydrothermal method using glucose as the reducing agent, which yield highly reduced suspensions in a way comparable to those provided by hydrazine.[161] They also reported the use of ionic liquid and ascorbic acid to improve the interaction between  $\text{TiO}_2$  and rGO during the synthesis.[162] The physical interaction of 1-butyl-3-

methylimidazolium hexafluorophosphate ([BMIM][PF<sub>6</sub>]) with the surfaces of GO makes ascorbic acid not only acts as dispersion and functionalization agents for GO, but also as active sites for the growth and decoration of nanoparticles on the surfaces of the GO.[162, 163] Shi et al. also attached peroxotitanium acid, a water soluble titanium precursor, to dextran reduced GO nanosheets by the hydrogen bond and van der Waals interactions, and then used hydrothermal method to prepare TiO<sub>2</sub>/rGO composite.[164] Gu et al. prepared TiO<sub>2</sub>/GR nanohybrids by a glucosamine-assisted hydrothermal strategy in alkaline conditions with TBOT and rGO as the start materials.[125] Glucosamine work as a morphology-controller agent and auxiliary dispersant, which can effectively regulate the growth and dispersity of TiO<sub>2</sub> nanoparticles on the graphene backbone.

Despite these improvements, the small TiO<sub>2</sub> nanoparticles tend to agglomerate and have poor interfacial contact with the GR surface because of the nanoparticle's nearly spherical shape. Other TiO<sub>2</sub> nanostructures with high surface area and enormous active sites, such as nanotubes (TNTs), nanowires (TNWs), nanofibers (TNFs), and hollow nanospheres (THNSs), can provide maximum interfacial contact with GR surface without aggregating, which is an essential factor for improving the photocatalytic and photovoltaic performance of GR-TiO<sub>2</sub> composites. Hydrothermal route is also widely used for the synthesis of these GR-based hierarchical composites. For example, Perera et al. prepared TNT/rGO nanocomposites by an alkaline hydrothermal process, which was achieved by decorating GO layers with commercially available TiO<sub>2</sub> nanoparticles (P90) followed by hydrothermal synthesis to converts the P90 to small diameter (~9 nm) TNTs on the deoxygenated rGO surface.[165] Zhai et al. obtained rGO modified TNT electrode by vapor-thermal treatment of highly ordered TNT arrays with GO solution.[166] In the TNF/rGO nanocomposite obtained from hydrothermal treatment of TNWs and GO, TNWs have more uniform distribution on GR sheets with less agglomeration, resulting in more direct contact between TiO<sub>2</sub> and GR.[167] Zhang et al. synthesized THNS/GR nanocomposites by direct hydrothermal treatment (120 °C, 24h) of the THNS and GO homogeneous suspension.[168] To improve the interaction between TiO<sub>2</sub> and GO, some coupling agents were applied before hydrothermal treatment. For example, Yan et al. prepared a rGO wrapped THNSs hybrid composite by using poly(L-lysine) (PLL) and ethylene glycol (EG) as coupling agents.[169] Moreover, amine functional groups are often introduced onto the surface of TiO<sub>2</sub> structure through the 3-aminopropyltriethoxysilane(APTMS) treatment, after which TiO<sub>2</sub> and GO can assemble together via peptide bond (-CONH-) formation.[170-172] For instance, GR wrapped

hierarchical THNSs[171] and TiO<sub>2</sub> nanospheres (TNSs)[170] have been prepared by the hydrothermal treatment of GO wrapped amine-modified THNSs and amorphous TNSs, respectively. Instead of hydrothermal process, Zhang et al. also prepared GR encapsulated mesoporous THNSs via a novel GR protected calcination process, where the GO-amine-modified SiO<sub>2</sub>@TiO<sub>2</sub> nanospheres were calcined to transform the TiO<sub>2</sub> layer into anatase TiO<sub>2</sub> along with thermal reduction of GO, and the inner SiO<sub>2</sub> template was final etched by NaOH.[172] It was found GR plays a substantial role in inhibiting the aggregation of TiO<sub>2</sub> grains during the high-temperature treatment. In addition, Tu et al. fabricated robust hollow nanospheres consisting of alternating negatively charged titania (Ti<sub>0.9</sub>O<sub>2</sub>) nanosheets and GO nanosheets by a layer-by-layer (LbL) assembly technique with poly (methyl methacrylate) (PMMA) beads as sacrificial templates using a microwave irradiation technique to simultaneously remove the template and reduce GO into GR (Figure 2.3e).[145] Electrospinning is often applied to prepare TNF/GR nanocomposites. Nasr et al. elaborated TNF/rGO composite by electrospinning GO and titanium precursor mixture solution and followed by calcined at 500 °C in N<sub>2</sub> environment, in which the presence of rGO sheets decreased the band gap energy of TNFs from 3.2 to 2.9 eV.[173] Lavanya et al. also prepared TNF/rGO hybrid by wrapping GO onto electrospinning-obtained anatase TNFs[174] or anatase/rutile mixed phase TNFs[175]. It was found low reduction temperature (around 300~500°C) is essential for the wrapped structures when 2–4 layers of rGO were present on the surface of nanofibers. [174] Moreover, ZrO<sub>2</sub>-doped TiO<sub>2</sub> NFs was also prepared by electrospinning, which was further used for GO loading through hydrothermal approach.[176] In addition to TiO<sub>2</sub>, other semiconductor materials were also used to hybridize with GR by hydrothermal route. Metal oxides, such as ZnO,[177, 178] MgO,[179] Nb<sub>2</sub>O<sub>5</sub>,[180], SrTiO<sub>3</sub>,[181] ZnSnO<sub>3</sub>,[182] and SrNb<sub>6</sub>O<sub>16</sub>,[183] have been combined with GR through the hydrothermal method. Similar to CNTs, GR/metal sulfide nanocomposites were mainly synthesized by hydrothermal method. Both synthesized metal sulfide particles and its precursor solutions can undergo the hydrothermal process with GO for preparation of GR based nanohybrids. For example, the CdS/GR nanocomposite was prepared by a facile hydrothermal treatment (120°C, 12h) of the CdS and GO aqueous mixture. [184] Chen et al. used the electrostatic assembly of positively charged CdS nanospheres (treated (3-aminopropyl)-triethoxysilane (APTES)) with negatively charged GO before the hydrothermal treatment to achieve the intimate interfacial contact between CdS and the GR sheets (Figure 2.3c). [143] In the simultaneous case of sulfide synthesis (such as ZnS,[185] CdS,[186]

NiS[187] and CoS<sub>2</sub>[188, 189]) and GO reduction, higher hydrothermal temperature is required, normally from 130~180 °C. For the synthesis of MoS<sub>2</sub>/GR nanocomposites, 200~240 °C hydrothermal temperature and 24h hydrothermal time were applied. [190, 191] Thiourea is widely used as the sulfur source for the synthesis of metal sulfide, which undergo the thermal hydrolysis/dissociation during the hydrothermal process. [188, 190, 191] Other sulfur sources, like Na<sub>2</sub>S,[185] dimethyl sulfoxide (DMSO),[186] sulfur powder,[187] and thioacetamide,[189] were also reported. Among them, DMSO also works as the dispersant to obtain homogeneous GO-DMSO dispersion. [186] Moreover, CoSe/GR nanocomposites were also fabricated by a simple low-temperature(120 °C, 12h) hydrothermal method using CoCl<sub>2</sub>, Se ultrafine and GO as the start materials.[192]

Other methods also have been reported to prepare GR-semiconductor nanocomposites. For example, the ZnO/GR nanocomposite was synthesized by the electrolysis method, where GR was first prepared by electrolysis of graphite rod and activated by sulfuric acid treatment, and then ZnO nanoparticles was deposited onto GR sheets by electrolysis.[193] CoS/GR or CoS/GO hybrid film has been prepared by repeating electrophoretic deposition (EPD) of GR or GO sheets and deposition of CoS nanoparticles on FTO via the successive ionic layer adsorption and reaction (SILAR).[194, 195] Low et al. prepared TiO<sub>2</sub>/rGO photoanodes by using metal plasma ion implantation approach to incorporate Ti<sup>4+</sup> ion onto the rGO nanosheets.[196] NiO/GR hybrid films have been fabricated by pulsed laser deposition (PLD)[197] and dry plasma reduction[198]. Biris et al. fabricated TiO<sub>2</sub>@GR core-shell nanostructures by CVD GR over P25 with methane as the carbon source.[199] The amount of GR shells covering the TiO<sub>2</sub> surfaces was found to vary linearly with the reaction time. Both TiO<sub>2</sub> and Al<sub>2</sub>O<sub>3</sub> layers also have been reported grown on GR nanosheets by atomic layer deposition (ALD) method.[200-203]

For two-dimensional (2D) GR or GO, physical contacts of the active materials to graphene sheets usually occur on only one-side plane, and thereby the carrier transport is dominantly restricted to the planar direction. On the other hand, three-dimensional (3D) GR possesses many additional interesting properties, such as divergent pathways for heat and electrons transport, increased surface area, control over size and shape, and ease of handling and reuse. Thus, developing of 3D GR- semiconductor hybrid materials has attracted increasing attention recently. It was GO can form 3D graphene hydrogel(GH) or aerogel(GA) structure by various supramolecular interactions including hydrogen bonding, coordination, electrostatic interaction, and  $\pi$ - $\pi$  stacking. Cong et al. developed GR/ $\alpha$ -FeOOH and magnetic

GR/Fe<sub>3</sub>O<sub>4</sub> hydrogels under the synergistic effects of the reduction of GO by ferrous ions and in situ simultaneous deposition of nanoparticles on graphene sheets in the pH controlled solvothermal process.[204] 3D P25/GH[205] and CuS/GH[206] have been prepared by a facile one-pot hydrothermal treatment of the mixture dispersion of GO and semiconductor particles at 180°C, in which GR nanosheets and the semiconductor nanoparticles self-assembled into 3D interconnected networks. Qiu et al. found using glucose as the dispersant and linker during the hydrothermal process could make ultra-dispersed mesoporous TiO<sub>2</sub> nanocrystals with exposed (001) facets grow in situ on a 3D GA surface. [207] Fan et al. further used the hydrothermal obtained GA and cetyltrimethylammonium bromide or chloride (CTAB or CTAC) to synthesize 3D AgX/GA(X = Br, Cl) structure (Figure 2.3d), in which the AgX NPs were firmly and uniformly distributed throughout the surface of the 3D GA's hierarchically porous structure.[144] Zhu et al. prepared 3D GR frameworks (GFs) by the rapid decomposition of fumaric acid particles in the presence of Na<sub>2</sub>CO<sub>3</sub>, which was further used to load CuS nanocrystals through an in-situ hydrothermal process.[208] Moreover, 3D GR structure can also be obtained from template method. Ni foam is often used as scaffold to grow 3D GR during CVD, which can be further applied to attach TiO<sub>2</sub> nanoparticles to form 3D TiO<sub>2</sub>/GR structures. [209, 210] However, using Ni foams are usually resulted multilayered graphene networks, in which their vertical stacking easily makes them opaque, thereby limiting their photocatalytic and photovoltaic applications. Lee et al. used Cu foam matrices for CVD growth GR and obtained a mostly single layer conformal coating of GR, which can be used to loading TiO<sub>2</sub> nanoparticles (Figure 2.3f).[146] After Cu etching, the obtained 3D TiO<sub>2</sub> nanostructures with encapsulated monolayer graphene networks showed good carrier mobility and enhanced light harvesting. Besides metal foams, polymer template can also be applied to construct 3D TiO<sub>2</sub>/GR frameworks. For example, Kim et al. prepared GR-embedded 3D TiO<sub>2</sub> inverse opal electrodes by using Polystyrene (PS) colloidal crystal templates to scaffold GO–TiO<sub>2</sub> mixture, and followed by template removing and GO reduction.[211]

To meet the high requirements of photocatalytic and photovoltaic application, third or fourth component is often introduced into the binary GR-semiconductor hybrid to form multifunctional ternary or quaternary composites.

Non-metal elements doping is an important approach to tailor the property of both semiconductor materials and GR. Carbon or nitrogen doping is more sustainable as they are earth abundant elements, which are widely used to narrow the band gap of semiconductor

expanding their light responsive or to increase the electrical conductivity of GR. Carbon-doped  $\text{TiO}_2(\text{C-TiO}_2)$ [212] and nitrogen-doped  $\text{TiO}_2(\text{N-TiO}_2)$  [213] have been applied to hybridize GR through the hydrothermal reaction with GO. Nitrogen doping also can be achieved during the synthesis of GR-semiconductor nanocomposites. For example, N-ZnO/GR[214] and N-TiO<sub>2</sub> nanoplate/GR have been prepared by a sol-gel process with GO using urea and  $\text{NH}_4\text{F}$  as the nitrogen source, respectively. Urea and ammonia were also respectively used to synthesized the N-GR/NiO[215] and quasi core-shell CoS/N-GR[216] hybrids by hydrothermal or solvothermal approach. Mohamed et al. prepared GO/N-SnO<sub>2</sub>/TiO<sub>2</sub> nanofibers via the two-step electrospinning-hydrothermal method with urea as nitrogen source.[217] Besides, nitrogen also can be introduced into GR-semiconductor hybrids through a one-step annealing treatment process under  $\text{NH}_3$  atmosphere, during which GO are reduced to RGO simultaneously.[218, 219]

Doping of metal cations is another means of bandgap engineering to shorten the wide bandgap of semiconductor into the visible region and noble metal NPs (e.g. Au, Ag, Pt) are able to serve as irreversible electron sinks, which remarkably inhibit the recombination of photogenerated electron-hole charge carriers. Meanwhile, when metallic nanoparticles are smaller than wavelength of exciting light, surface plasmons would be induced by the oscillation of conduction electrons with the electric field of light, which is beneficial in improving light absorption and charge collection. Many metal elements have been used to decorate GR- semiconductor nanohybrids. For instance, vanadium(V), [220] cerium ion (Ce), [221] copper(Cu) [222] and praseodymium (Pr) [223] cations have been reported as the doping metal elements to incorporate into GR/TiO<sub>2</sub> hybrids through sol-gel or hydrothermal method. Among them, Pr-TiO<sub>2</sub>/NGO (nanosized GO, less than 500 nm in lateral size) exhibited remarkably higher absorbance at the near infrared (NIR) wavelength region due to the reduction of NGO during the hydrothermal treatment for nanocrystal growth.[223] Besides, Qiu et al. reported a one-step vacuum thermal technology for preparing  $\text{Ti}^{3+}$  self-doped TiO<sub>2</sub>/GR composite using GO and P25 as the start materials.[224] Except for mechanical blending, [225] a reduction process of metal cation is always involved for metal NPs loading onto GR- semiconductor nanocomposites. The reduction means can be hydrothermal,[226, 227] UV-assisted photocatalytic reduction, [228, 229] and chemical reduction. [230-233]  $\text{NaBH}_4$  is commonly used as reducing agent. For example, Surendran et al. prepared Ag/RGO/ZnO nanocomposite via two-step microwave irradiation method and used  $\text{NaBH}_4$  to reduce  $\text{Ag}^+$ .[231] Besides, PVP was also reported as reducing agent during

the sol-gel synthesis of GO/TiO<sub>2</sub>/Ag/AgCl or GO/SiO<sub>2</sub>/Ag/AgCl. [234, 235] Moreover, a laser-based technique, ultraviolet matrix assisted pulsed laser evaporation (UV-MAPLE) method, also have been applied to prepare TiO<sub>2</sub>/Au/rGO[236] and TiO<sub>2</sub>/Ag/rGO[237] films. Electrochemical deposition method has been used for to deposit Na<sub>3</sub>[Ag(S<sub>2</sub>O<sub>3</sub>)<sub>2</sub>] GO colloidal onto TiO<sub>2</sub>NTs arrays to form dispersion rGO/Ag-TiO<sub>2</sub>NTs.[238]

Coupling two or three semiconductor materials with GR is another effective approach to overcome the limitation of GR based binary composites. For example, introducing of low band gap semiconductors (such as BiVO<sub>4</sub> (2.4–2.9 eV), BiOI (1.8 eV), CdS (2.4 eV), Sb<sub>2</sub>S<sub>3</sub> (1.74 eV) and g-C<sub>3</sub>N<sub>4</sub> (2.7 eV)) into GR-semiconductor binary composites by band structure engineering can improve the light harvesting, and the adding of some magnetic metal oxides (such as Fe<sub>3</sub>O<sub>4</sub>, ZnFe<sub>2</sub>O<sub>4</sub> and MgFe<sub>2</sub>O<sub>4</sub>) can make the separation and reuse/recycling of the photocatalyst from the waste water more easier and avoid the a new type of pollution. These are many kinds of method applied to fabricate these ternary or quaternary composites. For instance, rGO/Fe<sub>3</sub>O<sub>4</sub>(or magnetite)/TiO<sub>2</sub> hybrids can be synthesized simply by a wet chemical method[239] or an aerosol-based approach in a furnace aerosol reactor(FuAR) (Figure 2.4a).[240] Chen et al. prepared a Fe<sub>3</sub>O<sub>4</sub>@SiO<sub>2</sub>@TiO<sub>2</sub>/GO core/shell structure by a sol-gel process using APTES as covalent link to bond GO and Fe<sub>3</sub>O<sub>4</sub>@SiO<sub>2</sub>@TiO<sub>2</sub>.[241] Feng et al. also prepared ZnFe<sub>2</sub>O<sub>4</sub>@rGO@TiO<sub>2</sub> nanocomposite via an electrostatic layer-by-layer route followed by thermal calcine to form TiO<sub>2</sub> and reduce GO.[242] Microwave irradiation method was also reported to synthesize rGO/ZnWO<sub>4</sub>/Fe<sub>3</sub>O<sub>4</sub> nanocomposite.[243] RGO/BiVO<sub>4</sub>/TiO<sub>2</sub> nanocomposite have been fabricated by ultrasonic wave-assisted one pot hydrothermal method[244] or by deposition of BiVO<sub>4</sub>/GO solution onto the surface of sol-gel derived TiO<sub>2</sub> film followed with UV reduction.[245] The 3D flower-like SnS<sub>2</sub>-MgFe<sub>2</sub>O<sub>4</sub>/rGO[246], TiO<sub>2</sub>/SnS<sub>2</sub>/GR [247] and CdS-TiO<sub>2</sub>/rGO[248] nanocomposites have been prepared by one or twostep magnetic photocatalyst hydrothermal (or solvothermal) method. Dutta et al. used glutathione acting both as a reducing agent for GO and sulfur donor for CdS during the hydrothermal synthesis of CdS/TiO<sub>2</sub>/rGO and found that the pH variation evolved two distinctly different semiconducting nanocrystals of anatase/rutile TiO<sub>2</sub> and hexagonal yellow/cubic red CdS.[249] The dandelion-flower-like cobalt-phosphide(CoP) embedded with CdS nanostructures grown on rGO-MoS<sub>2</sub> nanosheets was fabricated via a hydrothermal route combined with a homogeneous chemical precipitation process (Figure 2.4b).[250] The rGO/BiOI/AgI hybrids was aslo prepared by precipitation method.[251] The g-C<sub>3</sub>N<sub>4</sub>/BiOI/GO was obtained by liquid mixing GO with hydrothermal obtained g-

C<sub>3</sub>N<sub>4</sub>/BiOI[252], while g-C<sub>3</sub>N<sub>4</sub>/CdS/RGO was got through the aqueous chemical method.[253] Moreover, ternary films also can be achieved by combining two or three different methods. For example, the TNTs/rGO/CdS film was obtained by electrophoretic deposition (EPD) of GO onto TiO<sub>2</sub> nanotube arrays and followed by successive ionic layer adsorption and reaction (SILAR) to grow CdS.[254] The GR/CuS/PbS nanocomposite film was also prepared by SILAR method to deposit CuS and PbS layers on the GR pre coated FTO substrates.[255] Chemical bath deposition (CBD) was used to grow Sb<sub>2</sub>S<sub>3</sub> onto the rGO coated TiO<sub>2</sub> nanorod arrays to form TiO<sub>2</sub>/rGO/Sb<sub>2</sub>S<sub>3</sub> hybrid film.[256]

Due to the different advantages of carbon nanomaterials, the combination different carbon materials into GR-semiconductor is expected to obtain novel compound materials with good performance. For example, the combination of CNT and GR could provide a large surface area by preventing stacking of GR and bundling of CNT, which also offers an excellent electron pathway to decrease the recombination rate of photoinduced electron-hole pairs. Activated semi-coke supported TiO<sub>2</sub>-rGO (TiO<sub>2</sub>/rGO/ASC), [257] TiO<sub>2</sub>/rGO/Ac,[258] and TiO<sub>2</sub>/CNTs/rGO[259] composites have been synthesized through one-pot hydrothermal method. Dong et al. prepared TiO<sub>2</sub>/CNT nanocomposites immobilized on thin graphite plate via sol-gel method, where MWCNTs were synthesized from thermal decomposing of hydrocarbon gas directly on thin graphite plate.[260] The urea-glass route was also applied to synthesize metal nitrides or carbides/CNT-GR nanocomposites, where metal precursor (such as TiCl<sub>4</sub>, MoCl<sub>5</sub> and WCl<sub>4</sub>) in a first step contacted with alcohols containing CNT and GO and then adding an appropriate amount of urea to form a polymer-like, glassy phase, which acts as the starting product for further conversions. After heating this phase it was possible to prepare either nitrides or carbides simply by changing the urea/metal precursor molar ratio (R). For example, TiN/CNT-GR was prepared with R=5 [261] and Mo<sub>2</sub>N/CNT-RGO was obtained with R=1. [262] It was also possible to synthesize Mo<sub>2</sub>C or MoS<sub>2</sub> instead of Mo<sub>2</sub>N by increasing R value to 8 or replacing urea with thiourea (R = 2) to result Mo<sub>2</sub>C/CNT-RGO, and MoS<sub>2</sub>/CNT-RGO composites, respectively (Figure 2.4).[262]



**Figure 2.4.** Schematic diagram of (a) the FuAR setup and the synthesis process of rGO/magnetite/TiO<sub>2</sub>, (b) the synthesis of cobalt-phosphide-modified CdS/RGO-MoS<sub>2</sub> nanocomposites. (c) Preparation routes of the Mo-compound/CNT-RGO composites with corresponding TEM images. Reprinted with permission from ref.[240, 250, 262] Copyright 2014 American Chemical Society, 2016 The Royal Society of Chemistry 2016 and 2013 WILEY-VCH.

In addition, some conductive polymers or functional organic molecules also have been researched to incorporate into GR-semiconductor hybrids. Polyaniline (Pani) is a conductive polymer with  $\pi$ -conjugate long-chain, which has shown good chemical stability, high absorption coefficient and mobility of charge carriers under the irradiation of visible light. The synthesis of Pani is facile and low cost. Pani/TiO<sub>2</sub>/GR[263] and Pani/ZnFe<sub>2</sub>O<sub>4</sub>/rGO[264] nanocomposites have been prepared by the in situ oxidative polymerization of aniline. Porphyrins can absorb a wide range of the solar spectrum owing to their strong absorption and in both visible and near infrared regions. Zargari et al. reported the synthesis of tin porphyrin (SnTCPP·Cl<sub>2</sub>) intercalated TiO<sub>2</sub>/GR nanocomposite intercalated simply by refluxing TiO<sub>2</sub>/GR and SnTCPP·Cl<sub>2</sub> in DMF.[265] TiO<sub>2</sub>/ $\beta$ -cyclodextrin/GR nanocomposite was synthesized by a simple water phase approach at 90 °C, in which  $\beta$ -cyclodextrin can stabilize GR in aqueous medium facilitating the self-assembly of in situ grown anatase TiO<sub>2</sub> NPs on GR nanosheets.[266]

Beside above mentioned, other materials were also reported for decoration of GR--semiconductor hybrids. Some upconversion (UC) materials were used to improve the utilization of photo energy, in which the sequential absorption of two or more low energy photons leads to the emission of a high energy visible photon. For example, UC materials ( $\beta$ -

NaYF<sub>4</sub>:Yb<sup>3+</sup>, Tm<sup>3+</sup>/N-P25/GR, [267] NaLuF<sub>4</sub>:Gd,Yb,Tm@SiO<sub>2</sub>@CeO<sub>2</sub>:Tm/GR[268] has been fabricated successfully via hydrothermal or solvothermal method, which extend the light-responsive range of composites to the NIR region. Yao et al. also prepared a hierarchical structure by coating porous TiO<sub>2</sub>:Al<sub>2</sub>O<sub>3</sub>:Eu<sup>3+</sup> NPs onto vertically grown one-dimensional TiO<sub>2</sub>:Er<sup>3+</sup>,Yb<sup>3+</sup> nanorods on FTO substrates coated with a TiO<sub>2</sub>/GR seed layer, in which UC material TiO<sub>2</sub>:Er<sup>3+</sup>,Yb<sup>3+</sup> and the downconversion (DC) material Al<sub>2</sub>O<sub>3</sub>:Eu<sup>3+</sup> facilitate the light harvesting via converting NIR and UV radiation to visible emission, respectively.[269] Hydroxyapatite (Ca<sub>10</sub>(PO<sub>4</sub>)<sub>6</sub>(OH)<sub>2</sub>, HA), which has a similar chemical composition to the mineral component in natural bones and teeth and can promote adhesion of microorganisms on the material surface, has also been used to prepare TiO<sub>2</sub>/HA/rGO composite coating through a liquid precipitation approach followed by liquid flame spray deposition. [270] The nanocomposites composed by a pure inorganic donor–acceptor (D–A) type polyoxometalate K<sub>6</sub>H<sub>4</sub> [α-SiW<sub>9</sub>O<sub>37</sub>Co<sub>3</sub> (H<sub>2</sub>O)<sub>3</sub>]·17H<sub>2</sub>O (SiW<sub>9</sub>Co<sub>3</sub>), rGO and P25 also has been reported.[271]

#### 2.2.4 Fullerene

Fullerenes is recognized as the additions to amorphous, graphite and diamond forms, a fourth form of the solid carbon, which have structural variations from smallest member C<sub>20</sub> (unsaturated version of dodecahedrane) to the most common C<sub>60</sub> and higher number (i.e., C<sub>70</sub>, and C<sub>84</sub>). Fullerene-semiconductor composites have attracted increasing attention because fullerenes contain an extensively conjugated 3D π system and have a high electron affinity and mobility, which can act as an excellent electron acceptor causing a rapid photoinduced charge separation. Besides, the band gap fullerene energy (1.6–1.9 eV), which has strong absorption in the UV region and weak but significant bands in the visible region.

Sol–gel method and hydrothermal method are two commonly used methods for preparation of fullerene-semiconductor hybrid, especially TiO<sub>2</sub>/C<sub>60</sub>. Similarly to CNTs, the chemical oxidation to functionalize the fullerene surface through refluxing in acid solution is necessary before the hybrid preparation. The m-chloroperbenzoic acid (mCPBA)-benzene system was widely used for this purpose[272-277] and sulfuric acid[278], nitric acid[279, 280] or their mixture[281] were also reported. After activation, many metal elementals such as V[272], Y[276, 282],Fe[277, 283] and Pt[273, 282] can be introduced into fullerene to form M-fullerene. For the sol-gel synthesis of TiO<sub>2</sub>/C<sub>60</sub> or TiO<sub>2</sub>/M-C<sub>60</sub>, TBOT was the often used as the Ti precursor, which can be diluted in alcohols or aqueous solution as the same as the

standard sol-gel procedures,[272, 284] or directly used without adding other solvent[273, 276, 277, 282, 283] or added into toluene[285] to mix with fullerene. The above solution were stirred at certain temperature to form a gel and followed by heating at high temperature (500-600 °C) to obtain the final composite. In addition,  $\text{WO}_3/\text{C}_{60}$ , [274]  $\text{CdSe-C}_{60}/\text{TiO}_2$ [275] and  $\text{MoO}_3\text{-TiO}_2/\text{fullerene}$ [284] hybrids have also been prepared by sol-gel method. In hydrothermal method, the titanium sol mixed with fullerene was transfer into autoclave and heated at certain temperature (100-180°C) for a period of time to get the composite. TBOT,[280, 286]  $\text{TiCl}_4$ [278, 281] and titanium sulfate ( $\text{Ti}(\text{SO}_4)_2$ )[279, 287, 288] could be used as the titanium source, in which CTAB was used as assistant in the case of  $\text{Ti}(\text{SO}_4)_2$ . Except  $\text{TiO}_2/\text{C}_{60}$ ,  $\text{TiO}_2/\text{C}_{70}$ ,[279, 288]  $\text{CoS}_2/\text{C}_{60}$ ,[289]  $\text{Bi}_2\text{MoO}_6/\text{C}_{60}$ ,[290]  $\text{PbMoO}_4/\text{C}_{60}$ ,[291]  $\text{C}_{60}\text{-SWCNTs}/\text{TiO}_2$ [287], and  $\text{MWCNT}/\text{TiO}_2/\text{C}_{60}$ [278, 281] have been fabricated by hydrothermal method.

Fullerene-semiconductor hybrid can also be obtained via chemical bonding due to the –COOH functional group formed on the surface of fullerene after acid treatment. For example,  $\text{TiO}_2$  NWs/fullerene-COOH[292] and  $\text{CdSe}/\text{C}_{60}$ [275] were formed through interfacial chemical bonding in solution. The  $\text{C}_{60}$  aminofullerene could be immobilized onto 3-(2-succinic anhydride) propyl functionalized silica gel through amide bond.[293] The  $\text{C}_{60}/\text{SiO}_2$  composite could also be prepared through the nucleophilic attack of a terminal amine (propyl-amine functionalized silica gel) onto pristine  $\text{C}_{60}$ 's cage under fluorescent light irradiation.[294] Lian et al. employed an evaporation induced self-assembly route with Pluronic F127 to fabricate  $\text{C}_{60}\text{-CdO}/\text{TiO}_2$  followed by an ionexchanged method to form  $\text{C}_{60}\text{-CdS}/\text{TiO}_2$  mesoporous architectures.[295] In addition, other method also have been applied to prepare fullerene-semiconductor composite. For example,  $\text{CdO}/\text{C}_{60}$ [295] and  $\text{Ag}_2\text{S}/\text{C}_{60}$  were prepared via a precipitation process. Single  $\text{C}_{60}$ -amorphous  $\text{TiO}_2$  nanocomposites of  $\text{TiO}_2$  can be prepared by atomic layer deposition (ALD),[296] and  $\text{C}_{60}$  also have been thermal deposited onto the nanostructured  $\text{SrTiO}_3(001)$  surfaces.[297] Besides, the electrophoresis deposition technique can also be used to deposit  $\text{C}_{60}$  onto  $\text{TiO}_2$  nanotube array growth on conductive substrate.[298]

### 2.2.5 Carbon dots

Carbon dots (CDs) including carbon nanodots (CNDs), carbon quantum dots (CQDs), and graphene quantum dots (GQDs) are a new class of carbon nanomaterials with sizes below 10 nm, which have attracted wide attention due to their fascinating properties as well as

abundant and inexpensive nature.[299-301] CNDs are normally referred to amorphous quasi-spherical nanodots which lack quantum confinement, while the nanodots present quantum confinement and crystalline structure can be distinguished between the spherical quantum dots referred to as CQDs and the  $\pi$ -conjugated single sheet referred to as GQDs. The coupling of CDs with semiconductor materials has great potential applications in the photocatalytic and photovoltaic areas as CDs possess distinct properties such as effective absorbance of solar light, tunable photoluminescence (PL), infrared-responsive up-converted photoluminescence (UCPL) and unique photoinduced electron transfer.[300, 302, 303]

The synthesis of CD-semiconductor hybrids can be divide into two approaches: ex situ technique and in situ technique. The ex situ approach can be further divide into three different processes. (1) CDs are prepared firstly and then are added into the synthesis process of semiconductor to form hybrid materials. The fabrication of CDs can generally be classified into “Top-down” and “Bottom-up” approaches, which have been well summarized in other review papers.[300, 301] Alkali-assisted electrochemical etching from graphite rods [304-310] and modified Hummer’s method [311-314], etc., in which CDs are synthesized from macroscopic carbon structures, can be defined as Top-down approach. Bottom-up approaches prepare CDs from molecular precursors, such as alkali-assisted ultrasonic treatment of glucose, [315, 316] dehydration of  $\gamma$ -butyrolactone,[317] pyrolysis of L-cysteine[318] or citric acid,[319] microwave synthesis, [320, 321] hydrothermal/solvothermal treatment of organic acids or various biomass-derived precursors, [322-333] etc. The size control and uniformity of CDs can be optimized via post-treatment, such as column chromatography separation [304-306] membrane dialysis [309-311, 315, 316, 320, 322, 326] and centrifugation.[307, 308] The obtained CDs are then introduced into the preparation of semiconductor, such as commonly used sol-gel and hydrothermal method. For example, CD/TiO<sub>2</sub> has been synthesised by so-gel using TBOT and CDs as start materials. [304] The nanohybrids of CDs/Fe<sub>2</sub>O<sub>3</sub>[305], Bi<sub>2</sub>MoO<sub>6</sub>/CDs, [334] WO<sub>3</sub>/CDs[326] and CD/TiO<sub>2</sub>[324] have been fabricated via hydrothermal method. Besides, Cu<sub>2</sub>O/CD nanohybrid was obtained by using CDs to reduce a copper–ammonium complex[331] and CD/Ag<sub>3</sub>PO<sub>4</sub> was fabricated through precipitation of Ag<sub>3</sub>PO<sub>4</sub> with CDs in solution. [306] (2) Semiconductor materials are synthesised first and then the obtained products are subjected to the preparation of CDs. For instance, CD/TiO<sub>2</sub> NWs was fabricated by hydrothermal treatment of the synthesized TNWs dispersion with vitamin C. [322] The TiO<sub>2</sub> film coated on FTO also could undergo a hydrothermal process in the solution of citric acid and ethanediamine to form a CD/TiO<sub>2</sub>

hybridized photoanode.[335] (3) CDs and semiconductor materials are synthesized independently first and then the two materials are coupled together through the post treatment. Impregnation or dip-coating is the most common method to get CD-semiconductor hybrids, simply immersing the semiconductor NPs or films into CDs solution to get CDs deposited on their surface. [308, 310-312, 314, 323, 333, 336] To improve the interaction between CDs and semiconductor materials, a reflux strategy (normally 90 °C for 3h) [307, 316, 325, 337] or a hydrothermal process [309, 320, 327, 338] was also applied to their mixture suspension. In addition, spin-coating was also reported to fabricate CD-semiconductor hybrid films. [313] In the in situ approach, the synthesis of CDs and semiconductor was carried out simultaneously. For example, the CD/Cu<sub>2</sub>O hybrids were prepared through one-step ultrasonic treatment of copper precursor with glucose. [315] The CD/TiO<sub>2</sub> composites were synthesized by a hydrothermal treatment of the mixture including citric acid, glycerol and TBPT.[324]

In addition of above approaches, the CD/CdS multilayered films grown on ITO glasses were fabricated by repeating the two steps: electrophoretic deposition of CDs and sequential chemical bath deposition of CdS from CdCl<sub>2</sub> and Na<sub>2</sub>S aqueous solution.[318]

### **2.3 Photo-degradation of pollutants**

Heterogeneous photocatalysis have been given considerable attention and in the past two decades due to its efficiency in degrading recalcitrant organic compounds. Semiconductor materials, such as TiO<sub>2</sub> and ZnO, are commonly chosen as photocatalysts because under illumination of incident light with photon energy higher than their band gap, the electrons in the valence band (VB) can be injected into the conduction band (CB) leaving behind the same amount of holes in the VB, which are powerful reducing and oxidizing agents, respectively. However, the use of bare TiO<sub>2</sub> or ZnO is limited because of their wide band gap and the high recombination rate of photogenerated charges. Coupling with carbon materials is an emerging strategy to improve the photocatalysis ability of bare semiconductors from three aspects: (1) enhancing the surface absorption of organic pollutants due to the large surface area of carbon materials, (2) benefiting the separation of photo-generated carriers owing to the excellent electro-conductivity of carbon materials, and (3) narrowing the band gap to make visible light responsive semiconductor materials.

### 2.3.1 Amorphous carbon

Many studies have showed that incorporation amorphous carbon into semiconductor nanostructures can improve the degradation rate of organic pollutants. The photocatalytic efficiency depends on several parameters such as the carbon loading amount and the morphology of semiconductor materials.

Carbon-decorated nanocrystalline  $\text{TiO}_2$  is widely used as photocatalysts for the pollutant degradation in water treatment. For example, the  $\text{TiO}_2$ /carbon composites showed the superior photocatalytic activity under UV irradiation toward both methylene blue (MB) and selected pharmaceuticals in multicomponent solution by enhancing the pollutant adsorption resulted from the higher surface area with carbon adding.[51] Moustakas et al. also tested the  $\text{C@TiO}_2$  powder for the degradation of MB under UVA (350–365 nm), visible (440–460 nm), and daylight (350–750 nm) illumination, which showed outperforms over the Degussa P25 and excellent photocatalytic reproducibility.[44] The carbon content in the nanocomposites have great influence on their photocatalytic activity. In the  $\text{TiO}_2$ -PEG-Ac system, the composite with 0.5% Ac loading showed significant improvement in photocatalytic degradation of methyl orange (MO) as compared to  $\text{TiO}_2$  alone or with other Ac contents.[58] For the r- $\text{TiO}_2$ /C nanocomposites, it was found that the Rhodamine B (RhB) degradation efficiency depended on the amount of glucose using, in which the composite using 1.5 mmol glucose achieved 92% degradation after 70 min under visible light irradiation, further increasing the amount of glucose would reduce the photocatalytic activity.[53] Indeed, moderate carbon content in the composite would promote the surface adsorption of dye molecules, improve the light harvest and facilitate the generation of electrons. However, further increased carbon content would result in a loss of the diffusion rate of dye and the light arriving on the catalysis surface.

The morphology of semiconductor materials also plays an important role in the photocatalytic activities of nanocomposite because of different pore sizes, surface area and electron transport paths for different shapes. For instance, the photocatalytic activity of  $\text{TiO}_2$ /C@ $\text{TiO}_2$  core-shell nanocomposite on degradation of RB under UV light irradiation is higher than that of the initial  $\text{TiO}_2$ /C core and pure  $\text{TiO}_2$  because  $\text{TiO}_2$  on the shell has high crystallinity and high content of surface oxygen vacancies (SOVs) after the second hydrothermal treatment.[54] The  $\text{TiO}_2$ /C hollow composite spheres possessed high specific surface area and rich pores, thus the mass transfer of dye molecules was facilitated, resulting

in an enhanced photo-degradation activity to decomposition of RhB under visible-light irradiation.[56] The peapod-like TiO<sub>2</sub>/C nanocomposite also showed a much faster photodegradation rate of RhB than bare TiO<sub>2</sub> and P25 due to the synergistic effect derived from TiO<sub>2</sub> nanoparticles(NPs) and carbon fibers.[55] Xu et al. doctor-bladed C@TiO<sub>2</sub> nanoparticles onto a conducting substrate, which can be further applied in photoelectrocatalytic(PEC) for RhB and 1-naphthol (1-NP) degradation.[45] The results showed that the C@TiO<sub>2</sub> film with multi-porous structure could efficiently extend visible light-harvesting, lower electron transfer resistance, and promote photocurrent response.

In addition to TiO<sub>2</sub>, other carbon-decorated semiconductor materials also have been applied in photo-degradation of organic dyes. For example, Karimi et al. prepared MgO/ZnO nanocomposite supported on activated carbon for photocatalytic degradation of MB.[339] The nanocomposite of ZnO doped with 10 % MgO and 10 % Ac showed the e best catalytic activity, which is much faster than the ZnO photo-assisted process. We also found introducing some Ag nanoparticles onto C@ZnO could effectively prolong the lifetime of the photogenerated electron-hole pairs thus leading to a remarkably improved photoactivity form MB degradation.[60] Chen et al. used the carbon coated WO<sub>3</sub> for MB degradation, which showed a considerable rate under UV-visible light as well as good stability due to the synergistic effect of the amorphous carbon and the large amounts of defects in WO<sub>3</sub>. [47] A ZnS-enwrapped amine-functionalized fly ash nanocomposite (ZnS/A-FA) was reported having higher catalytic activity compared to that of bare ZnS nanoparticles for the degradation of MB under UV irradiation and good antibacterial activity. [41] Lanfredi et al. prepared a C-KSr<sub>2</sub>(Ni<sub>0.75</sub>Nb<sub>4.25</sub>)O<sub>15-δ</sub> composite to degrade phenol red under UV-irradiation, in which the amorphous carbon beneficially influenced the photoactivity of the niobate-based material.[50]

Besides for degradation of organic water contaminants, the amorphous carbon-decorated nano hybrids can also be used in gas phase photocatalysis to control of volatile organic compounds (VOCs). Lu et al. reported the photocatalytic degradation of toluene by Zn<sup>2+</sup>-TiO<sub>2</sub> /A<sub>C</sub> under UV light, which reached 100% degradation for at 40 min and remained 75% after 160 min, while degradation by TiO<sub>2</sub> was only 30%. [46]

### **2.3.2 Carbon nanotubes**

The electron-accepting and -transport properties of CNT provide a convenient way to direct the flow of photogenerated charge carriers, which increases the lifetime of electron-hole

pairs generated by semiconductors upon light irradiation. Thus, the photocatalytic activity of semiconductors for organic pollutants degradation is expected to be improved by incorporation of CNTs.

For example, Zhu et al. have demonstrated the rice grains-shaped  $\text{TiO}_2/\text{CNT}$  composites enhanced the photocatalytic activity for degradation of Alizarin Red dye in the liquid phase in comparison to pure rice grains  $\text{TiO}_2$  and commercial P25.[99] However, the interfacial contact between CNT and  $\text{TiO}_2$  is critical for such improvement as the photon-excited electrons from  $\text{TiO}_2$  particles cannot be shuttled freely in the conducting network of CNTs without intimate interaction. This interfacial contact may relate to the preparation method. Yao et al. found the MWCNT/ $\text{TiO}_2$  composite prepared by a hydration/dehydration process, which cannot combine P25 and MWCNT effectively, showed lower photocatalytic activity for degradation of phenol than that over P25.[340] Xu et al. also observed that a simple mechanical mixing process was not able to produce an effective  $\text{TiO}_2/\text{MWCNT}$  composite photocatalyst for the organic pollutants degradation. [80]

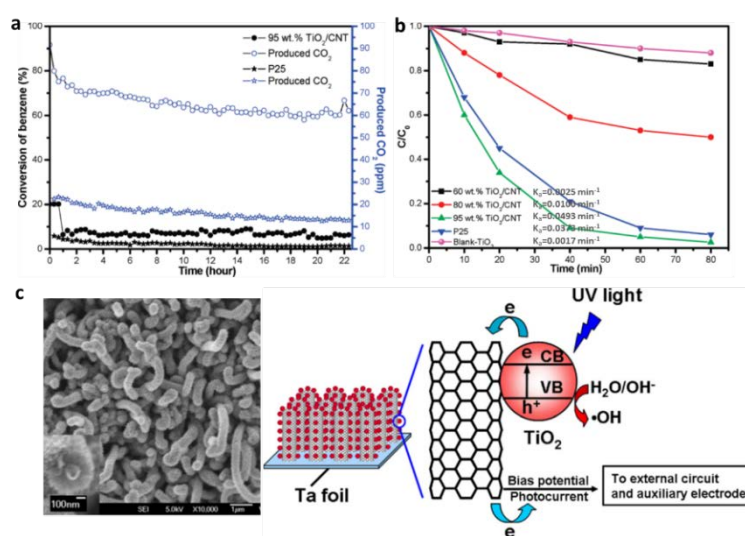


**Figure 2.5.** (a) Time-online photocatalytic degradation of benzene in the gas phase and (b) Photocatalytic degradation of methyl orange in the liquid phase over P25 and  $\text{TiO}_2/\text{MWCNT}$  prepared by an impregnation method, (c) SEM image of top view and schematic diagram of photocatalysis at the  $\text{TiO}_2/\text{MWCNT}$  array. Reprinted with permission from ref.[80, 94] Copyright 2010 American Chemical Society and 2010 Elsevier Ltd.

On the other hand, the controlling the composition ratio in  $\text{TiO}_2/\text{CNTs}$  is also crucial to obtain an optimal synergistic effect between CNTs and  $\text{TiO}_2$ , because it can influence the photo absorption and scattering, the size and the uniform distribution degree of the nanophase  $\text{TiO}_2$ . It was found that the  $\text{TiO}_2/\text{CNTs}$  composite containing about 5 wt.% of CNTs showed

good photocatalytic performance, as higher amount of CNTs may shield the light for the absorption by TiO<sub>2</sub>. [80, 82] For instance, for gas-phase degradation of benzene and liquid-phase degradation of MO under UV irradiation, the 95% TiO<sub>2</sub>/MWCNT composite exhibited an enhanced photocatalytic activity compared with that P25, while further increasing the content showed opposite trend, as shown in Figure 2.5a&b.[80]

The wide range applications for environmental remediation requires the development of immobilized photocatalytic systems, as powder photo-catalysts, possessing high surface energy, easily aggregate and are hard to separate and recycle after the photocatalytic process. Since both metal oxide and CNTs can be grown on substrates, it is easy to recover and reuse their composite photo-catalyst film without the need for laborious centrifugation or filtration. The layer-by-layer assembled TiO<sub>2</sub>@CNTs thin film showed a significant enhancement of the photocatalytic activity of TiO<sub>2</sub> in the degradation of Procion Red MX-50 dye.[108] The transparent, and super-hydrophilic TiO<sub>2</sub>@CNTs thin film prepared by spin-coating on quartz has nearly twofold photocatalytic performance towards the degradation of MO under UV light than pure TiO<sub>2</sub>. [82] Moreover, the photocatalytic degradation of RhB on the TiO<sub>2</sub> nanoparticles coated the vertically aligned MWCNT arrays on tantalum foils can be further enhanced by applying bias potential on the film to undergo a PEC process(Figure 2.5c).[94]

### 2.3.3 Graphene

On account of excellent electron conductivity and mobility of GR, the introduction of GR into the matrix of semiconductor materials via an appropriate manner should in principle boost the transfer and prolong the lifetime of the electrons photo-excited from semiconductor, which thus is able to drive the photo-degradation of pollutants (dyes, VOCs and bacteria) more efficiently. For example, Zhang et al. found the reaction rates of MB degradation under both UV and visible light on P25/GR was much faster than that on bare P25 and P25/CNTs with the same carbon content. [153]

TiO<sub>2</sub>/GR nanocomposites are the most widely studied photocatalysts for liquid-phase or gas-phase pollutant degradation. The GR nanosheets serve as an acceptor of the photo-generated electrons of TiO<sub>2</sub> and suppressed the charge recombination due to its highly conductive 2D  $\pi$ -conjugation structure.[147] In addition, the introduction of GR would result a red shift in the absorption edge compared with pure TiO<sub>2</sub>. [126] Thus, the obtained photocurrent on TiO<sub>2</sub>/GR hybrid is much higher than that of control TiO<sub>2</sub>. Despite of the improvement, several parameters such as GR/TiO<sub>2</sub> composition ratio, interaction between GR and TiO<sub>2</sub> and the

morphology of both TiO<sub>2</sub> and GR, would significantly affect the photocatalytic efficiency of TiO<sub>2</sub>/GR nanocomposites.

Similar to amorphous carbon and CNTs, the content of GR in TiO<sub>2</sub>/GR nanocomposites have great effect on their photocatalytic performance, in which the moderate adding of GR would improve stability and activity of TiO<sub>2</sub> effectively. Zhang et al. systematically examined the influence of GR addition ratios on the photocatalytic activity of P25 towards gas-phase benzene and liquid-phase MB degradation (Figure 2.6). [142] The highest benzene degradation efficiency was obtained on P25-0.5%GR and further increasing the GR content led to a decreased photocatalytic activity. Although the adsorption of MB increased with the content of GR, the same phenomenon is observed, where the P25-5%GR showed the best MB degradation efficiency under both UV and visible light, and the efficiency P25-30%GR was even lower than pure 25. Sher Shah et al. studied the photo degradation of RhB under visible light on hydrothermal synthesized TiO<sub>2</sub>/rGO hybrids and found the composite of 2.0 wt % rGO gave the best photocatalytic activity and photocatalytic activity decreased with further increasing concentrations of rGO in composites. [160] Wang et al. also found the addition of a low amount of rGO (0.2–1.5 wt. %) markedly improved the PEC activity of TiO<sub>2</sub> films and the optimum mass ratio of rGO to TiO<sub>2</sub> was 1.0 wt.% which showed approximately fourfold and fivefold enhancement in the degradation rate toward RhB and acid orange II (AO-II) compared with pure TiO<sub>2</sub> film. [135] The similar phenomenon was also observed on GR based other semiconductor nanocomposites. For instance, in the case of MB degradation on ZnO/rGO composites, the photocatalytic activities of samples decreased as the loading amount of GR exceeded 2.0 wt%. [132] For gaseous acetaldehyde (CH<sub>3</sub>CHO) degradation, ZnO/rGO composites with suitable rGO contents (1.0 and 3.0 wt%) displayed significantly enhanced photocatalytic activity in both CH<sub>3</sub>CHO degradation and CO<sub>2</sub> generation. [178] There are two main explanations for photoactivity decreasing with the exceeding content of GR in the composite. First, the excessive addition of black GR to GR-semiconductor nanocomposites means the significant amount decrease of primary photoactive ingredient semiconductor and meanwhile limits the surface contact of semiconductor particles with the light irradiation. [15] This is more evident in the case of TiO<sub>2</sub>/GR core-shell structure, where too thick GR coating layers would cause a decrease in the effective light absorption of TiO<sub>2</sub> leading to low efficiency in the decomposition of RhB dye. [199] This phenomenon is called the Second, excessive GR in composite increases the opportunity for the collision of electrons and holes resulting in the recombination of the photo-generated electron-hole

pairs.[127] However, the GR content could be higher than above when the semiconductor nanoparticles are extra small. For instance, the TiO<sub>2</sub>/GR nanocomposites only containing 25% TiO<sub>2</sub> gave a higher rate constant (0.0139 min<sup>-1</sup>) of the MB degradation reaction than P25 (0.0054 min<sup>-1</sup>) because TiO<sub>2</sub> nanoparticles at around 4–5 nm were embedded into graphene nanosheets homogeneously. [133] The TNT/rGO composites with 10% rGO showed the highest photocatalytic activity for the degradation of malachite green in both UV and a broad visible wavelength range as TNTs with small diameter (~9 nm) showed good interfacial contact with GR. [165]

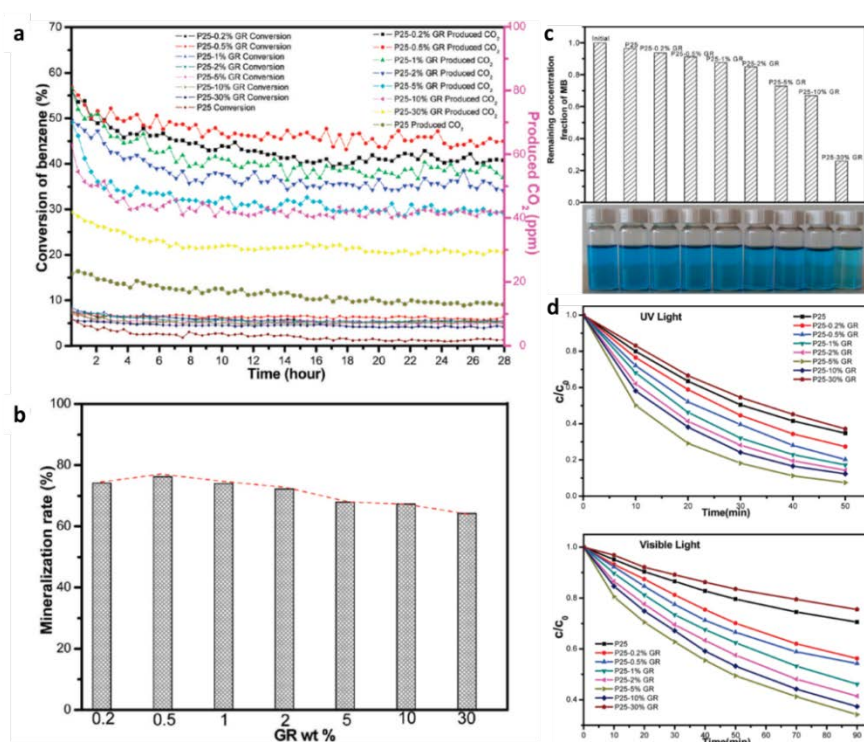


**Figure 2.6.** (a) Time-online data for gas-phase photocatalytic degradation of benzene and (b) mineralization ratio over the P25-GR nanocomposites, (c) the remaining methylene blue (MB) in solution after reaching the adsorption equilibrium in the dark and (d) liquid-phase photocatalytic degradation of MB under the irradiation of UV light and visible light ( $\lambda > 400$  nm) over the P25-GR nanocomposites. Reprinted with permission from ref. [142] Copyright 2010 American Chemical Society.

The interfacial contact between semiconductor and GR is quite important for the photocatalytic performance of their composite as it determines the transfer and lifetime of the photo-excited electrons. As mentioned in the previous section, the interfacial contact mainly depend on the preparation method of GR-semiconductor composites. Basically, the chemical synthesized composites have better interaction between semiconductor particles and GR sheets than that prepared by simply random integration of the two materials. For example, ZnO/GR composite prepared by situ chemical reduction showed four times higher activity

compared with mechanical mixture of ZnO and graphene on MB degradation.[132] In the case of TiO<sub>2</sub>/GR hybrids, it was found hydrothermal,[152] sonochemical method,[133] microwave assisted route,[134] etc. can effectively improve the interfacial contact between TiO<sub>2</sub> and GR to get uniform dispersion of TiO<sub>2</sub> nanoparticles on GR sheets. Liang et al. found slow hydrolysis of titanium precursor (TBOT) could facilitate the selective growth of TiO<sub>2</sub> on GO and suppresses growth of free TiO<sub>2</sub> in solution and the resulted TiO<sub>2</sub>/GR nanocrystals hybrid showed an impressive three-fold photocatalytic enhancement over P25 in the degradation of RhB.[156] Zhou et al. also found prolonging the hydrothermal reaction time (8h) moderately can obtain more homogeneous TiO<sub>2</sub>/GR products and cause a more quenching of photoluminescence leading to excellent photocatalytic activity to MB degradation under sunlight. [158] The structures and photocatalytic performances of TiO<sub>2</sub>/graphene composites are greatly affected by the final calcination temperature. In glucosamine-assisted hydrothermal synthesis of TiO<sub>2</sub>/graphene, Gu et al. found the product annealed at 700°C exhibited the best photocatalytic ability for the decomposition of MO, MB and RhB, which could be nearly degraded within 20 min under UV light.[125] Pastrana-Martínez et al. reported the TiO<sub>2</sub>/rGO calcined at 200°C showed better visible light photocatalytic activity than that calcined at 350°C.[341]

The easy agglomeration of small TiO<sub>2</sub> NPs on GR prohibits the direct chemical contact between the two components and therefore will dramatically diminish their synergistic effect for photocatalysis as the holes in TiO<sub>2</sub> cannot reach the targets adsorbed on GR. TiO<sub>2</sub> have been synthesized in a 1D or virtually one dimensional (1D) geometry (nanowires, nanorods, nanofibers, or nanotubes), which have more active sites and higher aspect ratio to increase the degree of interfacial contact with GR sheets leading to higher photocatalytic activity. For example, Pan et al. found TiO<sub>2</sub> NWs had more uniform distribution on GR with less agglomeration, resulting in more direct contact between TiO<sub>2</sub> and GR, and hence further improved electron and hole pair separation and transportation.[167] The photocatalytic activity of TNW/GR on photodegradation of MB under visible light was much higher than TNP/GR. The rate constant of photocatalytic degradation of MO under visible light on rGO/TiO<sub>2</sub> composite NFs is 6 times higher than that of commercial P25 when the optimal percentage of rGO(2 wt.%) was introduced.[173] Lavanya et al. prepared rGO wrapped anatase/rutile mixed phase TiO<sub>2</sub> NFs and found 99.2% of MO could be degraded in 120 min under UV irradiation due to the strong electronic interaction between 1D anatase/rutile mixed phase and rGO providing the improvement of electron transfer.[175] Zhai et al. prepared

rGO modified highly ordered TiO<sub>2</sub> NT arrays on Ti foil, which can be used for PEC degradation of MO under visible light irradiation and the degradation efficiency was further enhanced by suppressing the recombination of photo-generated electron-hole pairs under the external electric field.[166] Moreover, TiO<sub>2</sub> hollow nanospheres (THNSs) with mesoporous structures also have large surface area. Yan et al. found the 3D THNS/rGO hybrid composite exhibited markedly enhanced photocatalytic performance for the degradation of MB under UV light in comparison with P25.[169] Zhang et al. also synthesized THNS/rGO nanocomposites by loading of the hollow TiO<sub>2</sub> into GO sheet, which presented enormously high degradation of RhB by 75% within 3 h under the visible-light illumination.[168] In the case of GR encapsulated mesoporous THNS structure, up to 91% of RhB could be degraded in 90 min under UV irradiation, which is benefited from the electron transfer from inner THN to outer GR shells suppressing the recombination of photo-excited electrons and holes. [172] On the other hand, GR can also form 3D macrostructures (such as hydrogel and aerogel) with excellent electrical conductivity, mechanical strength, and thermal stability. Zhang et al. reported a self-assembled TiO<sub>2</sub>-GR nanocomposite hydrogel (TGH) with 3D interconnected networks and large surface area, which demonstrated high MB adsorption capacity and photocatalytic activity for degrading MB.[205] The 3D mesoporous TiO<sub>2</sub>/GR aerogels with exposed (001) facets of TiO<sub>2</sub> nanocrystals exhibited a highly recyclable photocatalytic activity for MO pollutant, which was floating on top of the liquid phase during the photo-degradation process could be easily separated for recycling using a tweezer.[207]

It is widely accepted that GR works as electron reservoir in TiO<sub>2</sub>-GR nanocomposite due to the slightly higher energy of the conduction band edge for TiO<sub>2</sub> (-4.20 eV) with respect to the calculated work function for pristine graphene (-4.42 eV).[170, 342] Under UV irradiation, the photo-generated electrons in the CB of TiO<sub>2</sub> will transfer into the GR sheet and the main oxidative species of the TiO<sub>2</sub>/GR systems are photo-generated holes on TiO<sub>2</sub>. [343] Under visible light irradiation, excited dye molecule can inject electrons into the GR plane directly or through the CB of TiO<sub>2</sub> to GR, which could be trapped by dissolved oxygen to form various reactive oxygen species (ROs) promoting the subsequent degradation.[149] However, the situation might different when GO or rGO was introduced as there are many defects on their sheets which could make them as light sensitizer into the system. For example, Chen et al. found GO could form p-type semiconductor in the TiO<sub>2</sub>/GO composite, which could be excited by visible light with wavelengths longer than 510 nm and acted as a sensitizer to enhance the MO degradation under visible light.[148] Besides,

remarkably enhanced visible light photoelectrochemical response was observed for the GO decorated TiO<sub>2</sub> NT composite electrode compared with pristine TiO<sub>2</sub> nanotube arrays, which showed about 15 times enhanced maximum photoconversion efficiency with the presence of GO. [115] The quenching effects of sacrificial hole and radical scavengers revealed that photogenerated holes are the primary active species for rGO/TiO<sub>2</sub> under UV–vis irradiation, while an enhanced contribution of radicals was evidenced under visible light.[341] This because electrons excited in localized sp<sup>2</sup> states of GO or rGO with suitable energetics would be injected to the conduction band of TiO<sub>2</sub> under visible light, where they can be readily scavenged by O<sub>2</sub> molecules to produce reactive radicals that would attack pollutant molecules (Figure 2.7a).[342] Thus, GO or rGO can act either as electron acceptor or electron donor (sensitizer) of TiO<sub>2</sub> under UV and visible light, respectively. In addition, the strong interaction between TiO<sub>2</sub> and GR lead to the formation of Ti-O-C bonding[167], which can narrow the bandgap of TiO<sub>2</sub> as well as change the energy level difference between GR and TiO<sub>2</sub>. Take rGR-wrapped TiO<sub>2</sub> NP [170] as an example, there could two paths for the MB degradation on under visible-light due to the bandgap narrowing (3.2 eV to 2.8 eV) of TiO<sub>2</sub> (Figure 2.7b). Path 1: Electrons from MB\* flow to the conduction band of TiO<sub>2</sub> NPs via graphene. Path 2: Valence electrons of TiO<sub>2</sub> are excited to the conduction band state by absorbing visible light, which can convert oxygen molecules in the solution to singlet oxygen, the ROSs. Thus, MB can be decomposed either by ROSs or by self-degradation under visible light irradiation.

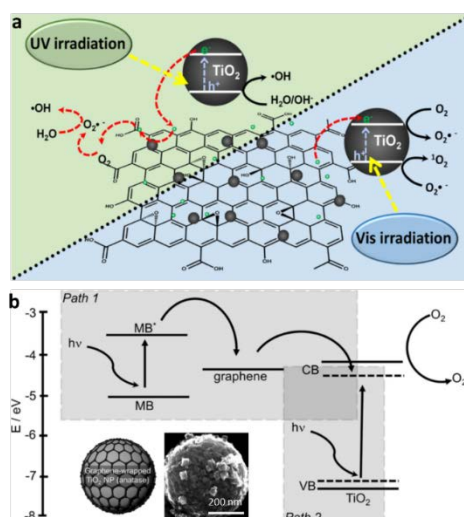


**Figure 2.7.** Schematic diagram of (a) representing mechanisms occurring over the GO-TiO<sub>2</sub> composite under UV and visible light irradiation, and (b) suggested mechanism for the photocatalytic degradation of MB by graphene-wrapped anatase TiO<sub>2</sub> NPs under visible-light. Reprinted with permission from ref. [170, 342] Copyright 2015 Elsevier B.V. and 2012 WILEY-VCH.

In addition to above mentioned dyes and benzene, TiO<sub>2</sub>/GR nanocomposites were also used to photo decompose other azo dyes (methyl red, orange G and acid orange 7),[37, 114] rose bengal, [134] 2,4-dichlorophenoxyacetic acid (2,4-D),[118] benzoic acid,[160] pesticides,[342] phenol,[152] diphenhydramine,[341] gaseous toluene, [163] and to convert poisonous heavy metal ions through photocatalytic oxidation or reduction, such as As(III) to As(V) [131] and Cr(VI) to Cr(III)[114] effectively. Besides TiO<sub>2</sub>, GR based other binary semiconductor nanohybrids, such as ZnO/GO,[113] ZnO/rGO,[132, 177] MgO/GR, [179] Y<sub>2</sub>O<sub>3</sub>/rGO, [141] SrNb<sub>6</sub>O<sub>16</sub>/GO, [183] BiPO<sub>4</sub>/GO,[116] MoS<sub>2</sub>/GR,[190] and Zn<sub>0.5</sub>Cd<sub>0.5</sub>S/rGO, [128] were applied for photo-degradation of pollutants. Compared with pure materials, the coupling with GR can significantly improve their photocatalytic activities and recyclability. For example, The ZnSnO<sub>3</sub> hollow nanospheres/rGO nanocomposite showed a large improvement (approx. 30.4% increase compared with pure ZnSnO<sub>3</sub>) in photodegradation of metronidazole under visible light irradiation.[182] Compared with the pristine AgBr, the AgBr/GR aerogel 3D hybrid gave preferable photocatalytic abilities and excellent cycling performance towards the oxidative degradation of MO and the reduction of Cr (VI). [144]

Furthermore, many studies have tried to introduce third or fourth functional ingredient to further improve the photocatalytic ability and recyclability of the binary GR-semiconductor hybrids in the liquid-phase or gas-phase pollutant degradation.

Non-metal element or metal cation doping is an effective approach to enhance the light harvest or electrical conductivity of the GR-semiconductor nanocomposites. For instance, the composites based on boron (B)-doped GR and rod-shaped TiO<sub>2</sub> showed an enhancement in the oxidative photo-destruction of NO<sub>x</sub> gas relative to the pure TiO<sub>2</sub> and GR/TiO<sub>2</sub> nanocomposite under UV light irradiation due to the strong electron-withdrawing capability of B atoms enriching free charge-carrier densities and enhancing the electrical conductivity of GR. [344] Shi et al. synthesized a nanocomposite photocatalysts consisted of GR and N-doped TiO<sub>2</sub> nanoplates with exposed (001) facets, which presented high photocatalytic activity for the decoloration of MB under visible light because of N-doping resulting the redshift of TiO<sub>2</sub> light absorption edge.[345] Similarly, the N-P90/N-rGO composites showed a significantly enhanced photocatalytic performance for the degradation of MB under visible light irradiation compared with P90, N-P90 and N-P90/rGO composites, which can be ascribed to the more efficient separation of the photogenerated charges resulting from the improved electrical conductivity of the N-RGO sheets, as well as the enhanced absorption in the visible light region.[218]In the Pr-doped TiO<sub>2</sub>/GO composite, the structural defects

resulted from  $\text{Ti}^{4+}$ - $\text{Pr}^{3+}$  replacement leading to band gap narrowing and the 4f electron transitions of Pr could incorporate additional energy levels in the band gap, which made the Pr- $\text{TiO}_2$ /GO exhibit enhanced photocatalytic activity towards degradation of MB under visible light irradiation.[223] The Cu/P25/GR nanocomposites with moderate  $\text{Cu}^{2+}$  doping showed the high degradation rate of MB under the visible light, whose removal efficiency could reach 98% after 100 min. [222] The  $\text{Ti}^{3+}$  self-doped  $\text{TiO}_2$ /GR composites also showed high photodegradation rate of MO in the visible light irradiation due to the strong red shift of absorption band resulted from the  $\text{Ti}^{3+}$  doping and the formation of Ti-O-C and O-Ti-C bonds.[224] He et al. found doping with a proper amount of N species could improve the visible photocatalytic activities of  $\alpha$ - $\text{Fe}_2\text{O}_3$ /GR for degradation of gas-phase acetaldehyde and liquid-phase phenol, in which the increased amount of doped quaternary-type N would be very favorable for photogenerated charge transfer and transportation and also for  $\text{O}_2$  adsorption due to the increased surface acidity.[346]The incorporation of nitrogen into the rGO structure make the  $\text{TiO}_2$ /Au/rGO nanocomposite show higher photocatalytic efficiency in the photodegradation of MB under UV light, around 153% and 260% higher as compared to  $\text{TiO}_2$ /Au/rGO without N-doping and pure  $\text{TiO}_2$ , respectively.[236]

The introduction of metal nanoparticles (such as Ag and Au) as bridges between semiconductor photocatalyst and GR sheets is expected to overcome the limited contact and favour the electron transfer. For example, the Ag/GR/surface-coarsened  $\text{TiO}_2$  nanobelts(SC-TNBs) ternary nanocomposite exhibited improved photocatalytic performances towards the degradation of RhB under UV light compared with blank SC-TNBs and its binary counterparts, which can be attributed to the judicious combination of GR, Ag NPs, and SC-TNBs in an intimate contact boosting the relay transfer of photogenerated electrons the prolonging lifetime of photogenerated electron-hole pairs.[229] The rGO/Ag/ $\text{TiO}_2$  NTs ternary photocatalyst also exhibited over 93 % removal efficiency of typical herbicide 2,4-D under simulated solar light irradiation with good stability and easy recovery compared with rGO/ $\text{TiO}_2$  NTs.[238] The hybrid nanostructure ZnO/rGO (5wt.%)/AuPd(1wt.%) exhibits high rhodamine 6G (R6G) photodegradation efficiency (~100% degradation in 20 min) with an improvement in rate constant (k) by a factor of 10 compared to that of the ZnO/rGO nanocomposite because AuPd and rGO layers act as traps for the photogenerated electrons, increasing the photocatalytic activity of ZnO nanorods.[232] Meanwhile, these noble metal nanoparticles can strongly absorb visible light due to their surface plasmon resonance (SPR), which would result in electron richness in GR-semiconductor nanocomposites. The ternary

Ag/rGO/ZnO nanocomposite showed enhanced photoactivity under visible light for the degradation of RhB due to surface plasmon resonance of Ag NPs and the effective interfacial hybridization between rGO and Ag with ZnO nanoparticles.[231] The quaternary nanocomposite of Ag/TiO<sub>2</sub>/γ-Fe<sub>2</sub>O<sub>3</sub>@r-GO showed high photocatalytic efficiency on degradation of wastewater's toxic crystal violet (CV) under visible light when 11.5 wt.% Ag nanoparticles are incorporated into TiO<sub>2</sub>/γ-Fe<sub>2</sub>O<sub>3</sub>@GO.[230] The Au/TiO<sub>2</sub> nanocomposite on monolayer GR had significantly higher performance on photodegradation of MO under solar light over TiO<sub>2</sub>/GR, which also can be used for antibacterial performance against Gram-positive bacteria, Gram-negative bacteria, and fungus.[227]

To improve light absorption and charge carrier transfer and transportation, ternary or quaternary photocatalysts are often designed by coupling two or three semiconductor materials with GR through band structure engineering. For instance, In the rGO/BiVO<sub>4</sub>/TiO<sub>2</sub> ternary nanocomposites, tuning of band gap energy of the BiVO<sub>4</sub> and TiO<sub>2</sub> were simultaneously achieved by modifying the concentrations of GO and TiO<sub>2</sub> during synthesis, which led to reduction in time needed for complete MB degradation from 40 min with rGO/BiVO<sub>4</sub> to 10 min with the ternary composite under visible light irradiation.[244] The TiO<sub>2</sub>/SnS<sub>2</sub>/rGO nanocomposite also showed high photoactivity for the degradation of RhB under visible-light irradiation due to the positive synergistic effect between layered SnS<sub>2</sub> and rGO components, which contributes to the enhanced photoactivity of TiO<sub>2</sub> nano-particles through.[247] Similarly, the hybrid material of CdS-TiO<sub>2</sub> NPs decorated rGO sheets exhibited a good photocatalytic activity for the visible-light-induced decomposition of MB and hydrolysis of ammonia borane due to the beneficial synergistic effect overcoming the problem of photo corrosion of CdS NPs and improving the electrons-holes transfer.[248] Dutta et al. introduced hexagonal yellow or cubic red CdS into TiO<sub>2</sub>/rGO hybrids and found the yellow CdS/TiO<sub>2</sub>/rGO shows maximum efficiency compared to the corresponding red ternary CdS/TiO<sub>2</sub>/rGO or their binary counterparts for crystal violet and RhB dye degradation under visible light irradiation, in which TiO<sub>2</sub> presented at the interface of rGO and CdS in inhibiting the direct interaction between rGO and CdS, while rGO also supported faster dye degradation by higher dye adsorption and rapid internal electron transfer.[249] The ternary CdS/RGO/TNTs hybrid film also show much higher visible-light-driven PEC and photocatalytic activity in degradation of MB compared with pure TNTs, RGO/TNTs, and CdS/TNTs. [254] Besides, the photocorrosion of CdS was effectively inhibited in this system.[10]The g-C<sub>3</sub>N<sub>4</sub>/CdS/rGO nanocomposites were also used for photodegradation of

RhB and Congo red dyes under irradiation with UV and visible light, which significantly enhanced the catalytic effect compared with pure g-C<sub>3</sub>N<sub>4</sub>, g-C<sub>3</sub>N<sub>4</sub>/CdS and g-C<sub>3</sub>N<sub>4</sub>/RGO composites.[253] Dai et al. designed a superior ternary catalyst composed of g-C<sub>3</sub>N<sub>4</sub>, BiOI and GO for MB degradation, where GO works as a buffer material to enhance electron transfer from g-C<sub>3</sub>N<sub>4</sub> to BiOI through the GO/g-C<sub>3</sub>N<sub>4</sub> and GO/BiOI interfaces.[252] The rGO/BiOI/AgI nanocomposite also exhibited extraordinary photocatalytic performance in the degradation of rhodamine B (RhB) under simulated sunlight irradiation, whose rate constant was six times higher than that of bare BiOI nanostructures.[251]

After degradation of wastewater contaminants, separation and manipulation of the nanocomposites from the waste water is another problem, which not only increases the cost requirements, but also possibly causes a new type of pollution. For these reasons, the incorporation of the third magnetic components, e.g. Fe<sub>3</sub>O<sub>4</sub>, MgFe<sub>2</sub>O<sub>4</sub> and ZnFe<sub>2</sub>O<sub>4</sub> into nanoparticle-based catalysts to deal with the recycling problems has attracted intense attention due to their unique magnetic response, chemically modifiable surface, and low cytotoxicity. Jiang et al. reported a ternary crumpled GR/TiO<sub>2</sub>/magnetite photocatalyst for MO degradation under UV light, which showed an over 20-fold enhancement compared with TiO<sub>2</sub> alone and could also be magnetically recoverable under low magnetic fields.[240] Benjwal et al. also fabricated rGO/Fe<sub>3</sub>O<sub>4</sub>/TiO<sub>2</sub> nanocomposites, which exhibited higher MB degradation efficiency (~100% within 5 minutes) and As(III) adsorption capacity (147.05 mg g<sup>-1</sup>) compared to binary composites.[239] The Fe<sub>3</sub>O<sub>4</sub>@SiO<sub>2</sub>@TiO<sub>2</sub>/GO core-shell nanocomposites also showed good photocatalytic activities for the degradation of RhB under high-pressure mercury lamp irradiation, in which the magnetic Fe<sub>3</sub>O<sub>4</sub> core makes the hybrids very easy to be separated from the solution and out-layer GO exhibits an excellent adsorption capacity to aromatic compounds via  $\pi$ - $\pi$  stacking.[241] Sadiq et al. synthesized a RGO-ZnWO<sub>4</sub>-Fe<sub>3</sub>O<sub>4</sub> nanocomposite by the one-step microwave irradiation method and studied its catalytic activity. The rGO/ZnWO<sub>4</sub>/Fe<sub>3</sub>O<sub>4</sub>[243] and rGO/MgFe<sub>2</sub>O<sub>4</sub>/SnS<sub>2</sub>[246] nanocomposites also exhibited high photocatalytic activity and stability for the photo degradation of MB under visible light. Feng et al. prepared a hierarchical structured ZnFe<sub>2</sub>O<sub>4</sub>@rGO@TiO<sub>2</sub>, which could reach 95.4% degradation of fulvic acid (FA) solution within 3 h under visible light irradiation and showed 90% efficiency up to 5 cycles.[242] The rGO, as the middle layer, can effectively promote the photo-induced electron flow between the ZnFe<sub>2</sub>O<sub>4</sub> and TiO<sub>2</sub> and further improve the efficiency of the photo-Fenton oxidation.

Introduction the other carbon materials into GR-semiconductor hybrids can also improve their photocatalytic activity towards pollution degradation. Yang et al. fabricated the photocatalysts of activated semi-coke supported TiO<sub>2</sub>/rGO nanocomposite, which presented the effective NO photo-oxidation performance under visible light irradiation.[257] On the TiO<sub>2</sub>/rGO/AC composite, the RhB degradation rate was 2.3 times higher than that of TiO<sub>2</sub>/rGO under simulated solar light irradiation because the adsorption of AC significantly increased the organic molecule concentration near the catalytic surface, allowing the effective transfer and separation of photogenerated electrons.[258] This TiO<sub>2</sub>/rGO/AC photocatalyst is also effective for the degradation of tetracycline in an aqueous solution. In the GR/CNT/TiO<sub>2</sub> composite photocatalysts, the apparent rate constants *k* for MB degradation and Cr(VI) reduction under UV light irradiation were 2.2 and 1.9 times as GR/TiO<sub>2</sub> composite, respectively. [259]The addition of CNTs can be served as charge transmitting paths thus decrease the recombination rate of photoinduced electron–hole pairs.[259] Dong et al. fabricated an immobilized TiO<sub>2</sub>/CNT nanocomposite on graphite plate, which had high and accessible specific surface area, pore volume and available inter-spaces and showed superior photocatalytic activities in the degradation of MO under UV light compared with TiO<sub>2</sub>/GP catalysts. [260]

In addition, other functional materials also have been incorporated into GR-semiconductor binary composites to enhance their photocatalytic performance. Polyaniline(Pani), as a conductive polymer, was introduced in TiO<sub>2</sub>/GR nanocomposite, which showed high photocatalytic activity to MB degradation under visible light due to the sensitizing effect of Pani and the electron scavenging property of GR.[263] The rGO/ZnFe<sub>2</sub>O<sub>4</sub>/Pani photocatalyst also presented a better photocatalytic activity of RhB degradation than that of rGO/ZnFe<sub>2</sub>O<sub>4</sub> composites as the interactions between Pani and rGO/ZnFe<sub>2</sub>O<sub>4</sub> composite laid a foundation for the high efficiency of electron transport and charge carrier separation.[264] Wang et al. fabricated a nanocomposite consisting of upconversion material ( $\beta$ -NaYF<sub>4</sub>:Yb<sup>3+</sup>,Tm<sup>3+</sup>), N doped P25, and GR, which showed improved photocatalytic activity in the degradation of RhB under the NIR and simulated sunlight irradiation compared with those of P25/GR.[267] Yin et al. developed a novel GR supported CeO<sub>2</sub>-based nanocomposite, including core/shell structure upconversion nanocrystals(UCNCs) of NaLuF<sub>4</sub>:Gd,Yb,Tm@SiO<sub>2</sub> and nanoparticles of Tm<sup>3+</sup>-doped CeO<sub>2</sub>, which showed significantly enhanced photocatalytic activity for degradation of RhB under sunlight. [268] The UCNCs absorb the NIR light and transfer energy to CeO<sub>2</sub>; Tm-doping narrows the band-gap of CeO<sub>2</sub>; and GR enhances adsorption of

pollutants and serves as an effective electron acceptor and transporter.[268] 100% photodegradation of MB was observed within 25 min under visible light using TiO<sub>2</sub>/β-cyclodextrin/GR nanocomposite due to increased visible light absorption and electron transfer via Ti-O-C between Ti and C which greatly retards the effective recombination of photogenerated electron-hole pairs.[266] Huang et al. fabricated TiO<sub>2</sub>/hydroxyapatite (Ca<sub>10</sub>(PO<sub>4</sub>)<sub>6</sub>(OH)<sub>2</sub>, HA)/rGO nanocomposite coating for degradation of MB and sterilization testing of Escherichia coli bacteria. [270] Addition of HA-rGO effectively increased the specific surface area of the coatings and markedly enhanced adherence of the bacteria for subsequent extinguishment.[270] Zargari et al. intercalated a tin complex of tetrakis(4-carboxyphenyl)porphyrin (SnTCPP·Cl<sub>2</sub>) between TiO<sub>2</sub> and GR nanosheets, which was effective for the efficient photocatalytic inactivation of bacteria under visible light illumination.[265]

### 2.3.4 Fullerene

The combination of fullerene and semiconductor may provide an ideal system to achieve an enhanced charge separation by photoinduced electron transfer, which further leads to the efficient photo-degradation of pollutants.

As mentioned before, fullerene/TiO<sub>2</sub> nanocomposite photocatalysts are the most commonly studied system. Similar to the case of TiO<sub>2</sub>/GO or rGO, the charge transfer between fullerene and TiO<sub>2</sub> might be different under UV and visible light as the triplet electronic states[347] existed in fullerene. Taking the degradation of sulfathiazole (SA) on C<sub>70</sub>/TiO<sub>2</sub> [288] as an example (Figure 2.8), under UV light, the photo-generated electrons in the CB of TiO<sub>2</sub> (-0.5V vs. NHE) would transfer into the band of C<sub>70</sub>/C<sub>70</sub><sup>-</sup> (-0.2V vs. NHE) due to their energy level position. Meanwhile, C<sub>70</sub> could be excited from the ground state to a transient state (<sup>1</sup>C<sub>70</sub>\*), and then went through a rapid intersystem crossing to a lower lying triplet state (<sup>3</sup>C<sub>70</sub>\*), in which the transference of electrons would reduce the probability of electrons falling down to the conduction band of TiO<sub>2</sub>. [288] On the other hand, the electrons could be excited both from the VB of TiO<sub>2</sub> to the mid-gap band and from mid-gap band to the CB of TiO<sub>2</sub> under visible light irradiation. The mid-gap band of TiO<sub>2</sub> was produced because C<sub>70</sub> has significant bands at the visible region which can be introduced into TiO<sub>2</sub> through the chemical bonds between the two compounds. Thus, visible light can be effectively utilized by the C<sub>70</sub>/TiO<sub>2</sub> hybrid and turned into photogenerated electrons and holes more efficiently. The

photo-generated holes and the reactive oxygen species such as  $\cdot\text{OH}$  in water and superoxide anion radical ( $\text{O}_2^-$ ) could be involved in the photocatalytic degradation.

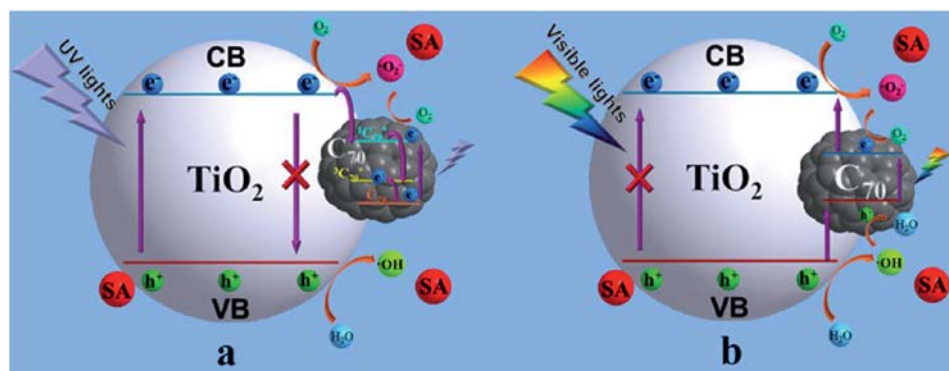


**Figure 2.8.** Photoreaction mechanism of the  $\text{C}_{70}/\text{TiO}_2$  hybrid under UV light irradiation (a) and visible light irradiation (b). Reprinted with permission from ref. [288] Copyright 2015 The Royal Society of Chemistry.

Similarly to other carbon materials, the content of fullerene in the composites also have great influence on their photocatalytic performance. Yu et al. used the  $\text{C}_{60}/\text{TiO}_2$  nanocomposites for the degradation of gas-phase acetone under UV light irradiation and found a low  $\text{C}_{60}$  loading (0.1–1.5 wt.%) significantly enhanced the photoactivity of  $\text{TiO}_2$ , where the composite containing 0.5 wt.%  $\text{C}_{60}$  gave the highest photocatalytic activity, exceeding that of  $\text{P}_{25}$  by a factor of 3.3. [280] For the MB degradation under sunlight, the  $\text{C}_{60}/\text{TiO}_2$  hybrid with a mass ratio of 1:20 demonstrated the highest enhancement of photocatalytic activity compared with the ones with other mass ratios (1:1, 1:10, and 1:100).[40] The introduction of fullerene can also extend the absorption spectrum of  $\text{TiO}_2$  to visible light region. Zhang et al. found the photocatalytic activity of  $\text{C}_{60}/\text{TiO}_2$  towards RhB degradation under visible light strongly depended on the contents of fullerene from 0.5% to 3% mass ratio, in which the one with 1wt.%  $\text{C}_{60}$  is optimal. [348] For the SA degradation on  $\text{C}_{70}/\text{TiO}_2$ , it was found the increase of  $\text{C}_{70}$  loadings cannot improve the photocatalytic activity significantly under UV light irradiation because the UV light adsorption and electron generation are mainly contributed to  $\text{TiO}_2$  NPs rather than  $\text{C}_{70}$  and small amount of  $\text{C}_{70}$  (0.75 wt.%) can effectively increase the photocatalytic activity of  $\text{TiO}_2$  due to the good dispersion and electrons transfer. [288] However, under visible light irradiation, no obvious enhancement was observed until the  $\text{C}_{70}$  content enhanced to 6 wt. % and the 18 wt.%  $\text{C}_{70}/\text{TiO}_2$  sample achieved the best photocatalytic performance as  $\text{C}_{70}$  can be excited by the visible light and contribute electrons for the system. [288] In both case, excessive  $\text{C}_{70}$  can aggregate to form clusters on the surface

of hybrids, which may hinder the photocatalyst to absorb the visible light, thereby inhibiting the photocatalytic activity.

Likewise, the interfacial contact between fullerene and semiconductor is crucial for the photo- activity of their composites. It was reported the photo performance towards MB degradation of the C<sub>60</sub>/TiO<sub>2</sub> composites prepared by directly solution mixing were even lower than the pure TiO<sub>2</sub>. [349] In the case of acetone photo-oxidation, the impregnating method did not produce an efficient C<sub>60</sub>/TiO<sub>2</sub> photocatalyst, which displayed a relatively lower activity than pure TiO<sub>2</sub> due to the lack chemical bonds at their interface. [280] On the other hand, the sample prepared by hydrothermal method showed higher efficiency because C<sub>60</sub> molecules could be dispersed as a monolayer onto TiO<sub>2</sub> via covalent bonding. [280] Similar results was observed in the case of C<sub>70</sub>/TiO<sub>2</sub> for degradation of SA, where the loose contact between C<sub>70</sub> and TiO<sub>2</sub> in the mechanical mixture would not lead to an efficient visible light activity. [288]

The morphology of fullerene and semiconductor have significant effects on the photocatalytic activity and applications of their hybrids. Wang et al. compared the photocatalytic performance of C<sub>60</sub>/TiO<sub>2</sub> and C<sub>70</sub>/TiO<sub>2</sub> under visible light and found the activity of C<sub>70</sub>/TiO<sub>2</sub> was 1.6 times as high as that of C<sub>60</sub>/TiO<sub>2</sub>. [288] This because C<sub>70</sub> has larger photo cross-sectional area, bigger delocalization effect and higher electron affinity, which leads to a high harvesting efficiency of light, benefits electrons transfer and facilitates the photogenerated electron-hole pairs separation. Similar phenomenon was also observed in the visible light degradation of MB on the C<sub>70</sub>/TiO<sub>2</sub> NW hybrids.[292] The fullerene/TiO<sub>2</sub> hybrids are easy to form thin films, which can be used for photo-destruction of microbes. For example, the polyhydroxy fullerene (PHF)/TiO<sub>2</sub> coating could photo-catalytically inactivate spores of *Aspergillus niger* under UV light[39] and C<sub>70</sub>/TiO<sub>2</sub> thin film could effectively inhibit the growth of *Escherichia coli* O157:H7 bacteria under visible light ( $\lambda > 420$  nm) irradiation.[279] The C<sub>60</sub>-modified TiO<sub>2</sub> nanotube array also showed the high efficiency for the PEC degradation of MB.[298]

Doping of with metals ions or nanoparticles can also improve the photoactivities of fullerene/TiO<sub>2</sub> hybrids. Oh's group have investigated various metal-fullerenes including, V,[272] Y,[276] Fe,[283] Pt[273] and Pd[282], to incorporate with TiO<sub>2</sub> for dye degradation under UV or visible light. Compared with C<sub>60</sub>/TiO<sub>2</sub>, these M-C<sub>60</sub>/TiO<sub>2</sub> hybrids gave better photocatalytic degradation of dyes, such as MB and MO, because the introduction of metal could enhance the photogenerated electrons transfer inhibiting electron-hole pair

recombination due to their variable valence. For example, the photofenton effect could be introduced into the  $C_{60}/TiO_2$  system after Fe doping, which can enhance the photocatalytic activity towards MB degradation. [273] The hybrids of  $C_{60}$  and V doped  $TiO_2$  have also been studied and the 1wt%  $C_{60}/1wt%$  V- $TiO_2$  showed highest photocatalytic performance the under visible light as the V-doped can decrease the band gap energy of  $TiO_2$ . [350]

Coupling with other semiconductors is another way to enhance the photocatalytic activity of fullerene/ $TiO_2$  composite. The  $WO_3-C_{60}/TiO_2$  photocatalyst showed better photocatalytic performance towards MO degradation under visible light irradiation compared with  $WO_3/C_{60}$  and  $C_{60}/TiO_2$  due to the high efficiency of charge separation induced by the synergistic effect of fullerene,  $WO_3$ , and  $TiO_2$ . [274] The presence of  $MoO_3$  in the fullerene/ $TiO_2$  could result in the large surface area, which can absorb more dye (Alizarin red S) for photodegradation. [284] The  $CdSe-C_{60}/TiO_2$  composites also showed the high discoloration effect of MB under visible-light irradiation as  $CdSe$  could provide excited electrons for  $TiO_2$  and engender hydroxyl radicals ( $\cdot OH$ ) and superoxide radical anions ( $\cdot O_2^-$ ) with the presence of  $H_2O$  and oxygen. [275] Besides semiconductors, other materials also have been introduced into fullerene/ $TiO_2$  for the same purpose. Shi et al. prepared the  $C_{60}/TiO_2/MWCNT$  catalyst for RhB degradation under UV light and found the adding of MWCNTs could significantly enhance the degradation rate. [281] This is because MWCNTs can orderly export electron from  $TiO_2$  and fleetly reduce electronic accumulation on the  $TiO_2$  NPs and the photocatalytic activity could be further improved and applied in visible range by using W-doped  $TiO_2/C_{60}/MWCNTs$ . [278] Mukther et al. synthesized a visible light responsive  $TiO_2/\beta$ -cyclodextrin/fullerene composite, which showed a reduced charge recombination ratio and enhanced photocatalytic activity for MB degradation and 4-chlorophenol. [351]

In addition to  $TiO_2$ , other semiconductors, including  $ZnO$ , [352]  $SiO_2$ , [293, 294, 353]  $Ag_2S$ , [354]  $CoS_2$ , [289]  $Bi_2WO_6$ , [355]  $Bi_2MoO_6$ , [290]  $PbMoO_6$ , [291]  $C_3N_4$ , [356] has been coupled with  $C_{60}$  for destruction of pollutants and the resulting in photocatalytic activity was indeed improved to a certain degree. Among them,  $SiO_2$  was used to immobilize  $C_{60}$  derivatives, which could reduce agglomeration of the photocatalyst, and increase the adsorption of pharmaceuticals to exposure to singlet oxygen for destruction. [293, 294] In MO degradation under visible light, ascorbic acid as an electron donor is needed for  $C_{60}/SiO_2$  to recover excited  $C_{60}$ . [353] For other light responsive semiconductors, the  $C_{60}$  content in the hybrids also have great influence on their performance. For example, the optimal amount of  $C_{60}$  in the  $C_3N_4/C_{60}$  [356] and  $Bi_2MoO_6/C_{60}$  [290] composites are 1 wt% and 3wt%,

respectively. The photocatalytic activity of  $\text{PbMoO}_4$  for RhB degradation increased 3.8 times at a  $\text{C}_{60}$  weight ratio of 0.5 wt.% under UV light irradiation, and 4.1 times at a  $\text{C}_{60}$  weight ratio of 5wt.% under visible light irradiation.[291]

### 2.3.5 Carbon dots

The small size of CDs make them ease in achieving surface functionalization towards coupling with semiconductor materials. The photocatalytic activities of CD-semiconductor nanohybrids are expected to be enhanced because the introducing of CDs favours the photo-induced electron transfer due to their conducting network and the up-conversion photoluminescence (UCPL) property of CDs can in turn excite the semiconductor to form electron-hole pairs.

Li et al. found  $\text{CD}/\text{TiO}_2$  and  $\text{CD}/\text{SiO}_2$  nanohybrids could complete the MB ( $50\text{mg L}^{-1}$ ) degrade within 25 or 15 min under visible light, while pure CDs,  $\text{TiO}_2$  or  $\text{SiO}_2$  resulted in no or only a very limited amount of MB degradation (Figure 2.9a).[304] This is because CDs can absorb visible light and emit shorter wavelength of light (325–425 nm) by UCPL, which further excites the electrons of  $\text{TiO}_2$  or  $\text{SiO}_2$  to generate more electron-hole pairs for subsequent MB degradation. Moreover, the relative position of the CD band edge permits the electrons transfer from the  $\text{TiO}_2/\text{SiO}_2$  surface in favour of charge separation, stabilization and hindering recombination. The  $\text{CD}/\text{WO}_3$  nanocomposites also exhibited good stability and higher photodegradation efficiency of MB compared with  $\text{WO}_3$  or CDs alone, which could reach 100% after 0.5 h visible light illumination due to enhancement of electron transfer by coupling with CDs. [326] The  $\text{CD}/\text{Fe}_2\text{O}_3$  nanocomposites displayed enhanced photocatalytic capability for toxic gas (benzene and methanol) degradation under visible light irradiation when compared with  $\text{Fe}_2\text{O}_3$  nanoparticles, which can be attributed to the large electron-storage capacity and UCPL of CDs and also the  $\pi$ - $\pi$  interaction between CDs and benzene enriching the benzene adsorption on the surface.[305] The introduction of CDs onto ZnS also resulted in the remarkable photocatalytic degradation of Alizarin red S(ARS) dye under visible light irradiation i.e. 89% within 250 min, as compared to bare ZnS (69%) under similar conditions. [323] Li et al. found  $\text{CD}/\text{Cu}_2\text{O}$  nanohybrid was NIR-sensitive, which could absorb significantly more light in the 600–2500 nm region compared to the pure commercial  $\text{Cu}_2\text{O}$ . [315] About 90% MB degradation was observed on  $\text{CD}/\text{Cu}_2\text{O}$  photocatalyst with 240 min of exposure under NIR light ( $\lambda > 700\text{ nm}$ ), while no or little (<3%) degradation of MB is only observed with pure CDs or  $\text{Cu}_2\text{O}$  as the photocatalyst. This is

because the nanostructures produced on CD/Cu<sub>2</sub>O surface allow multiple reflections of NIR light and CDs can absorb NIR light (>700 nm) and then emit a shorter wavelength of light (390–564 nm) by UCPL, which in turn further excites Cu<sub>2</sub>O to form electron–hole pairs, therefore offering improved photocatalytic activity (Figure 2.9b).[315]

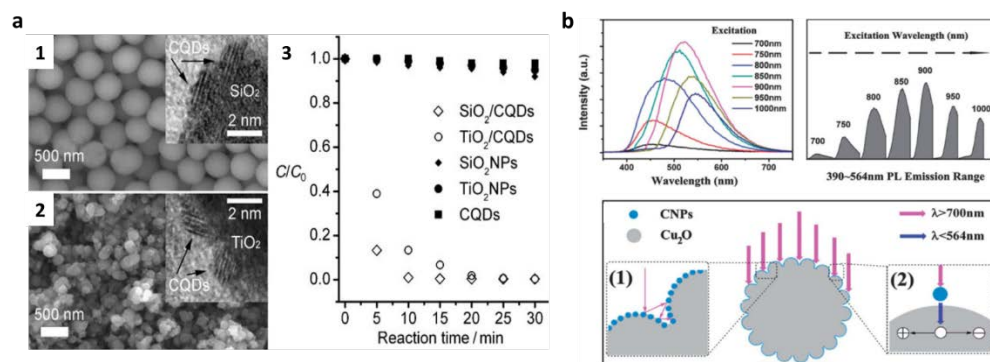


**Figure 2.9.** (a) SEM image of photocatalysts for SiO<sub>2</sub>/CQDs and TiO<sub>2</sub>/CQDs and relationship between MB concentration and reaction time for different catalysts: SiO<sub>2</sub>/CQDs, TiO<sub>2</sub>/CQDs, SiO<sub>2</sub> NPs, TiO<sub>2</sub> NPs, and CQDs; and (b) up-converted PL spectra of CDs, energy distributions of the up-converted emissions of CQDs located in the range from 390 to 564 nm (shown as shaded areas) and schematic photocatalytic mechanism for the CD/Cu<sub>2</sub>O composite under NIR light irradiation. Reprinted with permission from ref.[304, 315] Copyright 2010 Wiley-VCH and 2012 The Royal Society of Chemistry.

Similarly to other carbon materials, the CD content would affect the photocatalytic performance of these nanohybrids. Di et al. prepared CD/Bi<sub>2</sub>MoO<sub>6</sub> for photodegradation of four different kinds of pollutants: ciprofloxacin (CIP), bisphenol A (BPA), tetracycline hydrochloride (TC), and MB under visible light irradiation.[334] They found the photocatalytic activities of CQD modified Bi<sub>2</sub>MoO<sub>6</sub> increased with the increase of CD content from 0.5 to 2 wt.% but decreased when the mass ratios further increased to 4 wt.%. Similar results were observed on CD/BiVO<sub>4</sub>, where the composite with 3.5 wt.% CDs exhibited the highest photocatalytic activity for the degradation of MB dye.[307] The best degradation efficiencies of MB and RhB under simulated sunlight were obtained on 2wt.% CD/ZnS composite photocatalyst, which also possessed the lowest PL intensity suggesting an efficient transfer of photoexcited electrons from ZnS to CDs at this mass ratio.[325] Qian et al. used CD<sub>x</sub>/Bi<sub>2</sub>WO<sub>6</sub> (x=1–6 represents the mass (g) of CDs in stock solution) for removing gaseous VOCs (acetone and toluene) under UV and visible light irradiation. [334] In acetone degradation, it was found the rate of CO<sub>2</sub> production under visible light raised from 28 ppm/h to 47 ppm/h with increasing the content of CDs (x=2-4), while a relative large amount of CDs (x=6) resulted in the reduction of CO<sub>2</sub> production rate (26 ppm/h). Under UV–vis light,

CD2/Bi<sub>2</sub>WO<sub>6</sub> showed the highest CO<sub>2</sub> production but the CD4/Bi<sub>2</sub>WO<sub>6</sub> with large amount of CDs showed slightly decreased CO<sub>2</sub> production compared with pristine Bi<sub>2</sub>WO<sub>4</sub> mainly due to the shield effect of CDs toward UV light. Besides, CDs may also demonstrate down conversion PL emission at low excitation wavelengths[324], which would reduce the UV light absorption of semiconductor with wide band gap.

The interaction between CDs and semiconductor is important to their photocatalytic activities as well. Hazarika et al. have studied the photocatalytic degradation of paraoxon pesticide, benzene and phenol under normal solar light by the in situ prepared CD@TiO<sub>2</sub> and ex situ prepared CD-TiO<sub>2</sub> nanohybrids.[324] It was found around 90% of the three pollutants could be degraded within 6.5-7.5h on CD@TiO<sub>2</sub>, whereas only 60-70% degradations were observed on CD-TiO<sub>2</sub> after 9-9.5h. This is because CDs act as a better dispersing agent through in situ fabrication compared to the ex situ one, which would affect the morphology of TiO<sub>2</sub> in the nanohybrids.[324] Martin et al. also found the N-doped CD(N-CD)/P25 nanocomposites prepared by hydrothermal method showed better photocatalytic activities towards NO oxidation and MB degradation than the physical mixture of P25 and N-CDs. [320] Thus, the efficient attachment of CDs to semiconductor surface can improve their synergistic effect resulting in higher photocatalytic activity.

The structure and morphology of both CDs and semiconductor would also influence the final photocatalytic performance of their hybrids. Normally, CDs are considered as an electron reservoir in the hybrid to trap excited electrons from CB of semiconductor. However, Zhang et al. prepared a hybrid photocatalyst containing GO quantum dots (GOQD) and TiO<sub>2</sub> microspheres and found the GOQDs had p-semiconductor structure, which could be excited by visible light can transfer the excited electrons to the n-type TiO<sub>2</sub> through their interfacial energy band structure.[314] Thus, the GOQD/TiO<sub>2</sub> hybrids showed enhanced photocurrent and photocatalytic activity towards RhB degradation under visible light. Zhang et al. reported a CD/hydrogenated TiO<sub>2</sub> nanobelt (CD/H-TiO<sub>2</sub>) heterostructure and studied its photocatalytic performance for MO degradation under UV, visible, and near-infrared irradiation. [316] The efficiencies of the CD/H-TiO<sub>2</sub> were 86% and 50% within 25 min under UV and visible light, respectively, which were higher than H-TiO<sub>2</sub> nanobelt (82% and 45%) and TiO<sub>2</sub> nanobelt (63% and 17%). Under NIR light irradiation, 32% MO was decomposed after 120 min over the CD/H-TiO<sub>2</sub>, while no or little degradation of MO was observed on TiO<sub>2</sub> nanobelt and H-TiO<sub>2</sub> nanobelt. These results can be attributed the oxygen vacancies and Ti<sup>3+</sup> ions in TiO<sub>2</sub> nanobelts created by hydrogenation improving optical absorption, charge carrier trapping,

and hindering of the photogenerated electron–hole recombination under UV and visible light and the UCPL property of CDs converting NIR light into visible light for the utilization of H-TiO<sub>2</sub> nanobelts. [316] The direct Z-scheme CD/WO<sub>3</sub> nanorods composite also exhibited good stability, highly enhanced photo-response and broad-spectrum photocatalytic activity towards the degradation of RhB, tetracycline hydrochloride (TCH) and phenol.[337] For example, the removal efficiencies of RhB always decreased in the order CD/WO<sub>3</sub> (97.1, 99.1, 61.2%) > prepared WO<sub>3</sub> nanorods (66.6, 69.1, 22.4%) > commercial WO<sub>3</sub> nanoparticles (22.1, 11.6, ~0%) under UV, Visible and NIR irradiation, respectively. Tang et al. prepared BiVO<sub>4</sub> nanospheres and nanoplates with various exposed facets and coupling them with CDs for MB degradation under visible light irradiation. [307] The order of photocatalytic ability was founds CDs/m-BiVO<sub>4</sub> nanoplates > m-BiVO<sub>4</sub> nanoplates > CD/m-BiVO<sub>4</sub> nanospheres > m-BiVO<sub>4</sub> nanospheres. In addition to the helping of CDs, the m-BiVO<sub>4</sub> nanoplates gave better results than m-BiVO<sub>4</sub> nanospheres because nanoplates have the different surface structure, high specific surface area and optimal (001) active facets. [307]

The presence of different types of functional groups on the surface of CD may produce different emissive traps between  $\pi$  and  $\pi^*$  of C=C. For example, the self-passivated nitrogen and oxygen containing functional groups on CD surface may be responsible for the efficient PL by trapping excitons under excitation and the radiative recombination of those surface trapped excitons.[324] Thus, N-doping of CD (N-CD) has great potential for enhance the photocatalytic activity of CD-semiconductor composites. Zhang et al. have coupled the N-CDs with hierarchical rutile TiO<sub>2</sub> microspheres for the RhB degradation under visible light irradiation and found the pseudo-first-order reaction constant on N-CD/TiO<sub>2</sub> (0.11 min<sup>-1</sup>) was 1.3 times much larger than that of CDs/TiO<sub>2</sub> (0.086 min<sup>-1</sup>). [357] The photocurrent density of the N-CD/TiO<sub>2</sub> inverse opal structure (IOS) photoanode was also found approximately two times larger than the CD/TiO<sub>2</sub> IOS under the illumination of simulated sunlight and this N-CD/TiO<sub>2</sub> IOS film showed good photocatalytic ability for MB degradation.[333] N doping lowers the work function of CDs, which is probably main reason for enhanced photocatalytic activity of N-CD/TiO<sub>2</sub>. Besides, N can also be doped on semiconductor materials to enhance their visible light adsorption when coupling with CDs. Muthulingam et al. prepared CD/N-ZnO composites for dye (malachite green, MB and fluorescein dyes) photo-degradation and found it could degrade these dyes within 30–45 min under daylight irradiation and showed good stability.[311, 312] Thus, the synergetic effect of N-doping and CDs is great helpful to

prepare photocatalysts for environmental remediation under naturally available daylight source.

Introducing third compound into CD-semiconductor hybrids is another approach to improve their photocatalytic performance. For instance, MoS<sub>2</sub> nanosheet was introduced into the CD/H-TiO<sub>2</sub> nanobelt system for tetracycline (TC) photodegradation under UV, visible, and NIR light irradiation. [338] The 3D CD/MoS<sub>2</sub>@H-TiO<sub>2</sub> catalyst showed considerable photodegradation rate under UV light and a large promotion of the photocatalytic activity in both the visible and NIR region because the hierarchical structure had a favourable electron transfer pathway H-TiO<sub>2</sub>→MoS<sub>2</sub>→CDs, and CD/MoS<sub>2</sub> few-layer sheets provide more active edges and an UCPL effect. [338] De et al. synthesized a CD/Cu<sub>2</sub>O/ hyperbranched epoxy nanocomposite, which can be used as a tough, thermostable and reusable photo-catalyst for the degradation of pesticides under solar light. [331] The CD/Ag/Ag<sub>3</sub>PO<sub>4</sub> complex photocatalysts were studied for the degradation of MO dye under visible light irradiation, which displayed enhanced photocatalytic activity and good structural stability compared with CD/Ag<sub>3</sub>PO<sub>4</sub> and Ag/Ag<sub>3</sub>PO<sub>4</sub> due to the synergistic effect of CDs and the intense surface plasmon resonance of Ag. [306]

Due to the easy loading for CDs onto the surface of semiconductor materials, it is convenient to fabricate their hybrid film immobilized on conductive substrates, which avoid the separation or filtration steps and can be used for PEC degradation of pollutants. For example, CD/TiO<sub>2</sub> nanotube arrays [308] and CD/TiO<sub>2</sub> IOS films [333] have been reported and both of them showed good PEC performance and photocatalytic efficiency towards MB degradation. Zheng et al. prepared CQDs-Pt@Bi<sub>2</sub>WO<sub>6</sub>/FTO electrodes, which showed higher PEC activity and better stability than that of the Pt@Bi<sub>2</sub>WO<sub>6</sub>/FTO electrode towards methanol oxidation to CO<sub>2</sub> under solar light irradiation. [336] The introduction of CDs broadened the photoresponse range of the Bi<sub>2</sub>WO<sub>6</sub> material and improved the mobility of the photocarriers, which also acted as preferential adsorption sites for the intermediate carbonaceous species (such as CO, -CHO, -COOH and CH<sub>4</sub>) during methanol oxidation alleviating CO poisoning towards the Pt particles. [336]

## **2.4 Photocatalytic hydrogen or oxygen generation**

The utilization of solar energy for the conversion of water to hydrogen and oxygen has been considered as the most attractive solution to energy and environmental problems. There are

two main approaches for water splitting. One is the photoelectrochemical (PEC) method, which was first demonstrated by Fujishima and Honda In 1972.[358] In this PEC process, a bias was applied across a TiO<sub>2</sub> thin film and a Pt counter electrode (Figure 2.10a). The second way, proposed by Bard, [359] is simply using powdered catalyst for splitting water into H<sub>2</sub> and O<sub>2</sub> under light illumination without applying any bias (Figure 2.10b). As shown in Figure 2.10c, the mechanism for photo-catalytic water splitting is similar to that for photocatalytic degradation including the absorption of solar light, generation of electrons–holes and catalytic reactions for H<sub>2</sub> or O<sub>2</sub> evolution. However, the semiconductor band gap matching is required for water splitting. The bottom level of the CB has to be more negative than the redox potential of H<sup>+</sup>/H<sub>2</sub> (0 V vs. NHE), while the top level of the valence band (VB) be more positive than the redox potential of O<sub>2</sub>/H<sub>2</sub>O (1.23 V).[360-362] Using single semiconductor is hard to meet all the requirements for photocatalytic H<sub>2</sub> or O<sub>2</sub> generation. Thus, hybrid catalysts have been widely studied. CSHMs have received increased attention as the incorporation of carbon materials can broaden the absorption range to include visible light and reduce the recombination of photo-generated electrons and holes.

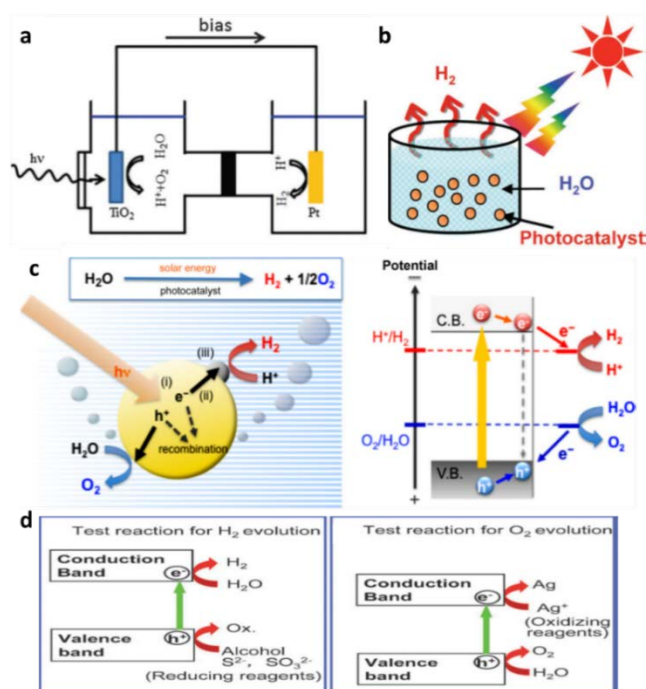


**Figure 2.10.** Schematic diagrams of the setup for water splitting (a) photoelectrochemical process after Fujishima and Honda[358], (b) using powdered photocatalysts after Bard[359], (c) Main processes of water splitting over semiconductor photocatalyst, (d) H<sub>2</sub> or O<sub>2</sub> evolution reaction in the presence of sacrificial reagents—half reactions of water splitting. Reprinted with permission from ref.[360-362] Copyright 2015 The Royal Society of Chemistry, 2009 The Royal Society of Chemistry and 2011 Elsevier B.V.

Although using Z-scheme photocatalyst may separate of H<sub>2</sub> evolved from O<sub>2</sub>, the overall water splitting is still a tough reaction.[360, 362] Thus, sacrificial reagents are often used in the second approach to evaluate if a certain photocatalyst satisfies the thermodynamic and kinetic potentials for H<sub>2</sub> and O<sub>2</sub> evolution(Figure 2.10d).[360] For H<sub>2</sub> evolution, instead of water, a reducing reagent (electron donors or hole scavengers), such as alcohol and a sulfide ion, is irreversibly oxidized by photogenerated holes. For enhancing O<sub>2</sub> evolution, the photogenerated electrons in the CB are consumed by oxidizing reagents (electron acceptors or electron scavengers) such as Ag<sup>+</sup> and Fe<sup>3+</sup>. These reactions are regarded as half reactions of water splitting and are widely employed as test reactions of photocatalytic H<sub>2</sub> or O<sub>2</sub> evolution.

#### **2.4.1 Carbon nanotubes**

P25/CNT nanocomposites prepared by hydrothermal method have been used for H<sub>2</sub> generation under UV-vis irradiation with alcohol as sacrificial reagent.[151] It was found the optimum mass ratio of P25/CNT is 1/0.3, but the rate of H<sub>2</sub> evolution on P25/CNT was lower than that of P25/rGO hydrothermal composite because the dispersion of P25 nanoparticles over CNTs was not as good as that over the GR sheets. Shen et al. also compared the TiO<sub>2</sub>/CNT and TiO<sub>2</sub>/rGO prepared from the same method and found the TiO<sub>2</sub>/CNT composite exhibited a hydrogen evolution rate of 15 μmol·h<sup>-1</sup> under UV light irradiation, which was much lower than that of TiO<sub>2</sub>/rGO. [162]

The sandwiched carbon/TiO<sub>2</sub>/carbon nanotube (CTCNT) composites were also used for H<sub>2</sub> evolution and a super-high H<sub>2</sub> production rate of 37.6 mmol h<sup>-1</sup>g<sup>-1</sup> is obtained under illumination of one AM 1.5G sunlight.[102] Due to the notably synergetic effect between TiO<sub>2</sub> nanotubes and graphitic carbon laminas outside and inside the nanotubes, the measured apparent quantum efficiency of CTCNT in the ultraviolet light region is even close to 100%. And, the minimum bandgap between the edges of band tails for the CTCNTs can conjecturally be narrowed to 0.88 eV. These result indicated the CTCNT structure can greatly enhance the utilization of sunlight and extremely suppress charge recombination during the H<sub>2</sub> evolution.

## 2.4.2 Graphene

Similar to photocatalytic degradation, the TiO<sub>2</sub>/GR nanohybrids are widely reported for H<sub>2</sub> evolution, where photogenerated electrons in TiO<sub>2</sub> are scavenged by graphene sheets suppressing the recombination of charge carriers and thus increasing the water-splitting performance. The content of GR in the composite is also a crucial factor. Morais et al. have used the TiO<sub>2</sub>/rGO composite films for PEC water splitting under 1.5 AM solar irradiation (100 mW cm<sup>-2</sup>) and found the TiO<sub>2</sub>/rGO photoelectrode with 0.1 wt.% rGO showed the highest photocurrent density values (0.20 mA cm<sup>-2</sup> at 1.23 VRHE), with an increase of 78% in relation to pristine TiO<sub>2</sub> film (0.11 mA cm<sup>-2</sup> at 1.23 VRHE).[155] However, at higher rGO content (0.5 to 5.0 wt%), the photocurrent density values sharply decreased due to the darkening and the agglomerations of rGO sheets in these films. Similar result was observed on the TiO<sub>2</sub>/rGO composite prepared from UV radiation, where the optimum photocurrent density of 3.4 mA cm<sup>-2</sup> and H<sub>2</sub> generation rate of 127.5 μmol cm<sup>-2</sup> h<sup>-1</sup> were obtained on the anode with 2 wt.% rGO and further increase in rGO content decreased the photocurrent and H<sub>2</sub> generation rate because of increased absorption of light in rGO.[119] The same phenomenon was showed in powdered catalyst cases. For the P25/rGO nanocomposite, the optimum mass ratio of P25 to rGO was found 1/0.2, which showed 1 order of magnitude higher of H<sub>2</sub> evolution rate than that over P25 alone. [151] On the P25/rGO nanocomposite loaded with 0.5 wt.% Pt, the optimum content of rGO was 0.5 wt% and the addition of higher GR in the composite led to a decreased photocatalytic activity.[154] The TiO<sub>2</sub>/rGO composites prepared from sol-gel method was also evaluated by H<sub>2</sub> evolution from water splitting with Na<sub>2</sub>S and Na<sub>2</sub>SO<sub>3</sub> as reducing reagent and the sample containing 5 wt.% rGO showed the highest photocatalytic activity.[127] For the TiO<sub>2</sub>/GR composites prepared from hydrothermal of TiCl<sub>4</sub> and GO, the average H<sub>2</sub> evolution rate increased from 4.5 mmol h<sup>-1</sup> for TiO<sub>2</sub>/0.8 wt.%GR to 5.4 mmol h<sup>-1</sup> for TiO<sub>2</sub>/2wt.%GR with the GS content increasing, while it decreased to 3.9 mmol h<sup>-1</sup> for TiO<sub>2</sub>/5wt.% GR and increases further to 4.7 mmol h<sup>-1</sup> for TiO<sub>2</sub>/10wt.%GR. [159] This is because the average size of TiO<sub>2</sub> nanoparticles changes from 16 nm to 6 nm with increasing the GR content, which not only causes quantum size effect but also induces the increase of relative amount of TiO<sub>2</sub> nanoparticles making the apparent ratio of GR decreasing even with the real GR content increasing. [159]

The strong interaction between semiconductor and GR sheets is also in favour of their photocatalytic performance in water splitting, which mainly depends on the preparation

method. Fan et al. compared the P25/rGO prepared by UV-assisted photocatalytic reduction, hydrazine reduction, and hydrothermal method, and found the rate of H<sub>2</sub> evolution decreased in the order of hydrothermal > UV>hydrazine.[151] Shen et al. found introduction moderate reducing agent, such as glucose[161] and ascorbic acid,[162] into the hydrothermal process could improve the H<sub>2</sub> evolution performance of TiO<sub>2</sub>/rGO nanohybrids. Zhang et al. found the TiO<sub>2</sub>/rGO composites calcined in nitrogen atmosphere showed higher photocatalytic H<sub>2</sub> evolution activities compared that calcined in air, due the generation of oxygen vacancies at nitrogen atmosphere, which can act as electron traps. [127]

Non-metal element, metal cation and metal particle doping can also enhance the photocatalytic H<sub>2</sub> evolution activities of GR-semiconductor hybrids. Kuang and Zhang found carbon doping could narrow the band gap of TiO<sub>2</sub> to 2.5 eV, which could further decreased to 2.2 eV after anchoring the C-TiO<sub>2</sub> to rGO. [212] The C-TiO<sub>2</sub>/rGO nanocomposite yielded high H<sub>2</sub> production rates of 1.50 ±0.2 mmol g<sup>-1</sup> h<sup>-1</sup> under visible light irradiation(400–690nm, 135 mW cm<sup>-2</sup>) and showed great stability of H<sub>2</sub> production.[212] The N-P25/GO also exhibited high photocatalytic efficiency of 716.0 or 112.0 μmol h<sup>-1</sup> g<sup>-1</sup> under UV light or Xenon lamp, which was about 9.2 or 13.6 times higher than P25 photocatalyst. [213] This is mainly attributed to the N-doping of TiO<sub>2</sub> and the incorporation of GO resulting in narrowed band gap, together with the synergistic effect of fast electron-transporting of photogenerated electrons and the efficient electron-collecting of GO retarding charge recombination. Similarly, the vanadium-doped TiO<sub>2</sub> nanorod/rGO (10 wt.% V doping) nanocomposite showed enhanced H<sub>2</sub> evolution under visible light illumination.[220] The Cu/P25/GR was studied for the PEC water splitting, in which 1.90 mmol g<sup>-1</sup> H<sub>2</sub> evolution was obtained after 5 h under visible light irradiation, higher than that of P25/GR(1.21 mmol g<sup>-1</sup>). [222] The doping of Cu<sup>2+</sup> ions results in the formation of surface state energy level below the CB of TiO<sub>2</sub>, which can inhibit the recombination of excitons and promote the transfer efficiency of charge carriers across the interface between GR and TiO<sub>2</sub>. Wang et al. also studied the Pt-TiO<sub>2</sub>/rGO nanocomposites for PEC water splitting and found rGO/Pt-TiO<sub>2</sub> nanocomposites with 2 wt.% rGO showed the superior solar-driven hydrogen generation rate (1075.68 μmol h<sup>-1</sup> g<sup>-1</sup>). [228] The formation of Ti-O-C bonds in the hybrid gave a path for the electrons transfer from TiO<sub>2</sub> to rGO, which were then rapidly transformed to Pt NPs thus hindering the recombination of electron-hole pairs.

In addition to TiO<sub>2</sub>/GR, other semiconductor/GR composites aslo have been reported for water splitting. The (Ga<sub>1-x</sub>Zn<sub>x</sub>)(N<sub>1-x</sub>O<sub>x</sub>)/rGO composites were used as the photocatalysts for

visible-light driven water splitting, in which the composites with 30 wt.% rGO gave the highest rate of H<sub>2</sub> production, almost 4.5 times higher than that of bare particles.[219] Reddy et al. used the CdS/rGO-MoS<sub>2</sub>@CoP photocatalyst for H<sub>2</sub> production in water under simulated sunlight irradiation with lactic acid as a sacrificial reagent. [250] The photocatalyst with 5 wt.% rGO, 4 wt.% MoS<sub>2</sub>, and 20 wt.% CoP exhibited an efficient H<sub>2</sub> production rate of 83 907 μmol h<sup>-1</sup> g<sup>-1</sup> with an apparent quantum efficiency of 22.5% ,where the wrapped rGO nanosheets can function as good electron collectors and transporters, while the MoS<sub>2</sub> and CoP nanostructures serve as a co-catalyst and electron acceptor, respectively.[250]

The ZnO/rGO composites was used as the photoanode in PEC water oxidation under white light illumination, which achieved 50% increase in O<sub>2</sub> evolution current over pure ZnO.[178] The TiO<sub>2</sub>/rGO/Sb<sub>2</sub>S<sub>3</sub> electrode was also used as the photocatalyst for the PEC water oxidation.[256]A higher photocurrent density of 0.96 mA cm<sup>-2</sup> was achieved for the TiO<sub>2</sub>/rGO/Sb<sub>2</sub>S<sub>3</sub> electrode measured at 0.82 V vs. RHE, as compared with those for the TiO<sub>2</sub>/Sb<sub>2</sub>S<sub>3</sub> (0.75 mA cm<sup>-2</sup>) and TiO<sub>2</sub> (0.15 mA cm<sup>-2</sup>) electrodes, due to the enhanced light absorption and conductivity respectively with the help of Sb<sub>2</sub>S<sub>3</sub> and rGO.[256] The N-doped α-Fe<sub>2</sub>O<sub>3</sub>/GR electrode also showed a 4-fold enhancement of O<sub>2</sub> production under visible light compared with pure α-Fe<sub>2</sub>O<sub>3</sub> due to enhancement of charge separation by GR coupling and N doping.[346]

Moreover, H<sub>2</sub> can also be produced from the photocatalytic conversion of hazardous H<sub>2</sub>S. Bhirud et al. used the N-doped ZnO/GR nanocomposites for the photocatalytic reaction to transform hazardous H<sub>2</sub>S waste into hydrogen in a NaOH solution.[214] They found the nanocomposite with 0.3wt.% GR exhibited an enhanced photocatalytic stable hydrogen production rate of 5072 mmol h<sup>-1</sup> under visible light irradiation.[214]

### 2.4.3 Fullerene

There are only a few reports involving fullerene based semiconductor hybrids for water splitting mainly due to the higher price of fullerene compared with other carbon materials.

Luo et al. used first-principles calculations based on density functional theory to investigate the effects of van der Waals (vdW) interactions on changes in the electronic structure, charge transfer and photoactivity in three typical monolayer MoS<sub>2</sub>/fullerene (C<sub>60</sub>, C<sub>26</sub>, and C<sub>20</sub>) heterostructures and found staggered band alignment could be obtained in the MoS<sub>2</sub>/C<sub>20</sub>

heterostructure, which has the ability to oxidize H<sub>2</sub>O to produce O<sub>2</sub> but cannot reduce H<sup>+</sup> to H<sub>2</sub>. [363]

Lian et al. prepared the C<sub>60</sub>-CdS/TiO<sub>2</sub> hybrid mesoporous architectures for H<sub>2</sub> evolution during the water-splitting under visible light irradiation and found the composite containing 0.5 wt.% of C<sub>60</sub> showed the best photocatalytic activity and good photo-stability, which gave a H<sub>2</sub> evolution rate of 6.03 μmol·h<sup>-1</sup>. [295] The C<sub>60</sub> clusters in the hybrids formed protection layers, which was favorable for both the photogenerated electron transfer through the heterojunctions for H<sub>2</sub> evolution and the prohibition of photocorrosion of CdS.

Chai et al. employed various nanostructured-carbon/TiO<sub>2</sub> nanocomposites for H<sub>2</sub> evolution. [287] Among these composites with same carbon content, the photoactivity was found decreasing in the order of C<sub>60</sub>-SWCNTs/TiO<sub>2</sub> > SWCNTs/TiO<sub>2</sub> > C<sub>60</sub>/TiO<sub>2</sub> > TiO<sub>2</sub> and the best carbon loading was 5wt.%. The 5wt.% C<sub>60</sub>-SWCNT/TiO<sub>2</sub> nanocomposites exhibited the highest H<sub>2</sub> evolution rate of 651 μmol h<sup>-1</sup>, which was higher than that (605 μmol h<sup>-1</sup>) of the SWCNTs/TiO<sub>2</sub>. This is because the C<sub>60</sub>-decorated SWCNTs were more beneficial for the photogenerated carrier transfer and separation than SWCNTs and C<sub>60</sub> alone.

#### 2.4.4 Carbon dots

There are also a few reports about using CD-semiconductor hybrids as photocatalyst for H<sub>2</sub> evolution.

Yu et al. utilized CD/P25 nanocomposites for the evolution of H<sub>2</sub> from aqueous methanol under exposure to UV and visible light and found the H<sub>2</sub> evolution rate was related to the CD content in the nanohybrid. [309] The nanohybrid with 1.5 wt.% CDs gave the highest evolution rate (9.1 mmol h<sup>-1</sup>) under UV-Vis light irradiation, 4 times higher than P25, while the highest H<sub>2</sub> evolution rate (0.5 mmol h<sup>-1</sup>) was achieved on the hybrid with 2 wt.% CDs loading under visible light. This is because the electron transfer mechanism differs from irradiated light sources. Under UV-Vis light irradiation, CDs serve as electron reservoirs to trap the photoinduced electrons from excited P25 for the efficient separation of photoexcited electron-hole pairs, while under visible light irradiation, the π conjugated CDs act as a photosensitizer, like organic dyes, to sensitize P25 into visible light responsive, in which the photoinduced electrons transfer from excited CDs to P25. [309] Wang et al. also studied the CD/TiO<sub>2</sub> NPs and CD/TiO<sub>2</sub> NWs prepared from hydrothermal treatment of TiO<sub>2</sub> and vitamin C for the H<sub>2</sub> evolution from water under illumination of a 300 W Xe lamp. [322] It was found

the CD/TiO<sub>2</sub> NP nanocomposites synthesized at 200 °C for 2 h with a VC amount of 0.001 g showed a 9.7-fold higher H<sub>2</sub> production rate (361.9 μmol g<sup>-1</sup> h<sup>-1</sup>) than bare TiO<sub>2</sub> NPs, while the CD/TiO<sub>2</sub> NW hybrids prepared at 90 °C for 4 h produced hydrogen at a rate of 1189.7 9 μmol g<sup>-1</sup> h<sup>-1</sup>, 4.2 times higher than TiO<sub>2</sub> NWs. Due to the superior interfacing of CDs with TiO<sub>2</sub>, CDs are able to serve as electron acceptors and donors, wherein the photo-induced electrons can transfer from CDs to TiO<sub>2</sub> surfaces, and then the redundant electrons on TiO<sub>2</sub> can transfer back to the CD particles.[322] The CD/hydrogenated TiO<sub>2</sub> nanobelt (CD/H-TiO<sub>2</sub>) loaded with 1 wt.% platinum was also used produce H<sub>2</sub>, which gave an evolution rate of 7.42 mmolh<sup>-1</sup>g<sup>-1</sup>, higher than H-TiO<sub>2</sub> (6.01 mmolh<sup>-1</sup>g<sup>-1</sup>) and TiO<sub>2</sub> (0.65 mmolh<sup>-1</sup>g<sup>-1</sup>) nanobelts at same condition. [316] The S, N co-doped GQD/P25 composites also exhibited high stability and excellent photocatalytic hydrogen generation activities under both UV and visible light and because S,N-GQDs have broad photoabsorption in wide spectral range, high carrier transport mobility and excellent chemical stability. [327] Under UV–vis light irradiation, the 3 wt% S,N-GQD/P25 showed the best photocatalytic ability, which was about 3.6 times higher than that of the pure P25.

## 2.5 Photocatalytic carbon dioxide (CO<sub>2</sub>) reduction

Photocatalytic reduction of CO<sub>2</sub> into fuels such as CO, CH<sub>4</sub> and CH<sub>3</sub>OH is an attractive strategy simultaneously converting solar energy into chemical energy and capturing the major greenhouse gas produced by human industrial activities.[364, 365] Unlike photocatalytic water splitting, photo-reduction of CO<sub>2</sub>, specifically the production of CH<sub>3</sub>OH and CH<sub>4</sub>, requires a reducing compound acting as the hydrogen source.[364] Water is the most attractive reducing agent among the various possibilities. However, it is still a great challenging as H<sub>2</sub>O reduction to H<sub>2</sub> is a competing reaction and the low solubility of CO<sub>2</sub> in water (approximately 33 μmol in 1 ml of H<sub>2</sub>O at 100 KPa and room temperature). Since the first PEC reduction of CO<sub>2</sub> reported by Halmann[366] and the first photocatalytic reduction of CO<sub>2</sub> over powdered semiconductor observation by Inoue's group[366], continuous efforts have been devoted to photocatalytic CO<sub>2</sub> conversion. Similarly, the solar energy harvesting, and charge separation and transportation are two crucial factors for the CO<sub>2</sub> reduction. The design of CSHMs is one of effective approaches to improve the efficiency based on these two factors.

Similarly, TiO<sub>2</sub>/GR nanocomposites is more frequently used in photocatalytic CO<sub>2</sub> reduction compared with other CSHMs because TiO<sub>2</sub> is abundant, stable and low toxic, and the

introducing of GR can effectively improve light absorption, charge separation and electron conductivity benefiting for the efficiency of photocatalytic CO<sub>2</sub> reduction. The TiO<sub>2</sub>/rGO hybrid with close interfacial contact between TiO<sub>2</sub> and GR sheets have been used for CO<sub>2</sub> reduction with water under a 15-W daylight bulb and achieved a maximum CH<sub>4</sub> product yield of 0.135 μmol g<sup>-1</sup> h<sup>-1</sup>, which is 2.1 and 5.6 fold higher than that achieved by GO and pure TiO<sub>2</sub>. [157] Park et al. studied a 3D TiO<sub>2</sub>/GR nanocomposite for photocatalytic CO<sub>2</sub> reduction in a gas phase system with CO<sub>2</sub> and triethylamine vapor under a mercury lamp irradiation (140 mW cm<sup>-2</sup>) and the amounts of CO generated was 1.26 μmol/mg after 4h which was 11 fold higher than P25. [209] Tu et al. investigated the photocatalytic CO<sub>2</sub> conversion on GR-Ti<sub>0.91</sub>O<sub>2</sub> hollow spheres in the presence of water vapor under a 300 W xenon arc lamp. [145] As show in Figure 2.11 a&b, the CO and CH<sub>4</sub> production rates on the GR-Ti<sub>0.91</sub>O<sub>2</sub> hollow spheres were 8.91 μmol g<sup>-1</sup> h<sup>-1</sup> and 1.14 μmol g<sup>-1</sup> h<sup>-1</sup>, respectively, while only CH<sub>4</sub> was observed on the Ti<sub>0.91</sub>O<sub>2</sub> hollow spheres with a rate of 1.41 μmol g<sup>-1</sup> h<sup>-1</sup>, higher than that on P25. The enhancement can mainly attribute to the presence of GR nanosheets compactly stacking with Ti<sub>0.91</sub>O<sub>2</sub> nanosheets making the photogenerated electron to migrate fast from Ti<sub>0.91</sub>O<sub>2</sub> nanosheets into GR, resulting in the spatial separation of the electrons-hole pairs. Moreover, the excellent electrical mobility of GR restrained the accumulation of the electrons and decrease local electron density, which favoured for two-electron interaction to form CO instead of eight-electron for CH<sub>4</sub>. [145]

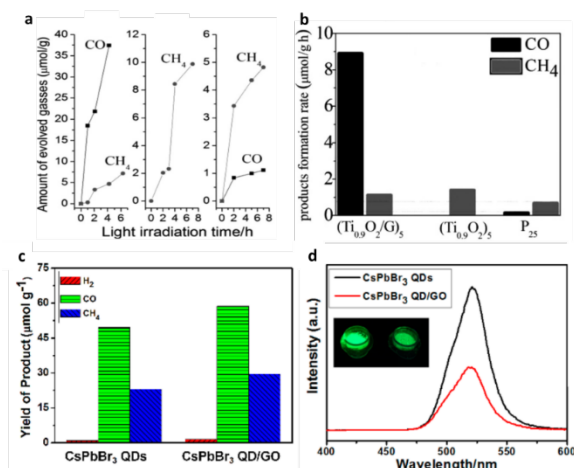


**Figure 2.11.** Photocatalytic CH<sub>4</sub> (dots) and CO (squares) evolution amounts for (G-Ti<sub>0.91</sub>O<sub>2</sub>)<sub>5</sub> hollow spheres, (Ti<sub>0.91</sub>O<sub>2</sub>)<sub>5</sub> hollow spheres, and P25 (from left to right), (b) comparison of the average product formation rates, (c) photocatalytic performance: yield of the CO<sub>2</sub> reduction products after 12 h of photochemical reaction, and (d) steady-state PL spectra with an excitation wavelength of 369.6 nm. Reprinted with permission from ref. [145, 367] Copyright 2012 WILEY-VCH and 2017 American Chemical Society.

Recently, Benedetti et al. prepared a TiO<sub>2</sub>/CdS/rGO/Pt quaternary nanocomposite and used for the photocatalytic reduction of CO<sub>2</sub> to CH<sub>4</sub> in the presence of water and simulated sun light.[233] After 5h illumination under visible light, 0.11 mmol of CH<sub>4</sub> was produced at an average production rate of 0.0867 mmol h<sup>-1</sup>, which was higher than the production of CH<sub>4</sub> measured from the TiO<sub>2</sub>/CdS and the TiO<sub>2</sub>/CdS/Pt control samples. Xu et al. reported the utilization of a CsPbBr<sub>3</sub> quantum dots (QDs)/GO material for the PEC conversion of CO<sub>2</sub> in ethyl acetate under solar light illumination (150 mW cm<sup>-2</sup>) for the first time. [367] Compared to the individual CsPbBr<sub>3</sub> QDs, the rate of electron consumption improved from 23.7 to 29.8 μmol g<sup>-1</sup>h<sup>-1</sup> after the introduction of GO and 58.7 μmol g<sup>-1</sup> CO and 29.6 μmol g<sup>-1</sup> CH<sub>4</sub> were obtained on CsPbBr<sub>3</sub> QD/GO after 12h respectively, which were higher than that on CsPbBr<sub>3</sub> QD (Figure 2.11c). The photocatalytic enhancement was caused by the electron extraction ability of conductive GO, which can be confirmed by the photoluminescence (PL) tests (Figure 2.11d).[367]

## 2.6 Photocatalytic reduction of nitro organics to amino organics

Liquid phase selective reduction of nitro organics to amino organics in water is one of the significant synthetic reactions in organic chemistry. As shown in Figure 2.12, a complete reduction of a nitro compound to amino compound requires six electrons. There are a few reports of utilizing GR-based semiconductor composite photocatalysts for this reaction since GR has excellent electrical mobility and conductivity favouring the transfer and prolong the lifetime of the electrons photoexcited from semiconductor. And, the introduction of GR could increase adsorptivity of reactants because of π-π conjugation between aromatic nitro organics and the aromatic regions of GR.

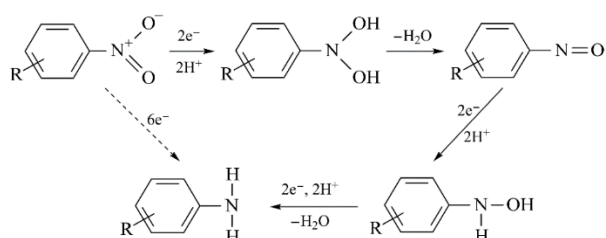


**Figure 2.12.** Photocatalytic reduction mechanism of aromatic nitro compounds in water. [186]

Wang et al used the hierarchical TiO<sub>2</sub> hollow spheres partially wrapped with rGO (TiO<sub>2</sub> HS/rGO) as a photocatalyst for reducing 4-nitroaniline (4-NA) to *p*-phenylenediamine (PPD) under a 300W Xe arc lamp with ammonium formate as hole scavenger and found the hybrid containing 3 wt.% rGO gave the best photocatalytic performance compared with P25, TiO<sub>2</sub>

HS and TiO<sub>2</sub> HS/rGO with other amount of rGO(1wt.% and 5wt.%).[171] Liu et al. utilized CdS/GR nanocomposites to photocatalyze selective reduction of various aromatic nitro compounds to the corresponding aromatic amines in aqueous phase under visible light irradiation.[186] They found that the CdS/GR nanocomposites with an appropriate weight addition ratio of GR (1-10wt.%) exhibit enhanced photocatalytic performance compared with blank-CdS, in which the one with 5wt.% GR showed the best result. Similar results were observed on the CdS nanospheres/GR (CdS NSPs/GR) hybrid nanocomposites, where the photocatalytic reduction efficiency of 4-NA follows the order: CdS NSPs/5% GR > CdS NSPs/2% GR > CdS NSPs/10% GR > bare CdS NSPs.[143] The CdS NSPs/5% GR also exhibited higher photoactivity than CdS NSPs/5% GO, which indicate that efficient reduction of GO to GR plays a positive role in this photocatalytic reduction. [143] Compared with the bare CdS, the improvement can be attributed to the increased adsorptivity and the improved lifetime and transfer of charge carrier with the GR adding. Moreover, the intimate interfacial contact between CdS and GR sheets could also inhibit the photocorrosion of CdS, which makes the CdS/GR nanocomposites have high stability towards the photo-reduction of 4-NA or 1-bromo-4-nitrobenzene. [143, 186]

In addition, Chai et al. compared the photocatalytic performances of CD/CdS, GO/CdS and CdS multilayered films grown on ITO via layer-by-layer method. [318] The CD/CdS films (6 cycles) exhibited good stability and highest photocurrent density (2.6 mA cm<sup>-2</sup>), although their absorption range was not as abroad as GO/CdS films. This is because the more intimate interfacial contact between CD and CdS layer are beneficial for charge separation and transfer. Under visible light irradiation, the photoreduction efficiency of nitro-aromatic compounds to their corresponding amino organics followed in the order of CD/CdS > GO/CdS > CdS films with the same number of deposition cycles. For instance, the conversion of p-nitroaniline after 2.5 hours using photocatalyst CD/CdS was 70%, while that of GO/CdS and CdS films were 49% and 24% respectively. Thus, the electron donor–acceptor heterojunction can expedite charge separation and effectively suppress electron–hole pair recombination.

## 2.7 Photocatalytic selective oxidation

The oxidations of alcohols to aldehydes and epoxidation of alkenes are vital reactions in synthetic organic chemistry, and high selectivity and mild conditions are the

key requirements for ease of operation and lower cost. Photocatalytic oxidation based on CSHMs is one of the promising approaches.

Yang et al. have compared a series of TiO<sub>2</sub>/GR, TiO<sub>2</sub>/CNT, and TiO<sub>2</sub>/C<sub>60</sub> nanocomposite photocatalysts towards the selective oxidation of benzyl alcohol to benzaldehyde under visible light irradiation and found the composites with optimum ratios, TiO<sub>2</sub>/0.1% GR, TiO<sub>2</sub>/0.5% CNT, and TiO<sub>2</sub>/1.0% C<sub>60</sub>, were very close to each other along with the same irradiation time.[286] There was no much difference in essence on affecting the photocatalytic performance of TiO<sub>2</sub> among these three different carbon allotropes. Zhang et al. also have studied the photocatalytic activities of TiO<sub>2</sub>/GR and TiO<sub>2</sub>/CNT synthesized by same method for this reaction in the solvent benzotrifluoride saturated with O<sub>2</sub> molecular under visible light irradiation.[15] It was found both of the two composites with 5wt.% of carbon gave the best photocatalytic activities but the TiO<sub>2</sub>/GR nanocomposite was over five times more active than its analogue TiO<sub>2</sub>/CNT due to the difference between GR and CNT on controlling the morphology of CSHMs. The TiO<sub>2</sub>/5% GR also showed high selectivity (90-100%) toward oxidation of a range of benzylic alcohols with various substituent groups and allylic alcohols to their corresponding aldehydes.[15] In addition, they also studied the photocatalytic performance of ZnS/GR nanocomposites on the selective oxidation of various alcohols and epoxidation of alkenes, and found the hybrid containing 5% GR gave the best results.[185] The addition of GR caused the band gap narrowing of ZnS to ca. 3.45 eV for ZnS/5%GR, which was still large to photo-excite electrons from VB CB of ZnS under visible light irradiation ( $\lambda > 420$  nm). Thus, they thought GR in the ZnS/GR nanocomposites acted as an photosensitizer for ZnS instead of an electron reservoir.[185] Ren et al. also reported the CdS/GR nanocomposites could serve as an efficient visible-light-driven photocatalyst for the selective oxidation of benzyl alcohol to benzaldehyde under ambient conditions. [184] It was found the interfacial contact between GR and CdS was crucial for their photocatalytic activities, where the hydrothermal synthesized samples were best and the optimal photocatalytic performance was achieved on the CdS/5%GR nanocomposite. [184]

## **2.8 Dye-sensitized solar cells (DSSCs)**

In addition to photocatalysis, another emerging application for CSHMs is in photovoltaic solar cells, which can directly convert sunlight into electricity. As one of third generation solar cells, DSSCs in particular have been attracted from their respectable efficiency, perspective of wide availability, low-cost, and easy fabrication process. A typical DSSC

device consists of a dye-sensitized mesoporous semiconductor scaffold as the photoanode, a hole-conducting electrolyte containing the redox couple, and a catalytic counter electrode (CE). CSHMs can be introduced into both photoanode and CE to boost the photovoltaic performance of DSSCs.

### **2.8.1 Photoanode**

Incorporating carbon materials enables the improvement of dye absorption on the photoanode because of their large surface area and also the possible enhancement of light harvesting due to light scattering effect and band gap narrowing through the strong interaction between carbon and semiconductor material. More importantly, the high electronic conductivity of carbon materials favour the electrons transfer within the photoanode, which can suppress the charge recombination. These functions can enable photocurrent enhancement and result in high power conversion efficiency (PCE) of DSSCs. The photovoltaic performances of DSSCs using various CSHMs as photoanodes are summarized in Table 1.

#### **2.8.1.1 Amorphous carbon**

In the photoanode of DSSCs, light arriving and being absorbed by dye molecules anchored on the surface of semiconductor is a key factor for high photocurrent. Carbon materials are black and a large amount of them in the hybrid would not only weaken the light harvesting but also reduce the dye adsorption on the surface of semiconductor. Thus, a small amount doping is a commonly used means to introduce amorphous carbon into the photoanode for improving DSSC performance. For example, Park et al. found the short-circuit current density ( $J_{sc}$ ) and PCE of DSSCs based on a C-doped  $TiO_2$  electrode was increased by 20% and 23% compared to DSSCs using a pure  $TiO_2$  electrode, respectively.[368] They attributed this to the enhancement of dye adsorption and high electrical conductivity of the carbon. Lin et al. used the C- $TiO_2$  prepared from the hydrothermal treatment of  $Ti(SO_4)_2$  and glucose as the photoanode and found both the short circuit current ( $J_{sc}$ ) and open circuit voltage( $V_{oc}$ ) were improved compared with the DSSCs assembled with non-doped  $TiO_2$ .[369] In this case, the enhancement of PCE should not be attributed to dye adsorption but the more efficient charge transport and a negatively shifted flat band potential after carbon doping, which would be affected the hydrothermal time.

The morphology and structure of the semiconductor materials in the photoanode are also crucial for the DSSC performance as they are responsible for dye absorption, charge collection and diffusion. Compared with small nanoparticles, the 1D or hierarchical nanostructures can provide direct or multiple transport paths for the injected electron diffusion and high surface area for dye loading resulting in the fast and strong electron flow and retardation of the charge recombination. On the basis of carbon doping, controlling the morphology and structure of semiconductor material in the photoanode is expected to further enhance the efficiency of DSSCs. Rho et al. used the carbon-doped TiO<sub>2</sub> NT arrays as the photoanode material for DSSCs and found the PCE of the open-ended TiO<sub>2</sub> NT arrays were higher than those of the closed-ended TiO<sub>2</sub> NT arrays due the increase of surface area.[78] Besides, the amount of carbon loading also have great effect, where a small amount of carbon doping could increase the PCE from 5.07% to 6.21% due to electron transport enhancement by  $\pi$ - $\pi$  conjugation with carbon doping, but a large amount of carbon doping reduced the PCE to 2.87% because of the reduced level of dye adsorption on TiO<sub>2</sub> NTs.[78] Jang et al. incorporated hierarchical C-TiO<sub>2</sub>@SiO<sub>2</sub> into P25 as the photoanode to improve the efficiency and stability of DSSC and found the both the particle size and content of the hierarchical structure would influence the cell performance. [68] The best PCE of 5.21% was obtained on the anode with 1wt.% large C-TiO<sub>2</sub>@SiO<sub>2</sub> beads(200nm), but the best content became 0.1 wt.% when using small size beads(50nm), gave a PCE of 5.11%. Thus, incorporating of moderate amount carbon species into the photoanode of DSSCs can enhance the charge transport and collection and the light scattering effect of particle size also need be considered.

Carbon-doped TiO<sub>2</sub> hollow spheres (HS) were also applied as photoanode and gave a PCE of 7.02%. [370] It was found these C-TiO<sub>2</sub> HS had narrowed band gap and the phase composition also affected the cell performance, where small amount of rutile phase in anatase showed high J<sub>sc</sub>. The PCE was further improved to 8.55%, when the C-TiO<sub>2</sub> HS was used a scattering layer on the top of an anatase NP layer. [370] We also prepared micron-sized carbon-doped TiO<sub>2</sub> beads containing rutile NRs and brookite NPs and used them as a scattering layer with anatase TiO<sub>2</sub> beads as bottom layer for the DSSC application. [59] The DSSC with bi-layer photoanode gave a high PCE of 7.24% because the hierarchical structure with carbon doping improved the electron transport and suppressed carrier recombination.

### 2.8.1.2 Carbon nanotubes

CNTs with 1D tubular structure coupling with semiconductor materials in the photoanode are promising to improve the DSSC performance since CNTs have higher surface area and electronic conductivity and can efficiently enhance the transport of electrons. Besides, the adding of CNT into the photoanode may also improve the stability of DSSCs. [30]

CNT/TiO<sub>2</sub> nanocomposites, including MWCNT/TiO<sub>2</sub> and SWCNT/TiO<sub>2</sub> have been widely studied as the photoanode materials. Similarly, the loading amount CNT in the photoanode is also a key factor for determining the performance of DSSCs. Various studies have shown that a small amount of CNT loading can effectively improve the photocurrent but high CNT content would decrease the efficiency of DSSC. This is because CNTs with black body nature would compete for optical absorption with molecules and at high content CNT aggregations may appear in the photoanode resulting in carrier recombination sites. For the TiO<sub>2</sub>/MWCNT composites prepared by mechanical blending or impregnation method, the identical CNT content normally did not exceed 0.1 wt.%, [30, 31, 81, 371, 372] which is much lower than in hybrids used for photocatalysis. The optimal value of 0.2 wt.% was found in the case of double-walled CNT/TiO<sub>2</sub> photoanode, in which J<sub>sc</sub> was increased by 43% and the PCE improved from 3.9% to 6.4% compared with pure TiO<sub>2</sub> electrode. [373] Lee et al. used the TiO<sub>2</sub>/SWNT composite to prepare a flexible photoanode and they found the flexibility and mechanical durability increased with an increasing concentration of CNT but J<sub>sc</sub> and overall PCE decreased at increased concentration (1.3 and 3.5 wt%), where the identical value was 1 wt.%. [374] For the TiO<sub>2</sub>/MWCNT prepared from sol-gel method, Wang et al. found the CNTs could uniformly disperse in TiO<sub>2</sub> photoanodes leading to high electron collection and photoelectric efficiency when the CNT content was at 1-3 wt.%, [84] while Guo et al. found the optimal content of MWCNTs in the nanocomposites was 0.06%. [85]

The efficient use of the outstanding electrical properties of TiO<sub>2</sub>/CNT nanostructure relies heavily on the quality of the interface. It can be seen from clearly from Table 1 that the PCEs of DSSCs based on the TiO<sub>2</sub>/CNT prepared by sol-gel or hydrothermal method are much higher than those prepared from simple mechanical blending. This is because in the TiO<sub>2</sub>/CNT hybrids obtained from mechanical mixing, few TiO<sub>2</sub> nanoparticles were coated on the surface of CNT and the heterogeneous interfaces formed between the CNTs and the bulk TiO<sub>2</sub>, which would decrease dye adsorption and result in carrier recombination sites. [30]

Wang et al. have compared the effect of TiO<sub>2</sub>/MWCNT nanocomposites prepared from in situ layer pyrolysis and direct post-mixing on the solid-state DSSC performance. [106] The cells based on in situ TiO<sub>2</sub>/MWCNT porous electrodes exhibited an enhanced efficiency associated with a larger J<sub>sc</sub> than that of cells based on ex situ post-mixed composites (Figure 2.13 a&b). Compared to a direct post-mixing sample, a dense coating of the nanotubes by TiO<sub>2</sub> particles was observed (Figure 2.13b), leading to enhanced electronic interactions between the TiO<sub>2</sub> and MWCNT, which reduced the charge recombination and improved charge extraction to the electrode. [106] Similar results were obtained on the TiO<sub>2</sub>/MWCNT photoanode prepared by hydrothermal growth TiO<sub>2</sub> onto the vertically-aligned MWCNTs mounted on a FTO glass, where the PCE increased from 6.51% to 7.00% compared with conventional TiO<sub>2</sub> electrode. [95] Due to the enhanced interconnectivity between CNTs and TiO<sub>2</sub> mesoporous structures, the band gap of TiO<sub>2</sub>/MWCNT was narrowed from 3.15 to 2.5 eV and the enhanced photocurrent extraction was evident. The PCE of this cell can be further improved to 7.27% when used FeS<sub>2</sub> as a counter electrode. [95] A higher PCE of 10.6% was achieved by using the SWNT/TiO<sub>2</sub> core-shell nanocomposites incorporated only 0.1 wt% SWNTs as photoanodes in DSSCs. [103]

Likewise, the morphology and structure of TiO<sub>2</sub> and CNTs in the photoanode also determine the final DSSC efficiency. Yu et al. compared the photovoltaic performance of DSSCs based on P25/MWCNT and TiO<sub>2</sub> HS/MWCNT photoanodes. [31] The TiO<sub>2</sub> HS/MWCNT cells showed higher PCE compared with those P25/MWCNT DSSCs due to the high specific surface areas and hierarchically nanoporous structures of hollow spheres, which would enhance adsorption of dye molecules, the light harvesting and the diffusion of electrolyte. The rice-grain shaped TiO<sub>2</sub>/MWCNT nanocomposites with high surface area and single TiO<sub>2</sub> crystallinity were also used as photoanode for DSSCs, which give a PCE of 6.12% with optimal CNT loading of 0.2 wt.%. [100] Guo et al. incorporated MWCNT with TiO<sub>2</sub> and TiO<sub>2-x</sub>N<sub>x</sub> respectively for the photoanode materials in DSSCs and found introducing MWCNT into TiO<sub>2-x</sub>N<sub>x</sub> suppressed photovoltaic performance of the DSSCs due to a larger electron transfer resistance and more recombination sites.[85] Dang et al. also have compared the effect of metallic and semiconducting SWNTs on the device performance in TiO<sub>2</sub>/CNT system and found they showed in opposite ways. [103] As shown in Figure 2.13d, semiconducting SWNTs have a non-continuous band structure with a diameter dependent bandgap and the electrons in the SWNT CB transferred from the TiO<sub>2</sub> CB can transport quickly to FTO without recombination or back reaction. In contrast, metallic SWNTs have

higher conductivity[109] but a continuous band structure. Thus, electrons transferred from  $\text{TiO}_2$  can stay at continuous energy levels near the Fermi level, accelerating recombination of electrons to the dye or back reaction to tri-iodide in the electrolyte, reducing the cell efficiency. It was also found that the oxidized SWNTs in  $\text{TiO}_2/\text{SWNT}$  hybrid photoanode showed better cell performance compared with the pristine SWNTs due to owing to the increase of roughness.[375] Besides, introducing small amount of metal nanoparticles into  $\text{TiO}_2/\text{CNT}$  photoanode may also enhance the DSSC performance due to the localized surface plasmon effect. Zhang et al. found the current density and the PCE increased when the amount of Ag NPs was increased from 0-0.8 wt.% in  $\text{TiO}_2/\text{SWNT}$  electrode, but further increased the Ag content would lead to decrease as the Ag NPs may act as recombination centres causing internal short-circuit.[109]

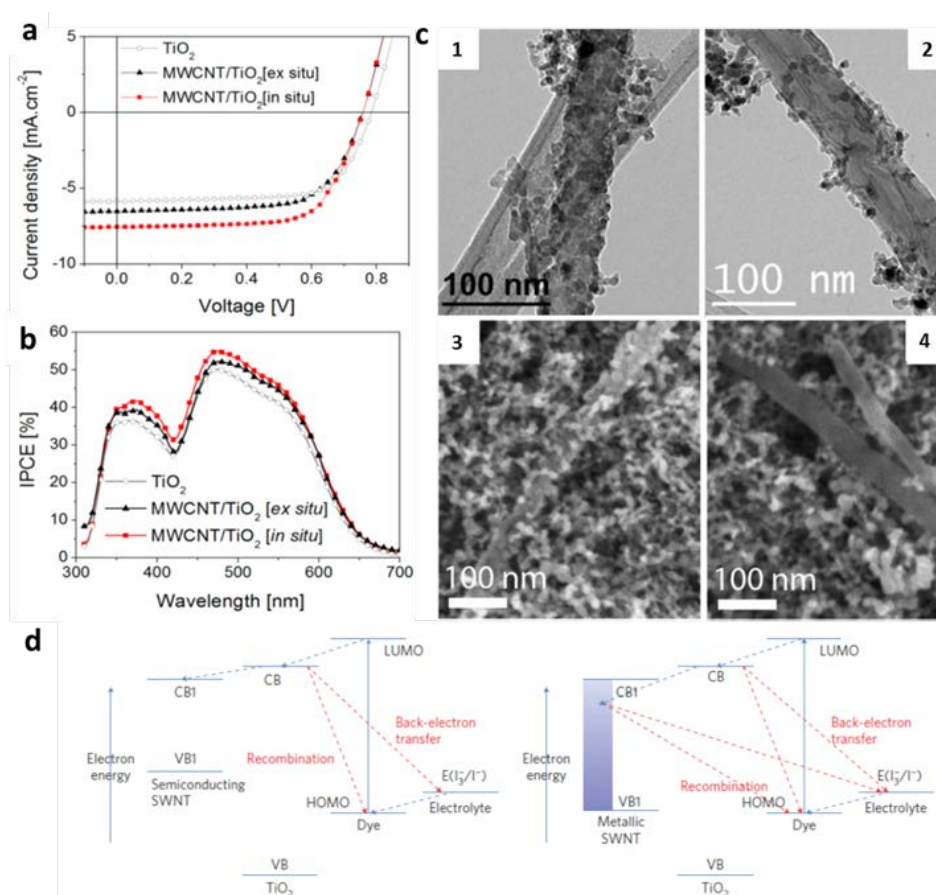


**Figure 2.13.** (a) Current density/voltage characteristics and (b) IPCE spectra of the DSSC based on pure  $\text{TiO}_2$ ,  $\text{MWCNT}/\text{TiO}_2$  [ex situ] and  $\text{MWCNT}/\text{TiO}_2$  [in situ] porous electrodes, (c) TEM images of (1) in situ and (2) ex situ MWCNTs/ $\text{TiO}_2$  nanocomposites and SEM top view images of  $\text{TiO}_2$  porous layers processed from (3) in situ and (4) ex situ composites, and (d) energy diagrams of DSSCs incorporating semiconducting SWNTs and metallic SWNTs. Reprinted with permission from ref. [106] and [103] Copyright 2014 American Chemical Society and 2011 Nature Publishing Group.

In addition to TiO<sub>2</sub>/CNT, ZnO/CNT nanocomposites also have been applied as photoanode in DSSCs. For example, Abdullah et al. fabricated the ZnO/MWCNT and ZnO/SWCNT hybrid photoanodes to enhance the efficiency of DSSCs. [86, 87, 376, 377] They found the DSSC based on ZnO/SWCNT exhibited better photovoltaic performance compared with those based on ZnO/MWCNTs due to highly efficient electron transport by the implementation of SWCNTs with ZnO.[87, 376] Chang et al. also have compared the influences of oxidized MWNTs (O-MWNT) and acid treated MWNTs (acid-MWNT) on the DSSC performance within the ZnO hybrid photoanodes, where the acid-MWNT modified cell had higher PCE because the acid-MWNTs were disentangled and better dispersed in the ZnO matrix.[378] Zeng et al. have coated ZnO nanostructures onto vertically aligned CNTs on stainless steel sheet and used them as the photoanode for DSSCs, which gave a 4-fold increased PCE compared to those randomly distributed ZnO/CNTs nanostructures.[107] However, the overall DSSC efficiencies on ZnO/CNT photoanodes are lower than that on TiO<sub>2</sub>/CNT because the Zn<sup>2+</sup> ions of the outer layer of the ZnO nanostructures would dissolve into the solution by the acidic carboxylate groups of the N719 dye molecule to form a Zn<sup>2+</sup>-dye complex layer hindering excited electrons moving from dye to ZnO nanostructures.

### 2.8.1.2 Graphene

Graphene(GR) has high specific surface area (about 2630 m<sup>2</sup>/g for a single layer)[379] and excellent electron mobility (up to 200,000 cm<sup>2</sup> V<sup>-1</sup> s<sup>-1</sup>),[380] which is much faster than ZnO (200–1000 cm<sup>2</sup> V<sup>-1</sup> s<sup>-1</sup>) and TiO<sub>2</sub> (0.1–4 cm<sup>2</sup> V<sup>-1</sup> s<sup>-1</sup>).[381] Compared with 1D CNT, 2D GR have more advantages to couple with 0D materials such as compactly anchoring and homogeneous dispersion. [32] Thus, applying GR into photoanode with semiconductor materials is promising to enhance dye adsorption, reduce internal resistances, expedite electron transport and lower charge recombination rate leading to high efficiency of DSSCs.

Again, the transparency of electrode film is quite important to get the absorbed dye totally sensitized by light in DSSCs. Due to the black nature, the GR content in the hybrid is a key factor to obtain a large number of photoinduced electrons from dye molecules. The optimum GR content varies across different researches, which may depend on the hybrid process or the DSSC system. Taking TiO<sub>2</sub>/GR as an example, Mehmood et al. found the optimum percentages of commercial GR were 0.08 wt.%, 0.09 wt.% and 0.16 wt.% in the TiO<sub>2</sub>/GR-N3,[36] TiO<sub>2</sub>/GR-N749[382] and TiO<sub>2</sub>/GR-Z907[383] photoanodes, respectively. For the TiO<sub>2</sub>/rGO electrodes prepared from hydrazine reduction, [32] vitamin C reduction [140] and

thermal reduction, [129] the optimal values were 0.6 wt.%, 0.75 wt.% and 0.25 wt.%. Sun et al. prepared P25/GR composites by heterogeneous coagulation with assistance of nafion and found GR sheets were only partly coated by P25 when the mass ratio of P25:GR=5:1, while GR were homogeneously and densely coated with P25 at the ratio P25: GR=20:1. [384] Fang et al. found the rutile contents in P25/GO photoelectrodes increased with increasing GO addition leading to higher cell performance but a large amount GO adding resulted in wrinkled and cracked films. [385] In the poly (vinyl alcohol) (PVA) gel electrolyte based DSSCs, the optimum GO content of TiO<sub>2</sub>/GO photoanode was 2.5 wt.%. [386] Wei et al. found the addition of excess rGO weakened the crystallization of TiO<sub>2</sub> particles on the surface of the photoelectrodes leading to the increase of charge recombination and the reduction of dye adsorption. [33] Kazmi et al. also found the increase in graphene concentration would cause a down shift in conduction band of TiO<sub>2</sub>/GR nanocomposites with respect to pure TiO<sub>2</sub> resulting in slight decrease in V<sub>oc</sub> and the optimum GR percentage was 3.0 wt%, in which the PCE was increased from 4.98% (pure TiO<sub>2</sub>) to 7.68%. [35] In general, presenting a small amount of GR in photoanode can effectively enhance the DDSS performance, especially the generated photocurrent due to the reducing of recombination of charge carriers and the improvement of the transport properties without sacrificing transparency.

The interaction between TiO<sub>2</sub> and GR determines the photo-generated electrons transfer rate at their interfaces and the loose contact will also result in charge recombination sites. To enhance their interaction, Low et al. have tried to prepare TiO<sub>2</sub>/rGO photoanodes via an ion implantation approach to incorporate the Ti<sup>4+</sup> ion onto the rGO nanosheet. [196] It was found the applied power had significant influence on the formation of TiO<sub>2</sub>/rGO nanocomposite and at 150 W, the obtained hybrid had lowest band gap (2.89 eV) and the highest electron transfer rate due to the formation of stronger Ti–O–C bonds. A PCE of 8.51% could be achieved in DSSC based on this photoanode.

Similarly, the photovoltaic performance of DSSCs strongly depends on the morphology of GR and TiO<sub>2</sub> and the structure of their hybrids. The rGO prepared from high-temperature (1000°C) thermal reduction haven been coupled with TiO<sub>2</sub> as the photoanodes in DSSCs, which showed enhanced PCE because the high degree reduced GO have lower resistivity and high transparency. [34] The TiO<sub>2</sub>/single-layered GR composites also have been prepared as photoanodes in DSSCs with iodine or cobalt redox electrolyte. [387] The specific surface area of photoanode was increased from 114 m<sup>2</sup> cm<sup>-3</sup> to 124 m<sup>2</sup> cm<sup>-3</sup> after introducing single-

layered GR, which resulted in higher dye loading and then  $J_{sc}$ . However, the charge collection efficiency was lower for the cobalt electrolyte compared to the iodide one.[387] Fan et al. have fabricated  $TiO_2$  nanosheets ( $TiO_2$ -NSs)/GR nanocomposite as photoanode for DSSCs. [388] The  $TiO_2$ -NSs with exposed (001) facets had good crystallization, high pore volume and large particle size, which favour the dye loading, electron transport and light scattering, and after coupled with a moderate amount of GR, the electrolyte–electrode interfacial resistance and the charge recombination rate were reduced and the transport of electrons from the  $TiO_2$ -NSs film to FTO substrate was enhanced resulting in high DSSC performance.[388] A high PCE of 7.5% was achieved in DSSCs based 3D  $TiO_2$ /rGO inverse opal electrodes because the local arrangement of GR sheets in the inverse opal structure effectively enhanced electron transport without significantly reducing light harvesting by the dye molecules. [211] Zhi et al. fabricated highly flexible DSSCs by employing 3D GR decorated  $TiO_2$  films as anode on plastic substrates, which gave an enhanced efficiency of 6.41% owing to the improved charge transportation and increased surface area from 3D conductive GR skeleton.[210] Lee et al. also prepared 3D tubular-structured monolayer GR networks to hybridize with  $TiO_2$  NP layer as electrode for DSSCs. [146] The continuous form of 3D GR with good carrier mobility provided a direct pathway for electrons to the current collector and the optimal hybrid anode exhibited the high PCE of 9.2%. [146]

The photovoltaic performance of DSSCs could be further enhanced by element doping or introducing third functional compound into the  $TiO_2$ /GR based photoanode. Each N atom has a single valence p electron and N doping can enhance the electron conductivity of both GR and semiconductor materials. Xiang et al. compared the DSSC performances on the photoanodes of  $TiO_2$ /GO and  $TiO_2$ /N-rGO and found the cells based on  $TiO_2$ /N-rGO showed higher  $V_{oc}$ ,  $J_{sc}$  and PCE because the conductivity of N-rGO was increased remarkably after N doping.[381] A high PCE of 9.75% was obtained on the DSSCs based on rGO/NiO/ $TiO_2$  hybrid anode, which was remarkably higher than that of the GO/ $TiO_2$  (8.55%), and NiO/ $TiO_2$  (9.11%) photoanodes.[215] Mohamed et al. fabricated GO/N-SnO<sub>2</sub>/ $TiO_2$  nanofiber (NF) photoanodes and the efficiency of 6.18% was achieved, which was higher than those of 5.01% and 3.1% for the DSSCs based on N-SnO<sub>2</sub>/ $TiO_2$  and SnO<sub>2</sub>/ $TiO_2$  NF photoanodes, respectively. [217] This is because the combination dopants of N and GO enhanced charge transfer and decreased the electrons/holes recombination. The ZrO<sub>2</sub>&GO@ $TiO_2$  NFs were also studied as the photoanode in DSSC and they found the GO could shorten the axial ratio of produced NFs, enhance the dye loading and decrease the resistance of the photoanode.[176]

A systematic increment in  $J_{SC}$  was also noticed while incorporating more Au NPs to the  $TiO_2/GO$  photoanode due to the combined effect of GO and Au NPs. [225] The DSSCs based on P25 anodes doped with an inorganic donor–acceptor (D–A) type  $SiW_9Co_3/rGO$  nanocomposite exhibited enhanced photovoltaic performance as  $SiW_9Co_3$  was excitable by nearly the full spectrum and the photoinduced electrons could be quickly and effectively transferred from  $SiW_9Co_3$  to the GR sheets. [271] The DDSC based on  $GR/TiO_2:Er^{3+}, Yb^{3+} NR /TiO_2:Al_2O_3:Eu^{3+}$  NPs showed superior PCE to that of the devices based on pure  $TiO_2$  because the upconversion (UC) material  $TiO_2:Er^{3+}, Yb^{3+}$  and the downconversion (DC) material  $Al_2O_3:Eu^{3+}$  can facilitate the light harvesting of solar cells via converting NIR and UV radiation to visible emission, respectively, while the GR layer provided faster electron transport from  $TiO_2$  to FTO. [269]

In addition to  $TiO_2/GR$ ,  $ZnO/GR$  nanocomposites were often used as photoanode materials for DSSCs. The presence of GR in  $ZnO$  could improve the dye and visible light adsorption, suppress the electron-hole recombination and increase the efficiency of the cells. [137] The GR weight percentage in the  $ZnO/GR$  composite also has a great influence on the DSSC performance. Bykkam et al. found an appropriate ratio of graphene (1.0 wt.%) in  $ZnO$  photoanode could effectively suppress the back electron–hole recombination, but higher GR loading would lead to the decrease of the efficiency of DSSC due to the light preserving of the layered. [136] Xu et al. have incorporated GR into the matrix of hierarchical  $ZnO$  photoanodes and found the incorporation of moderate GR (1.2 wt.%) could markedly prolong electron lifetime and effective diffusion length, which allowed the utilization of thicker photoanodes to afford enhanced surface area for higher dye loading and light harvesting. [389] However, the PCE of DDSCs based on  $ZnO/GR$  electrode are still relatively lower than those based on  $TiO_2/GR$ . Besides,  $Nb_2O_5/GR$  photoanodes were also reported, which showed a 52% increase in PCE and a 68% increase in fill factor compared to DSSCs based on pure  $Nb_2O_5$  electrode. [180] The presence of GR could decrease the band gap energy of  $Nb_2O_5$  and improve the dye adsorption and charge collection efficiency. [180]

### 2.8.1.3 Other carbon structures

In addition to the above mentioned carbon materials, other carbon structures were also reported to form CSHMs as photoanode materials in DSSCs. For example, Ramar et al. have used  $ZnO/fullerene$  as the photoanode of DSSCs, which displayed higher  $V_{oc}$  compared with  $ZnO/CNT$  and  $ZnO/GR$  composite electrodes. [390] Single-walled carbon nanohorns

(SWCNHs), which have semiconductor character, high porosity, and large surface areas, were also coupled with TiO<sub>2</sub> as photoanode for DSSCs. [375] A efficiency of 7.98 % was obtained when double-layer SWCNHs doped TiO<sub>2</sub> electrode was utilized, where those nanocarbons could serve as electron acceptors and mediators.[375] The graphitic carbon nanospheres (GCNSs) prepared by an acidic treatment of MWCNTs were added into TiO<sub>2</sub> photoanode, which gave a significant enhancement of 47% in the efficiency of DSSC as compare the cell with pure TiO<sub>2</sub> photoanode.[391] Zhao at al. applied the hierarchical TiO<sub>2</sub> nanoflower coated carbon nanofiber (TNF@CNF) with a large specific surface area of 336.5 m<sup>2</sup> g<sup>-1</sup> as photoanodes in DSSCs. [392] The incorporated carbon nanofiber not only reduced the interfacial resistance and the charge recombination rate, but also improved the light harvesting, resulting in a high photoelectric PCE up to 8.57% for the single-layered TNF@CNF based DSSC. And, the efficiency could be further enhanced to 9.21% when using an urchin-like TiO<sub>2</sub> hollow sphere (UTHS) as light-scattering layer.[392]

## 2.8.2 Counter electrodes

The role of the counter electrodes (CE) in DSSCs is to collect electrons from the external circuit and to reduce triiodide (I<sub>3</sub><sup>-</sup>) to iodide (I<sup>-</sup>) in the electrolyte. To keep a low overvoltage and to minimize energy loss, the CE should have low resistance and high electrocatalytic activity towards the I<sub>3</sub><sup>-</sup> reduction.[393] Platinum (Pt) is commonly used as CE material for DSSCs, but it is scarce, expensive and unstable in I<sub>3</sub><sup>-</sup>/I<sup>-</sup> electrolyte, which limits the largescale application. Thus, it is necessary to develop new Pt-free CE materials to reduce the production cost and increase the stability of DSSC performance. CSHMs may meet the requirements as carbon materials have high surface areas, excellent electrochemical stabilities and high corrosion resistances, and some semiconductor materials, such as metal nitrides and sulfides, have wonderful electrocatalytic activity for the electrode reaction of I<sub>3</sub><sup>-</sup>/I<sup>-</sup> redox couple. More importantly, these materials are earth-abundant and inexpensive. The photovoltaic performances of DSSCs based on various CSHM CEs are summarized in Table 2.

### 2.8.2.1 Amorphous carbon

Amorphous carbon, such as carbon black (Cb) and activated carbon (Ac), have been studied as main CE material for DDSCs due to their good electrical conductivity and reasonable catalytic activity for the triiodide reduction. Some semiconductor materials, such TiO<sub>2</sub>, ZnO

and SnO<sub>2</sub>, were added into those carbon based CEs as a binder in order to improve their adhesion between each other and also to the FTO substrate. The resulted CEs not only have enhanced mechanical stability but also higher surface area, which favours the electrolyte diffusion and reduces the charge-transfer resistance ( $R_{ct}$ ). Lim et al. used the nanocomposites of TiO<sub>2</sub> (particle size 40 nm) and Cb as CEs and studied the influence of Cb content on the DSSC performance. [28] They found the CE with a weight ratio of TiO<sub>2</sub>:Cb=5:1 ratio had lowest  $R_{ct}$  and the cell using this electrode presented an PCE of 7.4%. The TiO<sub>2</sub>/Ac composites with 10 wt.% of TiO<sub>2</sub> were also used to prepare CE of DSSCs, which gave a PCE of 8.73%, higher than TiO<sub>2</sub>/MWCNT and TiO<sub>2</sub>/GR CEs with the same carbon content due to the presence of high defective sites in Ac. [394] TiO<sub>2</sub> hydrogel also have been introduced into carbon past (Cb: graphite=1.5 :2.25 wt/wt) to fabricate CE for DSSCs. [395] The hybrid CE showed a better conductivity and stability compared with that of the pure carbon CE, while the catalytic activity was not influenced. SnO<sub>2</sub> NPs also haven be incorporated into a similar system to from SnO<sub>2</sub>/TiO<sub>2</sub>/carbon nanocomposites for CEs and the photovoltaic performances of DSSCs were influenced by the content of SnO<sub>2</sub>. [396] The best PCE of 6.15% was obtained when the hybrid with 30 wt.% SnO<sub>2</sub> was used, in which SnO<sub>2</sub> not only acted as “framework” to strengthen the mechanical stability of the composite film but also increased the specific surface area and root-mean-square roughness resulting in improved FF and  $J_{sc}$ . [396] Xu et al. also synthesized ZnO/mesoporous carbon (MC) CEs, whose performance was affected by the annealing temperature. [397] When annealed at 300 °C, the in-situ formed and dispersed ZnO nanoparticles could work as bridges to bind the MC particles and provide enough conductive paths for the electron transportation, which led to a PCE increasing from 2.5% (binder-free MC electrode) to 6.37%. Besides, Fe<sub>3</sub>O<sub>4</sub> with good redox stability were also coupled with Cb as the CE for DSSC, which showed a high PCE of 6.1% superior to that of sputtered Pt CE (4.1%). [29]

The DSSC performance is expected to be further improved when the using semiconductor material itself has electrocatalytic activity towards the reduction of redox couple. WO<sub>2</sub> was found having decent catalytic activity for the I<sub>3</sub><sup>-</sup> reduction. Wu et al. have imbedded WO<sub>2</sub> into MC as the CE catalyst and the triiodide/iodide-based DSSCs using WO<sub>2</sub>/MC CE showed a high PCE of 7.76%, which superior to those cells using pure WO<sub>2</sub> (6.69%) , MC(7.01%) and even Pt(7.55%) as CE. [66] In addition, this WO<sub>2</sub>/MC CE also showed higher catalytic activity than Pt in the regeneration of the organic redox couple of di-5-(1-methyltetrazole) disulfide/5-mercapto-1-methyltetrazole *N*-tet-ramethylammonium salt (T<sub>2</sub>/T<sup>-</sup>). [66] Compared

with metal oxides, metal nitrides, having similar electronic structure to noble metal, showed higher electrical conductivities and catalytic properties. For example, Chen et al. have compared the DSSC performances based on  $\text{Co}_3\text{O}_4/\text{MC}$  and  $\text{Co}_2\text{N}$  CEs and found the better electrocatalytic properties towards  $\text{I}_3^-$  reduction were achieved on the  $\text{Co}_2\text{N}/\text{MC}$  composites due to the presence of many active sites in the nitridation process. [67] The DSSC with  $\text{Co}_2\text{N}/\text{MC}$  CE gave a PCE of 5.26%, which was comparable to the one based on Pt CE (4.88%). The TiN-carbon nanohybrids with ordered mesoporous structure (OM TiN-C) also have been applied as CE in DSSCs, which exhibited an efficiency of 8.41%, whereas cell using Pt as CE showed a PCE of only 8.0% in the iodide electrolyte system.[57] Due to the low charge transfer resistance, enhanced electrical conductivity and abundance of active sites, the OM TiN-C CE also showed excellent catalytic activity and solar cell performance in the organic  $\text{T}_2/\text{T}^-$  electrolyte system (Figure 2.14a&b), compared with OM carbon, TiN NPs and Pt CEs. Moreover, OM TiN-C CE gave better chemical stability in the organic electrolyte compared with the Pt CE, where the  $R_{ct}$  of the OM TiN-C remained stable throughout the 36 days' study, as shown in Figure 2.14c. [57]

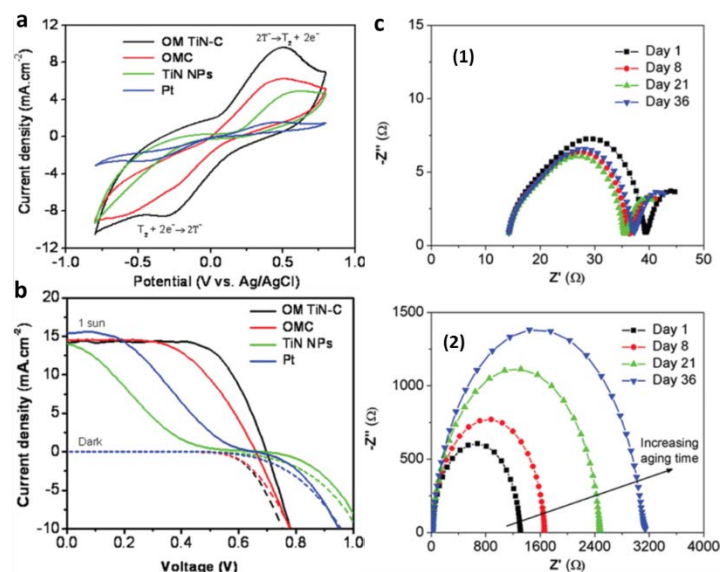


**Figure 2.14.** (a) CVs of the  $\text{T}_2/\text{T}^-$  redox couple for OM TiN-C, OMC, TiN NPs and Pt CEs, (b) Photovoltaic performance of the devices with various counter electrodes, and (c) temporal evaluation of Nyquist diagram of (1) OM TiN-C and (2) Pt electrode symmetric cells with  $\text{T}_2/\text{T}^-$  redox couple as electrolyte. Reprinted with permission from ref.[57]. Copyright 2012 American Chemical Society.

In addition, various metal sulfides also have showed excellent catalytic activity for the  $\text{I}_3^-$  reduction. The metal sulfide/carbon composite CE may have positive synergistic effects to the DSSC performance by increasing the active catalytic sites and improving interfacial charge transfer. The composites of  $\text{WS}_2/\text{P25}/\text{C}$ [398] and NiS/acetylene black(AB) [75] have

been used to make CEs for DSSCs, which gave a PCE of 4.56% and 6.75%, respectively. A PCE of 5.5% and 5.0% were obtained on the DSSCs using glass and plastic CEs coated with C@WS<sub>2</sub> NP film, respectively.[49] Sun et al. introduced Sb<sub>2</sub>S<sub>3</sub> into mesoporous carbon film by solution deposition (Sb<sub>2</sub>S<sub>3</sub>/C-S) and thermal evaporation (Sb<sub>2</sub>S<sub>3</sub>/C-T) and used them as CEs in DSSCs, which achieved a PCE of 6.69% and 6.24%, respectively. [79] However, those cell efficiencies are relatively lower than their Pt counterparts. Maiaugree et al. reported a bilayer carbon coated Ni<sub>3</sub>S<sub>2</sub> (C@Ni<sub>3</sub>S<sub>2</sub>) CE for DSSCs, which attained a high PCE of 9.64% superior than the Pt CE (8.38%). The enhancement was attributed to the fast electron transfer, high co-electrocatalytic activity, and large surface area of the hybrid materials.[399]

Besides, other amorphous carbon based hybrids with hierarchical structure prepared from thermal transformation were also used to fabricate CE of DSSCs. For example, the DSSC based on TiOPC CE with 24.6% carbon content delivered a PCE of 8.65%, which was increased by 29.8% compared with the cell with Pt CE (6.66%).[61] This is because the TiOPC composites possessed high catalytic activity of the Ti-O-P-C structure, good electronic conductivity of the interconnected carbon network as well as the hierarchical porous architecture for the fast electrolyte diffusion. Some compounds, such as cyanamide (NH<sub>2</sub>CN) and urea, can be used as carbon or nitrogen source in the thermal treatment. The hierarchical Fe<sub>3</sub>C@N-C nanocomposites, in which the relative amount of Fe<sub>3</sub>C and Fe<sub>3</sub>C could be adjusted by controlling the FeC<sub>2</sub>O<sub>4</sub>/NH<sub>2</sub>CN ratio, were studied as CE in DSSCs. [64] At a FeC<sub>2</sub>O<sub>4</sub>/NH<sub>2</sub>CN ratio of 2.5, the corresponding cell yielded the highest PCE of 7.36%, which was comparable to the cell based on Pt CE (7.15%). Yun et al. fabricated HfO<sub>2</sub>, HfO<sub>2</sub>-C and Hf<sub>7</sub>O<sub>8</sub>N<sub>4</sub>-HfO<sub>2</sub>-C composites by adjusting the molar ratio of urea to HfCl<sub>4</sub> before thermal treatment and used them as CE materials for DSSC application. [62] The cell based on Hf<sub>7</sub>O<sub>8</sub>N<sub>4</sub>-HfO<sub>2</sub>-C CE gave the highest PCE of 7.85%, higher than that with Pt CE (7.19%).

### **2.8.2.2 Carbon nanotubes**

CNTs show a great potential as a CE material because of their large specific surface area, high conductivity, good photochemical stability and mechanical strength. To overcome the limited of active sites for I<sub>3</sub><sup>-</sup> reduction on CNT surface, intrinsically electrocatalytic semiconductor materials such as, sulfides and nitrides, are often used to decorate CNTs for the CE applications.

The WS<sub>2</sub>/MWCNT nanocomposite prepared from hydrothermal method has been used as a Pt-free CE in DDSCs. [92] Due to the high catalytic activity from WS<sub>2</sub> and high electrical

conductivity from MWCNTs, the DSSC based on WS<sub>2</sub>/MWCNT achieved a PCE of 6.41%, which was comparable to cell with Pt CE(6.56%). Wu et al. also found adding appropriate glucose into the hydrothermal process could further improve the electrochemical properties of WS<sub>2</sub>/MWCNT CE. [93] This glucose aided (G-A) WS<sub>2</sub>/MWCNT electrode had low R<sub>ct</sub> and high electrocatalytic activity for I<sub>3</sub><sup>-</sup> reduction because of the synergistic effects of WS<sub>2</sub> and MWCNTs, as well as amorphous carbon introduced by glucose. A PCE of 7.36% was obtained on the DSSC with this CE. Lu et al. prepared Ni<sub>3</sub>S<sub>2</sub>/MWCNT hybrids through a similar process, but they found a thick layer of amorphous carbon derived from the hydrothermal carbonization of glucose would cover Ni<sub>3</sub>S<sub>2</sub> nanoparticle surface inhibiting the contact of active sites in Ni<sub>3</sub>S<sub>2</sub> nanoparticles with electrolyte. [90] After partially removing the amorphous carbon by annealing at 400 °C in a nitrogen atmosphere, the cell based on Ni<sub>3</sub>S<sub>2</sub>/MWCNT CE yielded an efficiency of 6.87%, which was higher than those of DSSCs based on the Ni<sub>3</sub>S<sub>2</sub> CE (5.77%) and MWCNT CE (3.76%) but lower than Pt CE (7.24%).[90] Tai et al. have prepared CNT@CoS<sub>1.097</sub> and CNT@Co<sub>9</sub>S<sub>8</sub> CEs by annealing at different temperatures in N<sub>2</sub> atmosphere. [89] The CNT@Co<sub>9</sub>S<sub>8</sub> CE showed a superior electrocatalytic activity towards I<sub>3</sub><sup>-</sup> reduction, although it had a relatively lower specific surface area than that of CNT@CoS<sub>1.097</sub> CE. The DSSC based on CNT@Co<sub>9</sub>S<sub>8</sub> CE exhibited a PCE of 7.78%, which was even superior to those of the cells assembled with the CNT@CoS<sub>1.097</sub> CE (7.29%) and Pt CE (7.46%).[89] Xiao et al. also found embedded CoS<sub>1.097</sub>/MWCNT nanocomposites into conductive Pani film could improve the CE properties for DSSC. [88]The DSSC based on CoS<sub>1.097</sub>/MWCNT/Pani CE achieved a PCE of 7.02%, which was higher than the cells on Pani CE (6.06%) and MWCNT@CoS<sub>1.097</sub> CE (5.54%).

The above CEs retain FTO glass as the conducting substrate. Some studies also have tried to replace FTO for extending the application of DSSCs. For example, Zhang et al. have reported the synthesis of transparent FTO-free Co<sub>8.4</sub>S<sub>8</sub>/SWCNT and Ni<sub>3</sub>S<sub>2</sub>/SWCNT CEs involving the spray coating of SWCNT film, sulfide precursor dispersing and annealing process.[400] However, the efficiencies of DDSCs based on these CEs were relatively low because of the small fill factor (FF). As MWCNTs could be deposited on Ti substrate via electrophoresis method, Xiao et al. prepared NiS/MWCNT/Ti hybrid film electrodes served as a Pt-free CE in DSSCs. [97] Due to the large surface area and the synergistic effects of NiS and MWCNTs, the DSSC on NiS/MWCNT/Ti CE attained a PCE of 7.90%, higher than the cell with Pt/Ti CE(6.36%). They also studied the CoS/MWCNT/Ti CE for DSSCs, which gave a higher PCE of 8.05.[98]

In addition to above metal sulfides, other CNT based hybrids materials also have been applied as CE in DSSCs. For instance, Li et al. fabricated TiN-CNT CE, in which TiN NPs with a size of 5–10 nm were stably dispersed on the surface of CNTs. [83] The TiN-CNT CE showed a comparable photovoltaic performance (5.41%) with the conventional Pt electrode(5.68%), which was attributed to the ideal combination of superior electrocatalytic activity and high electrical conductivity derived from the unique TiN-CNT structure. Pammi et al. coated crystallized indium-tin oxide (ITO) films onto SWCNTs by using nanocluster deposition and used the integration of Pt/ITO/SWCNT composites as CE resulted in an overall PCE of approximately 5.1%.[401] Recently, Wang et al. reported a stable perovskite  $\text{LaNiO}_3/\text{MWCNT}$  hybrid CE for DSSCs, which displayed a more attractive PCE of 9.81%, compared with 7.94 and 8.11% for the DSSCs with  $\text{LaNiO}_3/\text{Cb}$  and Pt CEs, respectively.[402] It was found that the oxygen vacancies and B-site metal valences in perovskite as well as the surface area and charge-transfer capability of the hybrid were important factors for the enhanced DSSC performance.

### 2.8.2.3 Graphene

Apart from large surface area and excellent electrical conductivity, the defects or oxygen-containing groups located at the edge site of GR can also act as active sites for electrocatalytic reaction. These features make GR an attractive candidate to replace the conventional Pt based CE in DSSCs. However, the basal plane of the GR is not electrocatalytically active and thus the GR-based CE should be thick enough to obtain the desired electrocatalytic activity.[403] Thus, GR-semiconductor hybrid materials with enhanced catalytic activity are often used as CEs for DSSCs.

Surface modification may improve the electrocatalytic demeanour of GR towards  $\text{I}_3^-$  reduction. Fan et al. synthesized a porous  $\text{SiO}_2/\text{GR}$  nanocomposite for the CE of DSSCs. [138] As compared to the nonporous GR film, the porous composite film demonstrated much better electrocatalytic performance due to the remarkably enhanced surface area. The DSSC with a 2.5 mm thick  $\text{SiO}_2/\text{GR}$  composite CE achieved a PCE of 6.82%, which was comparable to that of Pt CE (7.28%).[138] As a p-type semiconductor, NiO has a certain degree of catalytic activity for  $\text{I}_3^-$  reduction. Bajpai have prepared NiO/GR CE by directly depositing NiO NPs over few layered GR film using pulsed laser deposition.[197] The DSSC efficiency on this composite CE (3.06%) was improved compared with pure NiO and GR CEs, but it was relatively low because NiO NPs were only dispersed on the surface layer of

GR film. Dao et al. also fabricated NiO/rGR films by dry plasma reduction at a low temperature and used them as CE of DSSCs. [198] Due to the synergistic effect of NiO and rGO resulting in low  $R_{ct}$ , the corresponding cell exhibited a PCE of 7.42% (0.10%), which was comparable to a conventional Pt-sputtered CE (8.18%). Xiong et al. have reported nanocomposites consisted with rGO and perovskite-phase metal oxides, such as  $\text{La}_{0.65}\text{Sr}_{0.35}\text{MnO}_3$  [404] and  $\text{La}_{0.5}\text{Sr}_{0.5}\text{CoO}_{2.9}$  [405], working as CE for DSSCs. These nanocomposites exhibited excellent electrocatalytic performance for reduction of  $\text{I}_3^-$  and the DSSCs with the hybrid CEs yielded a higher PCE than that of using pristine perovskite or rGO CE, although they were still lower than the cells based on Pt CE.

Due to the excellent electrocatalytic activity, metal sulfides are often used to couple with GR as hybrid CE materials for DSSCs. Lin et al. hydrothermally synthesized  $\text{MoS}_2/\text{GR}$  nanocomposites and then deposited them onto FTO as CE by electrophoresis. [191] The obtained  $\text{MoS}_2/\text{GR}$  CE demonstrated Pt-like electrocatalytic activity for  $\text{I}_3^-$  reduction and the corresponding DSSC exhibited an impressive PCE of 5.81% up to 93% of Pt CE, which was higher than the cell based  $\text{MoS}_2/\text{GR}$  CE prepared by ultrasonic mixing [406]. Yu et al. also fabricated  $\text{MoS}_2/\text{GR}$  electrode by hydrothermally growing  $\text{MoS}_2$  on GR film, which was prepared from CVD and transferred onto FTO. [407] Due to the hexagonal lattice carbon of the GR film could easily interact with sulfur species derived from reaction precursors, which favored the uniform growth of 2D  $\text{MoS}_2$  nanosheets. With the well dispersed electrochemically active  $\text{MoS}_2$  crystals and high electrical conducting GR matrix, the DSSC showed a higher PCE of 7.1%. [407]  $\text{NiS}/\text{GR}$  [408] or  $\text{NiS}/\text{rGO}$  [187] CEs with superior electrochemically active to Pt CE also have been reported. Among them, the DSSC based on the hydrothermal prepared  $\text{NiS}/\text{GR}$  (0.4 wt.% GR) showed higher PCE (8.26%) than the one based on  $\text{NiS}/\text{GR}$  CE (5.25%) fabricated through dip-coating and decomposing of NiS precursor onto GR film (Table 2). Owing to the improved conductivity and positive synergetic effect, the hydrothermally synthesized  $\text{NiS}_2/\text{rGO}$  nanocomposites also exhibited excellent electrocatalytic performance for reduction of  $\text{I}_3^-$ . [409] The DSSC with the  $\text{NiS}_2/\text{rGO}$  CE produced a PCE of 8.55%, which was higher than the cells on  $\text{NiS}_2$  (7.02%), rGO (3.14%) and Pt (8.15%) CEs. [409]

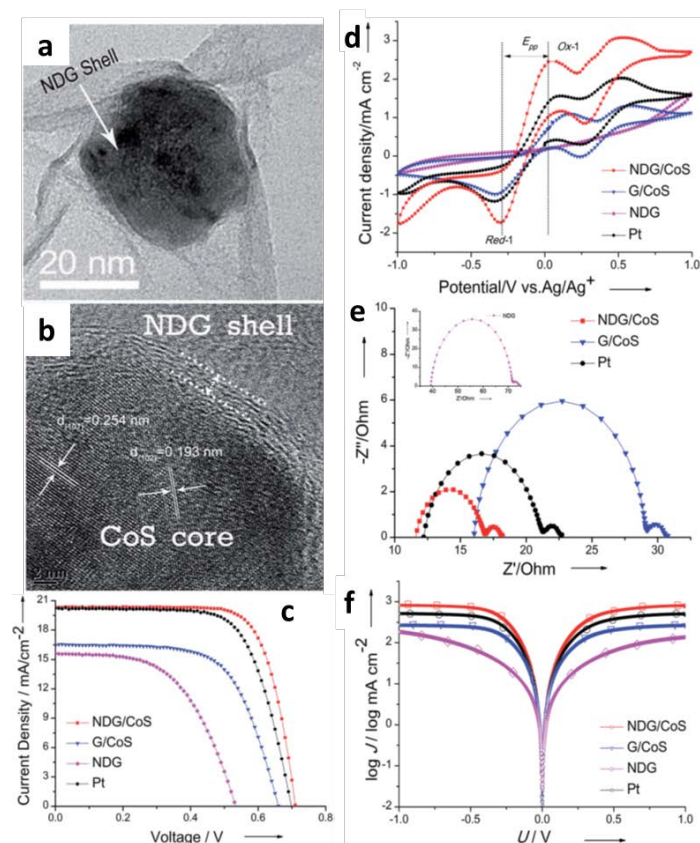


**Figure 2.15.** (a) TEM image and (b) HRTEM image of NDG/CoS; (c) photovoltaic performance of the devices with NDG/CoS, G/CoS, NDG, and Pt as CEs measured under AM 1.5 illumination; (d) CV of  $I_3^-/I^-$  redox couple for NDG/CoS, G/CoS, NDG and Pt on a FTO glass substrate (e) Nyquist diagram and (f) Tafel polarization curves of dummy cells fabricated with the four materials. Reprinted with permission from ref. [216] Copyright 2014 The Royal Society of Chemistry.

Cobalt sulfide ( $\text{CoS}$ ,  $\text{CoS}_2$ )/GR nanocomposites were often used as CE materials, [188, 189, 216, 408, 410, 411] in which the morphology and structure of both GR and cobalt sulfide have great effect on their DSSC performance. Miao et al. have fabricated CoS/functionalized GR (FGR) hybrids through an electrophoretic deposition followed by an oxidation and chemical bath process. [410] Compared with the composite prepared from SILAR, the CoS NPs were well dispersed on FGR nanosheets, which further resulted in better catalytic activity to the reduction of  $I_3^-$ . The DSSC based on this uniform composite CE yielded a PCE of 5.54%, while the cell with non-uniform CE only gave 4.45%. [410] Huo et al. also prepared CoS/rGO hybrid films with a sponge-like structure through a similar process. [411] Due to the sponge structure, the obtained CoS/rGO CE had large specific surface area and small  $R_{ct}$  at the electrode/electrolyte interface. With an optimal CoS/rGO CE, the DSSC could reach a PCE of 9.39%, which was increased by 27.93% compared with the one based on Pt (7.34%). [411] Bi et al. synthesized a novel quasi core-shell hybrid material consisting of a core of

CoS NPs coated with a shell of ultrathin N-doped GR (NDG or N-GR) layers via an in-situ solvothermal self-assembly method (Figure 2.15a&b). [216] As shown in Figure 2.15c, the DSSC with this quasi core-shell NDG/CoS CE showed a high  $J_{sc}$  ( $20.38 \text{ mA cm}^{-2}$ ) and a PCE of 10.71%, which was a notable improvement compared to the efficiency observed with GR/CoS (7.05%), NDG (4.49%) and even Pt CE (9.73%). This is because the quasi core-shell hybrid had better catalytic activity for the reduction of  $I_3^-$  to  $I^-$ , lower  $R_{ct}$  and higher exchange current density compared with other three, which can be observed from their cyclic voltammetry (CV) and electrochemical impedance spectroscopy (EIS) and Tafel polarization curves (Figure 2.15d-f). The shell of NDG layers acted as conductive paths to overcome the problem of low conductivity due to grain boundaries and defects between the CoS NPs. However, without N doping, the CoS NPs were uniformly distributed on rGO, but they were not encapsulated by the GR to form a core-shell structure, which indicated that ammonia facilitated formation of the quasi core-shell structure of NDG/CoS. [216]  $CoS_2/rGO$  nanohybrids also have been synthesized by a facile hydrothermal reaction between cobalt ions and thiourea in the presence of GO, by which the size and distribution of the formed  $CoS_2$  NPs onto GR sheet could be effectively controlled. [188] With optimal GO adding, the DSSC on the  $CoS_2/rGO$  offered a PCE of 6.55%, outperforming that of Pt CE based cell (6.20%). [188] Yuan et al. also fabricated a novel sandwich-like hierarchical  $CoS_2/rGO$  hybrid CE by one-step hydrothermal process, in which  $Co^{2+}$  cations attracted into GR framework by the electrostatic adsorption induced the growth of octahedral  $CoS_2$  NPs between the layers of GR. [189] This mesoporous sandwich-like structure favoured the electrolyte diffusion and also had excellent electrical conductivity and rich inner active sites for the reduction of  $I_3^-$ . As a result, the DSSC based on this CE showed outstanding stability and achieved a PCE of 7.69%, higher than the cell with Pt CE (7.38%). [189] Besides,  $CoSe_{0.85}$  NPs with a potato-chip-like morphology also have been coupled with rGO as CE for DSSCs. [192] It was found the CE with 75 wt.% GR loading exhibited higher electrocatalytic activity and lower  $R_{ct}$  at the CE/electrolyte interface than the other compositions and a PCE of 8.17% was obtained on that CE based DSSC.

#### **2.8.2.4 Other carbon structures or components**

In addition to above carbon structure, carbon nanofiber (CNF) based hybrid composites also have been used as CE in DSSCs. For example, Sigdel et al. have used the  $TiO_2/CNF$  composites (1: 1 by weight) as CE materials, which exhibited lower  $R_{ct}$  and higher interfacial

capacitance than those of Pt CEs. [412] The DSSC with TiO<sub>2</sub>/CNF CE showed a PCE of 7.25%, which was comparable to that of thermally deposited Pt based DSSC (7.57%). Theerthagiri et al. have also synthesized MoS<sub>2</sub>/CNF nanohybrids and used them as Pt free CE for DSSCs. [91] Compared with other carbon materials (AB, vulcan carbon, MWCNT, and rice husk ash) based composites, the MoS<sub>2</sub>/CNF CE exhibited highest electrocatalytic activity towards the regeneration of I<sup>-</sup> from I<sub>3</sub><sup>-</sup>.

It was also found combining different carbon materials together in the CSHMs could effectively improve their electrocatalytic properties as CE materials in DSSCs. For instance, Lin et al. fabricated MoS<sub>2</sub>/rGO-CNTs hybrids by combining MoS<sub>2</sub>/rGO nanocomposites with CNTs through electrophoretic deposition. [413] It was found the MoS<sub>2</sub>/rGO-CNTs hybrid benefited from the advantages of both MoS<sub>2</sub>/rGO and CNTs as a CE in DSSCs, where the incorporation of conductive networks of CNTs provided additional pathways for electron transport leading to increase of the charge-transfer rate at the CE/electrolyte interface. The DSSC based on this MoS<sub>2</sub>/rGO-CNTs CE achieved a PCE of 7.46 %, higher than those on MoS<sub>2</sub>/RGO CE (6.82%) and Pt CE (7.23 %).[413] The TiO<sub>2</sub>/Ac/MWCNT, TiO<sub>2</sub>/MWCNT/GR and TiO<sub>2</sub>/Ac/GR ternary composites also have been used as CEs in DSSCs, which gave better solar cell performance than their TiO<sub>2</sub> binary hybrids. [394] And, an attractive PCE of 10.73% was achieved on the DSSC using TiO<sub>2</sub>/AC/MWCNTs/GR as a CE.[394]

**Table 1.** Summary of the preparation methods of carbon-semiconductor hybrid materials and the photovoltaic performances of DSSCs and QDSSCs using them as anode.

Anode	Preparation method	Sensitizer	$\eta$ /%	$V_{oc}$ /mV	$J_{sc}/(\text{mA}\cdot\text{cm}^{-2})$	FF/%	Refs.
<b>Dye-sensitized solar cells (DSSCs)</b>							
C-TiO <sub>2</sub>	hydrothermal	N719	6.9	752	15.25	60	[369]
TiO <sub>2</sub> +C-TiO <sub>2</sub> HS	template impregnation	N719	8.55	710	20.38	57.2	[370]
TiO <sub>2</sub> +C-TiO <sub>2</sub>	hydrothermal	N719	7.24	721	15.67	64.1	[59]
C-TiO <sub>2</sub> NT	CVD	N719	6.21	750	11.49	72	[78]
C-TiO <sub>2</sub> @SiO <sub>2</sub> in P25	chemical coating and thermal treatment	N719	5.21	697	11.134	67.11	[68]
TiO <sub>2</sub> /MWCNTs	ultrasonic and stirring	N719	4.1	760	8.30	64	[30]
P25/MWCNTs	mortar	N719 <sup>1</sup>	3.05	650	8.88	53	[371]
P25/CNTs	electrophoresis deposition	N3	0.48	660	2.25	48	[96]
TiO <sub>2</sub> /MWCNTs+TiO <sub>2</sub>	mortar	N719	3.948	806	6.41	56.56	[372]
TiO <sub>2</sub> /MWCNTs	laser pyrolysis	D102 <sup>2</sup>	3.9	750	7.57	69	[106]
TiO <sub>2</sub> HS/MWCNTs	mortar	N719	4.71	609	12.1	63.9	[31]
P25/MWCNTs			4.25	607	11.7	63.6	
TiO <sub>2</sub> /MWCNT	electrospinning and sintering	N3	6.12	820	11.98	62	[100]
TiO <sub>2</sub> /MWCNTs	hydrothermal	N719	7.00	770	15.96	57	[95]
			7.27 <sup>3</sup>	770	16.86	56	
TiO <sub>2</sub> /MWCNTs	wet impregnation	N719 <sup>4</sup>	3.593	716	9.811	51.5	[81]
TiO <sub>2</sub> /MWCNT	sol-gel and	N719	7.66	752	15.27	66.7	[85]
TiO <sub>2-x</sub> N <sub>x</sub> /MWCNT	sintering		6.88	807	12.41	68.7	
P25/M-SWNTs	ultrasonic	N719	1.1	520	4.4	46.5	[374]
			0.51 <sup>5</sup>	380	3.0	44	
TiO <sub>2</sub> /MWCNTs	sol-gel	N719	5.78	741	10.78	74	[84]
TiO <sub>2</sub> /DWCNTs	stirring	N719	6.4	800	13.7	60	[373]
TiO <sub>2</sub> /SWNTs	biological template	N719	5.32	749	10.43	68	[109]
Ag/TiO <sub>2</sub> /SWNTs			5.99	751	11.79	68	
TiO <sub>2</sub> /SWNTs	Biological template	N719	10.6	770	21	-	[103]
TiO <sub>2</sub> /SWCNH		N719 <sup>6</sup>	6.22	730	14.68	58	[375]
TiO <sub>2</sub> /SWCNH <sub>ox</sub>			6.19	740	14.68	69	
TiO <sub>2</sub> /graphene	stirring		5.55	720	12.44	62	
TiO <sub>2</sub> /graphene <sub>ox</sub>			5.85	690	14.11	60	
TiO <sub>2</sub> /SWCNT			5.04	750	12.01	56	
TiO <sub>2</sub> /SWCNT <sub>ox</sub>			5.13	710	12.68	57	
ZnO/O-MWCNT	blending	N719	2.33	600	5.90	66	[378]
ZnO/acid-MWCNT			2.70	660	5.68	72	
ZnO/MWCNT	ultrasonic and stirring	N719	0.54	16	10.	33	[376]

ZnO/SWCNT			1.31	224	15.3	36	
ZnO/CNTs	CVD	N719	1.94	560	3.72	64	[107]
ZnO/MWCNT	mortar and stirring	N719	2.77	480	11.85	48.75	[390]
ZnO/C <sub>60</sub>			2.28	510	8.56	51.93	
ZnO/GR			2.16	490	8.40	52.04	
TiO <sub>2</sub> / GCNSs	ultrasonic	N719	5.03	720	15.43	45.34	[391]
TNF@CNF	In-situ growth	N719	8.57	690	21.40	58	[392]
TNF@CNF-UTHS <sup>7</sup>			9.21	740	19.04	65	
P25/Nafion-GR	heterogeneous coagulation	N719	4.28	730	8.38	-	[384]
P25/rGO	ultrasonic and stirring	N3	6.97	690	11.26	64.5	[32]
P25/ GO	ball-milling	N3	5.09	616	10.28	63.75	[385]
TiO <sub>2</sub> /rGO	ultrasonic	N719	5.83	740	13.43	59	[34]
TiO <sub>2</sub> /rGO	ultrasonic	N719	6.69	710	15.23	62	[33]
TiO <sub>2</sub> /GR	ultrasonic and grinding	N719	7.68	780	14.80	67	[35]
TiO <sub>2</sub> /GR	ultrasonic	N749	4.03	705	13.04	43.9	[382]
TiO <sub>2</sub> /GR	ultrasonic	N3	7.70	749	21.4	49	[36]
TiO <sub>2</sub> /rGO	precipitation-peptization	N719 <sup>8</sup>	7.20	540	28.36	47	[139]
TiO <sub>2</sub> /rGO	implantation	N719 <sup>9</sup>	8.51	630	25.02	54	[196]
TiO <sub>2</sub> /rGO	chemical reduction	N719 <sup>10</sup>	7.89	708	15.2	73.3	[140]
TiO <sub>2</sub> /rGO	thermal reduction	N719	5.62	645	13.04	67	[129]
TiO <sub>2</sub> /GR	ultrasonic	Z907	7.06	660	14.64	73.02	[387]
			5.64 <sup>11</sup>	720	10.17	77.06	
TiO <sub>2</sub> /GR	ultrasonic	Z907	4.03	697	16.54	34	[383]
TiO <sub>2</sub> /GO	stirring and calcination	N719 <sup>4</sup>	3.97	762	7.67	68	[386]
TiO <sub>2</sub> -NSs/GR	mortar	N719	5.77	606	16.8	56.7	[388]
TiO <sub>2</sub> /N-rGO	mortar	N3	7.19	722	18.74	53.1	[381]
TiO <sub>2</sub> /GR inverse opal (IO)	polymer template	N719	7.52	720	17.10	61	[211]
3D TiO <sub>2</sub> /GR	CVD, template	C106	9.2	750	16.7	74	[146]
3D TiO <sub>2</sub> /GR	impregnation	N719	6.41	660	12.89	76.03	[210]
GO &N-SnO <sub>2</sub> /TiO <sub>2</sub> NFs	electrospinning and hydrothermal	N719	6.176	825	10.32	72.55	[217]
ZrO <sub>2</sub> &GO@TiO <sub>2</sub> NFs	electrospinning and hydrothermal	N719	5.09	730	10.78	64.70	[176]
SiW <sub>9</sub> Co <sub>3</sub> /rGO@P25	stirring and ultrasonic	N719	6.88	705	17.5	55.8	[271]
TiO <sub>2</sub> :G/TiO <sub>2</sub> :Er <sup>3+</sup> , Yb <sup>3+</sup>	ultrasonic	N719	4.58	720	10.38	61	[269]
NRs/TiO <sub>2</sub> :Al <sub>2</sub> O <sub>3</sub> :Eu <sup>3+</sup>							
TiO <sub>2</sub> -GO-Au	ultrasonic	N719	6.78	710	15.81	57	[225]
ZnO/rGO	stirring	N719	5.86	670	17.11	42.03	[389]
ZnO/rGO	chemical reduction	rose bengal	1.50	700	1.60	53	[137]
		eosin yellow	1.10	690	0.98	51	
ZnO/rGO	ultrasonic and chemical reduction	N719	4.45	740	8.53	70	[136]

GO/TiO <sub>2</sub>	hydrothermal	N719	8.55	740	16.70	68	[215]
N-GR/NiO/TiO <sub>2</sub>			9.75	760	19.04	67	
Nb <sub>2</sub> O <sub>5</sub> /GO	hydrothermal	N3	0.11	196	0.363	42	[180]
<b>Quantum dots sensitized solar cells (QDSSCs)</b>							
TiO <sub>2</sub> /GR	ultrasonic	CdS QD	0.37	670	1.83	32	[414]
P25/rGO	ultrasonic	CdS QD	0.37	660	1.83	30	[415]
P25/GR	mixing	CdS QD <sup>12</sup>	1.44	580	7.1	35	[416]
ZnO/rGO	ultrasonic and thermal reduction	CdS/CdSe QD/ZnS <sup>13</sup>	2.2	570	8.72	44	[130]
Co@C/SnO <sub>2</sub> /TiO <sub>2</sub>	MOF derived	PbS QD/ZnS <sup>14</sup>	1.0	230	14.70	29	[417]

<sup>1</sup>quasi-solid state DSSCs using gel polymer electrolyte; <sup>2</sup>solid-state DSSCs using spiroOMeTAD as a hole transporter; <sup>3</sup> using iron pyrite (FeS<sub>2</sub>) counter electrode (CE); <sup>4</sup> using poly-vinyl alcohol gel electrolyte with triiodide/iodide redox couple; <sup>5</sup> flexible DSSCs; <sup>6</sup> all the PCE were achieved on the single-layer nanocarbon/TiO<sub>2</sub> composites electrodes; <sup>7</sup>urchin-like TiO<sub>2</sub> hollow sphere; <sup>8</sup> using graphene as a CE ; <sup>9</sup> the CE part was prepared by applying the 2B graphite pencil; <sup>10</sup> using rGO as a CE and KI electrolyte; <sup>11</sup> using Co-EI electrolyte with the [Co(Phen)<sub>3</sub>]<sup>2+/3</sup> redox couple; <sup>12</sup> using polysulfide electrolyte and Au-sputtered FTO glass as CE; <sup>13</sup> using polysulfide electrolyte and Cu<sub>2</sub>S CE; <sup>14</sup>using porous PbS CE.

**Table 2** Summary of the preparation methods of carbon-semiconductor hybrid materials and the photovoltaic performances of DSSCs and QDSSCs using them as counter electrode.

Counter electrode	Preparation method	Sensitizer	$\eta$ /%	V <sub>oc</sub> /mV	J <sub>sc</sub> / (mA·cm <sup>-2</sup> )	FF /%	Refs.
<b>Dye-sensitized solar cells (DSSCs)</b>							
TiO <sub>2</sub> /Cb	ultrasonication	N719	7.4	710	15.5	67.4	[28]
TiO <sub>2</sub> /Cb/graphite	mortar	N3	6.3	704	12.63	71	[395]
SnO <sub>2</sub> /TiO <sub>2</sub> / Cb/graphite	ball-milling	N3	6.15	740	12.98	64	[396]
TiO <sub>2</sub> /CNF	sonicating	N719	7.25	840	13.69	63	[412]
Pt/TiO <sub>2</sub> /CNF			7.46	840	13.47	66	
TiO <sub>2</sub> /AC	mixing	N719	8.73	726	20.46	58.31	[394]
TiO <sub>2</sub> / MWCNTs			6.69	697	17.92	53.53	
TiO <sub>2</sub> / GR			5.97	737	16.12	50.27	
TiO <sub>2</sub> /AC/MWCNTs			10.41	761	19.42	70.02	
TiO <sub>2</sub> /MWCNTs/GR			6.84	736	17.23	54.23	
TiO <sub>2</sub> /AC/GR			9.23	745	19.42	63.78	
TiO <sub>2</sub> /AC/MWCNTs/GR			10.73	760	21.55	65.48	
ZnO/C	mortar	N719	6.37	746	14.13	60.4	[397]
WO <sub>2</sub> /C	in situ synthesis	N719	5.22 <sup>1</sup>	636	12.98	63	[66]
			7.76	808	13.55	71	
Fe <sub>3</sub> O <sub>4</sub> /Cb	ultrasonic mixing	N719	6.1	665	14.40	51	[29]

Fe <sub>3</sub> C@N-C	carbothermal reduction	N719	7.36	741	14.97	66.35	[64]
Co <sub>3</sub> O <sub>4</sub> /C	hydrothermal and carbonization;	N719	5.08	688	16.26	45	[67]
Co <sub>2</sub> N/C	nitridation		5.26	724	12.60	58	
TiOPC	hydrothermal and carbothermic reduction	N719	8.65	780	16.64	67	[61]
HfO <sub>2</sub> -C	urea-metal route	N719	6.71	770	12.96	67	[62]
Hf <sub>7</sub> O <sub>8</sub> N <sub>4</sub> -HfO <sub>2</sub> -C			7.85	800	14.13	70	
WS <sub>2</sub> /P25/C	mechanical stirring	N719	4.56	699	13.0	50	[398]
C@WS <sub>2</sub>	carbonization of glucose	N719	5.5	670	13.1	62	[49]
C@Ni <sub>3</sub> S <sub>2</sub>	chemical bath deposition, arc evaporation	N719	9.64	750	20.75	62	[399]
Sb <sub>2</sub> S <sub>3</sub> /C-S	solution deposition;	N719	6.69	680	14.6	67.6	[79]
Sb <sub>2</sub> S <sub>3</sub> /C-T	thermal evaporation		6.24	650	14.5	6.24	
TiN-C	soft-template, nitridation	N719	6.71 <sup>1</sup>	697	14.36	67	[57]
			8.41	820	15.3	67	
NiS/AB (acetylene black)	electrochemical deposition	N3 <sup>2</sup>	6.75	720	14.01	67	[75]
TiN-CNTs	Hydrolysis and nitridation	N719	5.41	750	12.74	57	[83]
WS <sub>2</sub> /MWCNT	hydrothermal	N719	6.41	730	13.51	65	[92]
(G-A) WS <sub>2</sub> /MWCNT	hydrothermal	N719	7.36	750	13.63	72	[93]
NiS/MWCNT/Ti	electrophoresis and pulse potentiostatic method	N719	7.90	753	14.18	74	[97]
Ni <sub>3</sub> S <sub>2</sub> /MWCNT	hydrothermal	N719	6.87	770	13.96	63	[90]
CoS/MWCNT/Ti	electrophoresis and pulse potentiostatic method	N719	8.05	751	14.69	73	[98]
CoS <sub>1.097</sub> /MWCNT	hydrothermal;	N719	5.54	710	12.83	59	[88]
CoS <sub>1.097</sub> /MWCNT/Pani	electropolymerization		7.02	770	14.11	64	
CoS <sub>1.097</sub> /CNT	hydrothermal	N719	7.29	780	14.46	64	[89]
Co <sub>9</sub> S <sub>8</sub> /CNT			7.78	790	14.55	67	
LaNiO <sub>3</sub> /MWCNT	ball-milling	N719	9.81	760	18.1	71.2	[402]
LaNiO <sub>3</sub> /Cb			7.94	712	16.3	67.5	
MoS <sub>2</sub> /AB	hydrothermal	N3 <sup>2</sup>	1.31	640	10.27	20	
MoS <sub>2</sub> /vulcan carbon			2.97	640	10.81	43	
MoS <sub>2</sub> /MWCNT			3.08	620	12.43	40	[91]
MoS <sub>2</sub> /CNF			3.17	580	10.33	53	
MoS <sub>2</sub> /rice husk ash			2.10	600	10.95	32	
Co <sub>8.4</sub> S <sub>8</sub> /SWCNT	spray-coating precursor	Z907	3.13	700	15.16	30	[400]
Ni <sub>3</sub> S <sub>2</sub> /SWCNT			2.57	720	12.85	28	
Pt/ITO/SWCNT	nanocluster deposition	N719	5.1	710	10.72	66	[401]
NiO/GR	pulsed laser ablation	N3	3.06	670	7.53	61	[197]

NiO/rGO	dry plasma reduction	N719	7.42	763.33	15.57	62.40	[198]
SiO <sub>2</sub> /GR	chemical reduction	N719	6.82	720	15.52	61	[138]
La <sub>0.65</sub> Sr <sub>0.35</sub> MnO <sub>3</sub> /rGO	ultrasonical	N719	6.57	780	12.53	67.22	[404]
La <sub>0.5</sub> Sr <sub>0.5</sub> CoO <sub>2.9</sub> /rGO	mortar	N719	6.32	800	13.13	60.2	[405]
MoS <sub>2</sub> /GR	hydrothermal and electrophoretic deposition	N719	5.81	773	12.79	59	[191]
MoS <sub>2</sub> /GR	probe sonicating	-	4.35	646	11.91	56.5	[406]
MoS <sub>2</sub> /GR	CVD and hydrothermal	N719	7.1	660	16.1	67	[407]
MoS <sub>2</sub> /rGO	hydrothermal and electrophoretic deposition	N719	6.82	760	14.31	63	[413]
MoS <sub>2</sub> /rGO-CNT	deposition		7.46	760	14.59	67	
NiS/rGO	hydrothermal	N719	8.26	778	17.05	62.30	[187]
NiS <sub>2</sub> /rGO	hydrothermal	N719	8.55	749	16.55	69	[409]
NiS/GR	dip-coating	N719	5.25	724	10.31	70.36	[408]
CoS/GR			5.04	725	10.03	69.28	
CoS/GR	solvothermal	N749	7.05	660	16.42	65	[216]
N-GR @CoS			10.71	710	20.38	74	
CoS/FGR	electrophoretic deposition, oxidation and chemical bath process	N719	5.54	670	12.91	64	[410]
CoS/rGO	electrophoretic deposition, ion exchange deposition and chemical reduction	N719	9.39	764	19.42	63.3	[411]
CoS <sub>2</sub> /GO	hydrothermal	N719	6.55	730	15.12	60	[188]
CoS <sub>2</sub> /rGO	hydrothermal	N719	7.69	702	16.35	67	[189]
CoSe <sub>0.85</sub> /rGO	hydrothermal	N719	8.17	715	15.789	72.4	[192]
<b>Quantum dots sensitized solar cells (QDSSCs)</b>							
TiO <sub>2</sub> /Ac	ball-milling	CdS/CdSe/ZnS QDs	3.48	542	10.9	57	[38]
TiO <sub>2</sub> /C60			4.18	546	12.6	60	
$\alpha$ -MoO <sub>3</sub> /C	spray pyrolysis	CdS QDs	1.29	480	1.29	31	[48]
Co <sub>9</sub> S <sub>8</sub> NT@CF <sup>3</sup>	chemical bath deposition	CdS/CdSe QDs <sup>4</sup>	3.79	370	17.95	57	[418]
FeS/C	electrochemical deposition	CdS/CdSe QDs	4.58	440	20.33	51	[76]
FeS/C	compositing and chemical conversion	CdS/CdSe/ZnS QDs	5.61	450	19.57	64	[77]
CuS/C			4.75	430	19.49	57	
CoS/C			4.29	420	17.90	57	
NiS/C			4.71	400	18.97	62	
Cu <sub>1.8</sub> S/C	mortar and sulfidation	CdSeTe/ZnS/SiO <sub>2</sub> QDs	8.40	655	21.27	60	[419]
CuS/3D GR	decomposition of fumaric acid and hydrothermal	CdS/CdSe QDs	5.04	590	16.19	52.77	[208]
Cu <sub>2</sub> S/graphite	immersion and heat treatment	CdS/CdSe/ZnS QDs	4.59	599	16.34	46.90	[420]
CuS/GH <sup>5</sup>	hydrothermal	CdSeTe/ZnS QDs	10.74	786	20.69	66.02	[206]
GR/CuS/PbS	spin coating and SILAR <sup>6</sup>	CdS/CdSe/ZnS QDs	3.21	550	11.43	51	[255]

CoS/GR	electrophoretic deposition and SILAR	CdS/CdSe QDs	2.9	410	14.3	-	[194]
10% Sr-CoS/CNT	electrophoretic deposition and SILAR	CdS/CdSe/ZnS QDs	2.32	470	14.56	34	[195]
10% Sr-CoS/GR			2.35	470	16.14	31	
10% Sr-CoS/GO			2.81	470	16.17	37	
10% Ba-CoS/CNT			2.08	450	15.46	30	
10% Ba-CoS/GR			2.11	450	17.35	28	
10% Ba-CoS/GO			2.26	460	17.60	28	
TiN/GR	urea-glass route	CdS/CdSe QDs <sup>7</sup>	3.47	636	12.7	43	[261]
TiN/CNT			3.89	645	13.7	44	
TiN/CNT-GR			4.13	642	14.0	46	
Mo <sub>2</sub> N/CNT-rGO	urea-glass route	CdS/CdSe QDs <sup>7</sup>	5.41	680	16.93	47	[262]
Mo <sub>2</sub> C/CNT-rGO			4.84	670	16.42	44	
MoS <sub>2</sub> /CNT-rGO			3.44	650	16.02	33	

<sup>1</sup>electrolyte with disulfide/thiolate (T<sub>2</sub>/T<sup>-</sup>) organic redox couples; <sup>2</sup>using phthaloylchitosan (PhCh)-based polymer electrolyte as an electrolyte; <sup>3</sup>carbon fibers; <sup>4</sup>using spiral TiO<sub>2</sub> nanotube arrays (TNARs)@Ti electrodes as photoanode; <sup>5</sup>graphene hydrogel; <sup>6</sup>successive ionic layer adsorption and reaction (SILAR) method; <sup>7</sup>using ZnO nanowire arrays as photoanode

## 2.9 Quantum dots sensitized solar cells (QDSSCs)

Quantum dot (QD) has emerged as a promising agent in the field of solar energy conversion due to its distinct size-dependent optoelectronic characteristics, which allow the feasibility to control light absorption spectrum in a wide region and the possibility of multiple electron generation.[421] Quantum dot-sensitized solar cells (QDSSCs), as another candidates for cost-effective photoelectron-chemical solar cells, have great potential to meet global demand for clean energy. The idea of QDSSC have analogous configuration to the conventional DSSC consisting of semiconductor photoanodes sensitized with QDs, redox electrolytes, and counter electrodes (CEs). Cd chalcogenide and Pb chalcogenide QDs such as CdS, CdSe, CdTe, PbS, and PbSe are commonly used sensitizing materials in QDSSCs and a ZnS passivation layer is often applied to reduce carrier recombination.[422] Instead of the iodide/triiodide ( $I^-/I_3^-$ ) couple, a polysulfide ( $S^{2-}/S_n^{2-}$ ) redox couple aqueous solution electrolyte is commonly applied in QDSSCs due to its ability to stabilize the cadmium chalcogenide QDs.

### 2.9.1 Photoanodes

Like in DSSCs, photoanode provides specific surface area for QD adsorption and also acts as medium for collection and transportation of electrons from QDs to external circuit, which can affect photocurrent response and the PCE of QDSSC. Applications of CSHMs as photoanodes in QDSSCs also have been reported. The photovoltaic performances of QDSSCs using different CSHMs as photoanodes are summarized in Table 1.

Badawi et al. fabricated  $TiO_2/GR$  nanocomposite photoanodes for CdS QDSSCs and investigated the effect of GR/ $TiO_2$  ratio (0, 0.1, 0.2, 0.5, and 1.0 wt.%) on the photovoltaic performance. [414, 415] The cells based on 0.2 wt.% GR/ $TiO_2$  electrode achieve 32% increase in PCE compared with those based on plain  $TiO_2$  photoanode. Zhu et al. also investigated photovoltaic performances of CdS QDSSCs based on different  $TiO_2/GR$  photoanodes and the cell based on 0.8 wt.% GR/ $TiO_2$  anode demonstrated a maximum PCE of 1.44%, 56% higher than that without GR.[416] The enhancement was ascribed to the increased CdS adsorption, the reduction of electron-hole recombination and back-transport reaction as well as the enhancement of electron transport with the introduction of GR. Ghoreishi et al. used ZnO/rGO nanocomposite photoanodes for the CdS/CdSe QDSSCs, which gave a PCE of 2.20%, almost two times higher than cells based on pure ZnO

photoanode (1.28%) due to the increase of electron transfer rate in the ZnO/rGO anode.[130] Liu et al. reported a photoanode consisting of bottom porous Co/carbon conducting framework, middle SnO<sub>2</sub> mesoporous layer and a compact TiO<sub>2</sub> top layer for PbS QDSSCs, where the Co/carbon layer was converted from ZIF-67. [417] The photovoltaic performance of QDSSCs were greatly improved due to the introduction of the porous conducting framework and the corresponding TiO<sub>2</sub> compact layer, which benefits to the electron transporting and suppresses the charge carrier recombination, respectively.[417]

## 2.9.2 Counter electrodes

In QDSSCs, the CE materials should have fast catalytic kinetics for the polysulfide (S<sup>2-</sup>/S<sub>n</sub><sup>2-</sup>) redox couple as well as high electron transport abilities. Owing to the high conductivity, porous structure and outstanding stability in polysulfide, carbon materials are one of the best choices as the base electrode. After combining with some semiconductor materials having high catalytic activity for the S<sub>n</sub><sup>2-</sup> reduction, the CSHMs are promising to replace expensive noble metal CEs in QDSSCs and achieve considerable photovoltaic efficiency. The photovoltaic performances of QSSCs with various CSHM CEs are summarized in Table 2.

### 2.9.2.1 Amorphous carbon

Metal sulfides are commonly used as CE materials in QDSSCs due to their remarkable electrocatalytic activity compared to novel metals in polysulfide electrolyte. To overcome their poor conductivity, inexpensive amorphous carbon are often used to combine with these metal sulfides as the hybrid CE for QDSSCs. For example, Geng et al. have fabricated FeS/C composite CE by electrochemical deposition of FeS on 3D carbon mesoporous scaffold. [76] The QDSSC based on this FTO free FeS/C CE achieved a high PCE of 4.58% with a fill factor (FF) of 0.51, which was much higher than those based on FeS/FTO (0.27) and C/FTO CE (0.11). Moreover, the FeS/C CE exhibited excellent stability in photoelectric performance, which still performed high photoelectric conversion properties (PCE = 4.17%, V<sub>oc</sub> = 0.42 V, J<sub>sc</sub> = 20.25mA cm<sup>-2</sup> and FF = 0.49) after serving for 8 weeks.[76] They also have prepared a series of metal sulfide/C films including FeS/C, CuS/C, CoS/C and NiS/C through a metal/C chemical conversion method. [77] The obtained hybrids had good interfacial contact between metal sulfides and carbon, which promoted the interfacial electron transfer rate and improved their stability as CE in QDSSCs. Among them, the CdS/CdSe QDSSC on FeS nanosheets/C reached the highest PCE of 5.61% with a remarkable FF of 0.64.[77] Guo et al. also

fabricated  $\text{Cu}_{1.8}\text{S}/\text{C}$  hybrid CEs through the sulfidation of a copper/carbon (Ac and Cb) composite. [419] The assembled CdSeTe-sensitized QDSSCs achieved a high PCE of 8.40%, larger than that of pure carbon (5.25%) and comparable to that of conventional  $\text{Cu}_x\text{S}/\text{brass}$ -based QDSSCs (8.44%), which also showed satisfactory stability in a dark room for over 72 h without any obvious decrease in PCE.[419]

Beside metal sulfides, the low cost  $\alpha\text{-MoO}_3/\text{C}$  composite obtained from spray pyrolysis was also used as CE in QDSSCs. The CdS-sensitized QDSSC with this CE showed better energy-to-electricity conversion efficiency compared the cells used Pt and  $\text{Cu}_2\text{S}$  as CEs, but the PCE of 1.29% was still relatively low.[48]  $\text{TiO}_2/\text{Ac}$  composites also have been used as Ce in QDSSCs, where  $\text{TiO}_2$  worked as binder and a PCE of 3.48% was achieved. [38]

### 2.9.2.2 Graphene

Similarly, metal sulfide/GR composites were often reported as CE in QDSSCs. For instance, Samadpour and Arabzade found pre depositing a GR layer on FTO could simply modify the compact structure of the the SILAR deposited  $\text{CuS}/\text{PbS}$  CEs to a more porous structure. [255] The CdS/CdSe QD sensitized cells based on this GR/ $\text{CuS}/ \dots / \text{PbS}$  CEs showed enhanced PCE and FF compared with the cells with  $\text{CuS}/ \dots / \text{PbS}$  CEs. Hu et al. also prepared sandwich structural CoS/GS electrode by repeating electrophoretic deposition of GR nanosheets and deposition of CoS NPs and the obtained CE had a high specific surface area and displayed an excellent electrochemical activity toward the polysulfide electrolyte.[194]

Graphene materials have various structures and morphologies, which also have great effect on the hybrid CE in QDSSCs. Khalili et al. used GR and GO to couple with Sr or Ba doped CoS forming sandwich structural CEs for QDSSCs and found the cells based on Sr- or Ba-CoS/GO CEs showed better photovoltaic performance than that with GR based CEs. [195] Zeng et al. prepared a graphite powder (GP) film-supported  $\text{Cu}_2\text{S}$  CEs for QDSSCs, which showed smaller  $R_{ct}$  and higher catalytic activity and stability than Pt or bare  $\text{Cu}_2\text{S}$ .[420] The QDSSCs with  $\text{Cu}_2\text{S}/\text{GP}$  CEs gave a PCE of 4.59%, higher than those with Pt or  $\text{Cu}_2\text{S}$  but not a significant value.[420] 3D GR frameworks were also reported to load CuS nanocrystals as a composite CE for CdS/CdSe QDSSCs. [208] As the 3D architecture composite could provide multi-direction channels that facilitate electron transport and ion diffusion as well as offer more accessible catalytic active site, the corresponding QDSSCs achieved a higher PCE of 5.04%, superior to the 2D  $\text{CuS}/\text{GR}$ (4.17%).[208] Zhang et al. also prepared the  $\text{CuS}/\text{graphene}$  hydrogels (GH) composites by a hydrothermal reaction and compressed them

onto titanium mesh served as the CE for CdSeTe QDSSCs, which gave a more attractive PCE of 10.71% and  $V_{oc}$  of 786 mV, respectively. The high photovoltaic performance could be attributed to the synergistic effects of the water-rich GH (having a 3D porous structure accompanied by good conductivity) and highly catalytic CuS, reflected from the small series resistance ( $R_s$ ), high catalytic activity, small  $R_{ct}$ , and stability.[206]

### 2.9.2.3 Other carbon structures or components

Apart from amorphous carbon and GR, other carbon structures based hybrid materials were also reported as CEs in the QDSSCs application. For example, Zhang et al. prepared  $TiO_2/C_{60}$  CE for CdS/CdSe QDSSCs, which exhibited better electrocatalytic activity, lower  $R_{ct}$  and higher exchange current density compared to Pt or  $TiO_2/AC$  electrodes. [38] The CoS/CNT base composite CEs also have been reported in QDSSCs, but their electrocatalytic properties were relatively lower than the CoS/GR or CoS/GO counterparts as GR have better intrinsic conductivity.[195] Guo et al. presented a novel novel fiber-shaped flexible QDSSC which consisted of CdSe/CdS co-sensitized  $TiO_2$  nanotube array films around a spiral-shaped Ti wire as a working electrode, and  $Co_9S_8$  nanotube arrays (NTs) grown on the carbon fibers (CFs) ( $Co_9S_8$  NT@CF) as a CE (Figure 2.16). Compared to the traditional Pt and pure CF CEs, the  $Co_9S_8$  NT@CF electrode showed a much higher electrocatalytic ability toward the reduction of  $S_n^{2-}$  ions.[418] An absolute PCE of 3.79% was demonstrated by using this  $Co_9S_8$  NT@CF as CE, which was much higher than Pt (1.65%) and CF (0.46%) CEs.

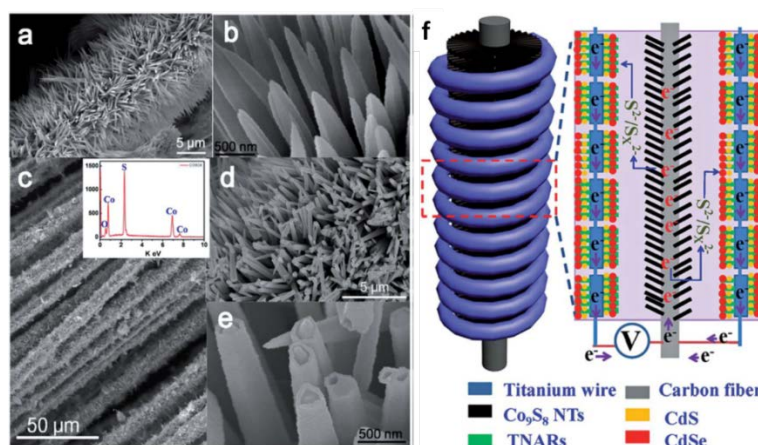


**Figure 2.16.** (a and b) SEM top-view images at different magnifications of  $Co(CO_3)_{0.35}Cl_{0.20}(OH)_{1.10}$  NWs grown on the CFs by CBD method at 90 °C for 3 h; (c–e) SEM top-view images at different magnifications of  $Co_9S_8$  NTs grown on the CFs by hydrothermal and template methods at 150 °C for 8 h, the inset in (c) is the EDX spectrum of the corresponding  $Co_9S_8$  NTs; (f) Design and principle of the fiber-shaped QDSSC. Reprinted with permission from ref. [418] Copyright The Royal Society of Chemistry 2014.

For the CE of QDSSCs, it was also found the CSHMs with different carbon structures had better conductivity and electrocatalytic activity towards the  $S_n^{2-}$  reduction. In the hybrid of TiN NPs and nanostructured carbon materials, Youn et al. found the combination of GR and CNTs led to a favorable morphology, which prevented stacking of graphene or bundling of CNTs, maximized the contact of the hybrid support with TiN NPs, and improved the electron transfer capability relative to either CNTs or GR alone. [261] The solar cell based on TiN/CNT-GR CE showed a PCE of 4.13%, which was much higher than that of the Au electrode (3.35%).[261] On this basis, they further prepared  $Mo_2N/CNT-rGO$ ,  $Mo_2C/CNT-rGO$ , and  $MoS_2/CNT-rGO$  composites for the CE of QDSSCs. [262] Among them, QDSSCs equipped with  $Mo_2N/CNT-rGO$  and  $Mo_2C/CNT-rGO$  CEs exhibited enhanced photovoltaic performances and remarkable stabilities, both of which were superior to the corresponding properties of the  $MoS_2/CNT-rGO$  and even the reference Au CE. The CdS/CdSe QDSSC assembled with  $Mo_2N/CNT-rGO$  counter electrode displayed an impressive PCE of 5.41%. [262]

## 2.10 Carbon dots sensitized solar cells (CDSSCs)

CDs have excellent photo-absorption capacity as well as electron accepting and transport properties, which provide new opportunities to use them for photo-energy conversion related solar cell applications.[423] Due to the cheap and nontoxic nature of CDs, CDSSCs have attracted tremendous interest recently.

Commonly, CDSSCs use the same basic structure as DSSCs, where  $TiO_2$ ,  $I_3^-/I^-$  redox couple and Pt work as anode, electrolyte and counter electrode, respectively. The only difference is CDs replacing dye as sensitizer to harvest light. As shown in Figure 2.17a, there may be three electron transfer routes in CDSSCs.[330] After the photo-excitation, an electron can be promoted from the ground-state ( $C^0$ ) to the excited-state ( $C^*$ ) of CDs, leaving a positive charge carrier ( $h^+$ ) at  $C^0$ . Without quenching, the photo-excited electron would have high probability to return to  $C^0$  and recombine with  $h^+$  to generate fluorescent emission (Route I) rather than extract to the external circuit for electricity generation. On the other hand, the photo-excited electrons could be directly consumed by a suitable electron acceptor to achieve the fluorescent quenching (Route II). Moreover, the positive charge carriers ( $h^+$ ) in the  $C^0$  of the excited CDs possess oxidative power that can be neutralized by extracting an electron from a suitable electron donor to quench the fluorescent emission (Route III). Thus, in the CDSSCs with  $TiO_2$  as anode, promoting Route III and inhibiting Route I could effectively

increase the probability of injecting the photo-excited electrons into the CB of TiO<sub>2</sub> then to the external circuit, which could lead to a dramatically enhanced utilization efficiency of the photo-excited electrons for electricity generation. The ideal band structure in CDSSCs would be like as shown in Figure 2.17b, where I serves a role of charge recombination blocker by donating electron to neutralize the h<sup>+</sup> of excited CDs. However, the differences in particle size, surface group and main structure would result in different emissive trap sites on CDs. Therefore, the actual band structure in CDSSCs would be more complicated, which may vary from the using of carbon source and the CD preparation method.

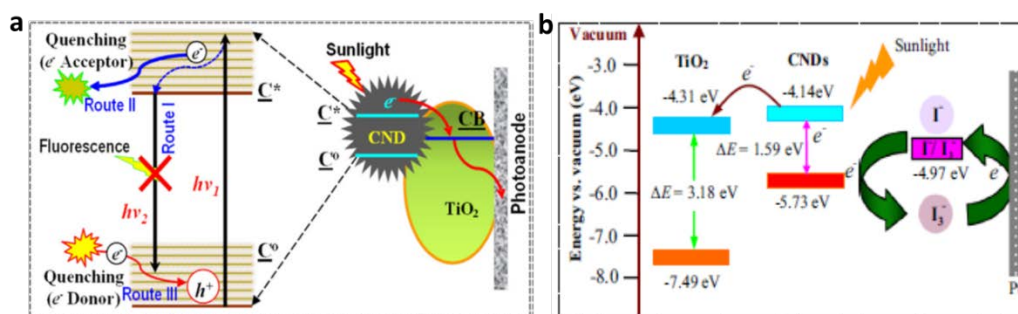


**Figure 2.17.** Schematic illustration of (a) the photo-excited electron quenched by an electron acceptor (Route II) and donor (Route III) and (b) energy band structures of CDSSCs. Reprinted with permission from ref.[330]Copy right 2015 Elsevier Ltd.

The solar cell performances based on CDs and their corresponding synthesis methods are summarized in Table 3. Likewise, TiO<sub>2</sub> is normally used as the anode materials in CDSSCs. For example, Mirtchev et al. have prepared water-soluble CDs via chemical carbonization of  $\gamma$ -butyrolactone and used them as the sensitizer for nanocrystalline-TiO<sub>2</sub> solar cell.[317] The obtained CDs with hydroxyl, carboxyl, and sulfonate surface groups could anchor on TiO<sub>2</sub> surface like common Ru-based dye and the resulted CDSSC displayed a PCE of 0.13%. A very low PCE of 0.0041% was also obtained on the CDSSC based on TiO<sub>2</sub> NT arrays, where the CDs was obtained by electrochemical-etching of graphite rods. [308] Margraf et al. used citric acid, urea, and formic acid as a precursor to synthesize CDs for solar cell application, achieved a PCE of 0.24%.[424] They found the assembly of CDs on TiO<sub>2</sub> electrodes could be controlled via the pH of the solution, where low pH led to significantly improved solar cell performance. The CD/TiO<sub>2</sub> photoanodes were normally prepared through post-adsorption method by immersing TiO<sub>2</sub> electrode into CD solution. However, Zhang et al. presented a pyrolysis strategy to grow CDs onto TiO<sub>2</sub> surfaces in situ and used as this hybrid as photoanode of CDSSC (based on QDSSC structure), which gave a PCE of 0.87% higher than all of the reported CDSSCs adopting the simple post-adsorption method.[335] This

result indicates that an in situ growing strategy has great advantages in terms of optimizing the performance of CDSSCs, which may favour the electron transfer Route II. It was also found CDSSCs based on N-doped CDs showed better photovoltaic performance. For example, Zhang et al. reported a N-CD based solar cell gave a PCE of 0.13%, while its N-free counterpart only showed 0.03%. [357] Wang et al. also reported a N-CD sensitized solar cell with a higher PCE of 0.79%. [319] This is because the N-doped CDs can introduce an additional energy level between  $\pi$  of carbon and  $\pi^*$  of oxygen and upon excited, N-CDs can absorb the relative low-energy photons at visible light range and generate the more photoexcited electrons. [319] From this perspective, CDs produced from biomass, which contain both carbon and nitrogen, might be good candidates for CDSSCs. For instance, Marinovic et al. have used polysaccharides (chitosan and chitin), monosaccharide (D-glucose), amino acids (l-arginine and l-cysteine) and raw lobster shells to produce CDs through hydrothermal carbonisation for CDSSCs. [329] The highest PCE of 0.362% was obtained by using CDs from l-arginine, whereas the cell using CDs from lobster shells (a model source of chitin) showed a PCE of 0.216%. Chitosan CDs also have amine groups present, and only demonstrated slightly higher efficiency than amide-containing chitin. The cell with glucose-derived CDs that contain C=O and OH but no amines, gave the lowest efficiency of 0.103% due to the formation of CD clusters. On the other hand, there were no clusters observed on those amino-acid-derived CDs, which indicated the addition of amine groups would limit cluster formation. They suggested the combination of amine and carboxylic acid functionalisation was particularly beneficial for the solar-cell performance because the carboxylic acid groups would aid in anchoring and charge transfer to the TiO<sub>2</sub>. [329] Guo et al. also have used the CDs derived from bee pollen as sensitizer in solar cells, which gave a PCE of 0.11%. [425] Zhang et al. obtained a PCE of 0.529% on the solar cell based CDs synthesized from Monkey Grass. [330]

In addition to TiO<sub>2</sub>, ZnO also have been used as photoanodes in CDSSCs. Dutta et al. report a solid-state solar cell device based of GQDs sensitized ZnO NWs photoanode exhibited a high  $V_{OC}$  of 0.8 V and PCE of 0.2%, where the GQDs were synthesized from GO by a simple one-step hydrazine reduction method. [313] Briscoe et al. firstly fabricated solid-state solar cells based on ZnO nanorods with biomass-derived (chitin, chitosan and glucose) CDs as sensitizer. [328] Compared with the CDs from chitin and glucose, the chitosan-derived CDs sensitized solar cell based gave higher efficiency because the free amine groups on chitosan-CQDs facilitated their binding onto the ZnO. The highest PCE of 0.077% was

obtained on the cell with a layer-by-layer combination of chitosan- and chitin-CDs, where the alternate layers of CDs led to an increased loading on the ZnO surface.[328]

In comparison with typical Ru-dye or inorganic QD based solar cells, the solar efficiencies of CDSSCs are more than an order of magnitude low. The  $J_{sc}$  is the main factor that limits better efficiencies because of the emissive trap sites on the surface of the CDs acting as recombination centers and the low charge injection from CDs to semiconductor.[317] Coupling with CDs may extend the light absorption towards longer wavelengths, but this feature is also related to trap states and hardly contribute to the photogenerated current.[424] Thus, improving the non-trap related absorptions of CDs as well as the charge-injection and regeneration kinetics are the main means to enhance the photovoltaic performance of CDSSCs.

Apart from as sensitizer alone, CDs also have been used as co-sensitizer in DSSCs. For example, Mihalache et al. have introduced GQDs into the N3-DSSC system and the improvements in PCE and  $J_{sc}$  were achieved although the  $V_{oc}$  was slight decreased compared with the DSSC sensitized with N3 solely. [321] Fang et al. also prepared GQDs assisting N719-sensitized solar cells and found the  $J_{sc}$ ,  $V_{oc}$  and PCE of the corresponding DSSCs were increased at first and then decreased as the increase of GQDs amounts, while dye-adsorption in the photoelectrodes showed the opposite change regularities. [426] The solar cell with optimal GQDs loading showed a  $J_{sc}$  of  $14.07 \text{ mA cm}^{-2}$  and PCE of 6.10 %, higher than those of the traditional N719-based DSSC by 30.9% and 19.6%, respectively. Ma et al. also reported that the CDs incorporation into the RhB-TiO<sub>2</sub> system can significantly improve the solar cell performance, leading to 7 times higher PCE relative to the non CDs-containing cell. [427] We also prepared CD-dye complexes through a single-step hydrothermal treatment of the extract from celery leaves and used them as sensitizer for TiO<sub>2</sub> solar cell.[332] It was found the cell based on the CD-dye complex obtained at an appropriate heat temperature (120°C) showed an improved PCE, which was 1.7 times higher than the one based on the original extract as the sensitizer, although some dye might decomposed during the hydrothermal process. Thus, it can be concluded that introducing a moderate amount of CDs into the DSSC system can effectively improve their photovoltaic performance. This improvement may arise from two main reason: (1) the overlap between CD photoluminescence and dye absorption spectra produces more photo excited electrons, and (2) CDs act as an electron transfer intermediate between dye and TiO<sub>2</sub> improves the electron transfer and suppress the recombination of photogenerated carriers.

**Table 3** Summary of the preparation methods and carbon sources for CDs and the photovoltaic performances of solar cell based on these CDs.

Photoanode	Preparation method	Carbon source	$\eta$ /%	$V_{oc}$ /mV	$J_{sc}$ /(mA·cm <sup>-2</sup> )	FF /%	Refs.
CDs/TiO <sub>2</sub>	hydrothermal	$\gamma$ -butyrolactone	0.13	380	0.532	64	[317]
N-CDs/ rutile TiO <sub>2</sub>	hydrothermal	CCl <sub>4</sub>	0.13	460	0.69	43	[357]
N-CDs/TiO <sub>2</sub>	pyrolysis	citric acid and ammonia	0.79	470	2.65	62.5	[319]
CDs/TiO <sub>2</sub>	microwave	citric acid, urea and formic acid	0.24	490	0.99	50	[424]
CDs/TiO <sub>2</sub> <sup>1</sup>	in situ pyrolysis	citric acid and ethanediamine	0.87	430	6.47	31	[335]
CDs/P25	hydrothermal	bee pollen	0.11	461	0.33	72.6	[425]
CDs/P25	hydrothermal	$\iota$ -cysteine	0.34	509	1.43	46.1	[329]
		$\iota$ -arginine	0.362	660	0.97	57	
		lobster shell	0.216	554	1.05	37	
		chitosan	0.167	550	0.80	38	
		chitin	0.139	469	0.83	35.7	
		<i>D</i> -Glucose	0.103	410	0.68	38	
CDs/TiO <sub>2</sub>	hydrothermal	Monkey Grass	0.529	498	1.92	55.3	[330]
CDs/pheophytin-pyropheophytin/P25	hydrothermal	celery leaf	0.48	600	1.11	73	[332]
CDs/TiO <sub>2</sub> NTs	electrochemical-etching	graphite rods	0.0041	580	0.02	35	[308]
CDs/RhB/P25	electrochemical-etching	graphite rods	0.147	500	0.64	-	[427]
GQDs/N3/ TiO <sub>2</sub>	microwave	D-(+) glucosamine and 2-amino-2 (hydroxymethyl)-1,3-propanediol	2.15	583	5.58	66	[321]
GQDs/N719/TiO <sub>2</sub>	hydrothermal	graphite oxide	6.10	0.66	14.07	59	[426]
CDs/ZnO nanorod <sup>2</sup>	hydrothermal	chitosan-chitin	0.077	265	0.674	43	[328]
GQDs/ZnO NWS <sup>3</sup>	hydrazine reduction	graphite oxide	0.20	800	0.45	50	[313]

<sup>1</sup>The electrolyte contains 1 mol·L<sup>-1</sup> Na<sub>2</sub>S and 1 mol·L<sup>-1</sup> S in ethanol/water mixture (3/7, v/v) and Cu<sub>2</sub>S on copper was selected as a counter electrode; <sup>2</sup> solid-state solar cells with CuSCN as a hole-transporting layer; <sup>3</sup> solid-state solar cell with N-N-diphenyl-N-N-bis(3-methylphenyl)-1,1-biphenyl)-4,4-dia-mine (TPD), as a hole-transporting layer and Au as a counter electrode.

## 2.11 Perovskite solar cells (PSCs)

After DSSCs and QDSSCs, the all-solid-state perovskite solar cells (PSCs) have been demonstrated as promising photovoltaic devices due to their attractive PCEs and low fabrication cost. The reported PCEs of PSCs have skyrocketed from 9.7% to 22.1% in the recent 5 years.[428, 429] Normally, a complete PSC device contains a transparent and conductive substrate, an electron-transporting layer (ETL), a perovskite light harvest layer, a hole-transporting layer (HTL) and an electrode for charge collection. Due to the chemical stability, environmental kindness and excellent conductivity, carbon materials have been widely applied in PCEs. [19, 430] With the advantages of both carbon and semiconductor materials, CSHMs also have been used in all the layers of PSCs to enhance their photovoltaic performance (Figure 2.18) and their photovoltaic performance are summarized in Table 4.

In the n-i-p type PSCs, ETL plays a vital role in light adsorption, electrons collection and transportation from perovskite to conductive substrate and external circuit. As shown in Table 4, GR, fullerenes and CDs based CSHMs have been applied in ETL to improve electron extraction from perovskite resulting in a higher  $J_{sc}$ . Ahmed et al. found using  $TiO_2/GO$  nanocomposite as ETL for HTL free PSCs could effectively improve the solar efficiency under high humidity and air compared with those using  $TiO_2$  as ETL due to the passivation of trap states, enhanced electron mobility, and suitable band alignments benefited from the composite.[431]  $TiO_2/GR$  nanohybrids also have been used as a compact ETL in meso-superstructured PSCs, which enabled the entire device fabrication at low temperatures ( $< 150\text{ }^\circ\text{C}$ ). [432] It was found the optimum GR content was 0.6 wt. % corresponding to just over one monolayer coverage of the GR by  $TiO_2$  NPs and further increasing the GR content would make a less selective electrode as the bare GR contacting the perovskite directly resulted in the electron-hole recombination. With superior charge-collection provided by GR, these solar cells showed better photovoltaic performance with a PCE up to 15.6%. [432] Wang et al. have used  $SrTiO_3/GR$  nanocomposites as a mesoporous ETL in PSCs and with moderate GR loading the best performance with a PCE of 10% and a  $J_{sc}$  of  $18.08\text{ mA cm}^{-2}$  was obtained, which increased by 46.0 and 45.6% respectively compared with the mp- $SrTiO_3$  based device.[181] Besides, a lithium-neutralized GO (GO-Li) layer also has been coated on mesoporous  $TiO_2$  (mp- $TiO_2$ ) to form a hybrid ETL for PSCs, in which the work function of GO was reduced to about  $-4.3\text{ eV}$  by lithium-neutralization matching with the CB of  $TiO_2$  ( $-4.23\text{ eV}$ ). [433] The resulted PSCs showed better moisture stability and photovoltaic

performance with  $J_{SC}$  and FF enhanced remarkably and hysteresis-less and achieved the efficiency over 11%.

Fullerenes as good electron acceptor also have been used to modify the  $TiO_2$  based ETL in PSCs. For example, the  $TiO_2/C_{60}$  bilayer have been used as the ETL in planar PSCs and the optimized PSC could achieve a PCE of 16.58% with a FF of 75.91% by adjusting the  $C_{60}$  solution concentration, which were much higher than those cells based on pure  $TiO_2$  or  $C_{60}$ . [434] PSCs with  $C_{60}$  interface layers also showed far less hysteresis as fullerene good contacted with two layers facilitated electron injection from perovskite into the compact  $TiO_2$  layer. Fullerene based self-assembled monolayer ( $C_{60}$ -SAM) also has been employed to modified the surface of mesoporous  $TiO_2$  in PSCs. [435] It was found that the  $C_{60}$ -SAM as an electron acceptor could effectively promote the photo-excited electron transfer from both the perovskite and the poly(3-hexylthiophene) (P3HT, HTL with light absorption) layers, but inhibited further electron transfer into the mesoporous  $TiO_2$  as the misalignment of energy level and poor electronic coupling, thus resulting in a non-significant PCE of 6.7%. Zhou et al. have tried to improve the function of ETL by surface engineering of the compact  $TiO_2$ (c- $TiO_2$ ) layer with [6,6]-phenyl- $C_{61}$ -butyric acid methyl ester ( $PC_{61}BM$ ) or ethanolamine (ETA)-functionalized fullerene ( $C_{60}$ -ETA), but resulted in only negligible changes in PCE. [436] However, the PCE was significantly improved when  $PC_{61}BM$  and  $C_{60}$ -ETA were used to modify  $TiO_2$  layer together. This because the  $PC_{61}BM$  layer could passivate the traps on the  $TiO_2$  surface, while the subsequent  $C_{60}$ -ETA layer could improve the wettability of the perovskite film on the ETL and also facilitate electron transport across the interface between the perovskite and the  $TiO_2$  ETL. [436] The best PCE of 18.49% and average of 16.31% were attained on these dual surface modified PCSs, which also showed dramatically suppressed hysteresis. A triblock fullerene derivative [6,6]-phenyl- $C_{61}$ -butyric acid-dioctyl-3,3'-(5-hydroxy-1,3-phenylene)-bis(2-cyanoacrylate) ester ( $PCBB-2CN-2C8$ ) also have been reported to engineer the low-temperature prepared c- $TiO_2$  film surface, which significantly improved charge extraction from the perovskite layer as well as the  $V_{oc}$  and FF compared with the PSCs without modification. [437] Due to the passivation effect of  $PCBB-2CN-2C8$ , the stability of these PSCs was also enhanced greatly. In addition, an interconnected  $TiO_2/PC_{70}BM$  ETL derived from nanoparticle inks also have been used in PCSs (Figure 2.18a). [438] The  $PC_{70}BM$  modification could change the direction of the surface band bending within the perovskite semiconductor and reduced its density of trap states at the

interface with the ETL layer. Based on this modification, a PCE of 17.2% was obtained on rigid PSCs, while flexible PSCs exhibited a remarkable stabilized PCE of 12.2%.

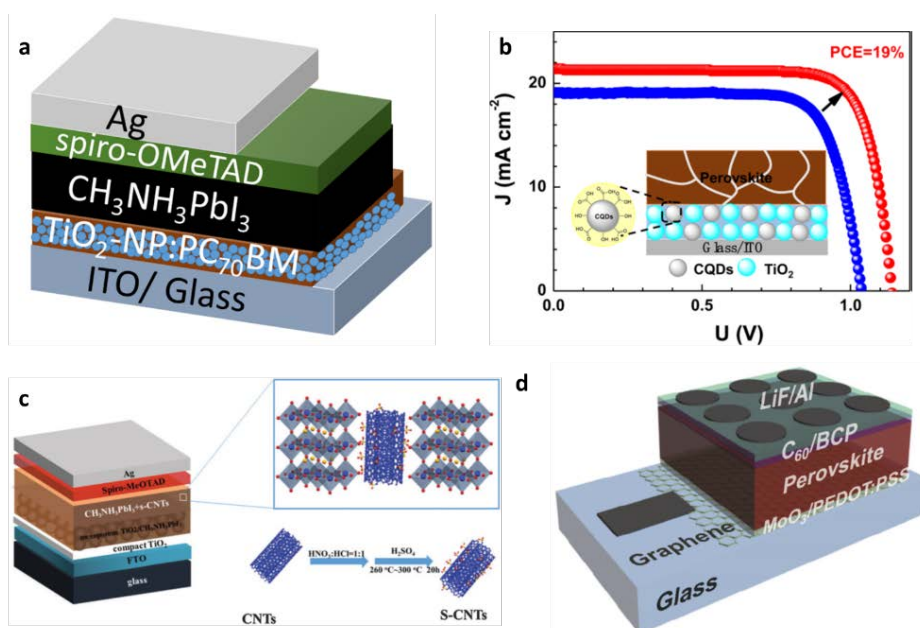


**Figure 2.18.** Planar n-i-p perovskite solar cell based on (a) a  $\text{TiO}_2$ -NP electron-transporting layer (ETL) surface modified with PC70BM and (b) a CD/ $\text{TiO}_2$  hybrid ETL reaching a champion ~ 19% efficiency, (c) mesoporous n-i-p perovskite solar cell with sulfonated carbon nanotubes (s-CNTs) incorporated into mesoporous perovskite film, (d) inverted perovskite solar cells utilizing graphene/ $\text{MoO}_3$  as a transparent electrode. Reprinted with permission from ref. [438], [439], [440]and[441] Copyright 2017 American Chemical Society, 2017 American Chemical Society, 2016 The Royal Society of Chemistry and 2015 WILEY-VCH.

In addition to GR and fullerenes, CDs have also be introduced to the ETL to facilitate electron extractions. For instance, Zhu et al. have deposited an ultrathin GQDs layer on the top of mp- $\text{TiO}_2$  layer as the ETL in PSCs, which displayed a higher  $J_{sc}$  and PCE compared with the reference cell without GQDs.[442] According to the ultrafast transient absorption spectroscopy measurements, it was found the electron extraction time at 90-106 ps in the perovskite/GQD/ $\text{TiO}_2$  film was considerably faster than in the perovskite/ $\text{TiO}_2$  film (260-307 ps), which could effectively compete with carrier trapping and thus provide a reasonable explanation to the GQDs-induced cell performance enhancement.[442] Li et al. also have introduced a homogeneous CD/ $\text{TiO}_2$  nanocolloid to form the ETL for  $\text{CH}_3\text{NH}_3\text{PbI}_{3-x}\text{Cl}_x$  based planar PSCs and found the CD/ $\text{TiO}_2$  hybrid increased both the  $V_{oc}$  and  $J_{sc}$  as compared to using  $\text{TiO}_2$  alone (Figure 2.18b). [439] This is because the CDs increased electronic coupling between the perovskite and  $\text{TiO}_2$  ETL interface and also formed well-matched energy levels and leading to efficient electron extraction and injection from perovskite to

TiO<sub>2</sub>. With optimized CDs modification contents, these PSCs could achieved an average and best PCE of 17.60 % and 18.89%, respectively. [439] Tavakoli et al. have employed rGO CDs to modify ZnO surface forming a quasi-core shell structure and used it as the ETL for PSCs. [443] The rGO CD shell could not only quicken electron transfer and reduce the charge carrier recombination but also worked as a protection layer for ZnO to prevent the formation of CH<sub>3</sub>NH<sub>3</sub>OH, which was generated from the reaction between methylammonium iodide (CH<sub>3</sub>NH<sub>3</sub>I) and hydroxide groups on the ZnO surface, resulting in stable perovskite layer. The rigid device with on ZnO/rGO CD layer achieved high efficiency of 15.2% and only dropped 10% of the PCE after 30 days' test, much better than that on ZnO lone. And, the low temperature fabrication process also allowed to prepare flexible PSCs, which showed a PCE of 11.2%.

The crystallinity and morphology of perovskite layers are the crucial factors for the high performance of PSCs. Carbon materials also have been incorporated with perovskite to improve the morphology and crystallinity of the light active layer in PSCs. Cheng et al. found embedding small amount of MWCNTs into the perovskite layer could improve the electrical connect between small and large perovskite NPs, which facilitated the collection of the photo-generated holes by the carbon electrode as the large perovskite NPs were directly connected with carbon electrode in the HTL free PSCs. [444] Owing to the faster charge transport provided by MWCNTs, the hybrid PSCs showed improved both J<sub>SC</sub> and V<sub>oc</sub> compared with the pristine ones. It was found that adding of sulfonate CNTs (s-CNTs) into perovskite precursor solution could effectively increase the grain size and reduce the boundaries of the obtained perovskite film (Figure 2.18c).[440] This is because the s-CNTs bonded with negative charged sulfonic acid (-SO<sub>3</sub>H) would have some interaction with CH<sub>3</sub>NH<sub>3</sub><sup>+</sup> in the precursor solution, which made CH<sub>3</sub>NH<sub>3</sub>I molecules continuously gather around the s-CNTs resulting in large size of perovskite grains and s-CNTs filled grain boundaries. As the large grain size and the s-CNTs staying in the boundaries could reduce the charge trap states, shorten the charge transporting distance and suppress charge recombination, the photovoltaic performance of the device with s-CNTs was improved significantly, with the best PCE of 15.1% higher than that with CNTs (10.3%) and pure perovskite (12.5%).[440] Fang et al. have also added GQDs into perovskite precursor, which could act as the nucleation and growth centers of the perovskite crystals resulting in the lager average grain size and merged adjacent crystals. [445] Moreover, the GQDs could effectively passivate the defect states at the perovskite grain boundaries, which would reduce the

recombination rate and improve the electron extraction. However, large amount of QDs adding would likely lead to agglomeration and forming new charge recombination centers. In their work, with the addition of 7 vol. % QDs solution ( $1.5 \text{ mg mL}^{-1}$ ) in perovskite precursor, the devices gave a higher PCE of 17.62 %, which was an 8.2% enhancement with respect to the devices without QDs. [445] Ye et al. fabricated  $\text{CH}_3\text{NH}_3\text{PbI}_3$ /carbon nanofiber (CNF) mat composites for metal-electrode-free PSCs, where the  $\text{CH}_3\text{NH}_3\text{PbI}_3$  grew along with the direction of the aligned CNFs. [446] It was found the free-electron diffusion length in the  $\text{CH}_3\text{NH}_3\text{PbI}_3$  phase of the  $\text{CH}_3\text{NH}_3\text{PbI}_3$ /carbon nanocomposite was almost twice that of bare  $\text{CH}_3\text{NH}_3\text{PbI}_3$ , and nearly 95% of the photogenerated free holes could be injected from the  $\text{CH}_3\text{NH}_3\text{PbI}_3$  phase into the CNF. The perovskite/CNF composite base solar cells gave a PCE of 13%, and such devices without expensive HTL and metal electrode are cheap and easy to fabricate.[446]

In addition, CSHMs also have been introduced into HTL or worked as conductive electrode to improve performance of PSCs. For example, Liu et al. have prepared a composite of poly(3,4-ethylenedioxythiophene):poly (styrenesulfonate) (PEDOT:PSS): silver trifluoromethanesulfonate ( $\text{AgOTf}$ )-doped GO as a HTL in PSCs. [447] It was found the work function of PEDOT:PSS film ( $\sim 5 \text{ eV}$ ) could reduce to 4.68 eV, which indicated a lower energy barrier for hole transport at the PEDOT:PSS :  $\text{AgOTf}$ -doped GO/perovskite interface than the GO/perovskite or PEDOT:PSS/perovskite interfaces. With also the higher conductivity, the PSCs based on the hybrid HTL showed higher  $J_{sc}$  and PCE compared with those with bare PEDOT:PSS and GO. Besides, GR bonded with an ultrathin  $\text{MoO}_3$  films have been used as the transparent conductive electrode for the p-i-n type PSCs (Figure 2.18d), where the  $\text{MoO}_3$  layer provided hydrophilicity to the GR surface, enhanced conductivity and elevated its lower work function (4.23 eV) to a higher level (4.71 eV) by hole doping of graphene resulting in a desirable energy level alignment with the highest occupied molecular orbital (HOMO) level of HTL (PEDOT:PSS).[441] The best PCE of 17.1% was achieved with the GR based devices incorporating a 2 nm thick  $\text{MoO}_3$  interfacial layer. Liu et al. have introduced thin composite films ( $\sim 1.8 \mu\text{m}$ ) made with NiO NPs and SWCNT as a CE in full printable meso-super-structured PSCs, in which addition of SWCNT into NiO could largely increase its electronic conduction.[448] Due to efficient charge collection ability of NiO/SWCNT CE, an appreciated PCE of 12.7% was reached, which was higher than 10.5% of the commonly used carbon black/graphite CE ( $\sim 10 \mu\text{m}$ ).

**Table 4.** Summary of the preparation methods of carbon-semiconductor hybrid materials or layers in PSCs and their corresponding architectures and their performances.

ETL/Scaffold	HTL	method	Perovskite	CE	$\eta$ /%	$V_{oc}$ /mV	$J_{sc}$ / ( $\text{mA}\cdot\text{cm}^{-2}$ )	FF /%	Refs.
TiO <sub>2</sub> /GO	-	sol-gel and spin-coating	CH <sub>3</sub> NH <sub>3</sub> PbI <sub>3</sub>	Au	5.9	720	14.6	56	[431]
c-TiO <sub>2</sub> -GR/Al <sub>2</sub> O <sub>3</sub>	spiro-OMeTAD <sup>1</sup>	ultrasonic and spin-coating	CH <sub>3</sub> NH <sub>3</sub> PbI <sub>3-x</sub> Cl <sub>x</sub>	Au	12.4	1000	18.5	70	[432]
c-TiO <sub>2</sub> /mp- SrTiO <sub>3</sub> /GR	spiro-OMeTAD	solvothermal	CH <sub>3</sub> NH <sub>3</sub> PbI <sub>3</sub>	Ag	9.41	950	17.09	58	[181]
c-TiO <sub>2</sub> /mp-TiO <sub>2</sub> /Li-GO	spiro-OMeTAD	spin coating	CH <sub>3</sub> NH <sub>3</sub> PbI <sub>3</sub>	Au	11.14	859	19.61	70.3	[433]
c-TiO <sub>2</sub> /C <sub>60</sub>	spiro-OMeTAD	spin coating	CH <sub>3</sub> NH <sub>3</sub> PbI <sub>3</sub>	Au	16.00	988	21.92	73.30	[434]
c-TiO <sub>2</sub> /mp-TiO <sub>2</sub> /C <sub>60</sub> SAM <sup>2</sup>	spiro-OMeTAD P3HT <sup>3</sup>	immersing	CH <sub>3</sub> NH <sub>3</sub> PbI <sub>3-x</sub> Cl <sub>x</sub>	Ag	11.7 <sup>4</sup> 6.7 <sup>4</sup>	840 810	19.6 14.9	72 -	[435]
c-TiO <sub>2</sub> /PCBB-2CN-2C8 <sup>3</sup>	spiro-OMeTAD	spin coating	CH <sub>3</sub> NH <sub>3</sub> PbI <sub>3-x</sub> Cl <sub>x</sub>	Au	16.45	1060	19.85	78	[437]
TiO <sub>2</sub> /PC <sub>70</sub> BM <sup>5</sup>	spiro-OMeTAD	spin coating;	CH <sub>3</sub> NH <sub>3</sub> PbI <sub>3</sub>	Ag	16.69	1050	21.82	72.98	[438]
c-TiO <sub>2</sub> /C <sub>60</sub> -ETA <sup>6</sup>	spiro-OMeTAD	spin coating	CH <sub>3</sub> NH <sub>3</sub> PbI <sub>3</sub>	Au	13.00	1060	18.88	63.45	[436]
c-TiO <sub>2</sub> /PC <sub>61</sub> BM <sup>7</sup>					13.33	1030	19.25	66.27	
c-TiO <sub>2</sub> /PC <sub>61</sub> BM/C <sub>60</sub> -ETA					16.31	1050	21.96	66.46	
c-TiO <sub>2</sub> /CDs	spiro-OMeTAD	spin coating	CH <sub>3</sub> NH <sub>3</sub> PbI <sub>3-x</sub> Cl <sub>x</sub>	Au	17.6	1120	20.2	78	[439]
c-TiO <sub>2</sub> /mp-TiO <sub>2</sub> /GQDs	spiro-OMeTAD	electrochemical method	CH <sub>3</sub> NH <sub>3</sub> PbI <sub>3</sub>	Au	10.15 <sup>4</sup>	937	17.06	63.5	[442]
ZnO/rGO QDs	spiro-OMeTAD	sol-gel and electrophoretic deposition	CH <sub>3</sub> NH <sub>3</sub> PbI <sub>3</sub>	Au	15.2 <sup>4</sup>	1030	21.7	68	[443]
PC <sub>61</sub> BM	PEDOT:PSS <sup>8</sup> : AgOTf <sup>9</sup> -doped GO	spin coating	CH <sub>3</sub> NH <sub>3</sub> PbI <sub>3-x</sub> Cl <sub>x</sub>	Au	11.90	880	19.18	70.51	[447]
LiF/Al-C <sub>60</sub> /BCP <sup>8</sup>	PEDOT:PSS	vacuum thermal evaporating	CH <sub>3</sub> NH <sub>3</sub> PbI <sub>3</sub>	MoO <sub>3</sub> /GR	16.1	1030	21.9	72	[441]
c-TiO <sub>2</sub> /mp-TiO <sub>2</sub> /Al <sub>2</sub> O <sub>3</sub>	-	ultrasonic, stirring, and ball-milling	CH <sub>3</sub> NH <sub>3</sub> PbI <sub>3</sub>	NiO/SWCNT	12.7 <sup>4</sup>	945	20.7	64	[448]
c-TiO <sub>2</sub> /mp-TiO <sub>2</sub>	-	spin coating	CH <sub>3</sub> NH <sub>3</sub> PbI <sub>3</sub> / carbon mat	-	13.0 <sup>4</sup>	980	19.1	68	[446]
c-TiO <sub>2</sub> /mp-TiO <sub>2</sub> /mp-SiO <sub>2</sub>	-	spin coating	CH <sub>3</sub> NH <sub>3</sub> PbI <sub>3</sub> /MWCNT	carbon	11.6	926	21.3	59	[444]

c-TiO <sub>2</sub> /mp-TiO <sub>2</sub>	spiro-OMeTAD	spin coating	CH <sub>3</sub> NH <sub>3</sub> PbI <sub>3</sub> /CNT	Ag	8.6	930	17.8	62.0	[440]
			CH <sub>3</sub> NH <sub>3</sub> PbI <sub>3</sub> /s-CNT		14.5	970	20.8	75.1	
c-TiO <sub>2</sub> /mp-TiO <sub>2</sub>	spiro-OMeTAD	spin coating	CH <sub>3</sub> NH <sub>3</sub> PbI <sub>3</sub> /GQD	Au	17.62	1030	22.49	76.09	[445]

<sup>1</sup> [2,2',7,7'-tetrakis(N,N-di-p-methoxyphenyl-amine)9,9'-spirobifluorene]; <sup>2</sup> C<sub>60</sub> based self-assembled monolayer; <sup>3</sup> poly(3-hexylthiophene); <sup>4</sup> not specified as average value; <sup>5</sup> [6,6]-phenyl-C71-butyric acid methyl ester; <sup>6</sup> ethanolamine (ETA)-functionalized C<sub>60</sub>; <sup>7</sup> [6,6]-phenyl-C61-butyric acid methyl ester; <sup>8</sup> poly(3,4-ethylene dioxythiophene):poly(styrene sulfonate); <sup>9</sup> silver trifluoromethanesulfonate.

## 2.12 Conclusions and outlook

In recent years, the extensive research of carbon-semiconductor hybrid materials (CSHMs) has demonstrated their importance in the conversion of solar energy into chemical and electrical energy. The morphology and structure of the composites, which depend on both carbon and semiconductor materials, are critical in determining their photo-catalytic and photovoltaic performance. According to different carbon allotropes, the CSHMs can be generally divided into (a) amorphous carbon-semiconductor nanocomposites, (b) carbon nanotube-semiconductor nanocomposites, (c) graphene- semiconductor nanocomposites, (d) fullerene-semiconductor nanocomposites, and (e) carbon dots- semiconductor nanocomposites. In this review, we have summarized various preparation methods of CSHMs and their applications in the field of photo/photoelectrochemical catalysis and solar cells. The photocatalytic pollutant degradation, photocatalytic H<sub>2</sub> generation, photocatalytic selective redox reaction and photovoltaic efficiencies of CSHMs are all greatly enhanced due to the synergistic effect of carbon and semiconductor, in which carbon materials provide excellent conductivity, large surface area and high chemical stability, while semiconductor materials possess good photoresponse and photocatalytic abilities. Great achievement in the development and application of CSHMs has been made with the researcher's efforts. However, there are still many challenges remain to be addressed.

For the photocatalyst and photoanode in solar cell, the loading amount of carbon materials in CSHMs is an extremely crucial factor for their photoelectric properties, as excessive carbon loading would not only hinder the light arriving the surface of semiconductor or light sensitizer (dye or QDs), but also result in carrier recombination sites due to their black nature and aggregations. Thus, founding an appropriate ratio between carbon and semiconductor is quite important, but it is still difficult to precisely modulate this key parameter due to the preparation and treatment variation. In addition, the interface content between carbon and semiconductor is another important factor for the application CSHMs in the photocatalytic and photovoltaic areas, as strong contact could facilitate the photoinduced charge transfer and suppress the electron-hole pair recombination as well as adjust the band gap of semiconductor expanding the light absorption range. Providing maximum interfacial contact between carbon and semiconductor materials without aggregating is a big challenge for easy preparation of CSHMs at the nanoscale. When using ternary or quaternary composites in photoelectric field, energy level alignment between different semiconductors as well as

carbon materials become critical as the energy level determines the photoinduced charge separation efficiencies, which further affect the photocatalytic or photovoltaic performance of these nanocomposites. Finding the right composition without losing the control inherent in a hierarchical structure would make the fabrication process of these hybrids more complicated. Moreover, in order to improve the interaction between carbon and semiconductor, the pretreatment to introduce functional group on the surface of carbon materials such as CNT and graphene is necessary. However, this process is not very eco-friendly and would partly destroy their structure resulting in reduced conductivity and stability. For example, the carbon bonds of acid-treated graphene could be cut by oxidation during the photocatalytic reaction resulting in degradation of graphene.[449] For some carbon materials, such as SWCNTs and fullerenes, the high price limited their wide applications. Although carbon dots are cheap and easy to prepare, uniformly and precisely controlling their particle size and trap states are still a technical challenge.

As summarized in this review, CSHMs with different nanostructures and compositions have shown promising potential for solar energy conversion, including photo-catalysis and solar cell applications. Beyond doubt, efforts in the tackling of the abovementioned challenges will lead to many breakthroughs in traditional photo-catalytic and photovoltaic nanomaterials as well as further work to promote the more effective and economical use of solar energy.

## References

1. Singh, R.L. and P.K. Singh, *Global Environmental Problems. Principles and Applications of Environmental Biotechnology for a Sustainable Future*, ed. R.L. Singh. 2017. 13-41.
2. Lewis, N.S., *Research opportunities to advance solar energy utilization*. Science, 2016. **351**(6271).
3. Khan, J. and M.H. Arsalan, *Solar power technologies for sustainable electricity generation - A review*. Renewable & Sustainable Energy Reviews, 2016. **55**: p. 414-425.
4. Li, X., J.G. Yu, and M. Jaroniec, *Hierarchical photocatalysts*. Chemical Society Reviews, 2016. **45**(9): p. 2603-2636.
5. Skubi, K.L., T.R. Blum, and T.P. Yoon, *Dual Catalysis Strategies in Photochemical Synthesis*. Chemical Reviews, 2016. **116**(17): p. 10035-10074.
6. Polman, A., et al., *Photovoltaic materials: Present efficiencies and future challenges*. Science, 2016. **352**(6283).
7. Di Giacomo, F., et al., *Progress, challenges and perspectives in flexible perovskite solar cells*. Energy & Environmental Science, 2016. **9**(10): p. 3007-3035.
8. Liu, J., et al., *Metal-free efficient photocatalyst for stable visible water splitting via a two-electron pathway*. Science, 2015. **347**(6225): p. 970-974.
9. Hernandez-Alonso, M.D., et al., *Development of alternative photocatalysts to TiO<sub>2</sub>: Challenges and opportunities*. Energy & Environmental Science, 2009. **2**(12): p. 1231-1257.

10. Tang, Y., X. Hu, and C. Liu, *Perfect inhibition of CdS photocorrosion by graphene sheltering engineering on TiO<sub>2</sub> nanotube array for highly stable photocatalytic activity*. *Physical Chemistry Chemical Physics*, 2014. **16**(46): p. 25321-25329.
11. Liu, X., et al., *Noble metal-metal oxide nanohybrids with tailored nanostructures for efficient solar energy conversion, photocatalysis and environmental remediation*. *Energy & Environmental Science*, 2017. **10**(2): p. 402-434.
12. Leonard, A., et al., *Whole-cell based hybrid materials for green energy production, environmental remediation and smart cell-therapy*. *Chemical Society Reviews*, 2011. **40**(2): p. 860-885.
13. Soler-Illia, G. and O. Azzaroni, *Multifunctional hybrids by combining ordered mesoporous materials and macromolecular building blocks*. *Chemical Society Reviews*, 2011. **40**(2): p. 1107-1150.
14. Titirici, M.-M., et al., *Sustainable carbon materials*. *Chemical Society Reviews*, 2015. **44**(1): p. 250-290.
15. Zhang, Y., et al., *Engineering the Unique 2D Mat of Graphene to Achieve Graphene-TiO<sub>2</sub> Nanocomposite for Photocatalytic Selective Transformation: What Advantage does Graphene Have over Its Forebear Carbon Nanotube?* *ACS Nano*, 2011. **5**(9): p. 7426-7435.
16. Sakthivel, S. and H. Kisch, *Daylight Photocatalysis by Carbon-Modified Titanium Dioxide*. *Angewandte Chemie International Edition*, 2003. **42**(40): p. 4908-4911.
17. Wang, Q., J. Yan, and Z. Fan, *Carbon materials for high volumetric performance supercapacitors: design, progress, challenges and opportunities*. *Energy & Environmental Science*, 2016. **9**(3): p. 729-762.
18. Zhu, H., et al., *Applications of carbon materials in photovoltaic solar cells*. *Solar Energy Materials and Solar Cells*, 2009. **93**(9): p. 1461-1470.
19. Hu, R., et al., *Carbon materials for enhancing charge transport in the advancements of perovskite solar cells*. *Journal of Power Sources*, 2017. **361**(Supplement C): p. 259-275.
20. Brennan, L.J., et al., *Carbon Nanomaterials for Dye-Sensitized Solar Cell Applications: A Bright Future*. *Advanced Energy Materials*, 2011. **1**(4): p. 472-485.
21. Wang, M.Y., et al., *Inorganic-modified semiconductor TiO<sub>2</sub> nanotube arrays for photocatalysis*. *Energy & Environmental Science*, 2014. **7**(7): p. 2182-2202.
22. Li, X., et al., *Graphene in Photocatalysis: A Review*. *Small*, 2016. **12**(48): p. 6640-6696.
23. Lan, Y.C., Y.L. Lu, and Z.F. Ren, *Mini review on photocatalysis of titanium dioxide nanoparticles and their solar applications*. *Nano Energy*, 2013. **2**(5): p. 1031-1045.
24. Rajeshwar, K., N.R. de Tacconi, and C.R. Chenthamarakshan, *Semiconductor-based composite materials: Preparation, properties, and performance*. *Chemistry of Materials*, 2001. **13**(9): p. 2765-2782.
25. Chen, J.W., et al., *Recent progress in the preparation and application of semiconductor/graphene composite photocatalysts*. *Chinese Journal of Catalysis*, 2013. **34**(4): p. 621-640.
26. Xie, X.Q., K. Kretschmer, and G.X. Wang, *Advances in graphene-based semiconductor photocatalysts for solar energy conversion: fundamentals and materials engineering*. *Nanoscale*, 2015. **7**(32): p. 13278-13292.
27. Han, C., et al., *Improving the photocatalytic activity and anti-photocorrosion of semiconductor ZnO by coupling with versatile carbon*. *Physical Chemistry Chemical Physics*, 2014. **16**(32): p. 16891-16903.
28. Lim, J., et al., *A study of TiO<sub>2</sub>/carbon black composition as counter electrode materials for dye-sensitized solar cells*. *Nanoscale Research Letters*, 2013. **8**(1): p. 227.
29. Bagavathi, M., A. Ramar, and R. Saraswathi, *Fe<sub>3</sub>O<sub>4</sub>-carbon black nanocomposite as a highly efficient counter electrode material for dye-sensitized solar cell*. *Ceramics International*, 2016. **42**(11): p. 13190-13198.
30. Dembele, K.T., et al., *Effect of multi-walled carbon nanotubes on the stability of dye sensitized solar cells*. *Journal of Power Sources*, 2013. **233**: p. 93-97.

31. Yu, J., J. Fan, and B. Cheng, *Dye-sensitized solar cells based on anatase TiO<sub>2</sub> hollow spheres/carbon nanotube composite films*. Journal of Power Sources, 2011. **196**(18): p. 7891-7898.
32. Yang, N., et al., *Two-Dimensional Graphene Bridges Enhanced Photoinduced Charge Transport in Dye-Sensitized Solar Cells*. ACS Nano, 2010. **4**(2): p. 887-894.
33. Wei, L., et al., *Reduced graphene oxide modified TiO<sub>2</sub> semiconductor materials for dye-sensitized solar cells*. RSC Advances, 2016. **6**(103): p. 100866-100875.
34. Lim, S.P., et al., *Reduced graphene oxide–titania nanocomposite-modified photoanode for efficient dye-sensitized solar cells*. International Journal of Energy Research, 2015. **39**(6): p. 812-824.
35. Kazmi, S.A., et al., *Electrical and optical properties of graphene-TiO<sub>2</sub> nanocomposite and its applications in dye sensitized solar cells (DSSC)*. Journal of Alloys and Compounds, 2017. **691**: p. 659-665.
36. Mehmood, U., *Efficient and economical dye-sensitized solar cells based on graphene/TiO<sub>2</sub> nanocomposite as a photoanode and graphene as a Pt-free catalyst for counter electrode*. Organic Electronics, 2017. **42**: p. 187-193.
37. Muthirulan, P., C.N. Devi, and M.M. Sundaram, *TiO<sub>2</sub> wrapped graphene as a high performance photocatalyst for acid orange 7 dye degradation under solar/UV light irradiations*. Ceramics International, 2014. **40**(4): p. 5945-5957.
38. Zhang, Q., et al., *Toward highly efficient CdS/CdSe quantum dot-sensitized solar cells incorporating a fullerene hybrid-nanostructure counter electrode on transparent conductive substrates*. RSC Advances, 2015. **5**(39): p. 30617-30623.
39. Bai, W., et al., *Enhancement of nano titanium dioxide photocatalysis in transparent coatings by polyhydroxy fullerene*. Applied Catalysis B: Environmental, 2012. **125**(Supplement C): p. 128-135.
40. Regulska, E. and J. Karpinska, *Investigation of Photocatalytic Activity of C-60/TiO<sub>2</sub> Nanocomposites Produced by Evaporation Drying Method*. Polish Journal of Environmental Studies, 2014. **23**(6): p. 2175-2182.
41. Kalpana, K. and V. Selvaraj, *Photodegradation and antibacterial studies of ZnS wrapped fly ash nanocomposite for multipurpose industrial applications*. RSC Advances, 2015. **5**(59): p. 47766-47777.
42. Chung, S.-L. and C.-M. Wang, *A sol–gel combustion synthesis method for TiO<sub>2</sub> powders with enhanced photocatalytic activity*. Journal of Sol-Gel Science and Technology, 2011. **57**(1): p. 76-85.
43. Potti, P.R. and V.C. Srivastava, *Comparative Studies on Structural, Optical, and Textural Properties of Combustion Derived ZnO Prepared Using Various Fuels and Their Photocatalytic Activity*. Industrial & Engineering Chemistry Research, 2012. **51**(23): p. 7948-7956.
44. Moustakas, N.G., et al., *Inorganic–organic core–shell titania nanoparticles for efficient visible light activated photocatalysis*. Applied Catalysis B: Environmental, 2013. **130**: p. 14-24.
45. Xu, Y.-Y., et al., *Visible-light driven C@TiO<sub>2</sub> porous films: Enhanced photoelectrochemical and photoelectrocatalytic performance*. Catalysis Communications, 2015. **69**: p. 63-67.
46. Lu, X., et al., *Characterization and photocatalytic activity of Zn<sub>2+</sub>–TiO<sub>2</sub>/AC composite photocatalyst*. Applied Surface Science, 2011. **258**(5): p. 1656-1661.
47. Chen, P., et al., *A novel approach to synthesize the amorphous carbon-coated WO<sub>3</sub> with defects and excellent photocatalytic properties*. Materials & Design, 2016. **106**: p. 22-29.
48. Tamboli, P.S., et al.,  *$\alpha$ -MoO<sub>3</sub>-C composite as counter electrode for quantum dot sensitized solar cells*. Solar Energy Materials and Solar Cells, 2017. **161**: p. 96-101.
49. Wang, Y., et al., *Dye-sensitized solar cells based on low cost carbon-coated tungsten disulphide counter electrodes*. Electrochimica Acta, 2013. **114**: p. 30-34.
50. Lanfredi, S., et al., *Photodegradation of phenol red on a Ni-doped niobate/carbon composite*. Ceramics International, 2014. **40**(7): p. 9525-9534.

51. Maletić, M., et al., *Hydrothermal synthesis of TiO<sub>2</sub>/carbon composites and their application for removal of organic pollutants*. Arabian Journal of Chemistry, 2016.
52. Zhang, G., et al., *Preparation of carbon-TiO<sub>2</sub> nanocomposites by a hydrothermal method and their enhanced photocatalytic activity*. RSC Advances, 2013. **3**(46): p. 24644-24649.
53. Sha, D., et al., *A novel and efficient synthesis of reduced TiO<sub>2</sub>/C nanocomposites with mesopores for improved visible light photocatalytic performance*. Materials Technology, 2017. **32**(7): p. 451-459.
54. Zhang, G., et al., *Enhanced photocatalytic activity of TiO<sub>2</sub>/carbon@TiO<sub>2</sub> core-shell nanocomposite prepared by two-step hydrothermal method*. Applied Surface Science, 2014. **311**: p. 384-390.
55. Peng, L., et al., *A Designed TiO<sub>2</sub>/Carbon Nanocomposite as a High-Efficiency Lithium-Ion Battery Anode and Photocatalyst*. Chemistry – A European Journal, 2015. **21**(42): p. 14871-14878.
56. Zhang, Z., et al., *A spontaneous dissolution approach to carbon coated TiO<sub>2</sub> hollow composite spheres with enhanced visible photocatalytic performance*. Applied Surface Science, 2013. **286**: p. 344-350.
57. Ramasamy, E., et al., *Soft-Template Simple Synthesis of Ordered Mesoporous Titanium Nitride-Carbon Nanocomposite for High Performance Dye-Sensitized Solar Cell Counter Electrodes*. Chemistry of Materials, 2012. **24**(9): p. 1575-1582.
58. Bagheri, S., et al., *Photocatalytic performance of activated carbon-supported mesoporous titanium dioxide*. Desalination and Water Treatment, 2016. **57**(23): p. 10859-10865.
59. Shen, Z., et al., *Bi-layer photoanode films of hierarchical carbon-doped brookite-rutile TiO<sub>2</sub> composite and anatase TiO<sub>2</sub> beads for efficient dye-sensitized solar cells*. Electrochimica Acta, 2016. **216**(Supplement C): p. 429-437.
60. Shen, Z., et al., *Green Synthesis of Carbon- and Silver-Modified Hierarchical ZnO with Excellent Solar Light Driven Photocatalytic Performance*. ACS Sustainable Chemistry & Engineering, 2015. **3**(5): p. 1010-1016.
61. Chen, M., et al., *Construction of Highly Catalytic Porous TiOPC Nanocomposite Counter Electrodes for Dye-Sensitized Solar Cells*. ACS Applied Materials & Interfaces, 2016. **8**(39): p. 26030-26040.
62. Yun, S., et al., *Economical hafnium oxygen nitride binary/ternary nanocomposite counter electrode catalysts for high-efficiency dye-sensitized solar cells*. Journal of Materials Chemistry A, 2013. **1**(4): p. 1341-1348.
63. Xie, Y., et al., *Review of Research on Template Methods in Preparation of Nanomaterials*. Journal of Nanomaterials, 2016. **2016**: p. 10.
64. Xu, H., et al., *Nitrogen-doped carbon and iron carbide nanocomposites as cost-effective counter electrodes of dye-sensitized solar cells*. Journal of Materials Chemistry A, 2014. **2**(13): p. 4676-4681.
65. Tian, H., et al., *Fabrication of core-shell, yolk-shell and hollow Fe<sub>3</sub>O<sub>4</sub>@carbon microboxes for high-performance lithium-ion batteries*. Materials Chemistry Frontiers, 2017. **1**(5): p. 823-830.
66. Wu, M., et al., *In Situ Synthesized Economical Tungsten Dioxide Imbedded in Mesoporous Carbon for Dye-Sensitized Solar Cells As Counter Electrode Catalyst*. The Journal of Physical Chemistry C, 2011. **115**(45): p. 22598-22602.
67. Chen, M., et al., *Cobalt oxide and nitride particles supported on mesoporous carbons as composite electrocatalysts for dye-sensitized solar cells*. Journal of Power Sources, 2015. **286**: p. 82-90.
68. Jang, Y.J., Y.H. Jang, and D.H. Kim, *Nanostructured Carbon-TiO<sub>2</sub> Shells Onto Silica Beads as a Promising Candidate for the Alternative Photoanode in Dye-Sensitized Solar Cells*. Science of Advanced Materials, 2015. **7**(5): p. 956-963.
69. Shen, K., et al., *Development of MOF-Derived Carbon-Based Nanomaterials for Efficient Catalysis*. ACS Catalysis, 2016. **6**(9): p. 5887-5903.
70. Chaikittisilp, W., K. Ariga, and Y. Yamauchi, *A new family of carbon materials: synthesis of MOF-derived nanoporous carbons and their promising applications*. Journal of Materials Chemistry A, 2013. **1**(1): p. 14-19.

71. Banerjee, A., et al., *MOF derived porous carbon-Fe<sub>3</sub>O<sub>4</sub> nanocomposite as a high performance, recyclable environmental superadsorbent*. Journal of Materials Chemistry, 2012. **22**(37): p. 19694-19699.
72. Yang, S.J., et al., *Preparation and Exceptional Lithium Anodic Performance of Porous Carbon-Coated ZnO Quantum Dots Derived from a Metal–Organic Framework*. Journal of the American Chemical Society, 2013. **135**(20): p. 7394-7397.
73. Zhang, G., et al., *High-Performance and Ultra-Stable Lithium-Ion Batteries Based on MOF-Derived ZnO@ZnO Quantum Dots/C Core–Shell Nanorod Arrays on a Carbon Cloth Anode*. Advanced Materials, 2015. **27**(14): p. 2400-2405.
74. Zou, F., et al., *MOF-Derived Porous ZnO/ZnFe<sub>2</sub>O<sub>4</sub>/C Octahedra with Hollow Interiors for High-Rate Lithium-Ion Batteries*. Advanced Materials, 2014. **26**(38): p. 6622-6628.
75. Theerthagiri, J., et al., *Electrochemical deposition of carbon materials incorporated nickel sulfide composite as counter electrode for dye-sensitized solar cells*. Ionics, 2017. **23**(4): p. 1017-1025.
76. Geng, H., et al., *Electrochemical Growth of FeS on Three-dimensional Carbon Scaffold as the High Catalytic and Stable Counter Electrode for Quantum Dot-sensitized Solar Cells*. Electrochimica Acta, 2015. **182**: p. 1093-1100.
77. Geng, H., et al., *Embedding iron sulfide (Fe-S) nanosheets into carbon electrode for efficient quantum dots-sensitized solar cells*. Solar Energy, 2017. **147**: p. 61-67.
78. Rho, W.-Y., et al., *Carbon-doped freestanding TiO<sub>2</sub> nanotube arrays in dye-sensitized solar cells*. New Journal of Chemistry, 2017. **41**(1): p. 285-289.
79. Sun, P., et al., *In-situ growth of antimony sulfide in carbon nanoparticle matrix: Enhanced electrocatalytic activity as counter electrode in dye-sensitized solar cells*. Journal of Power Sources, 2016. **319**: p. 219-226.
80. Xu, Y.-J., Y. Zhuang, and X. Fu, *New Insight for Enhanced Photocatalytic Activity of TiO<sub>2</sub> by Doping Carbon Nanotubes: A Case Study on Degradation of Benzene and Methyl Orange*. The Journal of Physical Chemistry C, 2010. **114**(6): p. 2669-2676.
81. Khannam, M., et al., *Enhanced conversion efficiency of quasi solid state dye sensitized solar cells based on functionalized multi-walled carbon nanotubes incorporated TiO<sub>2</sub> photoanode*. Journal of Materials Science: Materials in Electronics, 2016. **27**(10): p. 10010-10019.
82. Yi, Q.H., et al., *Self-Cleaning Glass of Photocatalytic Anatase TiO<sub>2</sub>@Carbon Nanotubes Thin Film by Polymer-Assisted Approach*. Nanoscale Research Letters, 2016. **11**.
83. Li, G.-r., et al., *Carbon Nanotubes with Titanium Nitride as a Low-Cost Counter-Electrode Material for Dye-Sensitized Solar Cells*. Angewandte Chemie International Edition, 2010. **49**(21): p. 3653-3656.
84. Wang, L.Q., *Synthesis of TiO<sub>2</sub> - CNT nanocomposites and its application to Dye-Sensitized Solar Cells*, in *Advances in Energy Science and Technology, Pts 1-4*, X. Tang, et al., Editors. 2013. p. 722-725.
85. Guo, W., et al., *Performance of Dye-Sensitized Solar Cells Based on MWCNT/TiO<sub>2</sub>-xNx Nanocomposite Electrodes*. European Journal of Inorganic Chemistry, 2011. **2011**(11): p. 1776-1783.
86. Abdullah, H., et al., *Structural and morphological studies of zinc oxide incorporating single-walled carbon nanotubes as a nanocomposite thin film*. Journal of Materials Science: Materials in Electronics, 2013. **24**(9): p. 3603-3610.
87. Abdullah, H., et al., *Photovoltaic properties of ZnO photoanode incorporating with CNTs for dye-sensitized solar cell application*. Ionics, 2014. **20**(7): p. 1023-1030.
88. Xiao, Y., et al., *In situ electropolymerization of polyaniline/cobalt sulfide decorated carbon nanotube composite catalyst toward triiodide reduction in dye-sensitized solar cells*. Journal of Power Sources, 2014. **266**: p. 448-455.
89. Tai, S.-Y., et al., *Investigation of carbon nanotubes decorated with cobalt sulfides of different phases as nanocomposite catalysts in dye-sensitized solar cells*. Electrochimica Acta, 2014. **143**: p. 216-221.

90. Lu, M.-N., et al., *Hierarchical nickel sulfide/carbon nanotube nanocomposite as a catalytic material toward triiodine reduction in dye-sensitized solar cells*. Journal of Power Sources, 2014. **270**: p. 499-505.
91. Theerthagiri, J., et al., *Synthesis of various carbon incorporated flower-like MoS<sub>2</sub> microspheres as counter electrode for dye-sensitized solar cells*. Journal of Solid State Electrochemistry, 2017. **21**(2): p. 581-590.
92. Yue, G., et al., *A counter electrode of multi-wall carbon nanotubes decorated with tungsten sulfide used in dye-sensitized solar cells*. Carbon, 2013. **55**: p. 1-9.
93. Wu, J., et al., *Glucose Aided Preparation of Tungsten Sulfide/Multi-Wall Carbon Nanotube Hybrid and Use as Counter Electrode in Dye-Sensitized Solar Cells*. ACS Applied Materials & Interfaces, 2012. **4**(12): p. 6530-6536.
94. Jiang, L.-C. and W.-D. Zhang, *Charge transfer properties and photoelectrocatalytic activity of TiO<sub>2</sub>/MWCNT hybrid*. Electrochimica Acta, 2010. **56**(1): p. 406-411.
95. Kilic, B., et al., *Preparation of Carbon Nanotube/TiO<sub>2</sub> Mesoporous Hybrid Photoanode with Iron Pyrite (FeS<sub>2</sub>) Thin Films Counter Electrodes for Dye-Sensitized Solar Cell*. 2016. **6**: p. 27052.
96. Zhang, M., et al., *A novel synthesis of CNTs/TiO<sub>2</sub> nanocomposites with enhanced performance as photoanode of solar cell*. Materials Letters, 2013. **109**: p. 240-242.
97. Xiao, Y., et al., *A high performance Pt-free counter electrode of nickel sulfide/multi-wall carbon nanotube/titanium used in dye-sensitized solar cells*. Journal of Materials Chemistry A, 2013. **1**(44): p. 13885-13889.
98. Xiao, Y., et al., *Pulse electrodeposition of CoS on MWCNT/Ti as a high performance counter electrode for a Pt-free dye-sensitized solar cell*. Journal of Materials Chemistry A, 2013. **1**(4): p. 1289-1295.
99. Zhu, P., et al., *TiO<sub>2</sub>-MWCNT rice grain-shaped nanocomposites—Synthesis, characterization and photocatalysis*. Materials Research Bulletin, 2011. **46**(4): p. 588-595.
100. Zhu, P., et al., *Rice grain-shaped TiO<sub>2</sub>-CNT composite—A functional material with a novel morphology for dye-sensitized solar cells*. Journal of Photochemistry and Photobiology A: Chemistry, 2012. **231**(1): p. 9-18.
101. Guerra-Nunez, C., et al., *Morphology and crystallinity control of ultrathin TiO<sub>2</sub> layers deposited on carbon nanotubes by temperature-step atomic layer deposition*. Nanoscale, 2015. **7**(24): p. 10622-10633.
102. Zhao, C., et al., *A novel composite of TiO<sub>2</sub> nanotubes with remarkably high efficiency for hydrogen production in solar-driven water splitting*. Energy & Environmental Science, 2014. **7**(5): p. 1700-1707.
103. Dang, X., et al., *Virus-templated self-assembled single-walled carbon nanotubes for highly efficient electron collection in photovoltaic devices*. Nat Nano, 2011. **6**(6): p. 377-384.
104. Pignon, B., et al., *Versatility of Laser Pyrolysis Applied to the Synthesis of TiO<sub>2</sub> Nanoparticles – Application to UV Attenuation*. European Journal of Inorganic Chemistry, 2008. **2008**(6): p. 883-889.
105. Kumar, M. and Y. Ando, *Chemical Vapor Deposition of Carbon Nanotubes: A Review on Growth Mechanism and Mass Production*. Journal of Nanoscience and Nanotechnology, 2010. **10**(6): p. 3739-3758.
106. Wang, J., et al., *Single-Step Preparation of TiO<sub>2</sub>/MWCNT Nanohybrid Materials by Laser Pyrolysis and Application to Efficient Photovoltaic Energy Conversion*. ACS Applied Materials & Interfaces, 2015. **7**(1): p. 51-56.
107. Zeng, G.-Y., K.-S. Nian, and K.-Y. Lee, *Characteristics of a dye-sensitized solar cell based on an anode combining ZnO nanostructures with vertically aligned carbon nanotubes*. Diamond and Related Materials, 2010. **19**(12): p. 1457-1460.
108. Tettey, K.E., M.Q. Yee, and D. Lee, *Photocatalytic and Conductive MWCNT/TiO<sub>2</sub> Nanocomposite Thin Films*. ACS Applied Materials & Interfaces, 2010. **2**(9): p. 2646-2652.

109. Zhang, X., et al., *DNA assembled single-walled carbon nanotube nanocomposites for high efficiency dye-sensitized solar cells*. Journal of Materials Chemistry A, 2013. **1**(36): p. 11070-11077.
110. Emtsev, K.V., et al., *Towards wafer-size graphene layers by atmospheric pressure graphitization of silicon carbide*. Nat Mater, 2009. **8**(3): p. 203-207.
111. Kim, K.S., et al., *Large-scale pattern growth of graphene films for stretchable transparent electrodes*. Nature, 2009. **457**(7230): p. 706-710.
112. Hummers, W.S. and R.E. Offeman, *Preparation of Graphitic Oxide*. Journal of the American Chemical Society, 1958. **80**(6): p. 1339-1339.
113. Wang, Y., et al., *Enhancing Stability and Photocatalytic Activity of ZnO Nanoparticles by Surface Modification of Graphene Oxide*. Journal of Nanoscience and Nanotechnology, 2012. **12**(5): p. 3896-3902.
114. Jiang, G., et al., *TiO<sub>2</sub> nanoparticles assembled on graphene oxide nanosheets with high photocatalytic activity for removal of pollutants*. Carbon, 2011. **49**(8): p. 2693-2701.
115. Song, P., et al., *Graphene oxide modified TiO<sub>2</sub> nanotube arrays: enhanced visible light photoelectrochemical properties*. Nanoscale, 2012. **4**(5): p. 1800-1804.
116. Lv, H., et al., *Synthesis of graphene oxide-BiPO<sub>4</sub> composites with enhanced photocatalytic properties*. Applied Surface Science, 2013. **284**: p. 308-314.
117. Williams, G., B. Seger, and P.V. Kamat, *TiO<sub>2</sub>-Graphene Nanocomposites. UV-Assisted Photocatalytic Reduction of Graphene Oxide*. ACS Nano, 2008. **2**(7): p. 1487-1491.
118. Ng, Y.H., et al., *To What Extent Do Graphene Scaffolds Improve the Photovoltaic and Photocatalytic Response of TiO<sub>2</sub> Nanostructured Films?* The Journal of Physical Chemistry Letters, 2010. **1**(15): p. 2222-2227.
119. Dubey, P.K., et al., *Synthesis of reduced graphene oxide-TiO<sub>2</sub> nanoparticle composite systems and its application in hydrogen production*. International Journal of Hydrogen Energy, 2014. **39**(29): p. 16282-16292.
120. Lu, Z., et al., *Mechanism of UV-assisted TiO<sub>2</sub>/reduced graphene oxide composites with variable photodegradation of methyl orange*. RSC Advances, 2015. **5**(89): p. 72916-72922.
121. Akhavan, O., *Photocatalytic reduction of graphene oxides hybridized by ZnO nanoparticles in ethanol*. Carbon, 2011. **49**(1): p. 11-18.
122. Liu, X., et al., *UV-assisted photocatalytic synthesis of ZnO-reduced graphene oxide composites with enhanced photocatalytic activity in reduction of Cr(VI)*. Chemical Engineering Journal, 2012. **183**(Supplement C): p. 238-243.
123. Abdolhosseinzadeh, S., et al., *UV-assisted synthesis of reduced graphene oxide-ZnO nanorod composites immobilized on Zn foil with enhanced photocatalytic performance*. Research on Chemical Intermediates, 2016. **42**(5): p. 4479-4496.
124. Pei, S. and H.-M. Cheng, *The reduction of graphene oxide*. Carbon, 2012. **50**(9): p. 3210-3228.
125. Gu, L., et al., *Glucosamine-induced growth of highly distributed TiO<sub>2</sub> nanoparticles on graphene nanosheets as high-performance photocatalysts*. RSC Advances, 2016. **6**(71): p. 67039-67048.
126. Zhang, Y. and C. Pan, *TiO<sub>2</sub>/graphene composite from thermal reaction of graphene oxide and its photocatalytic activity in visible light*. Journal of Materials Science, 2011. **46**(8): p. 2622-2626.
127. Zhang, X.-Y., et al., *Graphene/TiO<sub>2</sub> nanocomposites: synthesis, characterization and application in hydrogen evolution from water photocatalytic splitting*. Journal of Materials Chemistry, 2010. **20**(14): p. 2801-2806.
128. Zhang, X.-F., et al., *Facile preparation of Zn<sub>0.5</sub>Cd<sub>0.5</sub>S@RGO nanocomposites as efficient visible light driven photocatalysts*. Journal of Alloys and Compounds, 2017. **705**: p. 392-398.

129. Sacco, A., et al., *Investigation of Transport and Recombination Properties in Graphene/Titanium Dioxide Nanocomposite for Dye-Sensitized Solar Cell Photoanodes*. *Electrochimica Acta*, 2014. **131**: p. 154-159.
130. Ghoreishi, F.S., V. Ahmadi, and M. Samadpour, *Improved performance of CdS/CdSe quantum dots sensitized solar cell by incorporation of ZnO nanoparticles/reduced graphene oxide nanocomposite as photoelectrode*. *Journal of Power Sources*, 2014. **271**: p. 195-202.
131. Moon, G.-h., et al., *Platinum-like Behavior of Reduced Graphene Oxide as a Cocatalyst on TiO<sub>2</sub> for the Efficient Photocatalytic Oxidation of Arsenite*. *Environmental Science & Technology Letters*, 2014. **1**(2): p. 185-190.
132. Xu, T., et al., *Significantly enhanced photocatalytic performance of ZnO via graphene hybridization and the mechanism study*. *Applied Catalysis B: Environmental*, 2011. **101**(3): p. 382-387.
133. Guo, J., et al., *Sonochemical synthesis of TiO<sub>2</sub> nanoparticles on graphene for use as photocatalyst*. *Ultrasonics Sonochemistry*, 2011. **18**(5): p. 1082-1090.
134. Gayathri, S., M. Kottaisamy, and V. Ramakrishnan, *Facile microwave-assisted synthesis of titanium dioxide decorated graphene nanocomposite for photodegradation of organic dyes*. *AIP Advances*, 2015. **5**(12): p. 127219.
135. Wang, D., et al., *Enhanced photoelectrocatalytic activity of reduced graphene oxide/TiO<sub>2</sub> composite films for dye degradation*. *Chemical Engineering Journal*, 2012. **198**: p. 547-554.
136. Bykkam, S., et al., *Ultrasonic-assisted synthesis of ZnO nano particles decked with few layered graphene nanocomposite as photoanode in dye-sensitized solar cell*. *Journal of Materials Science: Materials in Electronics*, 2017. **28**(8): p. 6217-6225.
137. Jayabal, P., et al., *Preparation and characterization of ZnO/graphene nanocomposite for improved photovoltaic performance*. *Journal of Nanoparticle Research*, 2014. **16**(11): p. 2640.
138. Gong, F., et al., *Enhanced electrocatalytic performance of graphene via incorporation of SiO<sub>2</sub> nanoparticles for dye-sensitized solar cells*. *Journal of Materials Chemistry*, 2012. **22**(33): p. 17321-17327.
139. Low, F.W., C.W. Lai, and S.B. Abd Hamid, *Study of reduced graphene oxide film incorporated of TiO<sub>2</sub> species for efficient visible light driven dye-sensitized solar cell*. *Journal of Materials Science: Materials in Electronics*, 2017. **28**(4): p. 3819-3836.
140. Ding, H., et al., *Reduction of graphene oxide at room temperature with vitamin C for RGO-TiO<sub>2</sub> photoanodes in dye-sensitized solar cell*. *Thin Solid Films*, 2015. **584**: p. 29-36.
141. Saravanan, T., et al., *Synthesis and characterization of Y<sub>2</sub>O<sub>3</sub>-reduced graphene oxide nanocomposites for photocatalytic applications*. *Materials Research Express*, 2016. **3**(7): p. 075502.
142. Zhang, Y., et al., *TiO<sub>2</sub>-Graphene Nanocomposites for Gas-Phase Photocatalytic Degradation of Volatile Aromatic Pollutant: Is TiO<sub>2</sub>-Graphene Truly Different from Other TiO<sub>2</sub>-Carbon Composite Materials?* *ACS Nano*, 2010. **4**(12): p. 7303-7314.
143. Chen, Z., et al., *Synthesis of Uniform CdS Nanospheres/Graphene Hybrid Nanocomposites and Their Application as Visible Light Photocatalyst for Selective Reduction of Nitro Organics in Water*. *ACS Applied Materials & Interfaces*, 2013. **5**(10): p. 4309-4319.
144. Fan, Y., et al., *Convenient Recycling of 3D AgX/Graphene Aerogels (X = Br, Cl) for Efficient Photocatalytic Degradation of Water Pollutants*. *Advanced Materials*, 2015. **27**(25): p. 3767-3773.
145. Tu, W., et al., *Robust Hollow Spheres Consisting of Alternating Titania Nanosheets and Graphene Nanosheets with High Photocatalytic Activity for CO<sub>2</sub> Conversion into Renewable Fuels*. *Advanced Functional Materials*, 2012. **22**(6): p. 1215-1221.
146. Lee, D.H., et al., *Three-Dimensional Monolayer Graphene and TiO<sub>2</sub> Hybrid Architectures for High-Efficiency Electrochemical Photovoltaic Cells*. *The Journal of Physical Chemistry C*, 2015. **119**(12): p. 6880-6885.

147. Zhu, C., et al., *One-pot, water-phase approach to high-quality graphene/TiO<sub>2</sub> composite nanosheets*. Chemical Communications, 2010. **46**(38): p. 7148-7150.
148. Chen, C., et al., *Synthesis of Visible-Light Responsive Graphene Oxide/TiO<sub>2</sub> Composites with p/n Heterojunction*. ACS Nano, 2010. **4**(11): p. 6425-6432.
149. Zhang, J., Z. Xiong, and X.S. Zhao, *Graphene-metal-oxide composites for the degradation of dyes under visible light irradiation*. Journal of Materials Chemistry, 2011. **21**(11): p. 3634-3640.
150. Zhou, Y., et al., *Hydrothermal Dehydration for the "Green" Reduction of Exfoliated Graphene Oxide to Graphene and Demonstration of Tunable Optical Limiting Properties*. Chemistry of Materials, 2009. **21**(13): p. 2950-2956.
151. Fan, W., et al., *Nanocomposites of TiO<sub>2</sub> and Reduced Graphene Oxide as Efficient Photocatalysts for Hydrogen Evolution*. The Journal of Physical Chemistry C, 2011. **115**(21): p. 10694-10701.
152. Wang, P., et al., *One-step synthesis of easy-recycling TiO<sub>2</sub>-rGO nanocomposite photocatalysts with enhanced photocatalytic activity*. Applied Catalysis B: Environmental, 2013. **132**: p. 452-459.
153. Zhang, H., et al., *P25-Graphene Composite as a High Performance Photocatalyst*. ACS Nano, 2010. **4**(1): p. 380-386.
154. Cheng, P., et al., *TiO<sub>2</sub>-graphene nanocomposites for photocatalytic hydrogen production from splitting water*. International Journal of Hydrogen Energy, 2012. **37**(3): p. 2224-2230.
155. Morais, A., et al., *Nanocrystalline anatase TiO<sub>2</sub>/reduced graphene oxide composite films as photoanodes for photoelectrochemical water splitting studies: the role of reduced graphene oxide*. Physical Chemistry Chemical Physics, 2016. **18**(4): p. 2608-2616.
156. Liang, Y., et al., *TiO<sub>2</sub> nanocrystals grown on graphene as advanced photocatalytic hybrid materials*. Nano Research, 2010. **3**(10): p. 701-705.
157. Tan, L.-L., et al., *Reduced graphene oxide-TiO<sub>2</sub> nanocomposite as a promising visible-light-active photocatalyst for the conversion of carbon dioxide*. Nanoscale Research Letters, 2013. **8**(1): p. 465.
158. Zhou, K., et al., *Preparation of graphene-TiO<sub>2</sub> composites with enhanced photocatalytic activity*. New Journal of Chemistry, 2011. **35**(2): p. 353-359.
159. Zhang, X., et al., *A green and facile synthesis of TiO<sub>2</sub>/graphene nanocomposites and their photocatalytic activity for hydrogen evolution*. International Journal of Hydrogen Energy, 2012. **37**(1): p. 811-815.
160. Sher Shah, M.S.A., et al., *Green Synthesis of Biphasic TiO<sub>2</sub>-Reduced Graphene Oxide Nanocomposites with Highly Enhanced Photocatalytic Activity*. ACS Applied Materials & Interfaces, 2012. **4**(8): p. 3893-3901.
161. Shen, J., et al., *One step hydrothermal synthesis of TiO<sub>2</sub>-reduced graphene oxide sheets*. Journal of Materials Chemistry, 2011. **21**(10): p. 3415-3421.
162. Shen, J., et al., *Ionic liquid-assisted one-step hydrothermal synthesis of TiO<sub>2</sub>-reduced graphene oxide composites*. Nano Research, 2011. **4**(8): p. 795.
163. Ahmadkhaniha, R., F. Izadpanah, and N. Rastkari, *Reduced Graphene Oxide-TiO<sub>2</sub> Nanocomposite Facilitated Visible Light Photodegradation of Gaseous Toluene*. Journal of Environmental Protection, 2017. **Vol.08No.05**: p. 12.
164. Shi, M., et al., *Preparation of graphene-TiO<sub>2</sub> composite by hydrothermal method from peroxotitanium acid and its photocatalytic properties*. Colloids and Surfaces A: Physicochemical and Engineering Aspects, 2012. **405**: p. 30-37.
165. Perera, S.D., et al., *Hydrothermal Synthesis of Graphene-TiO<sub>2</sub> Nanotube Composites with Enhanced Photocatalytic Activity*. ACS Catalysis, 2012. **2**(6): p. 949-956.
166. Zhai, C., et al., *Reduced graphene oxide modified highly ordered TiO<sub>2</sub> nanotube arrays photoelectrode with enhanced photoelectrocatalytic performance under visible-light irradiation*. Physical Chemistry Chemical Physics, 2014. **16**(28): p. 14800-14807.

167. Pan, X., et al., *TiO<sub>2</sub>/graphene nanocomposite for photocatalytic application* A. Méndez-Vilas (Ed.), *Materials and processes for energy: communicating current research and technological developments* 2013: p. 913-920.
168. Zhang, L., et al., *Graphene-based hollow TiO<sub>2</sub> composites with enhanced photocatalytic activity for removal of pollutants*. *Journal of Physics and Chemistry of Solids*, 2015. **86**: p. 82-89.
169. Yan, W., et al., *A novel 3D structured reduced graphene oxide/TiO<sub>2</sub> composite: synthesis and photocatalytic performance*. *Journal of Materials Chemistry A*, 2014. **2**(10): p. 3605-3612.
170. Lee, J.S., K.H. You, and C.B. Park, *Highly Photoactive, Low Bandgap TiO<sub>2</sub> Nanoparticles Wrapped by Graphene*. *Advanced Materials*, 2012. **24**(8): p. 1084-1088.
171. Wang, X., et al., *Synthesis and catalytic performance of hierarchical TiO<sub>2</sub> hollow sphere/reduced graphene oxide hybrid nanostructures*. *Journal of Alloys and Compounds*, 2016. **656**: p. 181-188.
172. Zhang, J., et al., *Graphene encapsulated hollow TiO<sub>2</sub> nanospheres: efficient synthesis and enhanced photocatalytic activity*. *Journal of Materials Chemistry A*, 2013. **1**(11): p. 3752-3756.
173. Nasr, M., et al., *Enhanced Visible-Light Photocatalytic Performance of Electrospun rGO/TiO<sub>2</sub> Composite Nanofibers*. *The Journal of Physical Chemistry C*, 2017. **121**(1): p. 261-269.
174. Lavanya, T., et al., *Superior photocatalytic performance of reduced graphene oxide wrapped electrospun anatase mesoporous TiO<sub>2</sub> nanofibers*. *Journal of Alloys and Compounds*, 2014. **615**(Supplement C): p. 643-650.
175. Lavanya, T., et al., *Superior photocatalytic performance of graphene wrapped anatase/rutile mixed phase TiO<sub>2</sub> nanofibers synthesized by a simple and facile route*. *Journal of Environmental Chemical Engineering*, 2017. **5**(1): p. 494-503.
176. Mohamed, I.M.A., et al., *Synthesis of novel ZrO<sub>2</sub>&GO@TiO<sub>2</sub> nanocomposite as an efficient photoanode in dye-sensitized solar cells*. *Superlattices and Microstructures*, 2017. **102**: p. 235-245.
177. Yin, D., et al., *Preparation and Characterization of ZnO-Graphene Composite Photocatalyst*. *Journal of Nanoscience and Nanotechnology*, 2012. **12**(2): p. 937-942.
178. Chen, Y.-C., et al., *ZnO-graphene composites as practical photocatalysts for gaseous acetaldehyde degradation and electrolytic water oxidation*. *Applied Catalysis A: General*, 2015. **490**: p. 1-9.
179. Arshad, A., et al., *Graphene nanoplatelets induced tailoring in photocatalytic activity and antibacterial characteristics of MgO/graphene nanoplatelets nanocomposites*. *Journal of Applied Physics*, 2017. **121**(2): p. 024901.
180. Jamil, M., et al., *Studies on solution processed Graphene-Nb<sub>2</sub>O<sub>5</sub> nanocomposite based photoanode for dye-sensitized solar cells*. *Journal of Alloys and Compounds*, 2017. **694**: p. 401-407.
181. Wang, C., et al., *Graphene/SrTiO<sub>3</sub> nanocomposites used as an effective electron-transporting layer for high-performance perovskite solar cells*. *RSC Advances*, 2015. **5**(64): p. 52041-52047.
182. Dong, S., et al., *ZnSnO<sub>3</sub> hollow nanospheres/reduced graphene oxide nanocomposites as high-performance photocatalysts for degradation of metronidazole*. *Applied Catalysis B: Environmental*, 2014. **144**: p. 386-393.
183. Sheng, J.L., et al., *Synthesis and Photocatalytic Activity of Ultrafine SrNb<sub>6</sub>O<sub>16</sub> Nanoparticles Supported on Graphene Oxide Nanosheets*. *Science of Advanced Materials*, 2015. **7**(7): p. 1331-1340.
184. Ren, Z., et al., *Revisiting the construction of graphene-CdS nanocomposites as efficient visible-light-driven photocatalysts for selective organic transformation*. *Journal of Materials Chemistry A*, 2014. **2**(15): p. 5330-5339.
185. Zhang, Y., et al., *Graphene Transforms Wide Band Gap ZnS to a Visible Light Photocatalyst. The New Role of Graphene as a Macromolecular Photosensitizer*. *ACS Nano*, 2012. **6**(11): p. 9777-9789.
186. Liu, S., et al., *Nanocomposites of graphene-CdS as photoactive and reusable catalysts for visible-light-induced selective reduction process*. *Journal of Energy Chemistry*, 2014. **23**(2): p. 145-155.

187. Shen, J., et al., *Growth of NiS/graphene nanocomposites for enhanced performance of dye sensitized solar cells*. Journal of Solid State Electrochemistry, 2015. **19**(4): p. 1045-1052.
188. Duan, X., et al., *CoS<sub>2</sub>-graphene composite as efficient catalytic counter electrode for dye-sensitized solar cell*. Electrochimica Acta, 2013. **114**: p. 173-179.
189. Yuan, H., et al., *Sandwich-like octahedral cobalt disulfide/reduced graphene oxide as an efficient Pt-free electrocatalyst for high-performance dye-sensitized solar cells*. Carbon, 2017. **119**: p. 225-234.
190. Zhao, Y., et al., *The synthesis of hierarchical nanostructured MoS<sub>2</sub>/Graphene composites with enhanced visible-light photo-degradation property*. Applied Surface Science, 2017. **412**: p. 207-213.
191. Lin, J.-Y., C.-Y. Chan, and S.-W. Chou, *Electrophoretic deposition of transparent MoS<sub>2</sub>-graphene nanosheet composite films as counter electrodes in dye-sensitized solar cells*. Chemical Communications, 2013. **49**(14): p. 1440-1442.
192. Chen, X., et al., *Efficient dye-sensitized solar cells with CoSe/graphene composite counter electrodes*. Solar Energy, 2017. **144**: p. 342-348.
193. NANAKKAL, A.R. and L.K. ALEXANDER, *Photocatalytic Activity of Graphene/ZnO Nanocomposite Fabricated by Two-step Electrochemical Route*. Journal of Chemical Sciences, 2017. **129**(1): p. 95-102.
194. Hu, H., et al., *Layered CoS/graphene nanocomposite as high catalytic counter electrodes for quantum dot-sensitized solar cells*. Materials Letters, 2014. **114**: p. 7-10.
195. Khalili, S.S., H. Dehghani, and M. Afrooz, *Composite films of metal doped CoS/carbon allotropes; efficient electrocatalyst counter electrodes for high performance quantum dot-sensitized solar cells*. Journal of Colloid and Interface Science, 2017. **493**: p. 32-41.
196. Low, F.W., C.W. Lai, and S.B. Abd Hamid, *Surface modification of reduced graphene oxide film by Ti ion implantation technique for high dye-sensitized solar cells performance*. Ceramics International, 2017. **43**(1): p. 625-633.
197. Bajpai, R., et al., *NiO nanoparticles deposited on graphene platelets as a cost-effective counter electrode in a dye sensitized solar cell*. Carbon, 2013. **56**(Supplement C): p. 56-63.
198. Dao, V.-D., et al., *Graphene-NiO nanohybrid prepared by dry plasma reduction as a low-cost counter electrode material for dye-sensitized solar cells*. Nanoscale, 2014. **6**(1): p. 477-482.
199. Biris, A.R., et al., *Synthesis of tunable core-shell nanostructures based on TiO<sub>2</sub>-graphene architectures and their application in the photodegradation of rhodamine dyes*. Physica E: Low-dimensional Systems and Nanostructures, 2016. **81**: p. 326-333.
200. Sun, X., et al., *Atomic Layer Deposition of TiO<sub>2</sub> on Graphene for Supercapacitors*. Journal of The Electrochemical Society, 2012. **159**(4): p. A364-A369.
201. Li, M., et al., *Atomic layer deposition derived amorphous TiO<sub>2</sub> thin film decorating graphene nanosheets with superior rate capability*. Electrochemistry Communications, 2015. **57**(Supplement C): p. 43-47.
202. Vervuurt, R.H.J., et al., *Uniform Atomic Layer Deposition of Al<sub>2</sub>O<sub>3</sub> on Graphene by Reversible Hydrogen Plasma Functionalization*. Chemistry of Materials, 2017. **29**(5): p. 2090-2100.
203. Chunmei, B., et al., *Atomic layer deposition of amorphous TiO<sub>2</sub> on graphene as an anode for Li-ion batteries*. Nanotechnology, 2013. **24**(42): p. 424002.
204. Cong, H.-P., et al., *Macroscopic Multifunctional Graphene-Based Hydrogels and Aerogels by a Metal Ion Induced Self-Assembly Process*. ACS Nano, 2012. **6**(3): p. 2693-2703.
205. Zhang, Z., et al., *One-Pot Self-Assembled Three-Dimensional TiO<sub>2</sub>-Graphene Hydrogel with Improved Adsorption Capacities and Photocatalytic and Electrochemical Activities*. ACS Applied Materials & Interfaces, 2013. **5**(6): p. 2227-2233.
206. Zhang, H., et al., *Graphene hydrogel-based counter electrode for high efficiency quantum dot-sensitized solar cells*. Journal of Materials Chemistry A, 2017. **5**(4): p. 1614-1622.

207. Qiu, B., M. Xing, and J. Zhang, *Mesoporous TiO<sub>2</sub> Nanocrystals Grown in Situ on Graphene Aerogels for High Photocatalysis and Lithium-Ion Batteries*. *Journal of the American Chemical Society*, 2014. **136**(16): p. 5852-5855.
208. Zhu, Y., et al., *3D Graphene Frameworks with Uniformly Dispersed CuS as an Efficient Catalytic Electrode for Quantum Dot-Sensitized Solar Cells*. *Electrochimica Acta*, 2016. **208**: p. 288-295.
209. Park, J., et al., *Three-Dimensional Graphene–TiO<sub>2</sub> Nanocomposite Photocatalyst Synthesized by Covalent Attachment*. *ACS Omega*, 2016. **1**(3): p. 351-356.
210. Zhi, J., et al., *Efficient highly flexible dye sensitized solar cells of three dimensional graphene decorated titanium dioxide nanoparticles on plastic substrate*. *Journal of Power Sources*, 2015. **281**(Supplement C): p. 404-410.
211. Kim, H.-N., H. Yoo, and J.H. Moon, *Graphene-embedded 3D TiO<sub>2</sub> inverse opal electrodes for highly efficient dye-sensitized solar cells: morphological characteristics and photocurrent enhancement*. *Nanoscale*, 2013. **5**(10): p. 4200-4204.
212. Kuang, L. and W. Zhang, *Enhanced hydrogen production by carbon-doped TiO<sub>2</sub> decorated with reduced graphene oxide (rGO) under visible light irradiation*. *RSC Advances*, 2016. **6**(3): p. 2479-2488.
213. Pei, F., et al., *Nanocomposite of graphene oxide with nitrogen-doped TiO<sub>2</sub> exhibiting enhanced photocatalytic efficiency for hydrogen evolution*. *International Journal of Hydrogen Energy*, 2013. **38**(6): p. 2670-2677.
214. Bhirud, A., et al., *In situ preparation of N-ZnO/graphene nanocomposites: excellent candidate as a photocatalyst for enhanced solar hydrogen generation and high performance supercapacitor electrode*. *Journal of Materials Chemistry A*, 2015. **3**(33): p. 17050-17063.
215. Ranganathan, P., et al., *Enhanced photovoltaic performance of dye-sensitized solar cells based on nickel oxide supported on nitrogen-doped graphene nanocomposite as a photoanode*. *Journal of Colloid and Interface Science*, 2017. **504**: p. 570-578.
216. Bi, E., et al., *A quasi core-shell nitrogen-doped graphene/cobalt sulfide conductive catalyst for highly efficient dye-sensitized solar cells*. *Energy & Environmental Science*, 2014. **7**(8): p. 2637-2641.
217. Mohamed, I.M.A., et al., *Design of an efficient photoanode for dye-sensitized solar cells using electrospun one-dimensional GO/N-doped nanocomposite SnO<sub>2</sub>/TiO<sub>2</sub>*. *Applied Surface Science*, 2017. **400**: p. 355-364.
218. Yin, X., et al., *Simultaneous N-doping of reduced graphene oxide and TiO<sub>2</sub> in the composite for visible light photodegradation of methylene blue with enhanced performance*. *RSC Advances*, 2013. **3**(40): p. 18474-18481.
219. Li, X., et al., *(Ga<sub>1-x</sub>Zn<sub>x</sub>)(N<sub>1-x</sub>O<sub>x</sub>)–rGO composites with enhanced photocatalytic performance for visible-light driven water splitting*. *Applied Surface Science*, 2015. **358**: p. 57-62.
220. Agegnehu, A.K., et al., *Visible light responsive noble metal-free nanocomposite of V-doped TiO<sub>2</sub> nanorod with highly reduced graphene oxide for enhanced solar H<sub>2</sub> production*. *International Journal of Hydrogen Energy*, 2016. **41**(16): p. 6752-6762.
221. Hasan, M.R., et al., *Effect of Ce Doping on RGO–TiO<sub>2</sub> Nanocomposite for High Photoelectrocatalytic Behavior*. *International Journal of Photoenergy*, 2014. **2014**: p. 8.
222. Jin, Z., et al., *Fabrication of efficient visible light activated Cu–P25–graphene ternary composite for photocatalytic degradation of methyl blue*. *Applied Surface Science*, 2015. **356**: p. 707-718.
223. Jang, H., et al., *Dual-Wavelength Irradiation and Dox Delivery for Cancer Cell Ablation with Photocatalytic Pr Doped TiO<sub>2</sub>/NGO Hybrid Nanocomposite*. *Advanced Healthcare Materials*, 2015. **4**(12): p. 1833-1840.
224. Qiu, B., et al., *Facile synthesis of the Ti<sup>3+</sup> self-doped TiO<sub>2</sub>-graphene nanosheet composites with enhanced photocatalysis*. 2015. **5**: p. 8591.

225. Agarwal, R., et al., *Plasmon Enhanced Photovoltaic Performance in TiO<sub>2</sub>-Graphene Oxide Composite Based Dye-Sensitized Solar Cells*. *Ecs Journal of Solid State Science and Technology*, 2015. **4**(9): p. M64-M68.
226. Chang, X., et al., *Efficient synthesis of sunlight-driven ZnO-based heterogeneous photocatalysts*. *Materials & Design*, 2016. **98**: p. 324-332.
227. He, W., et al., *Photocatalytic and antibacterial properties of Au-TiO<sub>2</sub> nanocomposite on monolayer graphene: From experiment to theory*. *Journal of Applied Physics*, 2013. **114**(20): p. 204701.
228. Wang, P., et al., *The fundamental role and mechanism of reduced graphene oxide in rGO/Pt-TiO<sub>2</sub> nanocomposite for high-performance photocatalytic water splitting*. *Applied Catalysis B: Environmental*, 2017. **207**: p. 335-346.
229. Zhang, J., et al., *Self-assembly of a Ag nanoparticle-modified and graphene-wrapped TiO<sub>2</sub> nanobelt ternary heterostructure: surface charge tuning toward efficient photocatalysis*. *Nanoscale*, 2014. **6**(19): p. 11293-11302.
230. Ghavami, M., et al., *Visible light photocatalytic activity of reduced graphene oxide synergistically enhanced by successive inclusion of  $\gamma$ -Fe<sub>2</sub>O<sub>3</sub>, TiO<sub>2</sub>, and Ag nanoparticles*. *Materials Science in Semiconductor Processing*, 2014. **26**: p. 69-78.
231. Surendran, D.K., et al., *Synthesis of a ternary Ag/RGO/ZnO nanocomposite via microwave irradiation and its application for the degradation of Rhodamine B under visible light*. *Environmental Science and Pollution Research*, 2017. **24**(18): p. 15360-15368.
232. Panigrahy, B. and D.D. Sarma, *Enhanced photocatalytic efficiency of AuPd nanoalloy decorated ZnO-reduced graphene oxide nanocomposites*. *RSC Advances*, 2015. **5**(12): p. 8918-8928.
233. Benedetti, J.E., et al., *Synthesis and characterization of a quaternary nanocomposite based on TiO<sub>2</sub>/CdS/rGO/Pt and its application in the photoreduction of CO<sub>2</sub> to methane under visible light*. *RSC Advances*, 2015. **5**(43): p. 33914-33922.
234. Granbohm, H., et al., *Preparation and Photocatalytic Activity of Quaternary GO/TiO<sub>2</sub>/Ag/AgCl Nanocomposites*. *Water, Air, & Soil Pollution*, 2017. **228**(4): p. 127.
235. Granbohm, H., et al., *Effect of graphene oxide loading in GO/SiO<sub>2</sub>/Ag/AgCl photocatalyst*. *International Journal of Nanotechnology*, 2017. **14**(1-6): p. 87-99.
236. Datcu, A., et al., *One-step preparation of nitrogen doped titanium oxide/Au/reduced graphene oxide composite thin films for photocatalytic applications*. *RSC Advances*, 2015. **5**(61): p. 49771-49779.
237. György, E., et al., *Titanium oxide – reduced graphene oxide – silver composite layers synthesized by laser technique: Wetting and electrical properties*. *Ceramics International*, 2016. **42**(14): p. 16191-16197.
238. Wang, Y., et al., *Reduced graphene oxide-based photocatalysts containing Ag nanoparticles on a TiO<sub>2</sub> nanotube array*. *Journal of Materials Science*, 2013. **48**(18): p. 6203-6211.
239. Benjwal, P., et al., *Enhanced photocatalytic degradation of methylene blue and adsorption of arsenic(iii) by reduced graphene oxide (rGO)-metal oxide (TiO<sub>2</sub>/Fe<sub>3</sub>O<sub>4</sub>) based nanocomposites*. *RSC Advances*, 2015. **5**(89): p. 73249-73260.
240. Jiang, Y., et al., *Facile Aerosol Synthesis and Characterization of Ternary Crumpled Graphene–TiO<sub>2</sub>–Magnetite Nanocomposites for Advanced Water Treatment*. *ACS Applied Materials & Interfaces*, 2014. **6**(14): p. 11766-11774.
241. Chen, F., et al., *Fabrication of Fe<sub>3</sub>O<sub>4</sub>@SiO<sub>2</sub>@TiO<sub>2</sub> nanoparticles supported by graphene oxide sheets for the repeated adsorption and photocatalytic degradation of rhodamine B under UV irradiation*. *Dalton Transactions*, 2014. **43**(36): p. 13537-13544.
242. Feng, J., et al., *Hierarchical structured ZnFe<sub>2</sub>O<sub>4</sub>@RGO@TiO<sub>2</sub> composite as powerful visible light catalyst for degradation of fulvic acid*. *Journal of Nanoparticle Research*, 2017. **19**(5): p. 178.
243. Sadiq, M.M.J., U.S. Shenoy, and D.K. Bhat, *Novel RGO-ZnWO<sub>4</sub>-Fe<sub>3</sub>O<sub>4</sub> nanocomposite as high performance visible light photocatalyst*. *RSC Advances*, 2016. **6**(66): p. 61821-61829.

244. Nanakkal, A.R. and L.K. Alexander, *Graphene/BiVO<sub>4</sub>/TiO<sub>2</sub> nanocomposite: tuning band gap energies for superior photocatalytic activity under visible light*. Journal of Materials Science, 2017. **52**(13): p. 7997-8006.
245. Yousefzadeh, S., M. Faraji, and A.Z. Moshfegh, *Constructing BiVO<sub>4</sub>/Graphene/TiO<sub>2</sub> nanocomposite photoanode for photoelectrochemical conversion applications*. Journal of Electroanalytical Chemistry, 2016. **763**: p. 1-9.
246. Yuan, X., et al., *A novel SnS<sub>2</sub>-MgFe<sub>2</sub>O<sub>4</sub>/reduced graphene oxide flower-like photocatalyst: Solvothermal synthesis, characterization and improved visible-light photocatalytic activity*. Catalysis Communications, 2015. **61**(Supplement C): p. 62-66.
247. Zhang, W., et al., *Enhanced photocatalytic activity of TiO<sub>2</sub> nanoparticles using SnS<sub>2</sub>/RGO hybrid as co-catalyst: DFT study and photocatalytic mechanism*. Journal of Alloys and Compounds, 2016. **685**: p. 774-783.
248. Pant, B., et al., *One-pot synthesis of CdS sensitized TiO<sub>2</sub> decorated reduced graphene oxide nanosheets for the hydrolysis of ammonia-borane and the effective removal of organic pollutant from water*. Ceramics International, 2016. **42**(14): p. 15247-15252.
249. Dutta, S., et al., *Biomolecule-mediated CdS-TiO<sub>2</sub>-reduced graphene oxide ternary nanocomposites for efficient visible light-driven photocatalysis*. Dalton Transactions, 2015. **44**(1): p. 193-201.
250. Reddy, D.A., et al., *Hierarchical dandelion-flower-like cobalt-phosphide modified CdS/reduced graphene oxide-MoS<sub>2</sub> nanocomposites as a noble-metal-free catalyst for efficient hydrogen evolution from water*. Catalysis Science & Technology, 2016. **6**(16): p. 6197-6206.
251. Islam, M.J., et al., *Reduced-graphene-oxide-wrapped BiOI-AgI heterostructured nanocomposite as a high-performance photocatalyst for dye degradation under solar light irradiation*. Solid State Sciences, 2016. **61**: p. 32-39.
252. Dai, K., et al., *A high efficient graphitic-C<sub>3</sub>N<sub>4</sub>/BiOI/graphene oxide ternary nanocomposite heterostructured photocatalyst with graphene oxide as electron transport buffer material*. Dalton Transactions, 2015. **44**(17): p. 7903-7910.
253. Pawar, R.C., V. Khare, and C.S. Lee, *Hybrid photocatalysts using graphitic carbon nitride/cadmium sulfide/reduced graphene oxide (g-C<sub>3</sub>N<sub>4</sub>/CdS/RGO) for superior photodegradation of organic pollutants under UV and visible light*. Dalton Transactions, 2014. **43**(33): p. 12514-12527.
254. Li, H., et al., *Constructing ternary CdS/reduced graphene oxide/TiO<sub>2</sub> nanotube arrays hybrids for enhanced visible-light-driven photoelectrochemical and photocatalytic activity*. Applied Catalysis B: Environmental, 2015. **168**: p. 105-113.
255. Samadpour, M. and S. Arabzade, *Graphene/CuS/PbS nanocomposite as an effective counter electrode for quantum dot sensitized solar cells*. Journal of Alloys and Compounds, 2017. **696**: p. 369-375.
256. Song, Y.-T., L.-Y. Lin, and J.-Y. Hong, *Enhanced Visible-light Response and Conductivity of the TiO<sub>2</sub>/reduced graphene oxide/Sb<sub>2</sub>S<sub>3</sub> Heterojunction for Photoelectrochemical Water Oxidation*. Electrochimica Acta, 2016. **211**: p. 576-585.
257. Yang, W., et al., *Solvothermal fabrication of activated semi-coke supported TiO<sub>2</sub>-rGO nanocomposite photocatalysts and application for NO removal under visible light*. Applied Surface Science, 2015. **353**: p. 307-316.
258. Qu, L.-L., et al., *Novel titanium dioxide-graphene-activated carbon ternary nanocomposites with enhanced photocatalytic performance in rhodamine B and tetracycline hydrochloride degradation*. Journal of Materials Science, 2017. **52**(13): p. 8311-8320.
259. Wang, C., et al., *Preparation of graphene-carbon nanotube-TiO<sub>2</sub> composites with enhanced photocatalytic activity for the removal of dye and Cr (VI)*. Applied Catalysis A: General, 2014. **473**: p. 83-89.
260. Dong, Y., D. Tang, and C. Li, *Photocatalytic oxidation of methyl orange in water phase by immobilized TiO<sub>2</sub>-carbon nanotube nanocomposite photocatalyst*. Applied Surface Science, 2014. **296**: p. 1-7.

261. Youn, D.H., et al., *TiN Nanoparticles on CNT–Graphene Hybrid Support as Noble-Metal-Free Counter Electrode for Quantum-Dot-Sensitized Solar Cells*. *ChemSusChem*, 2013. **6**(2): p. 261-267.
262. Seol, M., et al., *Mo-Compound/CNT-Graphene Composites as Efficient Catalytic Electrodes for Quantum-Dot-Sensitized Solar Cells*. *Advanced Energy Materials*, 2014. **4**(4): p. 1300775-n/a.
263. Kumar, R., et al., *Facile route to a conducting ternary polyaniline@TiO<sub>2</sub>/GN nanocomposite for environmentally benign applications: photocatalytic degradation of pollutants and biological activity*. *RSC Advances*, 2016. **6**(112): p. 111308-111317.
264. Feng, J., et al., *In-depth study on adsorption and photocatalytic performance of novel reduced graphene oxide-ZnFe<sub>2</sub>O<sub>4</sub>-polyaniline composites*. *Journal of Alloys and Compounds*, 2016. **681**: p. 157-166.
265. Zargari, S., R. Rahimi, and A. Yousefi, *An efficient visible light photocatalyst based on tin porphyrin intercalated between TiO<sub>2</sub>-graphene nanosheets for inactivation of E. coli and investigation of charge transfer mechanism*. *RSC Advances*, 2016. **6**(29): p. 24218-24228.
266. Sharavath, V., et al., *Low Temperature Synthesis of TiO<sub>2</sub>-β-Cyclodextrin–Graphene Nanocomposite for Energy Storage and Photocatalytic Applications*. *Electrochimica Acta*, 2016. **210**: p. 385-394.
267. Wang, W., et al., *Graphene supported βNaYF<sub>4</sub>:Yb<sup>3+</sup>,Tm<sup>3+</sup> and N doped P25 nanocomposite as an advanced NIR and sunlight driven upconversion photocatalyst*. *Applied Surface Science*, 2013. **282**: p. 832-837.
268. Yin, D., et al., *Greatly enhanced photocatalytic activity of semiconductor CeO<sub>2</sub> by integrating with upconversion nanocrystals and graphene*. *RSC Advances*, 2016. **6**(105): p. 103795-103802.
269. Yao, N., et al., *Improving the photovoltaic performance of dye sensitized solar cells based on a hierarchical structure with up/down converters*. *RSC Advances*, 2016. **6**(14): p. 11880-11887.
270. Huang, J., et al., *Developing titania-hydroxyapatite-reduced graphene oxide nanocomposite coatings by liquid flame spray deposition for photocatalytic applications*. *Journal of the European Ceramic Society*, 2017. **37**(12): p. 3705-3711.
271. Shan, C.-H., et al., *Pure inorganic D-A type polyoxometalate/reduced graphene oxide nanocomposite for the photoanode of dye-sensitized solar cells*. *Journal of Materials Chemistry A*, 2016. **4**(9): p. 3297-3303.
272. Oh, W.-C., F.-J. Zhang, and M.-L. Chen, *Synthesis and characterization of V–C<sub>60</sub>/TiO<sub>2</sub> photocatalysts designed for degradation of methylene blue*. *Journal of Industrial and Engineering Chemistry*, 2010. **16**(2): p. 299-304.
273. Meng, Z.-D., et al., *Effect of Pt treated fullerene/TiO<sub>2</sub> on the photocatalytic degradation of MO under visible light*. *Journal of Materials Chemistry*, 2011. **21**(21): p. 7596-7603.
274. Meng, Z.-D., et al., *Preparation, characterization and photocatalytic behavior of WO<sub>3</sub>-fullerene/TiO<sub>2</sub> catalysts under visible light*. *Nanoscale Research Letters*, 2011. **6**(1): p. 459.
275. Meng, Z.-D., et al., *Fullerene modification CdSe/TiO<sub>2</sub> and modification of photocatalytic activity under visible light*. *Nanoscale Research Letters*, 2013. **8**(1): p. 189.
276. Meng, Z.D., et al., *Rare earth oxide doped fullerene and titania composites and photocatalytic properties of methylene blue under visible light*. *Asian J Chem*, 2011. **23**.
277. Meng, Z.-D. and W.-C. Oh, *Sonocatalytic degradation and catalytic activities for MB solution of Fe treated fullerene/TiO<sub>2</sub> composite with different ultrasonic intensity*. *Ultrasonics Sonochemistry*, 2011. **18**(3): p. 757-764.
278. Shi, X. and Z. Zhu, *Synthesis and characterization of W-doped TiO<sub>2</sub> supported by hybrid carbon nanomaterials of multi-walled carbon nanotubes and C<sub>60</sub> fullerene by a hydrothermal method*. *Journal of Wuhan University of Technology-Mater. Sci. Ed.*, 2013. **28**(2): p. 207-214.
279. Ouyang, K., et al., *Efficient Photocatalytic Disinfection of Escherichia coli O157:H7 using C<sub>70</sub>-TiO<sub>2</sub> Hybrid under Visible Light Irradiation*. *Scientific Reports* 2016. **6**: p. 25702.

280. Yu, J., et al., *Enhanced photocatalytic activity of bimodal mesoporous titania powders by C60 modification*. Dalton Transactions, 2011. **40**(25): p. 6635-6644.
281. Shi, X., et al., *Photocatalytic degradation of rhodamine B dye with MWCNT/TiO<sub>2</sub>/C60 composites by a hydrothermal method*. Journal of Wuhan University of Technology-Mater. Sci. Ed., 2011. **26**(1): p. 65-69.
282. Meng, Z.-D., et al., *Synthesis and characterization of M-fullerene/TiO<sub>2</sub> photocatalysts designed for degradation azo dye*. Materials Science and Engineering: C, 2012. **32**(8): p. 2175-2182.
283. Meng, Z.D. and W.C. Oh, *Photocatalytic degradation of methylene blue on Fe-fullerene/TiO<sub>2</sub> under visible-light irradiation*. Asian J Chem, 2011. **23**.
284. Navgire, M.E. and M.K. Lande, *Effect of nanocrystalline composite fullerene-doped MoO<sub>3</sub>-TiO<sub>2</sub> material on photoassisted degradation of Alizarin red S dye*. Inorganic and Nano-Metal Chemistry, 2017. **47**(3): p. 320-327.
285. Qi, K., et al., *Enhanced photocatalytic activity of anatase-TiO<sub>2</sub> nanoparticles by fullerene modification: A theoretical and experimental study*. Applied Surface Science, 2016. **387**(Supplement C): p. 750-758.
286. Yang, M.-Q., N. Zhang, and Y.-J. Xu, *Synthesis of Fullerene-, Carbon Nanotube-, and Graphene-TiO<sub>2</sub> Nanocomposite Photocatalysts for Selective Oxidation: A Comparative Study*. ACS Applied Materials & Interfaces, 2013. **5**(3): p. 1156-1164.
287. Chai, B., et al., *Synthesis of C60-decorated SWCNTs (C60-d-CNTs) and its TiO<sub>2</sub>-based nanocomposite with enhanced photocatalytic activity for hydrogen production*. Dalton Transactions, 2013. **42**(10): p. 3402-3409.
288. Wang, S., et al., *Fullerene C70-TiO<sub>2</sub> hybrids with enhanced photocatalytic activity under visible light irradiation*. Journal of Materials Chemistry A, 2015. **3**(42): p. 21090-21098.
289. Meng, Z.-D., et al., *Study of the photochemically generated of oxygen species by fullerene photosensitized CoS<sub>2</sub> nanocompounds*. Materials Research Bulletin, 2014. **49**(Supplement C): p. 272-278.
290. Zhao, X., et al., *Photocatalytic reduction of bromate at C60 modified Bi<sub>2</sub>MoO<sub>6</sub> under visible light irradiation*. Applied Catalysis B: Environmental, 2011. **106**(1): p. 63-68.
291. Dai, K., et al., *Enhancing the photocatalytic activity of lead molybdate by modifying with fullerene*. Journal of Molecular Catalysis A: Chemical, 2013. **374**(Supplement C): p. 111-117.
292. Cho, E.-C., et al., *Fullerene C70 decorated TiO<sub>2</sub> nanowires for visible-light-responsive photocatalyst*. Applied Surface Science, 2015. **355**(Supplement C): p. 536-546.
293. Lee, J., et al., *Photosensitized Oxidation of Emerging Organic Pollutants by Tetrakis C60 Aminofullerene-Derivatized Silica under Visible Light Irradiation*. Environmental Science & Technology, 2011. **45**(24): p. 10598-10604.
294. Moor, K.J. and J.-H. Kim, *Simple Synthetic Method Toward Solid Supported C60 Visible Light-Activated Photocatalysts*. Environmental Science & Technology, 2014. **48**(5): p. 2785-2791.
295. Lian, Z., et al., *C60-Decorated CdS/TiO<sub>2</sub> Mesoporous Architectures with Enhanced Photostability and Photocatalytic Activity for H<sub>2</sub> Evolution*. ACS Applied Materials & Interfaces, 2015. **7**(8): p. 4533-4540.
296. Justh, N., et al., *Photocatalytic C60-amorphous TiO<sub>2</sub> composites prepared by atomic layer deposition*. Applied Surface Science, 2017. **419**(Supplement C): p. 497-502.
297. Lu, C., et al., *C60 on Nanostructured Nb-Doped SrTiO<sub>3</sub>(001) Surfaces*. The Journal of Physical Chemistry C, 2010. **114**(8): p. 3416-3421.
298. Lin, J., et al., *Photoelectric catalytic degradation of methylene blue by C60-modified TiO<sub>2</sub> nanotube array*. Applied Catalysis B: Environmental, 2009. **89**(3): p. 425-431.
299. Zheng, X.T., et al., *Glowing Graphene Quantum Dots and Carbon Dots: Properties, Syntheses, and Biological Applications*. Small, 2015. **11**(14): p. 1620-1636.

300. Wang, R., et al., *Recent progress in carbon quantum dots: synthesis, properties and applications in photocatalysis*. Journal of Materials Chemistry A, 2017. **5**(8): p. 3717-3734.
301. Wang, Y. and A. Hu, *Carbon quantum dots: synthesis, properties and applications*. Journal of Materials Chemistry C, 2014. **2**(34): p. 6921-6939.
302. Fernando, K.A.S., et al., *Carbon Quantum Dots and Applications in Photocatalytic Energy Conversion*. ACS Applied Materials & Interfaces, 2015. **7**(16): p. 8363-8376.
303. De, B. and N. Karak, *Recent progress in carbon dot-metal based nanohybrids for photochemical and electrochemical applications*. Journal of Materials Chemistry A, 2017. **5**(5): p. 1826-1859.
304. Li, H., et al., *Water-Soluble Fluorescent Carbon Quantum Dots and Photocatalyst Design*. Angewandte Chemie International Edition, 2010. **49**(26): p. 4430-4434.
305. Zhang, H., et al., *Fe<sub>2</sub>O<sub>3</sub>/carbon quantum dots complex photocatalysts and their enhanced photocatalytic activity under visible light*. Dalton Transactions, 2011. **40**(41): p. 10822-10825.
306. Zhang, H., et al., *Carbon quantum dots/Ag<sub>3</sub>PO<sub>4</sub> complex photocatalysts with enhanced photocatalytic activity and stability under visible light*. Journal of Materials Chemistry, 2012. **22**(21): p. 10501-10506.
307. Tang, D., et al., *Carbon quantum dots enhance the photocatalytic performance of BiVO<sub>4</sub> with different exposed facets*. Dalton Transactions, 2013. **42**(18): p. 6285-6289.
308. Sun, M., et al., *A nanocomposite of carbon quantum dots and TiO<sub>2</sub> nanotube arrays: enhancing photoelectrochemical and photocatalytic properties*. RSC Advances, 2014. **4**(3): p. 1120-1127.
309. Yu, H., et al., *Carbon quantum dots/TiO<sub>2</sub> composites for efficient photocatalytic hydrogen evolution*. Journal of Materials Chemistry A, 2014. **2**(10): p. 3344-3351.
310. Qian, X., et al., *Carbon quantum dots decorated Bi<sub>2</sub>WO<sub>6</sub> nanocomposite with enhanced photocatalytic oxidation activity for VOCs*. Applied Catalysis B: Environmental, 2016. **193**: p. 16-21.
311. Muthulingam, S., I.-H. Lee, and P. Uthirakumar, *Highly efficient degradation of dyes by carbon quantum dots/N-doped zinc oxide (CQD/N-ZnO) photocatalyst and its compatibility on three different commercial dyes under daylight*. Journal of Colloid and Interface Science, 2015. **455**: p. 101-109.
312. Muthulingam, S., et al., *Carbon quantum dots decorated N-doped ZnO: Synthesis and enhanced photocatalytic activity on UV, visible and daylight sources with suppressed photocorrosion*. Journal of Environmental Chemical Engineering, 2016. **4**(1): p. 1148-1155.
313. Dutta, M., et al., *ZnO/Graphene Quantum Dot Solid-State Solar Cell*. The Journal of Physical Chemistry C, 2012. **116**(38): p. 20127-20131.
314. Zhang, Y., et al., *Graphene oxide quantum dot-sensitized porous titanium dioxide microsphere: Visible-light-driven photocatalyst based on energy band engineering*. Journal of Colloid and Interface Science, 2017. **498**: p. 105-111.
315. Li, H., et al., *Carbon quantum dots/Cu<sub>2</sub>O composites with protruding nanostructures and their highly efficient (near) infrared photocatalytic behavior*. Journal of Materials Chemistry, 2012. **22**(34): p. 17470-17475.
316. Tian, J., et al., *Carbon quantum dots/hydrogenated TiO<sub>2</sub> nanobelt heterostructures and their broad spectrum photocatalytic properties under UV, visible, and near-infrared irradiation*. Nano Energy, 2015. **11**: p. 419-427.
317. Mirtchev, P., et al., *Solution phase synthesis of carbon quantum dots as sensitizers for nanocrystalline TiO<sub>2</sub> solar cells*. Journal of Materials Chemistry, 2012. **22**(4): p. 1265-1269.
318. Chai, N.-N., et al., *Well-controlled layer-by-layer assembly of carbon dot/CdS heterojunctions for efficient visible-light-driven photocatalysis*. Journal of Materials Chemistry A, 2015. **3**(32): p. 16613-16620.
319. Wang, H., et al., *Nitrogen-Doped Carbon Dots for "green" Quantum Dot Solar Cells*. Nanoscale Research Letters, 2016. **11**: p. 27.

320. Martins, N.C.T., et al., *N-doped carbon quantum dots/TiO<sub>2</sub> composite with improved photocatalytic activity*. Applied Catalysis B: Environmental, 2016. **193**: p. 67-74.
321. Mihalache, I., et al., *Charge and energy transfer interplay in hybrid sensitized solar cells mediated by graphene quantum dots*. Electrochimica Acta, 2015. **153**: p. 306-315.
322. Wang, J., M. Gao, and G.W. Ho, *Bidentate-complex-derived TiO<sub>2</sub>/carbon dot photocatalysts: in situ synthesis, versatile heterostructures, and enhanced H<sub>2</sub> evolution*. Journal of Materials Chemistry A, 2014. **2**(16): p. 5703-5709.
323. Kaur, S., S. Sharma, and S.K. Kansal, *Synthesis of ZnS/CQDs nanocomposite and its application as a photocatalyst for the degradation of an anionic dye*, ARS. Superlattices and Microstructures, 2016. **98**: p. 86-95.
324. Hazarika, D. and N. Karak, *Photocatalytic degradation of organic contaminants under solar light using carbon dot/titanium dioxide nanohybrid, obtained through a facile approach*. Applied Surface Science, 2016. **376**: p. 276-285.
325. Ming, F., et al., *Dandelion-like ZnS/carbon quantum dots hybrid materials with enhanced photocatalytic activity toward organic pollutants*. RSC Advances, 2016. **6**(37): p. 31551-31558.
326. Yan, F., et al., *Construction of carbon nanodots/tungsten trioxide and their visible-light sensitive photocatalytic activity*. Journal of Colloid and Interface Science, 2016. **466**: p. 268-274.
327. Xie, H., et al., *S, N Co-Doped Graphene Quantum Dot/TiO<sub>2</sub>(2) Composites for Efficient Photocatalytic Hydrogen Generation*. Nanoscale Research Letters, 2017. **12**: p. 400.
328. Briscoe, J., et al., *Biomass-Derived Carbon Quantum Dot Sensitizers for Solid-State Nanostructured Solar Cells*. Angewandte Chemie International Edition, 2015. **54**(15): p. 4463-4468.
329. Marinovic, A., et al., *Carbon-Nanodot Solar Cells from Renewable Precursors*. ChemSusChem, 2017. **10**(5): p. 1004-1013.
330. Zhang, H., et al., *A fluorescent quenching performance enhancing principle for carbon nanodot-sensitized aqueous solar cells*. Nano Energy, 2015. **13**: p. 124-130.
331. De, B., B. Voit, and N. Karak, *Carbon dot reduced Cu<sub>2</sub>O nanohybrid/hyperbranched epoxy nanocomposite: mechanical, thermal and photocatalytic activity*. RSC Advances, 2014. **4**(102): p. 58453-58459.
332. Shen, Z., et al., *Carbon-Dot/Natural-Dye Sensitizer for TiO<sub>2</sub> Solar Cells Prepared by a One-Step Treatment of Celery Leaf Extract*. ChemPhotoChem, 2017. **1**(10): p. 470-478.
333. Zhang, W.J., et al., *A Nitrogen-Doped Carbon Dot-Sensitized TiO<sub>2</sub> Inverse Opal Film: Preparation, Enhanced Photoelectrochemical and Photocatalytic Performance*. Journal of the Electrochemical Society, 2015. **162**(9): p. H638-H644.
334. Di, J., et al., *The synergistic role of carbon quantum dots for the improved photocatalytic performance of Bi<sub>2</sub>MoO<sub>6</sub>*. Nanoscale, 2015. **7**(26): p. 11433-11443.
335. Zhang, Q., et al., *Improving the Power Conversion Efficiency of Carbon Quantum Dot-Sensitized Solar Cells by Growing the Dots on a TiO<sub>2</sub>(2) Photoanode In Situ*. Nanomaterials, 2017. **7**(6): p. 130.
336. Zheng, H., P. Niu, and Z. Zhao, *Carbon quantum dot sensitized Pt@Bi<sub>2</sub>WO<sub>6</sub>/FTO electrodes for enhanced photoelectro-catalytic activity of methanol oxidation*. RSC Advances, 2017. **7**(43): p. 26943-26951.
337. Zhang, J., et al., *Carbon nanodots/WO<sub>3</sub> nanorods Z-scheme composites: Remarkably enhanced photocatalytic performance under broad spectrum*. Applied Catalysis B: Environmental, 2017. **209**: p. 253-264.
338. Liu, C., et al., *Construction and enhanced photocatalytic activities of a hydrogenated TiO<sub>2</sub> nanobelt coated with CDs/MoS<sub>2</sub> nanosheets*. RSC Advances, 2017. **7**(14): p. 8429-8442.

339. Karimi, M.A., et al., *Synthesis, characterization, and application of MgO/ZnO nanocomposite supported on activated carbon for photocatalytic degradation of methylene blue*. *Research on Chemical Intermediates*, 2015. **41**(9): p. 6157-6168.
340. Yao, Y., et al., *Photoreactive TiO<sub>2</sub>/Carbon Nanotube Composites: Synthesis and Reactivity*. *Environmental Science & Technology*, 2008. **42**(13): p. 4952-4957.
341. Pastrana-Martínez, L.M., et al., *Advanced nanostructured photocatalysts based on reduced graphene oxide–TiO<sub>2</sub> composites for degradation of diphenhydramine pharmaceutical and methyl orange dye*. *Applied Catalysis B: Environmental*, 2012. **123**(Supplement C): p. 241-256.
342. Cruz, M., et al., *Bare TiO<sub>2</sub> and graphene oxide TiO<sub>2</sub> photocatalysts on the degradation of selected pesticides and influence of the water matrix*. *Applied Surface Science*, 2017. **416**(Supplement C): p. 1013-1021.
343. Zhu, Y., et al., *New insights into the relationship between photocatalytic activity and TiO<sub>2</sub>-GR composites*. *RSC Advances*, 2015. **5**(37): p. 29201-29208.
344. Li, H., et al., *A facile one-step hydrothermal synthesis of a B-doped graphene/rod-shaped TiO<sub>2</sub> nanocomposite*. *RSC Advances*, 2014. **4**(72): p. 37992-37997.
345. Shi, J.-W., et al., *One step to synthesize the nanocomposites of graphene nanosheets and N-doped titania nanoplates with exposed {001} facets for enhanced visible-light photocatalytic activity*. *Journal of Nanoparticle Research*, 2015. **17**(5): p. 223.
346. He, L., et al., *Enhanced Visible Activities of  $\alpha$ -Fe<sub>2</sub>O<sub>3</sub> by Coupling N-Doped Graphene and Mechanism Insight*. *ACS Catalysis*, 2014. **4**(3): p. 990-998.
347. Fraelich, M.R. and R.B. Weisman, *Triplet states of fullerene C<sub>60</sub> and C<sub>70</sub> in solution: long intrinsic lifetimes and energy pooling*. *The Journal of Physical Chemistry*, 1993. **97**(43): p. 11145-11147.
348. Zhang, X., et al., *Facile fabrication of titanium dioxide/fullerene nanocomposite and its enhanced visible photocatalytic activity*. *Journal of Colloid and Interface Science*, 2016. **466**(Supplement C): p. 56-61.
349. Katsumata, K.-i., N. Matsushita, and K. Okada, *Preparation of TiO<sub>2</sub>-Fullerene Composites and Their Photocatalytic Activity under Visible Light*. *International Journal of Photoenergy*, 2012. **2012**.
350. Kanchanapip, E., et al., *Degradation of paraquat under visible light over fullerene modified V-TiO<sub>2</sub>*. *Reaction Kinetics, Mechanisms and Catalysis*, 2011. **103**(1): p. 227-237.
351. Mukthar Ali, M. and K.Y. Sandhya, *Visible light responsive titanium dioxide–cyclodextrin–fullerene composite with reduced charge recombination and enhanced photocatalytic activity*. *Carbon*, 2014. **70**(Supplement C): p. 249-257.
352. Fu, H., et al., *Photocorrosion Inhibition and Enhancement of Photocatalytic Activity for ZnO via Hybridization with C<sub>60</sub>*. *Environmental Science & Technology*, 2008. **42**(21): p. 8064-8069.
353. Wakimoto, R., et al., *Decomposition of methyl orange using C<sub>60</sub> fullerene adsorbed on silica gel as a photocatalyst via visible-light induced electron transfer*. *Applied Catalysis B: Environmental*, 2015. **166**(Supplement C): p. 544-550.
354. Meng, Z.-D., et al., *Synthesis of fullerene modified with Ag<sub>2</sub>S with high photocatalytic activity under visible light*. *Journal of Materials Chemistry*, 2012. **22**(31): p. 16127-16135.
355. Zhu, S., et al., *Synergetic Effect of Bi<sub>2</sub>WO<sub>6</sub> Photocatalyst with C<sub>60</sub> and Enhanced Photoactivity under Visible Irradiation*. *Environmental Science & Technology*, 2007. **41**(17): p. 6234-6239.
356. Chai, B., et al., *Fullerene modified C<sub>3</sub>N<sub>4</sub> composites with enhanced photocatalytic activity under visible light irradiation*. *Dalton Transactions*, 2014. **43**(3): p. 982-989.
357. Zhang, Y.-Q., et al., *N-doped carbon quantum dots for TiO<sub>2</sub>-based photocatalysts and dye-sensitized solar cells*. *Nano Energy*, 2013. **2**(5): p. 545-552.
358. Fujishima, A. and K. Honda, *Electrochemical Photolysis of Water at a Semiconductor Electrode*. *Nature*, 1972. **238**(5358): p. 37-38.

359. Bard, A.J., *Design of semiconductor photoelectrochemical systems for solar energy conversion*. The Journal of Physical Chemistry, 1982. **86**(2): p. 172-177.
360. Kudo, A. and Y. Miseki, *Heterogeneous photocatalyst materials for water splitting*. Chemical Society Reviews, 2009. **38**(1): p. 253-278.
361. Babu, V.J., et al., *Review of one-dimensional and two-dimensional nanostructured materials for hydrogen generation*. Physical Chemistry Chemical Physics, 2015. **17**(5): p. 2960-2986.
362. Abe, R., *Recent progress on photocatalytic and photoelectrochemical water splitting under visible light irradiation*. Journal of Photochemistry and Photobiology C: Photochemistry Reviews, 2010. **11**(4): p. 179-209.
363. Luo, C.-Y., et al., *Electronic properties and photoactivity of monolayer MoS<sub>2</sub>/fullerene van der Waals heterostructures*. RSC Advances, 2016. **6**(49): p. 43228-43236.
364. Dhakshinamoorthy, A., et al., *Photocatalytic CO<sub>2</sub> reduction by TiO<sub>2</sub> and related titanium containing solids*. Energy & Environmental Science, 2012. **5**(11): p. 9217-9233.
365. Xie, S., et al., *Photocatalytic and photoelectrocatalytic reduction of CO<sub>2</sub> using heterogeneous catalysts with controlled nanostructures*. Chemical Communications, 2016. **52**(1): p. 35-59.
366. Inoue, T., et al., *Photoelectrocatalytic reduction of carbon dioxide in aqueous suspensions of semiconductor powders*. Nature, 1979. **277**(5698): p. 637-638.
367. Xu, Y.-F., et al., *A CsPbBr<sub>3</sub> Perovskite Quantum Dot/Graphene Oxide Composite for Photocatalytic CO<sub>2</sub> Reduction*. Journal of the American Chemical Society, 2017. **139**(16): p. 5660-5663.
368. Park, S.K., et al., *Preparation of Carbon-Doped TiO<sub>2</sub> and Its Application as a Photoelectrodes in Dye-Sensitized Solar Cells*. Journal of Nanoscience and Nanotechnology, 2015. **15**(2): p. 1529-1532.
369. Lin, A., et al., *Carbon-doped titanium dioxide nanocrystals for highly efficient dye-sensitized solar cells*. Catalysis Today, 2017. **281**(Part 3): p. 636-641.
370. Tabari-Saadi, Y. and M.R. Mohammadi, *Efficient dye-sensitized solar cells based on carbon-doped TiO<sub>2</sub> hollow spheres and nanoparticles*. Journal of Materials Science: Materials in Electronics, 2015. **26**(11): p. 8863-8876.
371. de Moraes, A., et al., *Enhancing in the performance of dye-sensitized solar cells by the incorporation of functionalized multi-walled carbon nanotubes into TiO<sub>2</sub> films: The role of MWCNT addition*. Journal of Photochemistry and Photobiology A: Chemistry, 2013. **251**: p. 78-84.
372. Quaranta, S., et al., *Efficiency improvement and full characterization of dye-sensitized solar cells with MWCNT/anatase Schottky junctions*. Journal of Power Sources, 2012. **204**: p. 249-256.
373. Khamwannah, J., et al., *Nanocomposites of TiO<sub>2</sub> and double-walled carbon nanotubes for improved dye-sensitized solar cells*. Journal of Renewable and Sustainable Energy, 2012. **4**(2): p. 023116.
374. Lee, J., et al., *Flexible photoanodes of TiO<sub>2</sub> particles and metallic single-walled carbon nanotubes for flexible dye-sensitized solar cells*. Carbon, 2014. **79**: p. 337-345.
375. Costa, R.D., et al., *Carbon Nanohorns as Integrative Materials for Efficient Dye-Sensitized Solar Cells*. Advanced Materials, 2013. **25**(45): p. 6513-6518.
376. Azimah, O., et al., *Morphological and electron transport studies in ZnO dye-sensitized solar cells incorporating multi- and single-walled carbon nanotubes*. Journal of Physics D: Applied Physics, 2013. **46**(16): p. 165503.
377. Omar, A., et al., *Characterization of zinc oxide dye-sensitized solar cell incorporation with single-walled carbon nanotubes*. Journal of Materials Research, 2013. **28**(13): p. 1753-1760.
378. Chang, W.-C., et al., *Enhancing performance of ZnO dye-sensitized solar cells by incorporation of multiwalled carbon nanotubes*. Nanoscale Research Letters, 2012. **7**(1): p. 166.
379. Stoller, M.D., et al., *Graphene-Based Ultracapacitors*. Nano Letters, 2008. **8**(10): p. 3498-3502.

380. Bolotin, K.I., et al., *Ultra-high electron mobility in suspended graphene*. Solid State Communications, 2008. **146**(9): p. 351-355.
381. Xiang, Z., et al., *Improving Energy Conversion Efficiency of Dye-Sensitized Solar Cells by Modifying TiO<sub>2</sub> Photoanodes with Nitrogen-Reduced Graphene Oxide*. ACS Sustainable Chemistry & Engineering, 2014. **2**(5): p. 1234-1240.
382. Mehmood, U., et al., *Enhanced Photovoltaic Performance of Dye-Sensitized Solar Cells Using TiO<sub>2</sub>-Graphene Microplatelets Hybrid Photoanode*. IEEE Journal of Photovoltaics, 2016. **6**(1): p. 196-201.
383. Mehmood, U., et al., *Improving the efficiency of dye sensitized solar cells by TiO<sub>2</sub>-graphene nanocomposite photoanode*. Photonics and Nanostructures - Fundamentals and Applications, 2015. **16**: p. 34-42.
384. Sun, S., L. Gao, and Y. Liu, *Enhanced dye-sensitized solar cell using graphene-TiO<sub>2</sub> photoanode prepared by heterogeneous coagulation*. Applied Physics Letters, 2010. **96**(8): p. 083113.
385. Fang, X., et al., *Improved properties of dye-sensitized solar cells by incorporation of graphene into the photoelectrodes*. Electrochimica Acta, 2012. **65**: p. 174-178.
386. Khannam, M., et al., *A graphene oxide incorporated TiO<sub>2</sub> photoanode for high efficiency quasi solid state dye sensitized solar cells based on a poly-vinyl alcohol gel electrolyte*. RSC Advances, 2016. **6**(60): p. 55406-55414.
387. Kusumawati, Y., S. Koussi-Daoud, and T. Pauporté, *TiO<sub>2</sub>/graphene nanocomposite layers for improving the performances of dye-sensitized solar cells using a cobalt redox shuttle*. Journal of Photochemistry and Photobiology A: Chemistry, 2016. **329**: p. 54-60.
388. Fan, J., S. Liu, and J. Yu, *Enhanced photovoltaic performance of dye-sensitized solar cells based on TiO<sub>2</sub> nanosheets/graphene composite films*. Journal of Materials Chemistry, 2012. **22**(33): p. 17027-17036.
389. Xu, F., et al., *Graphene Scaffolds Enhanced Photogenerated Electron Transport in ZnO Photoanodes for High-Efficiency Dye-Sensitized Solar Cells*. The Journal of Physical Chemistry C, 2013. **117**(17): p. 8619-8627.
390. Ramar, A., et al., *Incorporation of Multi-Walled Carbon Nanotubes in ZnO for Dye Sensitized Solar Cells*. International Journal of Electrochemical Science, 2012. **7**: p. 11734 - 11744.
391. Agarwal, R., et al., *Enhanced photovoltaic properties in graphitic carbon nanospheres networked TiO<sub>2</sub> nanocomposite based dye sensitized solar cell*. Journal of Alloys and Compounds, 2015. **641**: p. 99-105.
392. Zhao, P., et al., *Branched hierarchical titanium dioxide nanoflower on carbon nanofiber with efficient scattering layer for high performance dye-sensitized solar cells*. Electrochimica Acta, 2015. **182**: p. 257-263.
393. Kouhnavard, M., et al., *Carbonaceous Materials and Their Advances as a Counter Electrode in Dye-Sensitized Solar Cells: Challenges and Prospects*. ChemSusChem, 2015. **8**(9): p. 1510-1533.
394. Mehmood, U., et al., *Carbon/carbon nanocomposites as counter electrodes for platinum free dye-sensitized solar cells*. Organic Electronics, 2016. **35**: p. 128-135.
395. Hu, H., et al., *Stability study of carbon-based counter electrodes in dye-sensitized solar cells*. Electrochimica Acta, 2011. **56**(24): p. 8463-8466.
396. Sun, W., et al., *A low cost mesoporous carbon/SnO<sub>2</sub>/TiO<sub>2</sub> nanocomposite counter electrode for dye-sensitized solar cells*. Journal of Power Sources, 2012. **201**: p. 402-407.
397. Xu, S., et al., *In-situ formation of dispersed ZnO nanoparticles in mesoporous carbon counter electrode for efficient dye-sensitized solar cells*. Electrochimica Acta, 2013. **114**: p. 574-581.
398. Li, S., Z. Chen, and W. Zhang, *Dye-sensitized solar cells based on WS<sub>2</sub> counter electrodes*. Materials Letters, 2012. **72**: p. 22-24.
399. Maiaugree, W., et al., *Facile synthesis of bilayer carbon/Ni<sub>3</sub>S<sub>2</sub> nanowalls for a counter electrode of dye-sensitized solar cell*. Electrochimica Acta, 2015. **174**: p. 955-962.

400. Zhang, L., et al., *Metal/metal sulfide functionalized single-walled carbon nanotubes: FTO-free counter electrodes for dye sensitized solar cells*. *Physical Chemistry Chemical Physics*, 2012. **14**(28): p. 9906-9911.
401. Pammi, S.V.N., et al., *Crystallized Indium-Tin Oxide Composites Grown onto Single-Walled Carbon Nanotubes at a Low Temperature by Nanocluster Deposition*. *Journal of The Electrochemical Society*, 2012. **159**(5): p. K111-K115.
402. Wang, W., et al., *Rational Design of LaNiO<sub>3</sub>/Carbon Composites as Outstanding Platinum-Free Photocathodes in Dye-Sensitized Solar Cells With Enhanced Catalysis for the Triiodide Reduction Reaction*. *Solar RRL*, 2017. **1**(7): p. n/a-n/a.
403. Veerappan, G., K. Bojan, and S.-W. Rhee, *Sub-micrometer-sized Graphite As a Conducting and Catalytic Counter Electrode for Dye-sensitized Solar Cells*. *ACS Applied Materials & Interfaces*, 2011. **3**(3): p. 857-862.
404. Xiong, K., et al., *La<sub>0.65</sub>Sr<sub>0.35</sub>MnO<sub>3</sub>@RGO nanocomposites as an effective counter electrode for dye-sensitized solar cells*. *Materials Letters*, 2016. **164**: p. 609-612.
405. Xiong, K., et al., *La<sub>0.55</sub>Sr<sub>0.5</sub>CoO<sub>2.91</sub>@RGO nanocomposites as an effective counter electrode for dye-sensitized solar cells*. *Journal of Materials Science: Materials in Electronics*, 2017. **28**(2): p. 1679-1683.
406. Peter, L., et al., *Graphene-MoS<sub>2</sub> nanosheet composites as electrodes for dye sensitised solar cells*. *Materials Research Express*, 2016. **3**(3): p. 035007.
407. Yu, C., et al., *Graphene-mediated highly-dispersed MoS<sub>2</sub> nanosheets with enhanced triiodide reduction activity for dye-sensitized solar cells*. *Carbon*, 2016. **100**: p. 474-483.
408. Bi, H., et al., *Graphene films decorated with metal sulfide nanoparticles for use as counter electrodes of dye-sensitized solar cells*. *Carbon*, 2013. **61**: p. 116-123.
409. Li, Z., et al., *NiS<sub>2</sub>/Reduced Graphene Oxide Nanocomposites for Efficient Dye-Sensitized Solar Cells*. *The Journal of Physical Chemistry C*, 2013. **117**(13): p. 6561-6566.
410. Miao, X., et al., *Well-Dispersed CoS Nanoparticles on a Functionalized Graphene Nanosheet Surface: A Counter Electrode of Dye-Sensitized Solar Cells*. *Chemistry – A European Journal*, 2014. **20**(2): p. 474-482.
411. Huo, J., et al., *High performance sponge-like cobalt sulfide/reduced graphene oxide hybrid counter electrode for dye-sensitized solar cells*. *Journal of Power Sources*, 2015. **293**: p. 570-576.
412. Sigdel, S., et al., *Dye-sensitized solar cells based on spray-coated carbon nanofiber/TiO<sub>2</sub> nanoparticle composite counter electrodes*. *Journal of Materials Chemistry A*, 2014. **2**(29): p. 11448-11453.
413. Lin, J.-Y., et al., *Molybdenum Disulfide/Reduced Graphene Oxide–Carbon Nanotube Hybrids as Efficient Catalytic Materials in Dye-Sensitized Solar Cells*. *ChemElectroChem*, 2015. **2**(5): p. 720-725.
414. Badawi, A., N. Al-Hosiny, and S. Abdallah, *The photovoltaic performance of CdS quantum dots sensitized solar cell using graphene/TiO<sub>2</sub> working electrode*. *Superlattices and Microstructures*, 2015. **81**: p. 88-96.
415. Badawi, A., *Decrease of back recombination rate in CdS quantum dots sensitized solar cells using reduced graphene oxide*. *Chinese Physics B*, 2015. **24**(4): p. 047205.
416. Zhu, G., et al., *Graphene-incorporated nanocrystalline TiO<sub>2</sub> films for CdS quantum dot-sensitized solar cells*. *Journal of Electroanalytical Chemistry*, 2011. **650**(2): p. 248-251.
417. Liu, Y., Y. Sun, and J. Zhang, *Metal-organic-framework derived porous conducting frameworks for highly efficient quantum dot-sensitized solar cells*. *Journal of Materials Chemistry C*, 2017. **5**(17): p. 4286-4292.
418. Guo, W., et al., *Carbon fiber/Co<sub>9</sub>S<sub>8</sub> nanotube arrays hybrid structures for flexible quantum dot-sensitized solar cells*. *Nanoscale*, 2014. **6**(7): p. 3656-3663.

419. Guo, W., et al., *Controlled Sulfidation Approach for Copper Sulfide–Carbon Hybrid as an Effective Counter Electrode in Quantum-Dot-Sensitized Solar Cells*. *The Journal of Physical Chemistry C*, 2016. **120**(30): p. 16500-16506.
420. Zeng, J.H., et al., *Graphite powder film-supported Cu<sub>2</sub>S counter electrodes for quantum dot-sensitized solar cells*. *Journal of Materials Chemistry C*, 2015. **3**(46): p. 12140-12148.
421. Ye, M., et al., *Recent advances in quantum dot-sensitized solar cells: insights into photoanodes, sensitizers, electrolytes and counter electrodes*. *Sustainable Energy & Fuels*, 2017. **1**(6): p. 1217-1231.
422. Sharma, D., R. Jha, and S. Kumar, *Quantum dot sensitized solar cell: Recent advances and future perspectives in photoanode*. *Solar Energy Materials and Solar Cells*, 2016. **155**: p. 294-322.
423. Paulo, S., E. Palomares, and E. Martinez-Ferrero, *Graphene and Carbon Quantum Dot-Based Materials in Photovoltaic Devices: From Synthesis to Applications*. *Nanomaterials*, 2016. **6**(9): p. 157.
424. Margraf, J.T., et al., *Using carbon nanodots as inexpensive and environmentally friendly sensitizers in mesoscopic solar cells*. *Nanoscale Horizons*, 2016. **1**(3): p. 220-226.
425. Guo, X., et al., *Green Synthesis of Carbon Quantum Dots for Sensitized Solar Cells*. *ChemPhotoChem*, 2017. **1**(4): p. 116-119.
426. Fang, X., et al., *Graphene quantum dots optimization of dye-sensitized solar cells*. *Electrochimica Acta*, 2014. **137**: p. 634-638.
427. Ma, Z., et al., *Bioinspired Photoelectric Conversion System Based on Carbon-Quantum-Dot-Doped Dye–Semiconductor Complex*. *ACS Applied Materials & Interfaces*, 2013. **5**(11): p. 5080-5084.
428. Kim, H.-S., et al., *Lead Iodide Perovskite Sensitized All-Solid-State Submicron Thin Film Mesoscopic Solar Cell with Efficiency Exceeding 9%*. *Scientific Reports*, 2012. **2**: p. 591.
429. Nazeeruddin, M.K., *In retrospect: Twenty-five years of low-cost solar cells*. *Nature*, 2016. **538**(7626): p. 463-464.
430. Fang, Y., et al., *The Functions of Fullerenes in Hybrid Perovskite Solar Cells*. *ACS Energy Letters*, 2017. **2**(4): p. 782-794.
431. Ahmed, M.I., et al., *Ambient Air and Hole Transport Layer Free Synthesis: Towards Low Cost CH<sub>3</sub>NH<sub>3</sub>PbI<sub>3</sub> Solar Cells*. *Journal of Nanomaterials*, 2016. **2016**: p. 12.
432. Wang, J.T.-W., et al., *Low-Temperature Processed Electron Collection Layers of Graphene/TiO<sub>2</sub> Nanocomposites in Thin Film Perovskite Solar Cells*. *Nano Letters*, 2014. **14**(2): p. 724-730.
433. Agresti, A., et al., *Efficiency and Stability Enhancement in Perovskite Solar Cells by Inserting Lithium-Neutralized Graphene Oxide as Electron Transporting Layer*. *Advanced Functional Materials*, 2016. **26**(16): p. 2686-2694.
434. Zhou, Z., et al., *Efficient planar perovskite solar cells prepared via a low-pressure vapor-assisted solution process with fullerene/TiO<sub>2</sub> as an electron collection bilayer*. *RSC Advances*, 2016. **6**(82): p. 78585-78594.
435. Abrusci, A., et al., *High-Performance Perovskite-Polymer Hybrid Solar Cells via Electronic Coupling with Fullerene Monolayers*. *Nano Letters*, 2013. **13**(7): p. 3124-3128.
436. Zhou, W., et al., *Successive surface engineering of TiO<sub>2</sub> compact layers via dual modification of fullerene derivatives affording hysteresis-suppressed high-performance perovskite solar cells*. *Journal of Materials Chemistry A*, 2017. **5**(4): p. 1724-1733.
437. Li, Y., et al., *Multifunctional Fullerene Derivative for Interface Engineering in Perovskite Solar Cells*. *Journal of the American Chemical Society*, 2015. **137**(49): p. 15540-15547.
438. Ciro, J., et al., *Simultaneous Top and Bottom Perovskite Interface Engineering by Fullerene Surface Modification of Titanium Dioxide as Electron Transport Layer*. *ACS Applied Materials & Interfaces*, 2017. **9**(35): p. 29654-29659.
439. Li, H., et al., *Carbon Quantum Dots/TiO<sub>x</sub> Electron Transport Layer Boosts Efficiency of Planar Heterojunction Perovskite Solar Cells to 19%*. *Nano Letters*, 2017. **17**(4): p. 2328-2335.

440. Zhang, Y., et al., *Enhancing the grain size of organic halide perovskites by sulfonate-carbon nanotube incorporation in high performance perovskite solar cells*. Chemical Communications, 2016. **52**(33): p. 5674-5677.
441. Sung, H., et al., *Transparent Conductive Oxide-Free Graphene-Based Perovskite Solar Cells with over 17% Efficiency*. Advanced Energy Materials, 2016. **6**(3): p. 1501873-n/a.
442. Zhu, Z., et al., *Efficiency Enhancement of Perovskite Solar Cells through Fast Electron Extraction: The Role of Graphene Quantum Dots*. Journal of the American Chemical Society, 2014. **136**(10): p. 3760-3763.
443. Tavakoli, M.M., et al., *High Efficiency and Stable Perovskite Solar Cell Using ZnO/rGO QDs as an Electron Transfer Layer*. Advanced Materials Interfaces, 2016. **3**(11): p. 1500790-n/a.
444. Cheng, N., et al., *Multi-walled carbon nanotubes act as charge transport channel to boost the efficiency of hole transport material free perovskite solar cells*. Journal of Power Sources, 2016. **332**(Supplement C): p. 24-29.
445. Fang, X., et al., *Graphene quantum dot incorporated perovskite films: passivating grain boundaries and facilitating electron extraction*. Physical Chemistry Chemical Physics, 2017. **19**(8): p. 6057-6063.
446. Ye, T., et al., *Ultrafast Photogenerated Hole Extraction/Transport Behavior in a CH<sub>3</sub>NH<sub>3</sub>PbI<sub>3</sub>/Carbon Nanocomposite and Its Application in a Metal-Electrode-Free Solar Cell*. ChemPhysChem, 2016. **17**(24): p. 4102-4109.
447. Liu, T., et al., *Fine-tuning optical and electronic properties of graphene oxide for highly efficient perovskite solar cells*. Nanoscale, 2015. **7**(24): p. 10708-10718.
448. Liu, S., et al., *Full printable perovskite solar cells based on mesoscopic TiO<sub>2</sub>/Al<sub>2</sub>O<sub>3</sub>/NiO (carbon nanotubes) architecture*. Solar Energy, 2017. **144**: p. 158-165.
449. Akhavan, O., *Graphene Nanomesh by ZnO Nanorod Photocatalysts*. ACS Nano, 2010. **4**(7): p. 4174-4180.

*Every reasonable effort has been made to acknowledge the owners of copyright material. I would be pleased to hear from any copyright owner who has been omitted or incorrectly acknowledged.*

## **Chapter 3: Green synthesis of carbon and silver modified hierarchical ZnO with excellent solar light driven photocatalytic performance**

### **Abstract**

Super-structured ZnO has been the focus of intensive study due to its diverse applications. Here, we demonstrate a facile synthesis of hierarchical ZnO particles hybridized with carbon and silver via a simplified yeast mold broth hydrothermal process. Better than traditional microbial and biomimetic methods, our microbe-free strategy offers superior ease-of-preparation with minimal negative environmental impact. The relevant reaction parameters including zinc precursor concentration, broth pH value and broth content were systemically investigated to control the particle morphologies from solid micro-rod to mesocrystals of porous micro-cylinder, nano-disk, nano-cone, nano-flower and micro-hamburger. Silver nanoparticles were facilely deposited by photoreduction in the broth. The resultant ZnO@C-Ag composite exhibits a significant improvement in the solar light-irradiated photodegradation of methylene blue solution.

### **3.1 Introduction**

Zinc oxide mesocrystals are assemblies of crystallographically oriented ZnO of 0-D quantum dots, 1D-nanowire or 2-D nanoplates. Super structured ZnO particles represent a new class of semiconductors which have attracted much attention very recently due to their potential applications in fast UV photodetectors, high efficient dye-sensitized solar cell (DSC), the source of terahertz radiation and as high efficient photocatalyst.[1-6] Up to date, various methods have been developed to synthesize hierarchical ZnO, such as the template methods, the electrochemical deposition,[7, 8] the two-step hydrothermal method,[9] and thermal evaporation techniques.[10] Unfortunately, most of the preparations of such ZnO supercrystals are associated with high temperatures, complex procedures, organic solvents, or expensive surfactants.[10-14]

Alternately, advances in biotechnology have led to an environmentally friendly way to prepare ZnO nanocrystals with various green reactants include microorganisms like bacteria and fungi.[15-18] However, developing a biological process to supersede conventional chemical and physical nanosynthesis remains a great challenge due to its low yield, time-consuming microbe isolation or complicated peptide sequence screening. In addition, certain

properties of ZnO are strongly dependent on their extrinsic characteristics, such as the morphology, size, and exposed facets, but most of biogenic ZnO nanoparticles were spherical in nature and enclosed by the less-reactive (10-10) facets therefore have no obvious photocatalytic activity.[19] Although extensive efforts have been made toward the development of a high performance ZnO photocatalyst, there is still plenty of room left unexploited. This is mainly due to the fact that pure ZnO can only be excited by a small UV fraction of solar light. Another challenge is the unfavourable photocorrosion of ZnO under light irradiation, which lead to rapid decline in photoactivity and low stability of the photocatalysts. Therefore, forming a heterojunction nanostructure of noble metal or having a residual carbon coating is now an exciting area to improve the efficiency of ZnO in the visible-light region and to stabilize the catalyst. A low loading of Ag on ZnO has increased photodegradation of methylene blue (MB) and Rhodamine 6G (R<sub>6</sub>G) as the Ag clusters acting to response visible light, trap photogenerated electrons, and delay the electron-hole recombination process, and resulting in higher photocatalytic activity.[20, 21] Other research groups have shown that hydrothermal carbon (HTC) originated from biomass and poly- to monosaccharides ideally improved the photostability.[22, 23] For instance, Zhang et al. found that the combination of graphite-like carbon and ZnO nanoparticles can suppress the photocorrosion of ZnO.[24] More recently, Qiu's group reported the synthesis of ZnO@C gemel hexagonal microrods by a facile one-step hydrothermal method with furfural as the carbon precursor.[25] Nevertheless, achieving the carbon doping and the silver nanoparticle formation simultaneously through a green and facile route was scarcely successful.

In our previous studies, yeast mold broth (YMB), a mixture of vitamins, amino acids, proteins, peptone and dextrose, was utilized to implement fine and accurate control over the synthesis of Au and Ag nanoparticles.[26, 27] In contrast to conventional biogenic method, this microbe-free approach offers a number of distinct advantages: (1) Nanoparticles can be produced in a larger scale and shorter periods of time without microorganism involvement and (2) The significantly cheaper cost lies in less expensive raw materials compared to pure peptide, amino acid or enzyme. Herein, we attempt to explore further this topic by synthesizing 3D hierarchical ZnO structures modified with silver and carbon. Our results in this study demonstrate that monodisperse ZnO twin crystals like micro-hamburger can be fabricated with a combination of simplified hydrothermal and post-annealing technique. On the basis of electron microscopy, EDX and XRD analysis, we inferred that YMB may provide proteins and saccharides to compete with OH<sup>-</sup> in binding to (0001) facets of ZnO thus

facilitating dipole field guided orientated attachment of mesocrystals. Meanwhile, dextrose in YMB could be condensed to form amorphous carbon layer on the surface of ZnO particles as well as to reduce silver nitrate. It was found that this approach leads to a high performance carbon-doped ZnO with silver heterojunction structure at the interface for degradation of organic pollutant under solar light.

## **3.2 Experimental section**

### **3.2.1 Sample preparation**

All chemicals were of analytical grade and were used without further purification. Zinc acetate dihydrate ( $\text{Zn}(\text{CH}_3\text{COO})_2 \cdot 2\text{H}_2\text{O}$ ), silver nitrate ( $\text{AgNO}_3$ ) and sodium hydroxide ( $\text{NaOH}$ ) were purchased from Sigma-Aldrich. Dehydrated Yeast Mold Broth (YMB) was bought from BD Company. All stock solutions were prepared with deionized (DI) water. The aqueous YMB was prepared by suspending 42 or 21 g of the powder in 1 L DI water followed by autoclave at 121 °C for 15 min.

Carbon-doped ZnO nano- and microparticles ( $\text{ZnO}@C$ ) with different morphologies were synthesized by a simplified hydrothermal method through varying the experimental parameters. In a typical  $\text{ZnO}@C$  synthesis, pH of the YMB was firstly adjusted to a desired value by adding 1 M NaOH solution. After that, zinc acetate aqueous solution, 10 mL, 50 mM, was mixed with 10 mL YMB under vigorous stirring at room temperature for 5 min. The cloudy reaction mixture in a DURAN glass bottle of 100 mL volume was then autoclaved at 121°C for 30 to 120 min. Finally,  $\text{ZnO}@C$  particles were obtained by centrifugation, washed with DI water and dried in an oven at 50 °C for 5 h. Reference experiments were carried out to evaluate the influence of pH and the reactants contents. For example, the final concentration of zinc acetate in the reaction mixture was adjusted from 12.5 to 100 mM to control the size and morphology of the products, in which the other reaction parameters were kept constant. Growth of silver modified  $\text{ZnO}@C$  was performed by adding silver nitrate to zinc acetate solution at molar ratio of Ag : Zn = 2:100. The final samples were annealed at 500 °C for 30 min in a tube or muffle oven with or without nitrogen protection.

### 3.2.2 Characterization

The samples were characterized with an X-ray diffractometer (XRD; Bruker D8 Advance) equipped with Cu K $\alpha$  radiation ( $\lambda = 1.5418 \text{ \AA}$ ). The morphologies of ZnO 3D structures were investigated by Field-emission scanning electron microscope (Zeiss Neon 40EsB FIBSEM). Transmission electron microscope (TEM) images, high-resolution transmission electron microscope (HRTEM) images and the selected area electron diffraction (SAED) patterns were obtained on a JEOL-2010 microscope operated at accelerating voltage of 200 kV. Samples for TEM characterization were prepared by dropping the colloidal solutions onto a Formvar-coated copper grid and dried in air at room temperature. Fourier transform infrared (FTIR) spectra were measured by using a PerkinElmer Spectrum 100 spectrometer. The Raman spectrum was acquired with a Dilor Labram 1B dispersive Raman spectrometer using a 514.5 nm excitation line. The photoluminescence (PL) measurements were performed on a Perkin-Elmer luminescence spectrometer LS55 at room temperature. UV-vis absorption spectra of the samples in DI water were recorded using JASCO V-670 UV-Vis/NIR spectrophotometer. Thermogravimetric analysis (TGA) was performed using Mettler-Toledo with simultaneous differential thermal analysis (DTA). A heating rate of 5 °C/m from room temperature to 900 °C was used under an air atmosphere. Elemental analysis was performed by using the PerkinElmer 2400 Series II CHNS/O Elemental Analyzer.

### 3.2.3 Photocatalytic test

Methylene blue (MB) was chosen as a probe molecule to evaluate the performance of ZnO@C and ZnO@C-Ag. The photocatalytic degradation of MB was carried out in a glass beaker under a Sun Simulator illumination (550W, xenon lamp, ABET Technologies, Model 11016A Sun 3000). In a typical experiment, 15.0 mg of photocatalyst were dispersed in 15 mL,  $1.0 \times 10^{-5}$  M MB solution. The mixed suspensions were magnetically stirred for 30 min in the dark to reach an adsorption-desorption equilibrium of MB onto the ZnO catalyst. At certain time intervals of irradiation, 0.8 mL of the solution was withdrawn and centrifuged to remove ZnO particles. The reaction process was followed by measuring the absorption of MB in the filtrate at 664 nm. The reusability of ZnO@C-Ag was tested by three successive cycles for the degradation of MB. After each cycle, the particles were centrifuged and redispersed into fresh MB solution without further treatment.

### 3.3 Results and discussion

#### 3.3.1 Morphology and structure characterization of ZnO particles

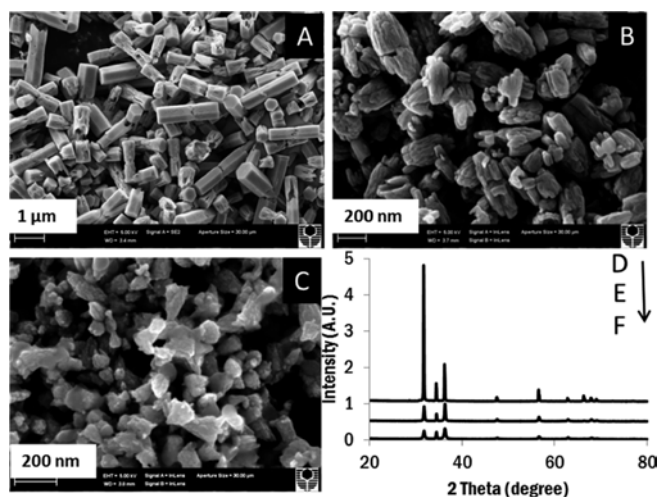


**Figure 3.1.** SEM images and XRD patterns of ZnO products synthesized in deionized water with increasing ratios of  $[\text{OH}^-]/[\text{Zn}^{2+}]$  from 1:1 (A,D, 25ZnDI500), 2:1 (B,E, 25ZnDI1000) to 3:1 (C,F, 25ZnDI1500).

To assess the effect of yeast mold broth (YMB), control samples (without addition of YMB) were firstly prepared by mixing 50 mM zinc acetate (10 mL), DI water (10 mL) and certain amount of 1M sodium hydroxide solution according to the procedure described in the experimental section. The samples with the total addition volume of NaOH at 500, 1000 and 1500  $\mu\text{L}$  were denoted as 25ZnDI500, 25ZnDI1000 and 25ZnDI1500, respectively. Figure 3.1A shows the as-prepared 25ZnDI500 consists of hexagonally prismatic micro-rods. The rods have lengths of 0.5-2  $\mu\text{m}$  and diameters of about 0.4  $\mu\text{m}$ . Some microrods are broken and truncated. In this reaction system, pH is the key factor influencing the morphology of the ZnO particles. Figure 3.1B reveals the image of 25ZnDI1000 in nanocones. When the NaOH volume was increased to 1500  $\mu\text{L}$ , irregular nanograins were obtained (Figure 3.1C). The XRD patterns of corresponding samples are shown in Figure 3.1D-E. In all cases, a highly crystalline wurtzite phase was identified (JSCPS card No. 36-1451). The relatively broader widths of the diffraction peaks in Figure 3.1E and F indicate the formation of smaller ZnO crystallites. These results are in consistent with ZnO single crystal growth behaviour in aqueous solution as reported by Li *et al.*[28] The authors defined the generally accepted reaction routes in an alkali medium as follows:





In their hydrothermal experiments, smaller nanograins were formed due to the larger shielding effect of  $\text{OH}^-$  ions at the interface of the (0001) planes; the growth rate along c-axis was significantly decreased relative to other directions.

It is well known that wurtzite ZnO structure with alternating polar surfaces of  $\text{Zn}^{2+}$ -terminated (0001) and  $\text{O}^{2-}$ -terminated (000 $\bar{1}$ ) along c-axis offers an intrinsic dipole moment and easy growth of hierarchical superstructures, such as spheroidal ZnO aggregates, nanocones, twin-brush, and so on.[29-32] Synthetic surfactants like cetyltrimethylammonium bromide (CTAB), Triton X-100, sodium dodecyl sulphate (SDS), and sodium bis(2-ethylhexyl) sulfosuccinate (NaAOT) are the most frequently employed molecules to mediate 3D ZnO assembly.[14, 33, 34] Recently, biomimetic approach towards synthesis of zinc oxide has attracted a growing interest due to its advantages of mild conditions and easiness of handling. Pure amino acids,[35-37] artificial peptides with an affinity for ZnO,[18] gelatin,[38] and proteins secreted by zinc metal tolerant soil fungus[16] have been common examples towards the development of an environmentally benign protocol for fabrication of ZnO nanoparticles. A number of ZnO assemblies have been mediated with natural polysaccharides, such as pectin,[15] hyaluronic acid and chondroitin-6-sulfate.[39] Gum arabic, a complex mixture of glycoproteins and highly branched polysaccharides, has been successfully employed to guide the evolution of twin-brush ZnO mesocrystals.[32] Based on our previous works, we note that yeast mold broth powder, not only rich with various amino acids but also containing 0.3 wt% *Saccharomyces cerevisiae* yeast extract thus abundant in yeast polysaccharide mannan, should have the potential to promote secondary ZnO aggregation.

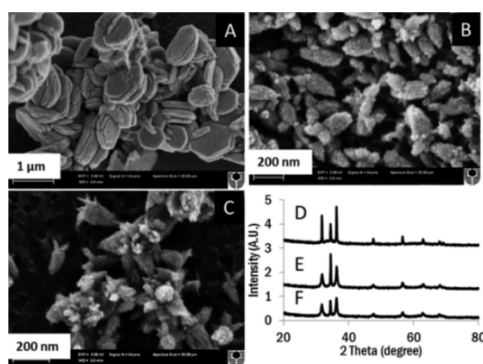


**Figure 3.2.** SEM images and XRD patterns of ZnO particles prepared in the presence of 1 x yeast mold broth (21 g yeast mold broth powder in 1 L DI water) with increasing ratios of  $[\text{OH}^-]/[\text{Zn}^{2+}]$  from 1:1 (A,D, 25ZnDI500), 2:1 (B,E, 25ZnDI1000) to 3:1 (C,F, 25ZnDI1500).

As part of our ongoing efforts to synthesize environmentally friendly nanoparticles, ZnO particles were prepared in the presence of 1 x YMB (21 g YMB powder in 1 L DI water). FESEM images of ZnO samples with varying 1 M NaOH volume are shown in Figure 3.2. Addition of 500  $\mu\text{L}$  NaOH resulted in pure and uniform nano-disks with diameter around 1  $\mu\text{m}$ . Li *et al.* fabricated similar hexagonal-based thin disks by employing an oil-in-water microemulsion method.[14] The formation of the hexagonal disks is suggested to be due to the self-assembly of NaAOT template. Recently, a template-free method using butanol as the reaction solvent has been demonstrated to obtain ZnO mesocrystals after 12 h reaction at 120  $^{\circ}\text{C}$ .[40] Butanol or  $\text{H}_2\text{O}$  adsorbed on the (0001) planes has been proposed to induce the energetically unfavourable growth of ZnO microspheres. In our study, we hypothesize that amino acids or other functional groups from the yeast mold broth may compete with  $\text{OH}^-$  in binding to the ZnO (0001) surface and suppress the growth along the c-axis. As the volume of NaOH increased to 1000 and 1500  $\mu\text{L}$ , although the 25ZnYM1000 and 25ZnYM1500 crystals still maintain comparable size as 25ZnDI1000 and 25ZnDI1500, the surface of the ZnO particles become rougher, nano-strawberry and nano-flower with grainy surface were formed respectively. These results illustrate that YMB components clearly assist in the oriented attachment of primary ZnO nanoparticles thus lead to the formation of the superstructures.

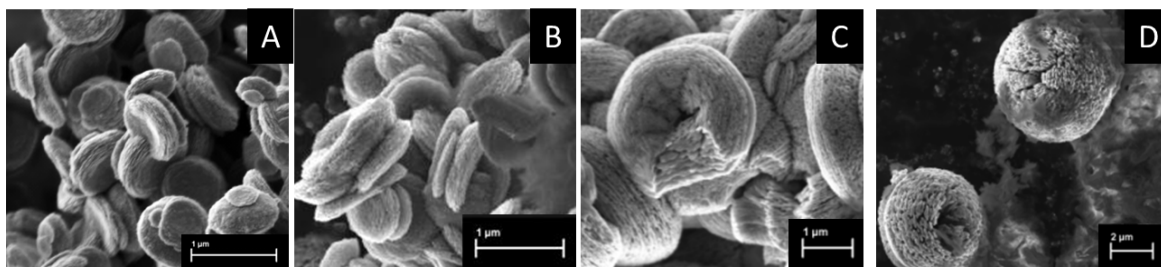


**Figure 3.3.** SEM images of ZnO products synthesized with increasing  $[\text{Zn}^{2+}]$  from 12.5 mM (A), 25 mM (B), 50 mM (C) to 100 mM (D). The concentration of NaOH was maintained same as 17 mM in the reaction solution. All samples were prepared with the presence of 1 x yeast mold broth.

To test the influence of zinc precursor concentration,  $[\text{OH}^-]$  was fixed at 17 mM, while  $[\text{Zn}^{2+}]$  was increased from 12.5 to 100 mM in 1x YMB. Figure 3.3 presents the variation of the particle thickness, morphology and size with increasing  $\text{Zn}(\text{OAc})_2$  concentration. Clearly, we can see thin nano-platelets, twin-nanodisks, thick micro-donuts and micro-apples were predominately formed when  $\text{Zn}^{2+}$  of 12.5, 25, 50 and 100 mM, respectively. A close examination reveals the particle surface is composed of loosely packed nanoplatelets of sizes

of 30–50 nm. It is worth noting the co-existence of graphene-like sheet. As shown in Fig 3D, the surface of ZnO particle is wrapped by the sheets.

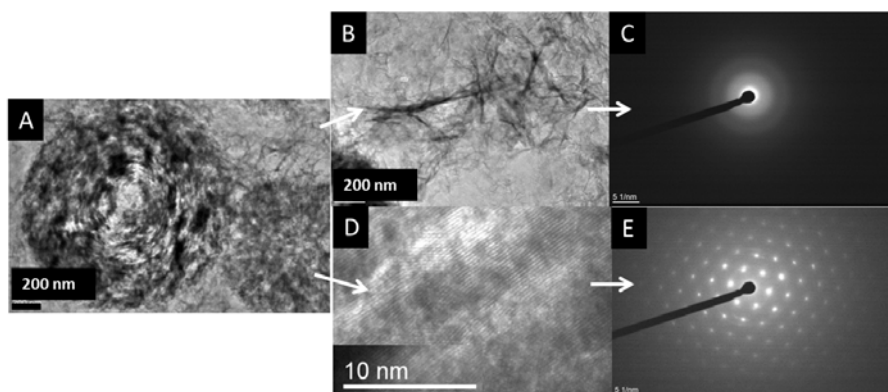


**Figure 3.4.** TEM images of ZnO particles enwrapped with amorphous hydrothermal carbon. The final concentration of  $\text{OH}^-$  and  $\text{Zn}^{2+}$  was 17 and 50 mM, respectively, in 1 x yeast mold broth.

TEM investigations were performed on samples using 50 mM of  $[\text{Zn}^{2+}]$  and 17 mM of  $[\text{OH}^-]$  after 60 min reaction. The HRTEM image in Figure 3.4D shows the lattice fringe with a 0.26 nm d-spacing for the (002) reflection.[41] A selected area electron diffraction (SAED) pattern indicates that the micro-donuts are single crystalline (Figure 3.4E). Graphene-like sheets (Figure 3.4B) were amorphous as indicated by SAED pattern in Figure 3.4C.

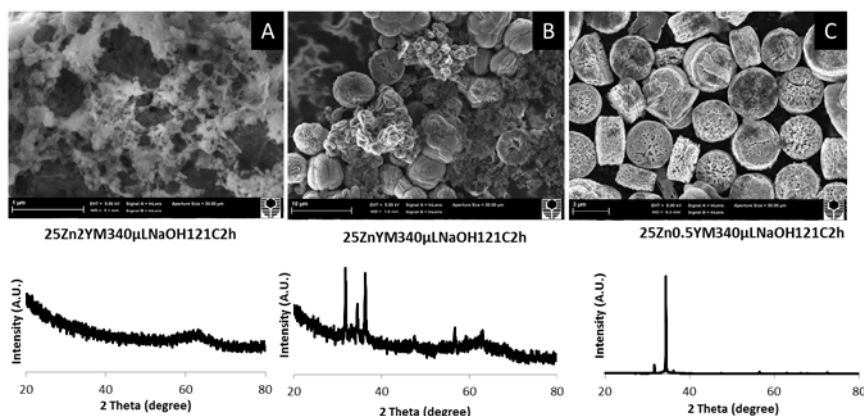


**Figure 3.5.** Effect of yeast mold broth concentration on the formation of ZnO mesocrystals. (A) Hydrothermal carbon was the mainly product when 2 x YMB (42 g YMB powder in 1 L DI water) was applied; (B) different size and morphology of ZnO particles and (C) highly crystalline ZnO microcylinders were formed when 1 x YMB and 0.5 x YMB was applied, respectively.

So far, we have confirmed the structure-directing function of YMB powder. However, the synthesis of a relatively uniform and high quality ZnO mesocrystal has not been successful. It is well reported in the literature that the crystal development is largely dependent on the dosage of morphology mediation agents. Therefore, we systematically investigated the

influence of the concentration of YMB powder. In the presence of 2 x YMB (42 g YMB in 1 L DI water, 4.2%), only amorphous black powder was obtained after 2 h reaction at 121 °C. From Figure 3.5A, we can see that the sample consists of microspheres with the diameter ranging from 0.3 to 1 μm in coexistence with primary nanoparticles with size around 10 nm. Decreasing the content of YMB powder from 4.2 % to 2.1 %, crystalline ZnO particles of various size and shape were revealed in Figure 3.5B. Interestingly, highly porous and crystalline micro-cylinders were formed with 1.05 % YMB. A high magnification SEM inset reveals that the cylinder consists of packed nanocrystallites. Up to now, most advantageous and porous ZnO superstructures were prepared by calcining a precursor at high temperature.[42, 43] To the best of our knowledge, this is the first report on porous ZnO fabrication at such low temperature (121 °C), in just 1 h and without addition of any template, which is much facile than that reported by other studies.[44, 45]

YMB powder is sugar rich, which is composed of 47.6% dextrose, 14.3% yeast extract, 23.8% peptone and 14.3% malt extract. We hypothesize that, under hydrothermal condition, the dextrose and mannan may follow the chemical reaction path, like the dehydration of sugar, formation of 5-hydroxymethyl-furfural-aldehyde (HMF), and the subsequent transformation to hydrothermal carbon.[22] This view is supported by SEM characterization. Morphology of black powder in Figure 3.5A is quite similar to the SEM images of hydrothermal carbons prepared using glucose and HMF as precursors. Moreover, high concentration of organic acids (acetic, lactic, propenoic, levulinic and formic acids) derivated from the decomposition of sugars[46] in 2 x YMB broth may competitively react with NaOH thus suppress the formation of  $Zn(OH)_4^{2-}$  and ZnO particles. Although 0.5 x YMB and addition of 340 μL 1M NaOH produces ZnO microparticles with intensified and sharp diffraction peaks, they are still partially covered by a certain amount of laminar precipitations, which indicates that NaOH is insufficient and the hydrothermal carbon has exceeded the amount needed to thinly cover the ZnO particles. By increasing NaOH addition to 500 μL, we finally obtained thin hydrothermal carbon (HTC) coated ZnO samples named as ZnO@C.

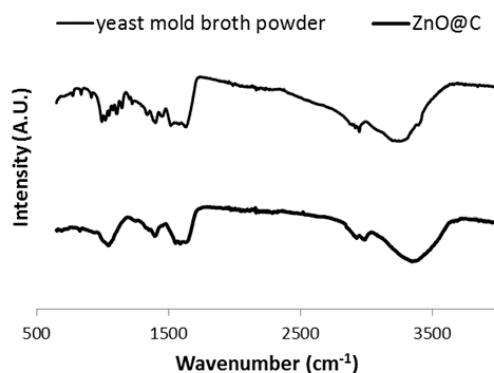


**Figure 3.6.** Typical FTIR spectra of yeast mold broth powder and ZnO@C samples.

FTIR spectroscopy was used to determine the functional groups contributing to ZnO assemblies (Figure 3.6). YMB shows expected absorption bands include: (1) the highest intensity of the  $\nu$  (OH) band at  $3372\text{ cm}^{-1}$ , (2)  $\nu_{\text{asym}}(\text{CH}_2)$  lipids at  $2925\text{ cm}^{-1}$ , [47] (3) The presence of amide I band at  $1636\text{ cm}^{-1}$  arising from C=O stretching and contribution of N-H bending, [48] (4)  $1552\text{ cm}^{-1}$ , amide II band of  $\delta_{\text{N-H}}$  or  $\nu_{\text{C-N}}$  vibrations in different protein conformations, (5)  $1405\text{ cm}^{-1}$ , s,  $\delta_{\text{CH}_3}$  stretching mainly in proteins, (6)  $1390\text{ cm}^{-1}$ , C=O of  $\text{COO}^-$  symmetric stretching in proteins, (7)  $1350\text{ cm}^{-1}$ ,  $\text{CH}_2$  wagging vibrations in lipids, (8)  $1042\text{ cm}^{-1}$ ,  $\beta(1\rightarrow3)$  glucans, and (9)  $828\text{ cm}^{-1}$ , mannans. [47] These bands could be found in the FTIR spectra of ZnO@C samples, indicating the involvement of proteins and mannans in the synthesis process.

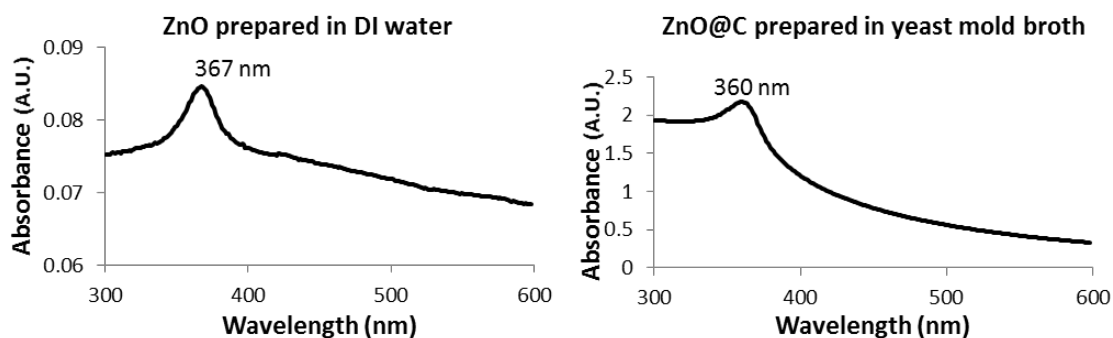


**Figure 3.7.** UV-visible absorption spectra of ZnO particles prepared in DI water (A) and in yeast mold broth (B).

The optical properties of the as-synthesized ZnO nanostructures were characterized by means of UV-vis measurements at room temperature. Figure 3.7 shows the extinction spectra of ZnO particles. For the control samples without the addition of YMB powder, a weak absorption peak appears at 367 nm. With the presence of YMB powder, the blue-shifted absorption becomes intense, and the absorption peak is wider than its counterpart.

### 3.3.2 Silver modified ZnO@C samples

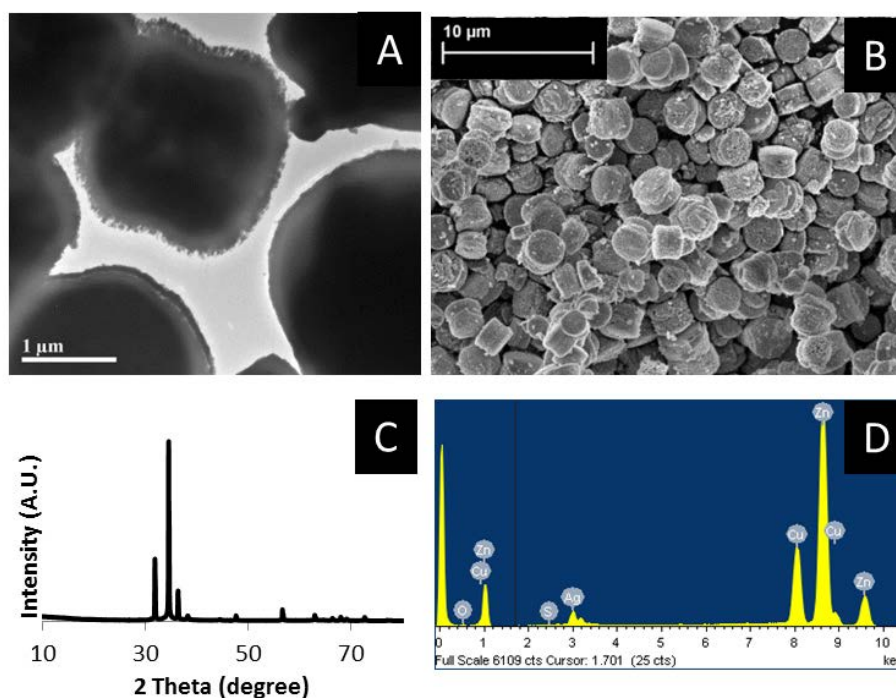


**Figure 3.8.** (A) TEM images showing the micro-hamburger morphology of the ZnO@C-Ag particles; (B) SEM images; (C) XRD pattern of ZnO and Ag NPs; (D) EDX analysis of ZnO@C-Ag after annealing at 400 °C for 30 min.

The Ag-modified ZnO@C samples denoted as ZnO@C-Ag was synthesized by mixing AgNO<sub>3</sub> and ZnO@C solution under sun simulator irradiation for 5 min. After centrifugation, the products were annealed at 400 °C in air for 30 min. There is virtually no change in the morphology, particle size and crystalline phase, after Ag modification, as confirmed by the TEM/SEM micrographs and XRD patterns (Figure 3.8). All major peaks in the diffraction patterns match with those of a typical wurtzite ZnO. The peaks at 2θ values of 38.1°, 44.4° and 64.4° were attributed to crystal planes of metallic Ag (JCPDS file: 65-2871). The silver modifying does not cause diffraction peaks shift of ZnO, implying that Ag simply clusters on the surface of ZnO rather than substituting the Zn<sup>2+</sup> and going into the lattice of ZnO, due to the big difference between the radius of Ag<sup>+</sup> and Zn<sup>2+</sup>.<sup>50</sup> The presence of Ag, carbon and ZnO was further revealed by EDS analysis HRTEM, and Raman analysis (Figure 3.8D, 3.9 and 3.10).

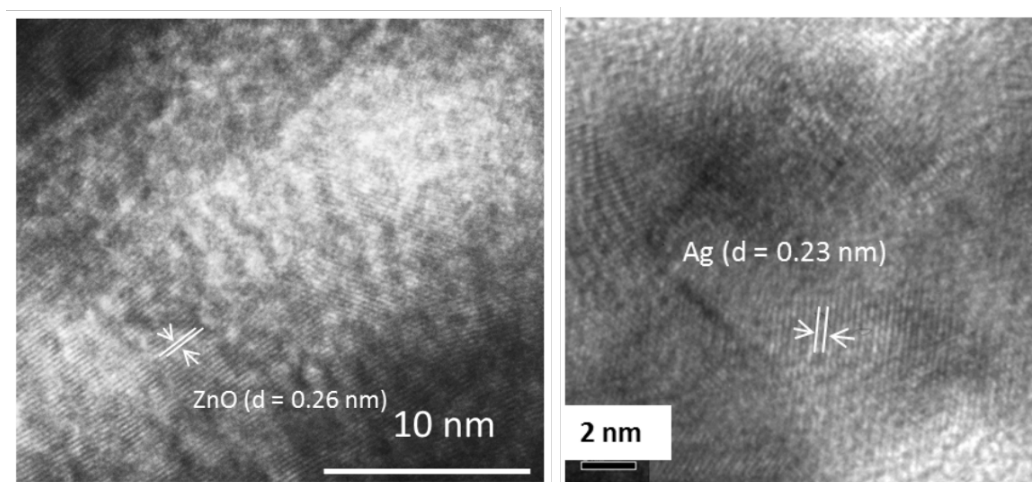


**Figure 3.9.** HRTEM images of ZnO@C-Ag\_400C30m. The spacing of 0.26 nm in (A) and 0.23nm in B between adjacent lattice planes corresponds to (002) lattice planes of ZnO and (111) lattice planes of Ag respectively.

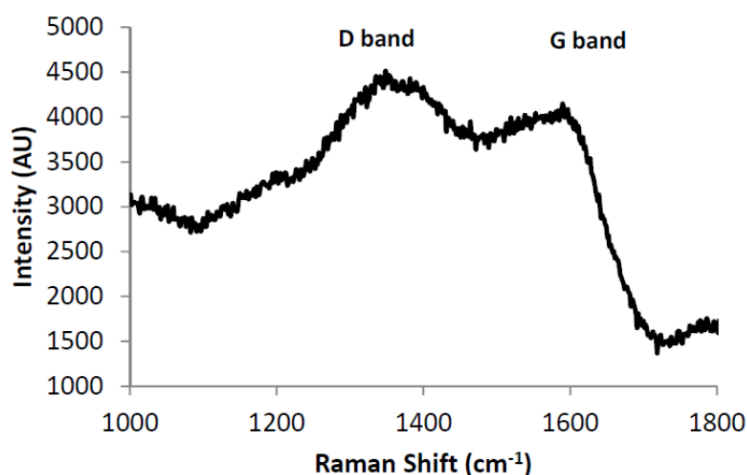


**Figure 3.10.** Raman spectrum of ZnO@C-Ag\_400C30m. The broad peaks at 1348 cm<sup>-1</sup> (D band) and 1595 cm<sup>-1</sup> (G band) identify that the hydrothermal carbon layers are composed of amorphous carbon owing to the low reaction temperature.

Elemental analysis was carried out for the ZnO@C and ZnO@C-Ag samples (Table 3.1). C and N content in YMB powder is 40.9% and 6.3%, respectively. The samples prepared with 4.2, 2.1 and 1.05 % YMB solution are named as YMZnO@C, 0.5 YMZnO@C and 0.25YMZnO@C, and their C content decreased from 9.1 to 3.8 and 2.3 %, indicating that the C is from hydrothermal of YMB powder mainly. After annealing 0.5YMZn@C in air and N<sub>2</sub>, the content of C dropped to 0.8 and 1.7%. Ag incorporating has no obvious influence on the carbon content of the samples as confirmed by determining the C content of 0.5YMZn@C and 0.5YMZn@C-Ag to be 3.8% and 4.0%, respectively. The weight percentage of the

carbon in thermally annealed ZnO@C-Ag\_400C30m sample (400 °C for 30 min in air) is 0.9%.

**Table 3.1** Synthesis conditions and chemical elemental analysis of ZnO products.

Samples	Carbon (wt.%)	Nitrogen (wt.%)
Yeast mold broth powder	40.9	6.3
YMZnO@C	9.1	2.4
0.5YMZnO@C	3.8	0.9
0.25YMZnO@C	2.3	0.5
0.5YMZnO@C_400C30m in air	0.8	0.2
0.5YMZnO@C_400C30m in N <sub>2</sub>	1.7	0.3
0.5YMZnO@C-Ag	4.0	1.1
0.5YMZnO@C-Ag_400C30m in N <sub>2</sub>	1.3	0.3
0.5YMZnO@C-Ag_400C30m in air	0.9	0.1

TGA analysis further reveals the trend of decreased hydrothermal carbon (HTC) in the ZnO@C-Ag composites as shown in Figure 3.11. It was clear that the weight loss of HTC started from 220 °C, and continuously decreased up to 500 °C due to the combustion of the carbon on the sample surface.<sup>25</sup> It is worth noticing that the weight loss percentage of all samples was higher than C content as indicated by elemental analysis result. The extra weight loss may be due to the decomposition of Ag<sub>2</sub>O in ZnO system.[21] Ag<sub>2</sub>O has been reported to be stable at 300 °C but decomposes to metallic silver at 400 °C. The result is consistent with better photocatalytic performance of annealed samples as discussed in the following section.

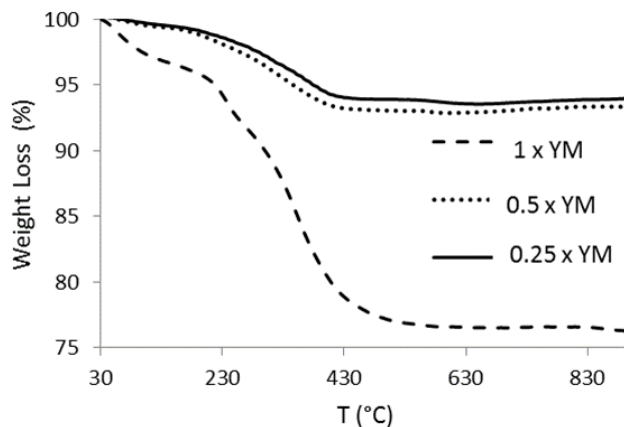


**Figure 3.11.** TGA curves of thermal decomposition of ZnO@C-Ag prepared with different concentration of yeast mold broth powder.

### 3.3.3 Photocatalytic activity and reusability

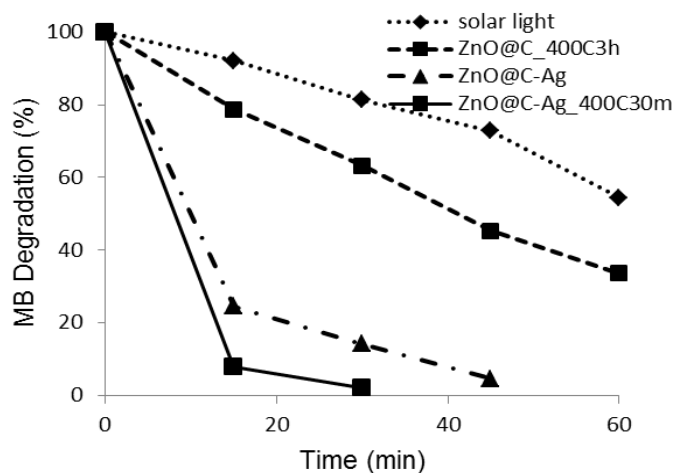


**Figure 3.12.** The photocatalytic degradation of methylene blue under solar light irradiation over different ZnO samples.

The photodegradation of MB catalysed by different ZnO samples under solar light is shown in Figure 3.12. To screen high performance catalyst efficiently, MB solution of low concentration ( $1 \times 10^{-5}$  M) was employed. Although the blank experiment results show a self-photodegradation of MB, the entire synthesized samples exhibit enhanced degradation efficiency. Nevertheless, the samples without post-thermal treatment exhibited little positive effect. It may be related to a high content of carbon that shields the light reaching the surface of ZnO photocatalyst. Similarly, ZnO@C-Ag annealed in  $N_2$  exhibited lower activity compare to the count parts annealed in air (data not show).[49] For a clear view, we presented MB degradation curves of several typical samples only. When exposed to solar light, about 66% of MB can be degraded by ZnO@C after 60 min. ZnO@C-Ag degraded nearly 100%

MB in 60 min. The annealed ZnO@C-Ag\_400C30m ternary composite shows the best performance, evidenced by the fact that nearly 100% of the MB has been degraded in 15 min. It is known that efficient light absorption and the charge transportation and separation are crucial factors in enhancing the photocatalytic performance. Ag nanoparticles have been reported as “electron reservoirs” and effectively prolong the lifetime of the photogenerated electron-hole pairs thus leading to a remarkably improved photoactivity.

To evaluate the photostability of the catalyst, three successive cyclic MB degradation tests under solar light were carried out and it is found that ZnO@C-Ag\_400C30m remains 96% photocatalytic efficiency after three times recycles, indicating that there is no serious corrosion of ZnO due to the hybridized HTC coating layer.

### 3.4 Conclusions

In summary, we present a green method for rapid growth of high-quality ZnO nano-microstructures enwrapped with a thin carbon layer. By optimizing the reaction parameters, ZnO@C of various sizes and shapes have been produced through a hydrothermal process with yeast mold broth powder as both the carbon precursor and directing agent of ZnO nucleation. Subsequently, the ZnO@C-Ag composites have been facilely prepared and demonstrated excellent photocatalytic activities, which were evaluated by the degradation of MB under sun simulator.

### References

1. Li, Y., et al., *Physical processes-aided periodic micro/nanostructured arrays by colloidal template technique: fabrication and applications*. Chem. Soc. Rev., 2013. **42**: p. 3614.
2. Li, Y., et al., *Untraditional approach to complex hierarchical periodic arrays with trinary stepwise architectures of micro-, submicro-, and nanosized structures based on binary colloidal crystals and their fine structure enhanced properties*. ACS Nano, 2011. **5**: p. 9403.
3. Gedamu, D., et al., *Rapid fabrication technique for interpenetrated ZnO nanotetrapod networks for fast UV sensors*. Adv. Mater., 2014. **26**: p. 1541.
4. Shi, Y., et al., *Solid-state synthesis of ZnO nanostructures for quasi-solid dye-sensitized solar cells with high efficiencies up to 6.46%*. Adv. Mater., 2013. **25**: p. 4413.
5. Wu, X.L., et al., *Green light stimulates terahertz emission from mesocrystal microspheres*. Nat. Nanotechnol., 2011. **6**: p. 103.
6. Wang, M., et al., *Rapid room-temperature synthesis of nanosheet-assembled ZnO mesocrystals with excellent photocatalytic activity*. CrystEngComm., 2013. **15**: p. 754.
7. Dong, Z., et al., *Accurate control of multishelled ZnO hollow microspheres for dye-sensitized solar cells with high efficiency*. Adv. Mater., 2012. **24**: p. 1046.

8. Elias, J., et al., *Hollow urchin-like ZnO thin films by electrochemical deposition*. Adv. Mater., 2010. **22**: p. 1607.
9. Guo, H., et al., *Effect of particle size in aggregates of ZnO-aggregate-based dye-sensitized solar cells*. Electrochim. Acta, 2014. **120**: p. 23.
10. Kong, X.Y., et al., *Single-crystal nanorings formed by epitaxial self-coiling of polar nanobelts*. Science, 2004. **303**: p. 1348.
11. Tang, G., et al., *ZnO micro/nanocrystals with tunable exposed (0001) facets for enhanced catalytic activity on the thermal decomposition of ammonium perchlorate*. J. Phys. Chem. C, 2014. **118**: p. 11833.
12. McLaren, A., et al., *Shape and size effects of ZnO nanocrystals on photocatalytic activity*. J. Am. Chem. Soc., 2009. **131**: p. 12540.
13. Li, P., et al., *Systematic synthesis of ZnO nanostructures*. Chem.—Eur. J., 2013. **19**: p. 3735.
14. Li, F., et al., *Single-crystal hexagonal disks and rings of ZnO: low-temperature, large-scale synthesis and growth mechanism*. Angew. Chem., 2004. **116**: p. 5350.
15. Wang, A.J., et al., *Apple pectin-mediated green synthesis of hollow double-caged peanut-like ZnO hierarchical superstructures and photocatalytic applications*. CrystEngComm, 2012. **14**: p. 256.
16. Jain, N., et al., *A biomimetic approach towards synthesis of zinc oxide nanoparticles*. Appl. Microbiol. Biotechnol., 2013. **97**: p. 859.
17. Hussein, M.Z., et al., *Bacillus cereus as a biotemplating agent for the synthesis of zinc oxide with raspberry- and plate-like structures*. J. Inorg. Biochem., 2009. **103**: p. 1145.
18. Umetsu, M., et al., *Bioassisted room-temperature immobilization and mineralization of zinc oxide—The structural ordering of ZnO nanoparticles into a flower-type morphology*. Adv. Mater., 2005. **17**: p. 2571.
19. Jayaseelan, C., et al., *Novel microbial route to synthesize ZnO nanoparticles using Aeromonas hydrophila and their activity against pathogenic bacteria and fungi*. Spectrochim. Acta. A, 2012. **90**: p. 78.
20. Height, M., et al., *Ag-ZnO catalysts for UV-photodegradation of methylene blue*. Appl. Catal., B, 2006. **63**: p. 305.
21. Georgekutty, R., M. Seery, and S. Pillai, *A highly efficient Ag-ZnO photocatalyst: Synthesis, properties, and mechanism*. J. Phys. Chem. C, 2008. **112**: p. 13563.
22. Titirici, M., M. Antonietti, and N. Baccile, *Hydrothermal carbon from biomass: A comparison of the local structure from poly- to monosaccharides and pentoses/hexoses*. Green Chem., 2008. **10**: p. 1204.
23. Sun, X. and Y. Li, *Colloidal carbon spheres and their core/shell structures with noble-metal nanoparticles*. Angew. Chem., Int. Ed., 2004. **43**: p. 597.
24. Zhang, L., et al., *Photocorrosion suppression of ZnO nanoparticles via hybridization with graphite-like carbon and enhanced photocatalytic activity*. J. Phys. Chem. C, 2009. **113**: p. 2368.
25. Zhang, P., et al., *Furfural-induced hydrothermal synthesis of ZnO@C gemel hexagonal microrods with enhanced photocatalytic activity and stability*. ACS Appl. Mater. Interfaces, 2014. **6**: p. 8560.
26. Liu, L., et al., *Are microorganisms indispensable in green microbial nanomaterial synthesis?* RSC Adv., 2014. **4**: p. 14564.
27. Liu, L., et al., *Less is more, greener microbial synthesis of silver nanoparticles*. Enzyme Microb. Technol., 2014. **67**: p. 53.
28. Li, W., et al., *Growth mechanism and growth habit of oxide crystals*. J. Cryst. Growth, 1999. **203**: p. 186.
29. Distaso, M., et al., *Influence of the counterion on the synthesis of ZnO mesocrystals under solvothermal conditions*. Chem.—Eur. J., 2011. **17**: p. 2923.

30. Wu, D., et al., *Hierarchical ZnO aggregates assembled by orderly aligned nanorods for dye-sensitized solar cells*. CrystEngComm, 2013. **15**: p. 1210.
31. Klaumünzer, M., et al., *ZnO superstructures via oriented aggregation initiated in a block copolymer melt*. CrystEngComm, 2014. **16**: p. 1502.
32. Liu, M., et al., *Dipole field guided orientated attachment of nanocrystals to twin-brush ZnO mesocrystals*. Chem.—Eur. J., 2012. **18**: p. 16104.
33. Tang, H., et al., *Surfactant-assisted alignment of ZnO nanocrystals to super structures*. J. Phys. Chem. B, 2008. **112**: p. 4016.
34. Jung, M. and M. Chu, *Synthesis of hexagonal ZnO nanodrums, nanosheets and nanowires by the ionic effect during the growth of hexagonal ZnO crystals*. J. Mater. Chem. C, 2014. **2**: p. 6675.
35. Subramanian, N. and A.A. Ghaferi, *An amino acid-based swift synthesis of zinc oxide nanostructures*. RSC Adv., 2014. **4**: p. 4371.
36. Brif, A., et al., *Bio-inspired band gap engineering of zinc oxide by intracrystalline incorporation of amino acids*. Adv. Mater., 2014. **26**: p. 477.
37. Ramani, M., et al., *Amino acid-mediated synthesis of zinc oxide nanostructures and evaluation of their facet-dependent antimicrobial activity*. Colloids Surf., B, 2014. **117**: p. 233.
38. Tseng, Y., et al., *Biomimetic ZnO plate twin-crystals periodical arrays*. Chem. Commun., 2012. **48**: p. 3215.
39. Waltz, F., et al., *Evolution of the morphologies of zinc oxide mesocrystals under the influence of natural polysaccharides*. Cryst. Growth Des., 2012. **12**: p. 3066.
40. Wang, S. and A. Xu, *Template-free facile solution synthesis and optical properties of ZnO mesocrystals*. CrystEngComm, 2013. **15**: p. 376.
41. Ge, M.Y., et al., *Nanostructured ZnO: From monodisperse nanoparticles to nanorods*. J. Cryst. Growth, 2007. **305**: p. 162.
42. Song, R.Q., et al., *From layered basic zinc acetate nanobelts to hierarchical zinc oxide nanostructures and porous zinc oxide nanobelts*. Adv. Funct. Mater., 2007. **17**: p. 296.
43. Yang, Y., et al., *Control of the formation of rod-like ZnO mesocrystals and their photocatalytic properties*. CrystEngComm, 2013. **15**: p. 2608.
44. Dong, L., et al., *From one nanobelt precursor to different ZnO nano/micro structures: porous nanobelts self-standing film and microtubes*. CrystEngComm, 2013. **15**: p. 9916.
45. Yin, J., et al., *Water amount dependence on morphologies and properties of ZnO nanostructures in double-solvent system*. Sci. Rep., 2014. **4**: p. 3736.
46. Sevilla, M. and A.B. Fuertes, *The production of carbon materials by hydrothermal carbonization of cellulose*. Carbon, 2009. **47**: p. 2281.
47. Cavagna, M., et al., *Use of ATR-FTIR microspectroscopy to monitor autolysis of Saccharomyces cerevisiae cells in a base wine*. J. Agric. Food Chem., 2010. **58**: p. 39.
48. Galichet, A., et al., *FTIR spectroscopic analysis of Saccharomyces cerevisiae cell walls: Study of an anomalous strain exhibiting a pink-colored cell phenotype*. FEMS Microbiol. Lett., 2001. **197**: p. 179.
49. Liu, J., et al., *Facile synthesis of carbon-doped mesoporous anatase TiO<sub>2</sub> for the enhanced visible-light driven photocatalysis*. Chem. Commun., 2014. **50**: p. 13971.

*Every reasonable effort has been made to acknowledge the owners of copyright material. I would be pleased to hear from any copyright owner who has been omitted or incorrectly acknowledged.*

## **Chapter 4: Bi-layer photoanode films of hierarchical carbon-doped brookite-rutile TiO<sub>2</sub> composite and anatase TiO<sub>2</sub> beads for efficient dye-sensitized solar cells**

### **Abstract**

Dye-sensitized solar cell (DSSC) is one of the most promising alternatives to the conventional p-n junction photovoltaic device. Here, we have explored the morphology and structure variation and the accompanying solar cell performance change of two different TiO<sub>2</sub> beads-based photoanodes made from the same precursor. The first was synthesized hydrothermally at acidic condition whereas the second was synthesized solvothermally at slightly basic condition. The first material, referred as Bead-A with an average particle size of ~2.0 μm consists of rutile and brookite TiO<sub>2</sub> phases while the second material, Bead-B, with smaller diameter of ~500 nm consists solely of anatase TiO<sub>2</sub> phase. The pertaining formation mechanisms for both materials are explored. The performances of DSSCs based on Bead-A-P25 and Bead-B-P25 bi-layer photoanodes are higher than that based on pure P25. Cell based on Bead-B showed slightly better DSSC performance than Bead-A. It becomes apparent that Bead-A is advantageous in terms of fast electron transport due to its larger particle size and the presence of 1D rutile nanorods in addition to the carbon doping. Bead-B, on the other hand, gives advantages of superior light scattering properties and high surface area for dye loading. We further improved the cell performance by combining the advantages from both materials *via* optimized layer arrangement. By placing larger Bead-A particles on top of the smaller Bead-B particles, the top layer suppresses carrier recombination and confines the incident light within the photoanode, essentially enhancing charge harvest and collection efficiency. The performance of DSSC based on bi-layer Bead-A and Bead-B photoanode is superior to their counterpart based on bead-P25 bi-layer films. The cell operated using this bi-

layer photoanode demonstrated short-circuit current density ( $J_{sc}$ ) of 15.67 mA cm<sup>-2</sup>, open circuit voltage ( $V_{oc}$ ) of 721 mV and power conversion efficiency of 7.24 %.

## 4.1 Introduction

Solar energy is an abundant and low-cost renewable energy resource. There will be a major shift towards leaving conventional fossil-fuel based resources and harnessing more solar energy, by using solar cell to convert solar energy into electricity. As the amount of greenhouse gas emission generated during such conversion can be negligible, development of solar energy help to mitigate the carbon emission. Based on their main material components, several different types of solar cells exist such as semiconductor,[1] polymer-inorganic hybrid,[2] perovskite,[3] quantum dot-sensitized,[4] or dye-sensitized solar cells (DSSCs).[5] DSSCs in particular are attractive from the perspective of wide availability, low-cost, and facile fabrication process.[6, 7]

TiO<sub>2</sub> is one of the most widely used materials in DSSCs given its functionality for dye loading, electron injection, transport, and collection.[8, 9] The photovoltaic performance of DSSCs is however strongly tied to the crystalline structure, morphology, surface area, and phase compositions of TiO<sub>2</sub>. [9, 10] In photocatalysis field, crystal phase mixture of TiO<sub>2</sub>, such as rutile/anatase, brookite/anatase or brookite/rutile, have been known to display good electron-hole separation efficiency enabled by vectorial displacement of electron transfer between different phases. [11-13] This effect can also be exploited into DSSCs to improve the photovoltaic performance.[14-17]. Li et al., for example, reported that the addition of 10–15 wt. % rutile to anatase nanoparticles (NPs) led to significant improvement in the light harvesting and the overall solar conversion efficiency on their DSSCs.[14]

To be an efficient photoanode in DSSCs, TiO<sub>2</sub> should ideally have large surface area, strong light scattering property, and high electronic conductivity to suppress the charge recombination phenomenon. Conventional TiO<sub>2</sub> NPs based electrodes may not always fulfill these criteria. In fact, slow electron transport and short electron lifetime

may occur due to the presence of electron “trapping” sites on their surfaces and/or randomly distributed network of crystallites may exist which results in the formation of very large amount of grain boundaries.[18, 19] These grain boundaries in turn act as “trapping” sites which increases the probability for electron recombination. TiO<sub>2</sub> electrode with quasi-one dimensional (quasi-1D) or one dimensional (1D) nanostructures [20-23] and hierarchical architectures [18, 24, 25] have been developed to address these issues. Quasi-1D or 1D nanostructures provide a direct transport path for the injected electron diffusion while hierarchical structures with small building blocks provide high surface area for dye loading and multiple electron transport paths which facilitates light harvesting as well as efficient electron transport. [9] These properties in addition to the excellent light scattering property, render hierarchical TiO<sub>2</sub> microspheres attractive photoanode materials.[24-31] For example, power conversion efficiency (PCE) of more than 10 % has been achieved on DSSC based on mesoporous anatase TiO<sub>2</sub> beads and C101 dye.[32] Furthermore, photoanode based on dandelion-like rutile microspheres which also incorporates P25 NPs displays a conversion efficiency of 7.95 %.[29]

Besides tailoring the phase composition and morphology of TiO<sub>2</sub>, introducing more conductive additional components such as carbonaceous materials becomes an alternative option to obtain faster and more efficient electron transport in DSSCs. [33-36] Graphenes [37] and carbon nanotubes,[35] for example, have been utilized as additive components into TiO<sub>2</sub>. However, obtaining uniform dispersion of carbon and TiO<sub>2</sub> remains a challenge. Templating [34] has been shown to alleviate this problem though with the drawback of a more complicated procedure. A simpler route involves the addition of aqueous solution of glucose into TiO<sub>2</sub> NPs as the carbon precursor to form uniform carbon coating into TiO<sub>2</sub> following the heat treatment step.[38] Likewise, surfactants with long alkyl chains such as cetyltrimethylammonium bromide (CTAB) [39] and hexadecylamine (HDA) [40] can also be added during the sol-gel synthesis of TiO<sub>2</sub>, which can be converted into carbon *in situ* during heat treatment to achieve homogeneous carbon-TiO<sub>2</sub> composite.

Accordingly, in this work, we prepared two different TiO<sub>2</sub> beads to obtain improved TiO<sub>2</sub>-based photoanode performance in DSSCs. To this end, two different synthesis routes were performed; one involves HCl and another involves ammonia. The first synthesis leads to hierarchical carbon-doped TiO<sub>2</sub> beads which are comprised of rutile nanorods and rutile and brookite nanoparticles (Bead-A) while the second synthesis results in anatase TiO<sub>2</sub> beads (Bead-B). Relative to the conventional P25 and the anatase TiO<sub>2</sub> beads, the first bead (Bead-A) features higher electronic conductivity enabled by the hierarchical structure formed by the carbon-doped nanorods backbones as well as the synergy between the brookite and rutile particles. To exploit the high surface area functionality on the second bead (Bead-B), a bi-layer photoanode has been made by placing Bead-A film on top of Bead-B film. DSSC based on this bi-layer photoanode demonstrates an overall PCE of 7.24 % which compares favorably against the conventional pure P25 anode with only 5.41 %.

## 4.2 Experimental

### 4.2.1. Materials and syntheses

Titanium (IV) isopropoxide (TTIP), hexadecylamine (HDA), potassium chloride (KCl), hydrochloric acid (HCl, 32 wt.%), titanium tetrachloride (TiCl<sub>4</sub>), glacial acetic acid (HOAc), acetonitrile, ethyl cellulose (EC, 46070 and 46080), terpineol, and fluorine-doped tin oxide (FTO) glass (resistance ~8 Ω/sq., transmittance 80~81.5 %) were purchased from Sigma-Aldrich. Sodium hydroxide (NaOH), ammonia solution (NH<sub>4</sub>OH, 25 wt.%), and tert-butanol were purchased from Chem-Supply, Fisher Scientific and Ajax Finechem, respectively. N719 dye (MS003190), triiodide/iodide (I<sub>3</sub><sup>-</sup>/I<sup>-</sup>) electrolyte (MS005615) and platinum (Pt) counter-electrode solution (CELS, MS006220) were obtained from Dyesol. P25 (TiO<sub>2</sub>) was purchased from Degussa Co. Ltd.

#### 4.2.1.1. Synthesis of TiO<sub>2</sub> precursor beads

Amorphous TiO<sub>2</sub> precursor beads were prepared *via* a sol-gel process [40] with a

molar ratio of 0.5 HDA: 6.0 H<sub>2</sub>O: 0.0055 KCl: 224.1 ethanol:1.0 TTIP in the mixture solution.

#### **4.2.1.2. Synthesis of Bead-A**

One gram of precursor beads was dispersed in 30 mL 10 wt.% HCl solution and then transferred to an autoclave, which was maintained at 150 °C for 12 hours. The resultant precipitates were centrifuged and washed with de-ionized (DI) water and ethanol and finally dried at 60 °C in air. As-prepared powder was annealed at 500 °C for 2 hours in a muffle furnace and is denoted as Bead-A.

#### **4.2.1.3. Synthesis of Bead-B**

Bead-B was synthesized *via* a modified solvothermal treatment.[32, 40, 41] Briefly, one gram of precursor beads was dispersed in a mixture of 20 mL ethanol and 10 mL of 2 wt.% ammonia solution. The dispersion was autoclaved at 160 °C for 16 hours. The products were washed thoroughly with DI water and ethanol and then dried at 60 °C, followed by annealing at 500 °C for 2 hours.

#### **4.2.2. Preparation of TiO<sub>2</sub> working electrode**

A mixture of TiO<sub>2</sub> beads (Type A or B), P25, terpineol, EC, and HOAc at weight ratio of 1: 0.1: 2: 0.25: 0.21 (in their respective order) was dispersed in ethanol and magnetic stirred vigorously with mill balls for 20 hours. P25 nanoparticle was used as the void filler to improve the dye loading. The solvent (ethanol) was then evaporated at 60 °C, resulting in a viscous paste. The paste containing Bead-A or Bead-B was denoted as Paste-A or Paste-B, respectively. P25 paste was prepared according to the previous report,[42] where a mixture of P25, terpineol, and EC in the weight ratios of 1:4:0.5 was ball milled with ethanol for 2 hours and then subjected to rotary evaporation process at 40 °C to remove the solvent (ethanol). The FTO glasses were ultrasonically cleaned sequentially in detergent solution, water, ethanol, and acetone. The cleaned FTO glass plates were then immersed in a 40 mM aqueous TiCl<sub>4</sub> solution

at 70 °C for 30 min and were thoroughly rinsed with water and ethanol. P25 paste was firstly applied on the FTO glass at consistent thickness using doctor blade method. After relaxing the first layer at room temperature for 6 minutes and then drying at 125 °C for 6 minutes, Paste-A or B was applied on the top of P25 layer using doctor blade method. The area of the film and the thickness of the anodes were carefully adjusted to be 0.5 cm<sup>2</sup> and 12 μm (P25: 8-μm and beads: 4-μm), respectively. Following the staged sintering processes, i.e., at 325 °C for 5 minutes, 375 °C for 5 minutes, 450 °C for 15 minutes, and finally at 500 °C for 15 minutes, TiO<sub>2</sub> films were again subjected with a 40 mM aqueous TiCl<sub>4</sub> solution to improve the cell performance. After re-sintering at 500 °C for 30 minutes, the resultant TiO<sub>2</sub> films were immersed into 0.5 mM N719 dye solution in acetonitrile/tert-butanol (1:1 by volume) and kept at room temperature for 24 hours to complete the dye adsorption. After that, these films were rinsed by acetonitrile to remove the loosely physisorbed dye molecules.

#### **4.2.3. Fabrication of dye-sensitized solar cell**

For photovoltaic performance probing, these as-prepared dye-sensitized TiO<sub>2</sub>/FTO films were assembled with Pt counter electrodes. Pt counter electrodes were fabricated by spin-coating Pt CELS solution onto the FTO glasses and heat treatment at 450 °C for 30 minutes. The I<sub>3</sub><sup>-</sup>/I<sup>-</sup> electrolyte was injected into the void spaces between the photoanode and the counter electrode. The DSSC based on Bead-A-P25 or Bead-B-P25 bi-layer photoanode was denoted as Cell-A or Cell-B. As a control material, a cell with a 12-μm thick film of pure P25 was also prepared, referred as Cell-P25.

#### **4.2.4. Characterization**

The crystal structure, size and morphology of the samples were characterized by powder X-ray diffractometer (XRD, Bruker D8 Advance with Cu-Kα Radiation, λ = 1.5418 Å), field-emission scanning electron microscopy (FIBSEM, Zeiss Neon 40EsB), transmission electron microscopy (TEM, Titan G2 80-200), high-resolution

transmission electron microscopy (HRTEM), and selected area electron diffraction (SAED). The specific surface area and pore size distribution of the samples were analyzed by N<sub>2</sub> sorption (Micromeritics TriStar II 3020). The dye was desorbed into 0.1 M NaOH water/ethanol (1:1 by volume) solution to measure the adsorbed amount on the TiO<sub>2</sub> film. Ultraviolet-visible (UV-Vis) absorption spectra of the desorbed dye solution and the reflectance of TiO<sub>2</sub> films were recorded using a JASCO V-670 UV-Vis/NIR spectrophotometer. Thermogravimetric analysis (TGA, Mettler-Toledo) was performed with a heating rate of 5 °C min<sup>-1</sup> from room temperature to 900 °C under an air atmosphere. Elemental analysis and Fourier transform-infrared spectra (FT-IR) were performed by using a PerkinElmer 2400 Series II CHNS/O elemental analyzer and a PerkinElmer Spectrum 100 FTIR Spectrometer, respectively. The current-voltage characteristics of the DSSCs were recorded by an electrochemical workstation (Zahner Zennium and XPOT) under simulated AM 1.5 G illumination (100 mW cm<sup>-2</sup>) provided by a solar simulator (TriSOL, OAI). The incident light intensity was calibrated using a reference Si solar cell. The incident monochromatic photo-to-electron conversion efficiency (IPCE) spectra were measured as a function of wavelength from 400 to 800 nm using Oriel QE/IPCE DC Type Measurement Kit (Newport). The electrochemical impedance spectra (EIS) were measured by Zahner Zennium workstation at a bias potential of -0.761V in the dark with the frequency range from 10 mHz to 1 MHz and a 10 mV alternative signal. Intensity-modulated photovoltage spectroscopy (IMVS) and intensity-modulated photocurrent spectroscopy (IMPS) measurements were performed on Zahner CIMPS system (457 nm) under modulated light emitting diodes light (599 nm). The modulated light intensity was 10 % or less than the base light intensity with the frequency range change from 0.1 Hz to 1 kHz.

## 4.3 Results and discussion

### 4.3.1. Structure and morphology

Figure 4.1a shows the scanning electron microscope (SEM) image of Bead-A sample synthesized *via* hydrothermal route using hydrochloric acid (HCl). The sphere-shaped particles have an average diameter size of 2.0  $\mu\text{m}$  which are substantially larger than the average diameter size for the  $\text{TiO}_2$  precursor beads of 525 nm (Figure 4.2a). Its higher magnification image (Inset of Figure 4.1a) reveals the hierarchical structure of this sample which consists of radially assembled nanoparticles. The powder X-ray diffraction (XRD) pattern for Bead-A (Figure 4.1c) can be indexed according to a mixture of the characteristic peaks for rutile (JCPDS No.21-1276) and brookite  $\text{TiO}_2$  (JCPDS No.29-1360), indicating the simultaneous presence of these two phases. We also found that the concentration of HCl influences the morphology and phases structures. Hydrochloric acid at 10 wt.% is required to obtain the morphology displayed in Figure 4.1b. When 1 wt.% HCl was utilized, non-spherical particles formed with the deposited  $\text{TiO}_2$  nanoparticles spread over the entire surface area (Figure 4.2b). In the case of 5 wt.% HCl, despite the resultant hierarchical structure, irregular micrometer-sized particles appeared (Figure 4.2c). Powder XRD patterns for the 1 and 5 wt.% HCl samples additionally reveal the simultaneous co-existence of brookite, anatase, and rutile phases (Figure 4.2d). Whereas the 1 wt.% HCl sample is dominated by the anatase phase, 5 wt.% HCl sample has an equal proportion of anatase and rutile phases. Qualitative inspection on the intensities of the characteristic peaks of brookite phase on both samples suggest that approximately equal amount of brookite phase (as a minor phase) are present in both samples.

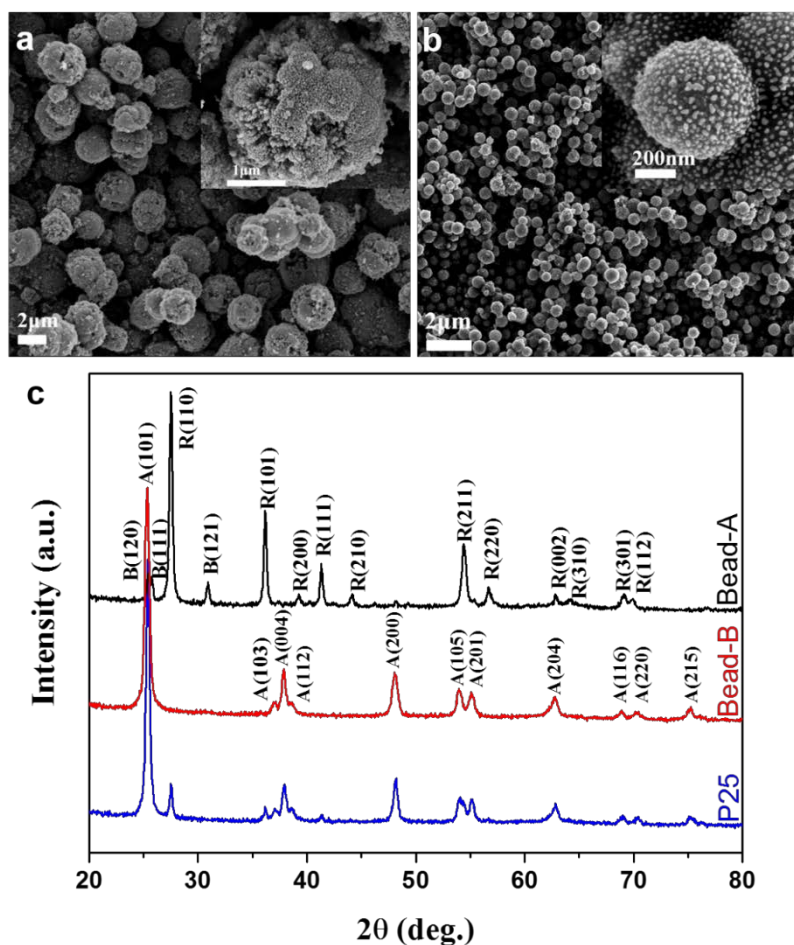


**Figure 4.1.** Scanning electron microscopy images of (a) Bead-A, (b) Bead-B and (c) Powder X-ray diffraction patterns of Bead-A, Bead-B, and P25.

Figure 4.1b depicts the morphology of Bead-B sample synthesized *via* modified solvothermal route using ammonia. The resultant spherical particles have relatively narrow particle size distribution with an average diameter size of 500 nm. Relative to its precursor (Figure 4.2a), the resultant particles have rougher surface and slightly smaller diameter after the synthesis process due to the particles shrunk during the synthesis. Powder XRD pattern for Bead-B sample shows only the characteristic peaks of anatase  $\text{TiO}_2$  as also reported in another work (Figure 4.1c).[40] These observations clearly highlight the pH-dependent phase selective crystallization of  $\text{TiO}_2$ ; in other words, it is possible to tailor the phase composition of  $\text{TiO}_2$  by adjusting the pH of the hydrothermal solution. In general, highly acidic condition favors the rutile phase formation while slightly basic condition promotes the formation of the

anatase phase.[43] Brookite phase, on the other hand, is considered as an intermediate metastable phase between the anatase and rutile phases.[43] The appearance of this phase in TiO<sub>2</sub> synthesized *via* HCl involving routes is likely related to the templating effect of Cl<sup>-</sup> ions in mild acidic solution.[44]

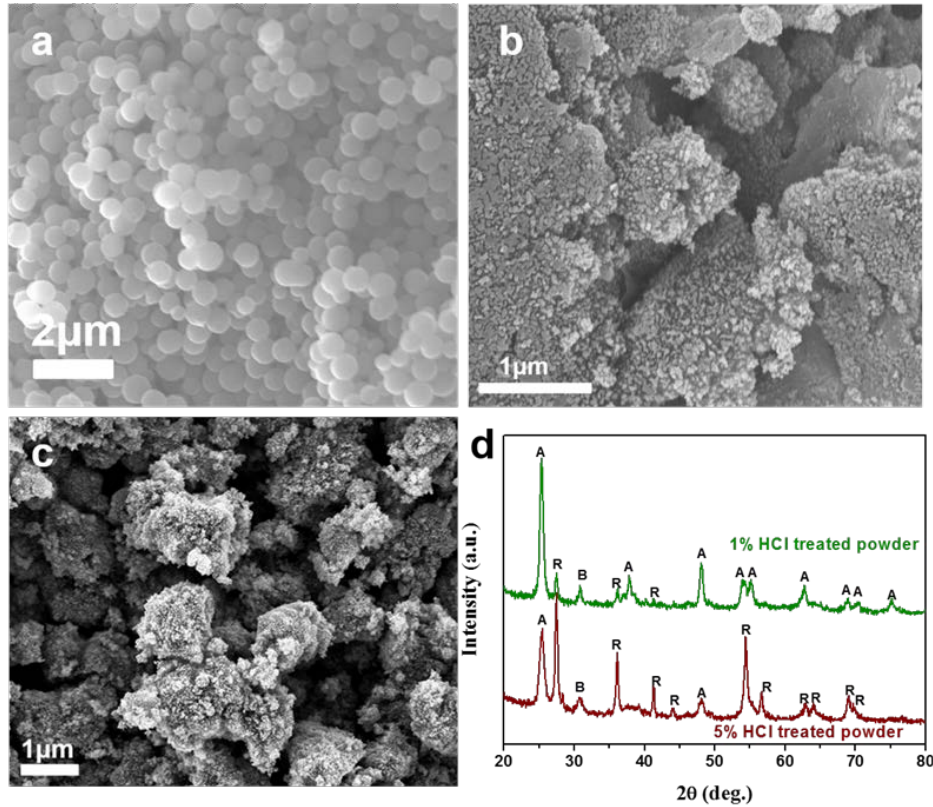


**Figure 4.2.** Scanning electron microscopy images of (a) precursor materials, (b) 1 wt% HCl sample, (c) 5 wt% HCl sample and (d) Powder X-ray diffraction patterns of 1 wt% HCl and 5 wt% HCl samples.

The morphologies and the interior structure features of two types of bead samples were further characterized using transmission electron microscopy (TEM). A typical Bead-A particle has fuzzy round shape morphology with rough edges (Figure 4.3a1). The corresponding selected area electron diffraction (SAED) pattern (Figure 4.3a2) shows the formation of polycrystalline ring patterns which can be indexed according to rutile and brookite phases. The calculated lattice spaces on these rings match the lattice spaces obtained on the powder XRD pattern for Bead-A sample, i.e., R(110), R(101), R(211), R(210) for rutile and B(111), B(120), B(121) for brookite phase. The fact that the diffraction rings are not composed entirely of continuous bright spots

alludes to the possible presence of amorphous material in Bead-A sample. High resolution transmission electron microscopy (HRTEM) image obtained at the edge of Bead-A sample (Figure 4.3a3) reveal the presence of ordered fringes with the lattice spaces of 0.351, 0.248 and 0.324 nm, corresponding to brookite (120), rutile (101) and rutile (110) planes, respectively. Rutile (110) plane in particular has perpendicular orientation relative to the radial direction. This indicates that Bead-A sample mainly consists of rutile nanorods which grew along the [001] direction,[29, 45] as also confirmed by an additional TEM image of the ultrasonic cracked sample (Figure 4.3a4). Several small nanoparticles (30-60 nm in size) appear along the nanorods and the edges of Bead-A sample. TEM elemental mapping on the cracked Bead-A sample further evidences the uniform carbon distribution on the material (Figure 4.3a5). It is worth noting that the carbon signals on the blank area surrounding the samples originate from the carbon film on the copper TEM grid. Some carbons are located within the nanorods. We attribute this to the HAD alkyl chain embedded within the beads during synthesis, which was carbonized *in situ* during the heat treatment at 500 °C for 2 hours in air. Carbon components on these brookite and rutile nanoparticles and rutile nanorods are expected to contribute to the improved electronic conductivity in DSSCs.[9, 34] Figure 4.3b1 displays a typical Bead-B particle which has a more uniform spherical shape (relative to Bead-A particle) and is densely packed by TiO<sub>2</sub> nanocrystals with an average size of 20 nm. The respective SAED pattern (Figure 4.3b2) in turn displays ring patterns characteristics of anatase phase. Moreover, HRTEM image (Figure 4.3b3) additionally reveals the presence of fringes with lattice space of 0.352 nm which matches the (101) planes of the anatase TiO<sub>2</sub>.

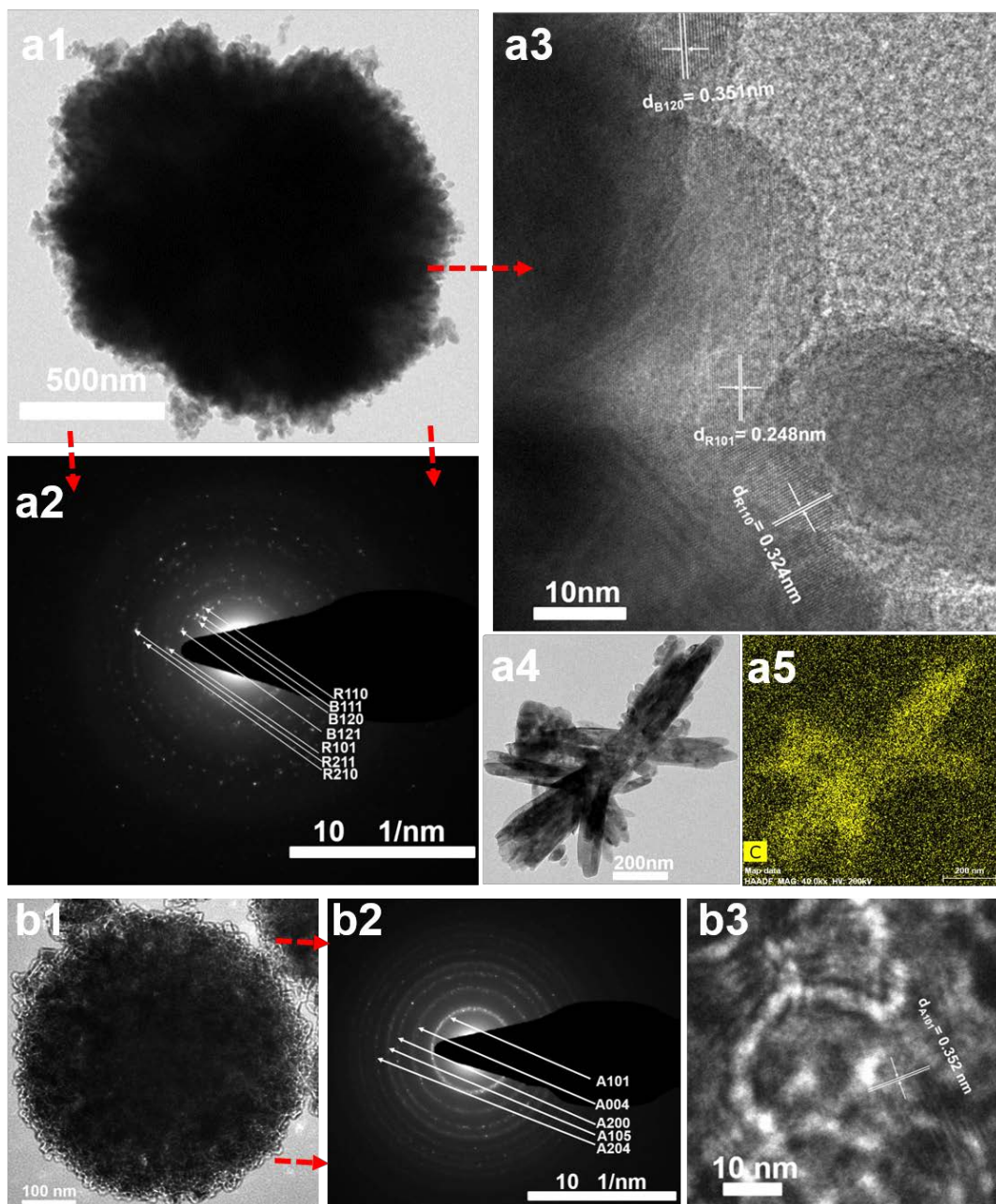


**Figure 4.3.** (a1) Transmission electron microscopy (TEM) image of Bead-A and its corresponding (a2) selected area electron diffraction (SAED) pattern and (a3) high resolution transmission electron microscopy (HRTEM) image (showing rutile and brookite phases); (a4) TEM image of cracked Bead-A sample and its (a5) carbon elemental mapping; (b1) TEM image of Bead-B sample and its corresponding (b2) SAED pattern and (b3) HRTEM image (showing anatase phase).

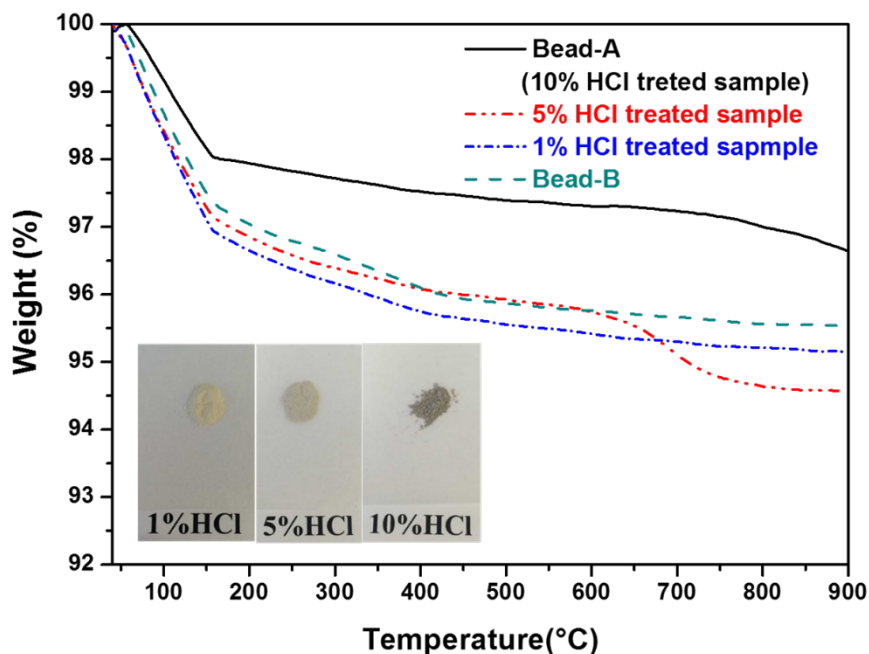


**Figure 4.4.** Thermal gravimetric analysis plots for four different TiO<sub>2</sub> samples prepared using the same precursor materials (Bead-A (10 wt% HCl), 5 wt% HCl, 1 wt% HCl and Bead-B (2 wt% ammonia)) and Inset – images for the three HCl samples.

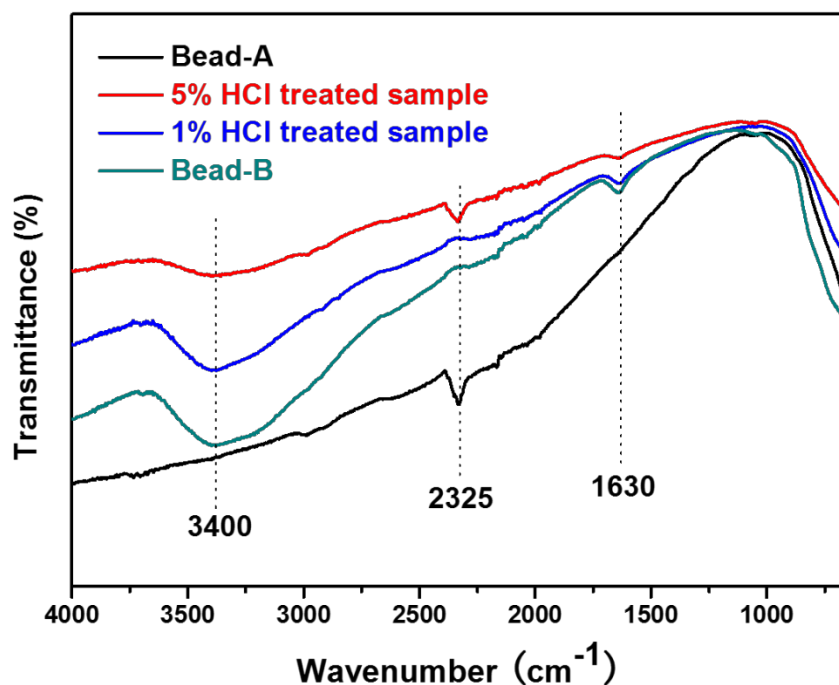


**Figure 4.5.** Fourier Transform-Infra Red spectra for four different TiO<sub>2</sub> samples prepared using the same precursor materials (Bead-A (10 wt% HCl), 5 wt% HCl, 1 wt% HCl and Bead-B (2 wt% ammonia)).

Thermal gravimetric analyses (TGA) were performed to examine the relative amount of water and organic content and the thermal weight loss as a function of temperature for 1 wt.%, 5 wt.%, and 10 wt.% HCl (Bead-A) and Bead-B samples, the results of which are shown in Figure 4.4. The 1 wt.% HCl sample exhibits an identical weight loss trend to the Bead-B sample. The weight loss below 150 °C reflects the evaporation of physically adsorbed water whereas the weight loss between 150 and 425 °C (accounting for about 1.5 wt% loss) corresponds to the removal of more strongly bound water molecular.[43] Fourier Transform-Infra Red (FTIR) spectra (Figure 4.5) for these four samples show the presence of other peaks at around 1630  $\text{cm}^{-1}$  that signify the bending vibrations of O–H on 1 wt.%, 5 wt.% HCl and Bead-B samples. Another broad band is additionally observed at 3400  $\text{cm}^{-1}$  for these three samples which represent surface hydroxyl groups and absorbed water molecules.[46] Beyond 600 °C, the profiles for 5 wt.% HCl and 10 wt.% HCl (Bead-A) samples demonstrate the on-going weight loss which is not the case for the other two samples. This is likely due to the decomposition of the embedded carbon as depicted earlier (Figure 4.3a5) and indicated also by the color difference between the three acid treated samples (Figure 4.4). Carbon doping is further proved by the peaks at 2325  $\text{cm}^{-1}$  appearing again only on the FTIR spectra of 5 wt.% HCl and 10 wt.% HCl (Bead-A) samples which can be assigned to  $\text{C}\equiv\text{C}$  bonds.[47] The carbon content of 5 wt.% HCl sample is approximately 1.1 wt.%. While the thermal carbon oxidation on 5 wt.% HCl sample can be completed below 800 °C; on 10 wt.% HCl (Bead-A) sample, this process still occurs up to 900 °C. Accordingly, the elemental analyses on these two samples reveal higher carbon content for 10 wt.% HCl (Bead-A) sample, i.e., approximately 15 wt.% higher than 5 wt.% HCl sample (the data is not shown here). These results imply that  $\text{TiO}_2$  nanoparticles in 10 wt.% HCl (Bead-A) sample were more densely stacked relative to the other samples. Another supporting piece of evidence is the specific surface area data, i.e., Brunauer-Emmett-Teller surface area from nitrogen sorption (Table 4.1) which shows that Bead-A has lower surface area (25.98  $\text{m}^2 \text{g}^{-1}$ ) and pore volume (0.16  $\text{cm}^3 \text{g}^{-1}$ ) than Bead-B (84.69  $\text{m}^2 \text{g}^{-1}$  and 0.31  $\text{cm}^3$

g<sup>-1</sup>) and P25 (58.33 m<sup>2</sup> g<sup>-1</sup> and 0.21 cm<sup>3</sup> g<sup>-1</sup>). This is additionally reflected by the Barrett-Joyner-Halenda pore size distribution plots (Figure 4.6). Bead-A plot displays two pore volumes distributions with one peaking at ~3 nm and another peaking at ~32 nm. The former may indicate the small “internal” pores (within the limit of N<sub>2</sub> sorption analysis) while the latter represents the voids between TiO<sub>2</sub> aggregates. Unlike Bead-A plot, Bead-B plot presents two peaks at ~4 nm and ~16 nm which correspond to the small “internal” pores within the beads and the spaces between beads, respectively.

**Table 4.1.** Nitrogen sorption results for Bead-A, Bead-B and P25

Sample name	S <sub>BET</sub> (m <sup>2</sup> /g)	V <sub>sp</sub> (cm <sup>3</sup> /g)
Bead-A	25.98	0.16
Bead-B	84.69	0.31
P25	58.33	0.21

S<sub>BET</sub> = Brunauer-Emmett-Teller (BET) specific surface area from N<sub>2</sub> sorption data in the P/Po range from 0.1 to 0.28. V<sub>sp</sub> = single-point pore volume calculated from the N<sub>2</sub> adsorption isotherm at P/Po = 0.98.

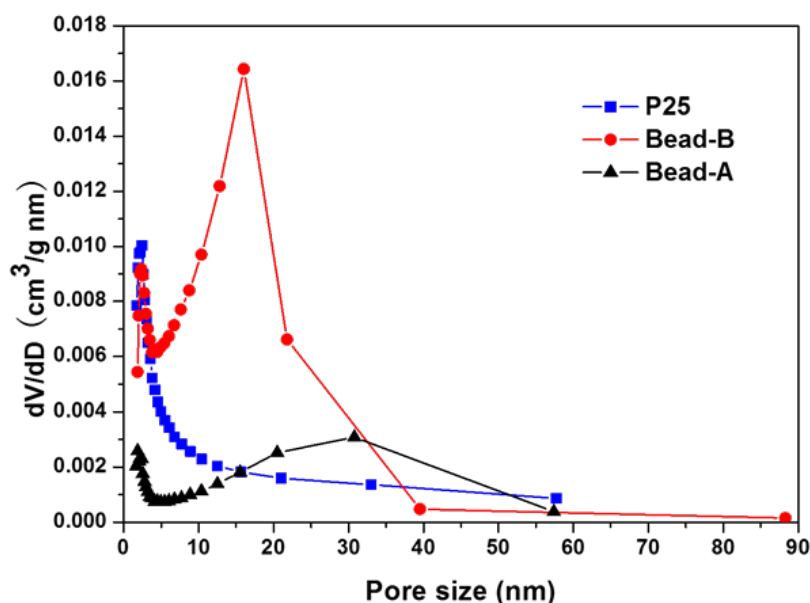


**Figure 4.6.** Barrett-Joyner-Halenda adsorption pore size distribution curves of P25, Bead-A and Bead-B.

### 4.3.2. Formation mechanism of TiO<sub>2</sub> beads

The formation mechanism of the two types of TiO<sub>2</sub> beads is illustrated in Figure 4.7. In the synthesis of TiO<sub>2</sub> precursor beads, hexadecylamine (HDA) works as a structure-directing agent interacting with titanium species by hydrogen-bonding to form organic-inorganic composites, which are further hydrolyzed and polymerized to form a condensed phase and finally precipitated from the solution.[40] The spherical shape of the precursor particles is driven by the minimization of the surface free energy.[40, 48] During the basic solvothermal process, ammonia may replace some HDA molecules that are bonded to titanium species but does not damage the structure integrity of the precursor beads.[40, 41] This explains the obtained narrow particle size and uniform distribution of Bead-B in spherical shape.

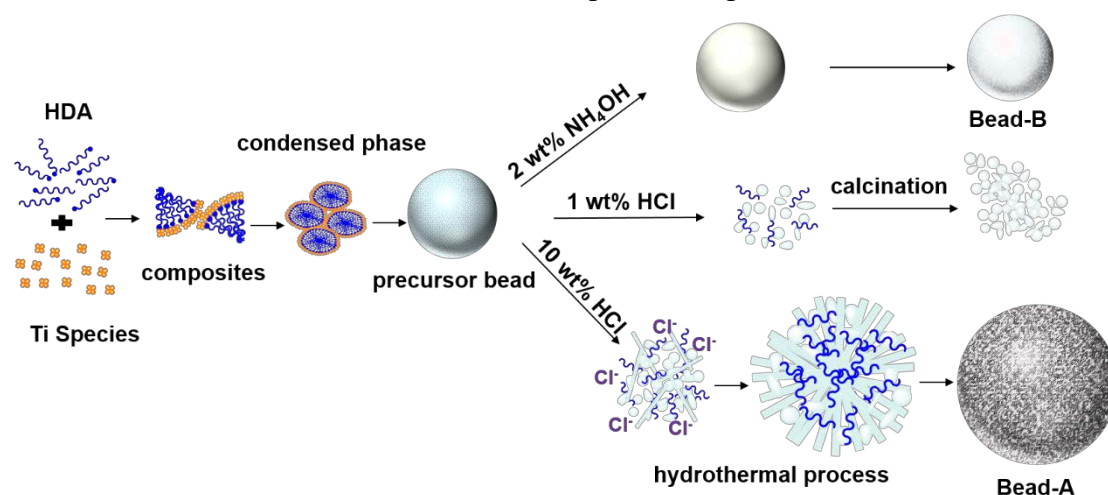


**Figure 4.7.** Schematic representation of the formation mechanism of different TiO<sub>2</sub> beads.

However, with the presence of hydrochloric acid, the hydrogen bond between HAD and titanium species would be broken down by the reaction between HCl and HAD. Under such circumstance, the spherical shape of the precursor beads can no longer be maintained during the solvothermal process. Moreover, highly acidic condition can also promote the phase transformation from anatase to rutile while accelerating the crystal growth.[43, 45, 49] In the case of HCl solution in low concentration (i.e., 1 %), despite the decomposed precursor bead structure, its acidity is not sufficiently strong to ensure fast subsequent crystal evolution rate. Therefore, the anatase phase becomes dominant in 1 wt.% HCl sample and leads to the formation of bulky aggregates

consisting of small particles (Figure 4.2b). The remaining alkyl chains of HAD on the surface of these particles are removed during the subsequent calcination. When higher concentration of HCl (i.e., 5 wt.% HCl) is employed, the rates of phase transformation and crystal growth are significantly enhanced, resulting in rutile dominated micrometer-sized hierarchical particles (Figure 4.2c). During the fast synthesis, some alkyl chains embedded inside these particles are converted into carbon after calcination. At even higher HCl concentration (i.e., 10 wt.% HCl), more chlorine ions would be selectively adsorbed on the rutile (110) plane, accelerating the anisotropic growth along [001] direction of the resultant nanorods.[29, 43, 45] These TiO<sub>2</sub> nanorods agglomerate into micrometer-sized sphere particles, quite identical to the morphology of Bead-A. The driving force behind such morphology change again is the reduction in the total surface energy which would cause grain contact and growth. Still, rutile nanoparticles oriented in (101) plane and brookite nanoparticles are also observed in Bead-A. In light of Ostwald ripening law, anatase nucleates and grows initially while rutile or brookite nuclei are formed at later stages by epitaxial growth at the expense of the anatase crystallites *via* dissolution and precipitation processes.[49] The low surface energy of (101) facet causes anatase to grow along (101) plane.[50] Recently, it has been reported that the preferentially oriented crystallographic (101) planes of rutile nanorods can grow on top of thick anatase seed layers at 120 °C.[51] Our work further showed that the aggregated anatase particles will lead to the anisotropic growth along (101) orientation in rutile phase. As such, more alkyl chains of HAD are entrapped within the beads given the rapid crystal growth and stacking between TiO<sub>2</sub> nanorods and nanoparticles, and subsequently transfers to carbon species.

### 4.3.3. Solar cells performances

The photocurrent density-photovoltage ( $J$ - $V$ ) plots of the three DSSCs are shown in Figure 4.8 while their respective photovoltaic parameters are listed in Table 4.2. Cell-A and Cell-B clearly demonstrate higher powder conversion efficiency (PCE,  $\eta$ )

relative to Cell-P25. Cell-A in particular displays short-circuit current density ( $J_{sc}$ ) of 13.25 mA cm<sup>-2</sup>, open circuit voltage ( $V_{oc}$ ) of 761 mV and PCE of 6.54 %. Cell-B, on the other hand, presents  $J_{sc}$  of 13.64 mA cm<sup>-2</sup>,  $V_{oc}$  of 738 mV and PCE of 6.53 %. These two cells compare favorably against Cell-P25 which delivers  $J_{sc}$  of 10.97 mA cm<sup>-2</sup>,  $V_{oc}$  of 706 mV and PCE of 5.41 %. The improved photovoltaic performance of Cell-A and Cell-B relative to Cell-P25 originates from the enhancements on  $J_{sc}$  and  $V_{oc}$ . Higher  $J_{sc}$  on Cell-B is contributed by its higher amount of dye uptake (116.8 nmol cm<sup>-2</sup>) as suggested by the highest specific surface area for Bead-B (relative to Bead-A and P25 – Table 4.1). Despite the lower amount of dye uptake for Cell-A (76.30 nmol cm<sup>-2</sup>) relative to that for Cell-P25 (88.38 nmol cm<sup>-2</sup>), higher  $J_{sc}$  for Cell-A reflects the superior light scattering properties and fast electron transport of Bead-A.[18, 25] This becomes apparent on the ultraviolet visible (UV-Vis) reflectance spectra (Figure 4.9). The reflectance of the bi-layer film consisting of P25 and Bead-B is higher than the other two bi-layer films in the wavelength range of 430 to 800 nm. The bi-layer film of P25 and Bead-A on the other hand show higher reflectance percentage (relative to the single film of P25) only beyond 530 nm wavelength. In spite of its larger particle size compared to Bead-B, Bead-A has inferior reflectance properties, most likely as the embedded carbon component exhibit visible light absorption properties.[34, 52] The presence of carbon species may, to some extent, decreases the light absorption by dye molecules leading to reduced light harvesting efficiency.[52] Therefore, the relatively high  $J_{sc}$  for Cell-A compared to Cell-B reflects the increased collection efficiency. The variation in the open circuit voltages ( $V_{oc}$ ) for the three different DSSCs is attributed to different recombination resistance and electron lifetime.

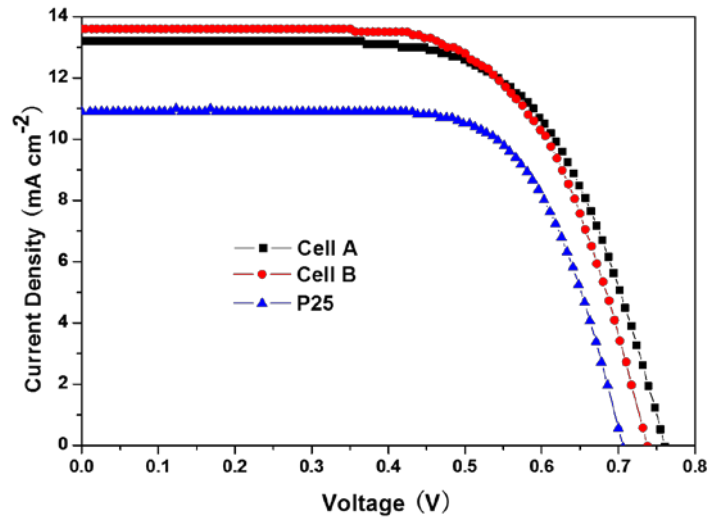


**Figure 4.8** Photocurrent density-photovoltage ( $J$ - $V$ ) characteristics of dye-sensitized solar cells based on three different  $\text{TiO}_2$  photoanodes measured under an illumination of one sun (AM 1.5G,  $100 \text{ mW cm}^{-2}$ ).

**Table 4.2.** Photovoltaic parameters of dye sensitized solar cells based on three different  $\text{TiO}_2$  photoanodes measured under AM 1.5 G one sun illumination.

Cell	$J_{sc}$ ( $\text{mA cm}^{-2}$ )	$V_{oc}$ (mV)	$FF$	$\eta$ (%)	Dye adsorption ( $\text{nmol cm}^{-2}$ )
Cell-A	13.25	761	0.65	6.54	76.30
Cell-B	13.64	738	0.65	6.53	116.80
Cell-P25	10.97	706	0.70	5.41	88.38

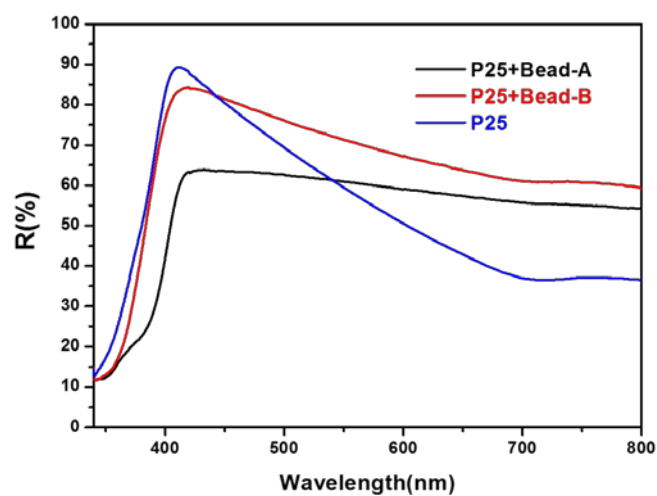


**Figure 4.9.** Diffused reflectance spectra of for bi-layer films of P25 + Bead-A and P25 + Bead-B including the single film of P25 (All films have the same thickness).

Electrochemical impedance spectroscopy (EIS), intensity-modulated photovoltage spectroscopy (IMVS), and intensity-modulated photocurrent spectroscopy (IMPS) were employed to investigate the dynamics of interfacial charge transfer process within the three DSSCs. Nyquist representation of the EIS spectra for these cells are depicted in Figure 4.10a. The semicircle arc in the high frequency region of 1 kHz to 1 MHz (at the left hand side of the plot) represents the charge transfer resistance and the capacitance from electrolyte|Pt interface whereas the larger semicircle in the low frequency region of 10 mHz to 1 kHz corresponds to the recombination resistance and capacitance from TiO<sub>2</sub>|electrolyte interface.[24] Typical equivalent circuit (shown as inset in Figure 4.10a) was used to resolve the values of the different circuit components, i.e., using ZSimpWin software. For example, the recombination resistance ( $R_2$ ) for Cell-A, Cell-B, and Cell-P25 is 36.1, 34.3, and 31.1  $\Omega$ , respectively. Higher resistance translates to slower electron-hole recombination rate. The electron lifetimes of Cell-A and Cell-B obtained from the respective Bode plot are approximately 37.3 ms, which is higher than that for Cell-P25 of 19.6 ms. The improved lifetime for Cell-A is attributed to the presence of 1D rutile nanorods and carbon doping which facilitates faster electron transport to suppress the recombination reaction. Moreover, the co-existence of brookite, rutile and anatase leads to more efficient electron/hole separation *via* vectorial displacement of electrons from one semiconductor to another. [53] In Cell-B case, dense packing of TiO<sub>2</sub> nanocrystals and their intimate contact is envisioned to suppress the “electron trapping” effect of the grain boundaries.[32] As such, the electron lifetime is enhanced.

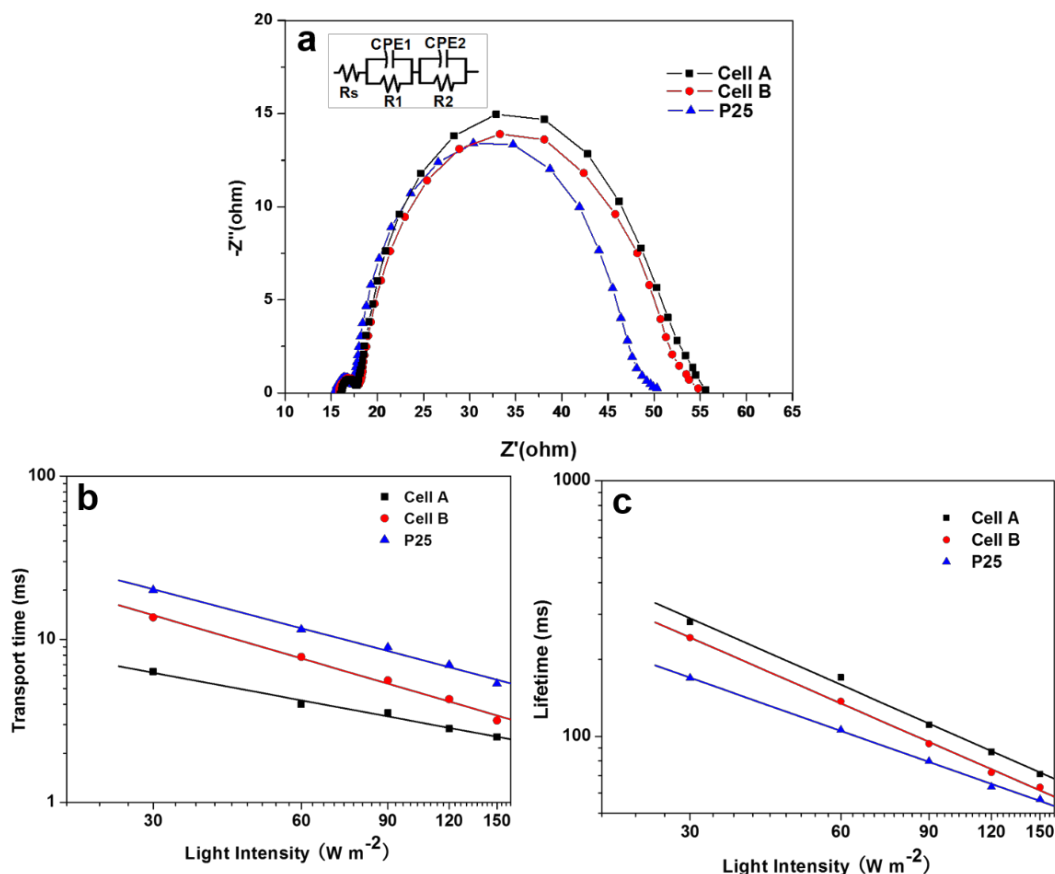


**Figure 4.10.** (a) Nyquist plot representation of the electrochemical impedance spectra; (b) Incident light intensity dependent transport time constant and (c) Lifetime constant for Cell-A, Cell-B and Cell-P25. Electrochemical impedance spectroscopy was performed in the dark at -0.761 V bias potential.

Figure 4.10b and c plot the electron transport time ( $\tau_d$ , IMPS) and electron lifetime ( $\tau_r$ , IMVS) as a function of light intensity. Due to the increasing injected electron concentration at higher light intensity, both time-related variables decrease with increasing light intensities. Cell-A provides the lowest electron transport time. The electron lifetimes for Cell-A and Cell-B are also higher than that for Cell-P25, consistent with the EIS results above. The electron lifetime decreases in the order of Cell-A, B and P25, echoing their open circuit voltages trends which also decrease in the same order. The charge-collection efficiency, i.e.,  $\eta_{cc}=1-(\tau_d/\tau_r)$ , [54] was calculated using the values obtained from IMPS and IMVS tests. The efficiency of Cell-A (~98-97%) is higher than Cell-B (~94-95%) and Cell-P25 (~88-90%) between the light intensity range of 30 to 150  $\text{W m}^{-2}$  (Figure 4.11). Taking into account the relation of

$J_{sc}=q\eta_{lh}\eta_{inj}\eta_{cc}I_0$ , [25] high photocurrent density for Cell-A is thus likely ascribed to its high charge-collection efficiency whereas the high photocurrent density for Cell-B is possibly contributed by its high charge harvest efficiency ( $\eta_{lh}$ ) given the high surface area of Bead-B which favors accommodating more dye molecules and its better light scattering properties. We hypothesized that DSSC by combining Bead-A and Bead-B will provide an even better performance than the individual cells.

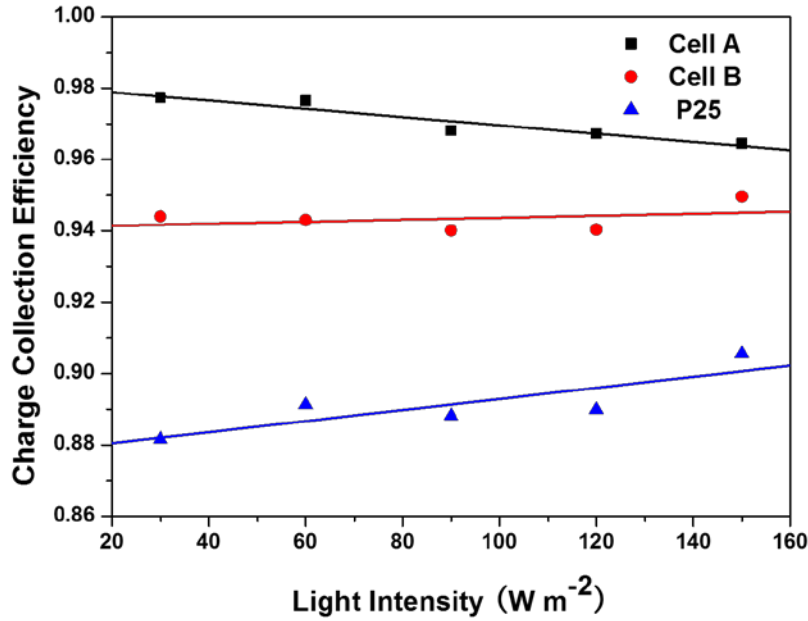


**Figure 4.11.** Charge collection efficiencies as a function of light intensity for Cell-A, Cell-B and Cell-P25.

The advantages of Bead-A in terms of fast electron transport and Bead-B for high dye loading can be combined *via* optimized arrangement to give synergy effect. This fourth cell is denoted as Cell-AB. The conduction band of anatase is generally viewed to lie about 0.2 eV above the conduction band of rutile so that the photogenerated electron should be transferred from anatase to rutile.[55] Nonetheless, recent studies showed that anatase has higher electron affinity than rutile, thus leading to photogenerated electron flow from rutile to anatase instead.[14, 56] With this logic, 4  $\mu\text{m}$ -thick film of Bead-A was coated on top of 7  $\mu\text{m}$ -thick film of Bead-B, forming Cell-AB. The photovoltaic performance of Cell-AB is displayed in Figure 4.12a, giving short-circuit current density ( $J_{sc}$ ) of 15.67  $\text{mA cm}^{-2}$ , open circuit voltage ( $V_{oc}$ ) of 721 mV, and PCE of 7.24 %. The dye loading for Cell-AB is 136.90  $\text{nmol cm}^{-2}$ ;

resulting in higher  $J_{sc}$  relative to their individual Bead-P25 components. Figure 4.12b in turn shows the Nyquist representation of the EIS spectra. The equivalent circuit fitting provides recombination resistance of 44.6  $\Omega$  and electron lifetime of 52.7 ms, both of which are larger than the three cells discussed above. The configuration we adopted here appears to suppress the reverse parasitic reaction between the injected electron and the triiodide ions ( $I_3^-$ ) in the electrolyte. Furthermore, the incident photo-current efficiency (IPCE) spectra for Cell-AB and Cell-P25 are displayed in Figure 4.12c. Cell-AB shows higher efficiency (relative to Cell-P25) over the tested wavelength range which we attribute to higher dye loading (400-600 nm) and enhanced light scattering properties from the combined films (600-800 nm). The conduction band of brookite was reported to be above the conduction band of rutile.[13, 53] The photogenerated electron should therefore flow from brookite to rutile in Bead-A. We propose one of the most possible mechanisms for photogenerated electron transfer in Cell-AB (Figure 4.12d). Two different transfer routes are actually taking place for the photoelectrons excited from dye molecules. The first route involves the conduction bands of three different  $TiO_2$  phases with the active role from the 1D rutile nanorods in Bead-A to enhance the electron transport rate. The alternative route involves photoelectron transfer *via* carbon species which remains in Bead-A to Bead-B. Although carbon may act as photosensitizer, carbon role as charge carrier is likely to be more dominant in this context. The electrons excited from the dye molecules or the electron that are transferred between the conduction bands can hop into carbon species which essentially contributes to reduced charge recombination and enhanced electron transport. Thus, the optimized performance for Cell-AB is due to the enhanced charge harvest efficiency and charge-collection efficiency.

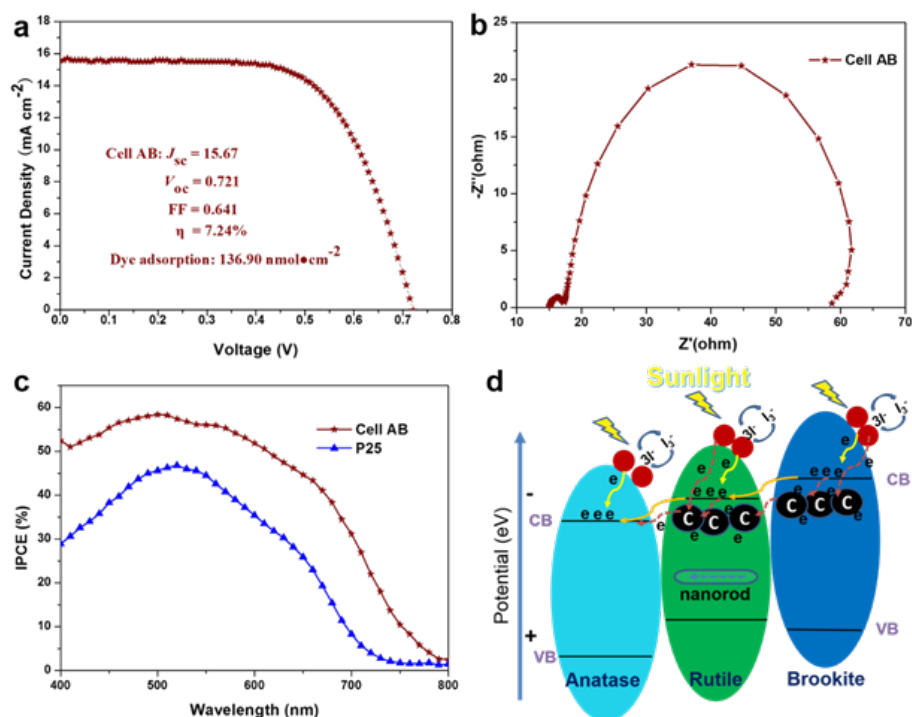


**Figure 4.12.** (a) Photocurrent density-photovoltage ( $J$ - $V$ ) characteristics of dye-sensitized solar cells based on the combination of Bead-A and Bead B photoanode (denoted as Cell-AB) measured under an illumination of one sun (AM 1.5G,  $100 \text{ mW cm}^{-2}$ ); (b) The respective Nyquist plot representation of the electrochemical impedance spectra (performed in the dark at  $-0.761 \text{ V}$  bias potential); (c) Incident photo-to-current efficiency spectra for Cell-AB and Cell-P25; and (d) Schematic diagram of one of the most possible mechanisms for photogenerated electron transfer in Cell-AB.

## 4.4 Conclusions

Two different hierarchical TiO<sub>2</sub> composites have been synthesized and characterized and their applications in solar cells have been explored. Bead-A was synthesized hydrothermally in the presence of 10 wt.% HCl while Bead-B was synthesized solvothermally in the presence of ammonia. Bead-B has smaller particle size than Bead-A, thus, it is superior in terms of surface area. In DSSC, this translates to superior dye loading. Bead-A, in contrast, has superior electronic conductivity from the carbon doping and the presence of 1D rutile nanorods. The synergy between these two composites can be achieved by placing the film of Bead-A above the film of

Bead-B. DSSC based on such bi-layer photoanode indeed displayed excellent performance exceeding the counterpart DSSCs based on their individual beads and P25 bi-layer films.

## References

1. Avrutin, V., N. Izyumskaya, and H. Morkoç, *Semiconductor solar cells: Recent progress in terrestrial applications*. Superlattices And Microstructures, 2011. **49**(4): p. 337-364.
2. Xu, T.T. and Q.Q. Qiao, *Conjugated polymer-inorganic semiconductor hybrid solar cells*. Energy & Environmental Science, 2011. **4**(8): p. 2700-2720.
3. Green, M.A., A. Ho-Baillie, and H.J. Snaith, *The emergence of perovskite solar cells*. Nature Photonics, 2014. **8**(7): p. 506-514.
4. Ruhle, S., M. Shalom, and A. Zaban, *Quantum-Dot-Sensitized Solar Cells*. Chemphyschem, 2010. **11**(11): p. 2290-2304.
5. Gong, J.W., J. Liang, and K. Sumathy, *Review on dye-sensitized solar cells (DSSCs): Fundamental concepts and novel materials*. Renewable & Sustainable Energy Reviews, 2012. **16**(8): p. 5848-5860.
6. Grätzel, M., *Dye-sensitized solar cells*. Journal of Photochemistry and Photobiology C: Photochemistry Reviews, 2003. **4**(2): p. 145-153.
7. Grätzel, M., *Recent Advances in Sensitized Mesoscopic Solar Cells*. Accounts Of Chemical Research, 2009. **42**(11): p. 1788-1798.
8. Bai, Y., et al., *Titanium Dioxide Nanomaterials for Photovoltaic Applications*. Chemical Reviews, 2014. **114**(19): p. 10095-10130.
9. Chen, H.Y., D.B. Kuang, and C.Y. Su, *Hierarchically micro/nanostructured photoanode materials for dye-sensitized solar cells*. Journal of Materials Chemistry, 2012. **22**(31): p. 15475-15489.
10. Abdi-Jalebi, M., M.R. Mohammadi, and D.J. Fray, *Double-Layer TiO<sub>2</sub> Electrodes with Controlled Phase Composition and Morphology for Efficient Light Management in Dye-Sensitized Solar Cells*. Journal Of Cluster Science, 2014. **25**(4): p. 1029-1045.
11. Luo, Z., et al., *Crystalline Mixed Phase (Anatase/Rutile) Mesoporous Titanium Dioxides for Visible Light Photocatalytic Activity*. Chemistry Of Materials, 2015. **27**(1): p. 6-17.
12. Jiao, Y., et al., *Anatase grain loaded brookite nanoflower hybrid with superior photocatalytic activity for organic degradation*. Colloids and Surfaces A: Physicochemical and Engineering Aspects, 2012. **402**: p. 66-71.
13. Boppella, R., P. Basak, and S.V. Manorama, *Viable Method for the Synthesis of Biphasic TiO<sub>2</sub> Nanocrystals with Tunable Phase Composition and Enabled Visible-Light Photocatalytic Performance*. Acs Applied Materials & Interfaces, 2012. **4**(3): p. 1239-1246.
14. Li, G., et al., *Synergistic effect between anatase and rutile TiO<sub>2</sub> nanoparticles in dye-sensitized solar cells*. Dalton Transactions, 2009(45): p. 10078-10085.
15. Subramanian, A., C.-Y. Ho, and H. Wang, *Investigation of various photoanode structures on dye-sensitized solar cell performance using mixed-phase TiO<sub>2</sub>*. Journal Of Alloys And Compounds, 2013. **572**: p. 11-16.
16. Hwang, Y.K., et al., *Preparation of Anatase/Rutile Mixed-Phase Titania Nanoparticles for Dye-*

- Sensitized Solar Cells*. Journal of Nanoscience and Nanotechnology, 2013. **13**(3): p. 2255-2261.
17. Xu, J., et al., *Composite electrode of TiO<sub>2</sub> particles with different crystal phases and morphology to significantly improve the performance of dye-sensitized solar cells*. RSC Advances, 2015. **5**(41): p. 32536-32545.
  18. Wu, W.Q., et al., *Hierarchical Oriented Anatase TiO<sub>2</sub> Nanostructure arrays on Flexible Substrate for Efficient Dye-sensitized Solar Cells*. Scientific Reports, 2013. **3**: p. 1892.
  19. Huang, Q., et al., *TiO<sub>2</sub> nanorod arrays grown from a mixed acid medium for efficient dye-sensitized solar cells*. Energy & Environmental Science, 2011. **4**(6): p. 2145-2151.
  20. Lv, M., et al., *Densely aligned rutile TiO<sub>2</sub> nanorod arrays with high surface area for efficient dye-sensitized solar cells*. Nanoscale, 2012. **4**(19): p. 5872-5879.
  21. Liao, J.Y., et al., *Hydrothermal Fabrication of Quasi-One-Dimensional Single-Crystalline Anatase TiO<sub>2</sub> Nanostructures on FTO Glass and Their Applications in Dye-Sensitized Solar Cells*. Chemistry – A European Journal, 2011. **17**(4): p. 1352-1357.
  22. Roy, P., et al., *TiO<sub>2</sub> nanotubes and their application in dye-sensitized solar cells*. Nanoscale, 2010. **2**(1): p. 45-59.
  23. Yu, H., et al., *Hydrothermal Synthesis of a Crystalline Rutile TiO<sub>2</sub> Nanorod Based Network for Efficient Dye-Sensitized Solar Cells*. Chemistry – A European Journal, 2013. **19**(40): p. 13569-13574.
  24. Liao, J.Y., et al., *High-performance dye-sensitized solar cells based on hierarchical yolk-shell anatase TiO<sub>2</sub> beads*. Journal Of Materials Chemistry, 2012. **22**(4): p. 1627-1633.
  25. Liao, J.Y., et al., *Tri-functional hierarchical TiO<sub>2</sub> spheres consisting of anatase nanorods and nanoparticles for high efficiency dye-sensitized solar cells*. Energy & Environmental Science, 2011. **4**(10): p. 4079-4085.
  26. Zhang, H., et al., *Rutile TiO<sub>2</sub> microspheres with exposed nano-acicular single crystals for dye-sensitized solar cells*. Nano Research, 2011. **4**(10): p. 938-947.
  27. Wu, X., G.Q. Lu, and L. Wang, *Dual-Functional Upconverter-Doped TiO<sub>2</sub> Hollow Shells for Light Scattering and Near-Infrared Sunlight Harvesting in Dye-Sensitized Solar Cells*. Advanced Energy Materials, 2013. **3**(6): p. 704-707.
  28. Wu, X., G.Q. Lu, and L. Wang, *Shell-in-shell TiO<sub>2</sub> hollow spheres synthesized by one-pot hydrothermal method for dye-sensitized solar cell application*. Energy & Environmental Science, 2011. **4**(9): p. 3565-3572.
  29. He, Z., et al., *A one-pot solvothermal synthesis of hierarchical microspheres with radially assembled single-crystalline TiO<sub>2</sub>-nanorods for high performance dye-sensitized solar cells*. Journal of Materials Chemistry C, 2014. **2**(8): p. 1381-1385.
  30. Yang, W., et al., *A facile synthesis of anatase TiO<sub>2</sub> nanosheets-based hierarchical spheres with over 90% {001} facets for dye-sensitized solar cells*. Chemical Communications, 2011. **47**(6): p. 1809-1811.
  31. Fan, K., et al., *A simple preparation method for quasi-solid-state flexible dye-sensitized solar cells by using sea urchin-like anatase TiO<sub>2</sub> microspheres*. Journal Of Power Sources, 2013. **222**: p. 38-44.
  32. Sauvage, F., et al., *Dye-Sensitized Solar Cells Employing a Single Film of Mesoporous TiO<sub>2</sub> Beads Achieve Power Conversion Efficiencies Over 10%*. Acs Nano, 2010. **4**(8): p. 4420-4425.
  33. Dembele, K.T., et al., *Hybrid Carbon Nanotubes–TiO<sub>2</sub> Photoanodes for High Efficiency Dye-*

- Sensitized Solar Cells*. The Journal of Physical Chemistry C, 2013. **117**(28): p. 14510-14517.
34. Quan, L.N., et al., *Mesoporous Carbon-TiO<sub>2</sub> Beads with Nanotextured Surfaces as Photoanodes in Dye-Sensitized Solar Cells*. Chemsuschem, 2014. **7**(9): p. 2590-2596.
  35. Mehmood, U., et al., *Hybrid TiO<sub>2</sub>-multiwall carbon nanotube (MWCNTs) photoanodes for efficient dye sensitized solar cells (DSSCs)*. Solar Energy Materials And Solar Cells, 2015. **140**: p. 174-179.
  36. Lee, T.Y., P.S. Alegaonkar, and J.-B. Yoo, *Fabrication of dye sensitized solar cell using TiO<sub>2</sub> coated carbon nanotubes*. Thin Solid Films, 2007. **515**(12): p. 5131-5135.
  37. Yang, N., et al., *Two-Dimensional Graphene Bridges Enhanced Photoinduced Charge Transport in Dye-Sensitized Solar Cells*. ACS Nano, 2010. **4**(2): p. 887-894.
  38. Jang, Y.J., Y.H. Jang, and D.H. Kim, *Carbohydrate-Derived Carbon Sheaths on TiO<sub>2</sub> Nanoparticle Photoanodes for Efficiency Enhancement in Dye-Sensitized Solar Cells*. Particle & Particle Systems Characterization, 2013. **30**(12): p. 1030-1033.
  39. Lee, D.U., et al., *CTAB facilitated spherical rutile TiO<sub>2</sub> particles and their advantage in a dye-sensitized solar cell*. Solar Energy, 2008. **82**(11): p. 1042-1048.
  40. Chen, D.H., et al., *Synthesis of Monodisperse Mesoporous Titania Beads with Controllable Diameter, High Surface Areas, and Variable Pore Diameters (14–23 nm)*. Journal Of The American Chemical Society, 2010. **132**(12): p. 4438-4444.
  41. Chen, D.H., et al., *Mesoporous Anatase TiO<sub>2</sub> Beads with High Surface Areas and Controllable Pore Sizes: A Superior Candidate for High-Performance Dye-Sensitized Solar Cells*. Advanced Materials, 2009. **21**(21): p. 2206-2210.
  42. Ito, S., et al., *Fabrication of thin film dye sensitized solar cells with solar to electric power conversion efficiency over 10%*. Thin Solid Films, 2008. **516**(14): p. 4613-4619.
  43. Li, J.G., T. Ishigaki, and X.D. Sun, *Anatase, Brookite, and Rutile Nanocrystals via Redox Reactions under Mild Hydrothermal Conditions: Phase-Selective Synthesis and Physicochemical Properties*. The Journal of Physical Chemistry C, 2007. **111**(13): p. 4969-4976.
  44. Pottier, A., et al., *Synthesis of brookite TiO<sub>2</sub> nanoparticles by thermolysis of TiCl<sub>4</sub> in strongly acidic aqueous media*. Journal Of Materials Chemistry, 2001. **11**(4): p. 1116-1121.
  45. Zhou, J., et al., *Effects of acid on the microstructures and properties of three-dimensional TiO<sub>2</sub> hierarchical structures by solvothermal method*. Nanoscale Research Letters, 2012. **7**(1): p. 217-217.
  46. Tian, B., et al., *Synthesis and characterization of nitrogen-doped titanium dioxide nanomaterials derived from nanotube sodium titanate precursor*. Journal Of Materials Research, 2012. **27**(18): p. 2408-2416.
  47. Malik, D.S., C.K. Jain, and A.K. Yadav, *Preparation and characterization of plant based low cost adsorbents*. Journal of Global Biosciences, 2015. **4**(Special Issue 1): p. 1824-1829.
  48. Yu, C., et al., *Morphology Development of Mesoporous Materials: a Colloidal Phase Separation Mechanism*. Chemistry Of Materials, 2004. **16**(5): p. 889-898.
  49. Wu, M., et al., *Sol-Hydrothermal Synthesis and Hydrothermally Structural Evolution of Nanocrystal Titanium Dioxide*. Chemistry Of Materials, 2002. **14**(5): p. 1974-1980.
  50. Penn, R.L. and J.F. Banfield, *Morphology development and crystal growth in nanocrystalline aggregates under hydrothermal conditions: insights from titania*. Geochimica Et Cosmochimica Acta, 1999. **63**(10): p. 1549-1557.
  51. Soundarrajan, P., et al., *Controlled (110) and (101) crystallographic plane growth of single*

- crystalline rutile TiO<sub>2</sub> nanorods by facile low cost chemical methods*. CrystEngComm, 2014. **16**(37): p. 8756-8768.
52. Kim, H.N., H. Yoo, and J.H. Moon, *Graphene-embedded 3D TiO<sub>2</sub> inverse opal electrodes for highly efficient dye-sensitized solar cells: morphological characteristics and photocurrent enhancement*. Nanoscale, 2013. **5**(10): p. 4200-4204.
53. Di Paola, A., M. Bellardita, and L. Palmisano, *Brookite, the Least Known TiO<sub>2</sub> Photocatalyst*. Catalysts, 2013. **3**(1): p. 36.
54. Schlichthörl, G., N.G. Park, and A.J. Frank, *Evaluation of the Charge-Collection Efficiency of Dye-Sensitized Nanocrystalline TiO<sub>2</sub> Solar Cells*. The Journal of Physical Chemistry B, 1999. **103**(5): p. 782-791.
55. Nakajima, H., et al., *Photoluminescence study of mixtures of anatase and rutile TiO<sub>2</sub> nanoparticles: Influence of charge transfer between the nanoparticles on their photoluminescence excitation bands*. Chemical Physics Letters, 2005. **409**(1-3): p. 81-84.
56. Scanlon, D.O., et al., *Band alignment of rutile and anatase TiO<sub>2</sub>*. Nat Mater, 2013. **12**(9): p. 798-801.

*Every reasonable effort has been made to acknowledge the owners of copyright material. I would be pleased to hear from any copyright owner who has been omitted or incorrectly acknowledged.*

## **Chapter 5: Carbon-dot/natural-dye sensitizer for TiO<sub>2</sub> solar cells**

### **prepared by a one-step treatment of celery leaf extract**

#### **Abstract**

Attempts have been made to create artificial photovoltaic (PV) devices that can harness sunlight in an economic, clean, and efficient way by mimicking natural photosynthesis process. Inspired by the role of chlorophyll in such photosynthesis, we introduced pheophytins/pyropheophytins capped carbon dots (CDs), a non-toxic and biocompatible sensitizer, into the dye-sensitized solar cell system. The CDs hybrids were synthesized *via* a single step hydrothermal treatment of celery leaves extracts. The effects of hydrothermal temperature on the particle size, surface composition, optical properties of CDs, and the survival rate of the natural dyes were studied. CDs heated at 120 °C (C-120) display relatively homogenous smaller particle size distribution around the average size of 5.9 nm and lower photoluminescence emission intensity relative to their counterparts that were obtained at higher temperatures (150 °C and 180 °C). In C-120 case, graphitic carbon adhered on its surface. It also has higher amount of surviving dye molecules which were subsequently converted into pheophytins or pyropheophytins given its relatively low hydrothermal temperature. The nanocrystalline TiO<sub>2</sub> solar cells based on C-120 demonstrated the highest power conversion efficiency (PCE) of 0.48% under AM 1.5G one full sun illumination. Such performance represents significant achievement given the normally lower than 0.20% conversion efficiencies for most biomass-derived carbon dots sensitized devices. Besides functioning as light sensitizer, C-120 CDs with lower amount of trap states can also work as an effective electron transfer intermediate to improve the interaction between dye and TiO<sub>2</sub> and suppress the photogenerated carrier recombination, thus providing improved solar cell performance. This work paves a potential route to fabricate highly efficient PV devices and light-to-energy conversion systems with minimized environmental impact.

## 5.1 Introduction

To address the increasing global energy demand, efficient conversion and utilization of solar energy has become one of the most important research goals. Using photovoltaic (PV) devices to convert sunlight into electricity is an attractive solution.[1] The third-generation PVs, such as dye-sensitized, polymer-inorganic hybrid, quantum dot, and perovskite solar cells, have been developed to reduce the cost and improve the performance.[2, 3] However, noble or highly toxic metals containing materials, such as Ru-based dyes,[4] Cd chalcogenides (i.e., CdS, CdSe, and CdTe) for quantum dots,[5] and perovskites with Pb,[6] have been widely used to achieve higher power conversion efficiency (PCE). It is important to find more economic and environmentally benign alternatives for the sustainable development of solar cells.

Carbon dots (CDs) is a cheap, non-toxic, and biocompatible member of carbonaceous nanomaterial family that can be potentially be used as sensitizers for PV application because of their stable light absorption, good polar solvent solubility, compatible surface chemistry, unique electron transport properties, and edge and quantum confinement effects.[7-10] For example, Mirtchev et al. have prepared water-soluble CDs *via* chemical carbonization of  $\gamma$ -butyrolactone and used them as sensitizer for nanocrystalline-TiO<sub>2</sub> solar cell that displayed a PCE of 0.13%.[9] Zhang et al. reported a solar cell based on nitrogen-doped CDs with an identical PCE.[11] Briscoe et al. firstly fabricated solid-state solar cells based on ZnO nanorods with biomass-derived CDs as sensitizer, which shows 0.077% efficiency.[12] Recently, Wang et al. reported a nitrogen-doped CD solar cell that can provide a PEC of 0.79%.[13] Our group also achieved a PEC of 0.11% on the solar cell based on CDs derived from bee pollens.[14] Unlike the semiconductor quantum dot solar cell, the low short-circuit current density ( $J_{sc}$ ) is the main factor behind the low efficiency of CD solar cell. This is since CDs have narrow light absorption that is mainly centered at ultra-violet (UV) region and various trap states as demonstrated by their excitation-dependent

fluorescence which lead to the recombination of photoinduced carriers.[7, 13]

CDs can also function as an electron transfer intermediate in the dye-semiconductor complex system for the solar cell application. Ma et al. reported that the CDs incorporation into the rhodamine B-TiO<sub>2</sub> system can significantly improve the solar cell performance, leading to 7 times higher PCE relative to the non CDs-containing cell.[15] They also demonstrated that the simultaneous use of CDs as electron donors and acceptors could enhance the UV-Vis absorbance of rhodamine B, improve the electron transfer, and suppress the recombination of photogenerated carriers. Therefore, the CD-doped dye/semiconductor system provides a new approach to obtain dye-sensitized solar cells (DSSCs) with high efficiency.

As the main light harvester, dye is one of the key determinants for the efficiency of DSSCs. Employing synthetic dyes as sensitizer may provide high efficiency and durability, but they have high cost, high degradation tendency, and toxicity. In terms of safety and economy, natural plant pigments such as anthocyanin, flavonoid, carotenoid, and chlorophyll, can be considered as an attractive sensitizer alternative for DSSCs.[16] Among them, chlorophyll with porphyrin-based chromophores has been utilized in nature to harvest light for the conversion of solar energy in the complex photosynthetic processes.[17] In mimicking the natural photosystems, CDs having aromatic carbon framework with functional groups may work synergistically with the porphyrin ring of chlorophylls as a bridge to improve the electron/energy transfer in the chlorophyll-TiO<sub>2</sub> system.[18]

Instead of adding CDs into dye solution, in this work, we obtained a CD-dye complex *via* a facile single step hydrothermal treatment of green extractives from celery leaves. Carbon dots can be synthesized from natural bio-resources *via* bottom-up route.[19, 20] Chlorophylls, on the other hand, can be converted to pheophytins and/or pyropheophytins maintaining the porphyrin structure *via* an appropriate heat treatment.[21] The hydrothermal temperature influenced the formation of CDs and the survival of dye molecules. For example, after heating at 120 °C for 2.5 hours, the obtained CDs with graphitic carbon adhered on the main body have smaller particles

sizes (average of 5.9 nm), lower aggregation tendency, and less trap states relative to the CDs prepared at higher temperatures. These features reduced the photoluminescence emission intensity of CD and dye molecules, indicating the facile electron transport between dye and CDs. By affording the presence of more dyes at low temperature and graphitic carbon as electron transfer bridge, the nanocrystalline TiO<sub>2</sub> solar cells based on the 120 °C treated sensitizer achieved the highest PCE of 0.48% under AM 1.5G one full sun illumination. This is 1.7 times higher than the solar cell based on the original extract as the sensitizer and is 1.5 times higher than the one based on the 180 °C treated sensitizer. In addition, this work highlights the potential to such CDs that features the excellent photo-generated electron collection and donation properties as an intermediate for the directional control of light excited electron transfer, leading to significant improvement in the solar cell performance.

## **5.2 Experimental Section**

### **5.2.1 Materials**

Fresh celery was purchased from local market. The leaves were plucked off the thin stems at the top of the stalk and were washed thoroughly prior to their use. The commercial TiO<sub>2</sub> powder (P25, with an average particle size of ~20 nm) was purchased from Degussa Co. Ltd. Ethyl cellulose (EC, 46070 and 46080). Titanium tetrachloride (TiCl<sub>4</sub>), terpineol, and quinine sulfate were purchased from Sigma-Aldrich while triiodide/iodide (I<sub>3</sub><sup>-</sup>/I<sup>-</sup>) electrolyte (MS005615) and fluorine-doped tin oxide (FTO) glass substrates (TEC8, 2.2 mm, resistance ~8 Ω/sq) were bought from Dyesol.

### **5.2.2 Dye extraction and Carbon Dots synthesis**

About 50 g fresh celery leaves were crushed in a blender. The crushed biomass was mixed with 250 mL absolute ethanol and was filtered to obtain a stock solution. The green stock solution was kept at ~5 °C away from light for further use. About 20 mL

of this stock solution was then transferred into a 60 mL Teflon-lined stainless steel autoclave and was heated at different temperatures for 2.5 h in an oven. The autoclaved products were centrifuged at 15,000 rpm for 10 min to remove larger particles. These CD supernatants after 120 °C, 150 °C and 180 °C autoclaving are denoted as C-120, C-150, C-180, respectively. For comparison, the stock solution was also centrifuged at 15,000 rpm for 10 min. The product is denoted as C-000.

### 5.2.3 Solar cell fabrication

The TiO<sub>2</sub> photoanodes were fabricated according to our previous report.[22] The cleaned FTO glasses were immersed in 40 mM TiCl<sub>4</sub> aqueous solution at 70 °C for 30 min and were washed with water and ethanol. A TiO<sub>2</sub> paste (P25, terpineol and EC with the weight ratios of 1:4:0.5) was doctor bladed onto FTO glasses and the films were then calcined at 325 °C for 5 min, 375 °C for 5 min, 450 °C for 15 min, and finally at 500 °C for 15 min. Following dipping into the TiCl<sub>4</sub> solution and re-sintering at 500 °C for 30 min, the resultant TiO<sub>2</sub> films were immersed into C-000, C-120, C-150, and C-180 solution at room temperature for 24 h. The dye and CDs-sensitized TiO<sub>2</sub> films were washed with absolute ethanol and dried at nitrogen gas stream. The solar cells were fabricated by injecting I<sub>3</sub><sup>-</sup>/I<sup>-</sup> electrolyte into the void space between the photoanode and the platinum coated FTO counter electrode.

### 5.2.4 Characterization and Measurement

Transmission electron microscopy (TEM) and high-resolution TEM (HRTEM) images were obtained with a Titan G2 80-200 transmission electron microscope. The morphology of centrifuged precipitation samples was characterized by field-emission scanning electron microscope (FESEM, Zeiss Neon 40EsB). Ultraviolet-visible (UV-Vis) absorption spectra of dye or/and CDs solutions and the sensitized TiO<sub>2</sub> anodes were recorded using a JASCO V-670 UV-Vis/NIR spectrophotometer. Fourier transform-infrared spectra (FT-IR) and photoluminescence (PL) emission spectra was performed by using a PerkinElmer Spectrum 100 FTIR spectrometer and

PerkinElmer LS 55 Fluorescence spectrometer, respectively. X-ray photoelectron spectroscopy (XPS) measurements were conducted on a Kratos AXIS Ultra DLD machine with a monochromatic Al-K $\alpha$  X-ray gun. The current-voltage characteristics of the solar cells and the transient short-circuit photocurrent of sensitized TiO<sub>2</sub> anodes were recorded by an electrochemical workstation (Zahner Zennium and XPOT) under simulated AM 1.5 G illumination (100 mW cm<sup>-2</sup>) provided by a solar simulator (TriSOL, OAI). The quantum yields of CDs were calculated by:

$$\Phi_S = \Phi_R \left( \frac{A_R}{A_S} \right) \left( \frac{I_S}{I_R} \right) \left( \frac{\eta_S^2}{\eta_R^2} \right)$$

where  $\Phi$  is the quantum yield,  $I$  is the integrated PL intensity,  $A$  is the optical density and  $\eta$  is the refractive index of the solvent. The subscript  $S$  and  $R$  refer to the sample and the reference, respectively. Here, quinine sulfate was chosen as the reference, whose quantum yield is 54% in 0.1M sulfuric acid solution.[13]

## 5.3 Results and Discussion

### 5.3.1 Structure and morphology

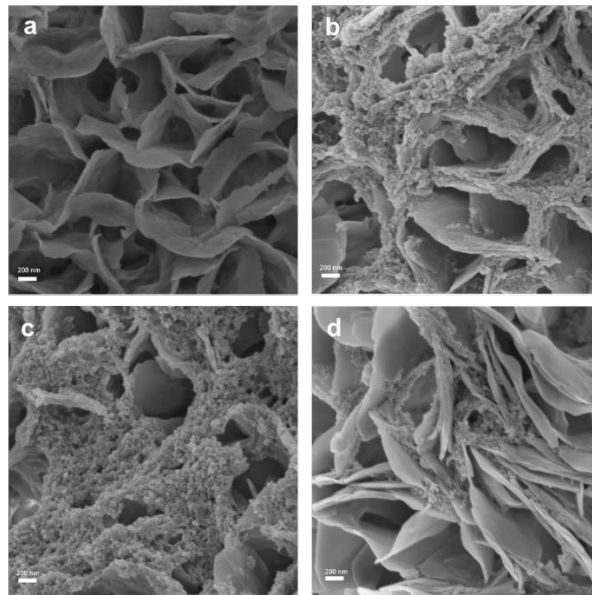


**Figure 5.1.** SEM images of centrifugal precipitations from (a) C-000, (b) C-120, (c) C-150 and (d) C-180.

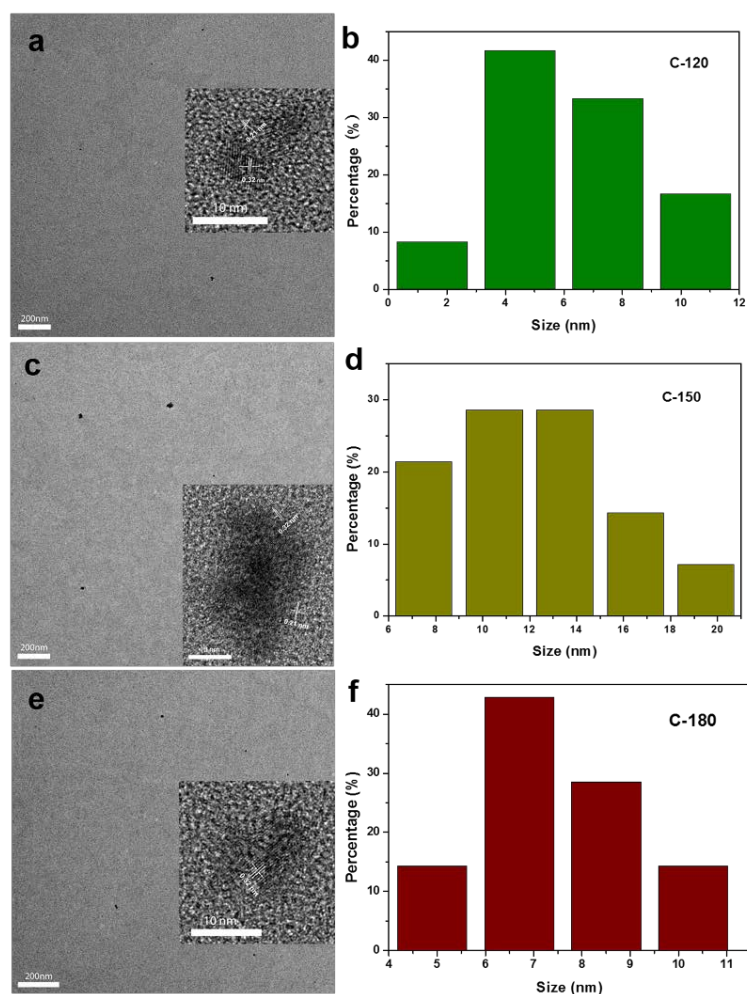


**Figure 5.2.** TEM images and particle size distribution of CDs from (a, b) C-120; (c, d) C-150; and (e, f) C-180.

Carbon dots can be prepared *via* hydrothermal carbonization of numerous organic precursors such as sugar, citric acid, chitosan, banana juice, orange juice, and protein.[23] The possible precursors in celery leaf extracts were likely to be soluble sugars<sup>[24]</sup> or proteins since all the chlorophyll exists as chlorophyll-protein complexes.[25] The formation of CDs is evident from the SEM images of the centrifuged precipitates (Figure 5.1). Only layered fiber tissues with smooth surface were found after centrifuging C-000 samples while nanoparticles with size ranged from 25-35 nm were observed on the surface of these tissues in C-120, C-150, and C-180 precipitates. The morphology of CDs in supernatants was further characterized using TEM analyses; the results of which are shown in Figure 5.2. The particle sizes of CDs from C-120 are mainly distributed in the range of 2-11 nm with an average

size of 5.9 nm. Two different lattice plane spaces with  $d_1=0.21$  nm and  $d_2=0.32$  nm are observed in the high resolution TEM images of CDs from both C-120 and C-150. The first value matches the (100) facet of aromatic or graphitic carbon structure while the latter corresponds to the spaces between two such structures stacked on top of each other forming the main part of the CDs.[26, 27] The CDs from C-150 have wider particle size distribution (6-20 nm) with an average diameter of 12.1 nm (Figure 5.2 (d)) due to the nanoparticle aggregation. Only one lattice spacing with  $d=0.32$  nm is observed in the CDs from C-180, which have an average size of 7.6 nm.

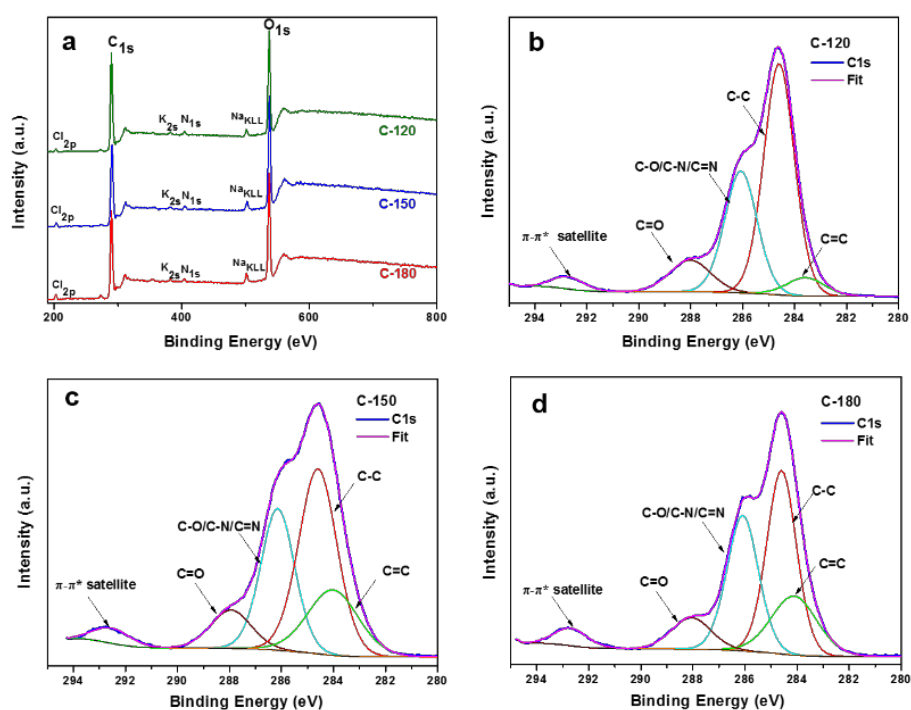


**Figure 5.3.** XPS spectra of CDs obtained from different temperatures. (a) Survey scan spectra; and C1s with corresponding deconvoluted spectra of the CDs from (b) C-120; (c) C-150; and (d) C-180.

XPS was used to investigate the chemical compositions and the functional groups of the as-prepared CDs. The XPS survey spectra (Figure 5.3(a)) reveals the existence of carbon, oxygen, nitrogen, sodium, potassium, and chlorine atoms. The signals of Na, K, and Cl come from the salt content of celery leaves. The content of each element is shown in Table 5.1. The C-120 CDs have the lowest O/C atomic ratio, indicating lower amount of hydroxyl, carboxyl, and carbonyl groups in the surface relative to

CDs obtained at higher hydrothermal temperatures. It is worth noting that the CDs from C-180 have the highest N content relative to the other two. The high resolution scan of the C<sub>1s</sub> region (Figure 5.3(b), (c), and (d)) can be deconvoluted into five single peaks at about 284.0 eV, 284.6 eV, 286.1 eV, 288.0 eV, and 292.5 eV. These peaks are attributed to C–C, C=C, C–O/C–N/C=N, C=O, and  $\pi$ – $\pi^*$  satellite peak, respectively.[28, 29] The  $\pi$ – $\pi^*$  satellite peak is a characteristic of conjugated systems or aromatic groups.[30] The peak intensity increases with increasing hydrothermal temperature. The percentage contributions to C<sub>1s</sub> of each carbon bond is listed in Table 5.2. The percentage areas of C=C bonding (sp<sup>2</sup> carbon) in CDs from C-150 and C-180 are substantially higher than that from C-120, which is consistent with an increase in the intensity of the  $\pi$ – $\pi^*$  satellite peak. On the other hand, the percentage of carboxyl C=O bonding is slightly reduced with increasing temperature. Peak deconvolution analysis of the O<sub>1s</sub> and N<sub>1s</sub> XPS spectra were also performed; the result of which is shown in Figure 5.4. The peaks at 532.2 eV and 533.0 eV in O<sub>1s</sub> spectra are assigned to the presence of C–O bonds and carboxyl C=O bonds on the surface of CDs, respectively. A peak at 536.2 eV, attributed to sodium auger (Na KLL), is also observed in O<sub>1s</sub> spectra of C-180 (Figure 5.4(e)) because of the relatively high Na content in CDs from C-180 (Table 5.1). The N<sub>1s</sub> spectra has two peaks at around 399.0 and 400.0 eV, which are attributed to the pyridinic-N and pyrrolic-N, respectively.[31] The intensity of pyridinic-N in the C–N configuration showed an increasing trend with the increase in hydrothermal temperature. The intensity of pyrrolic-N, on the other hand, displayed an opposite trend.

**Table 5.1.** Elemental compositions of CDs prepared at different temperatures

Sample	C/atom%	O/atom%	N/atom%	Na/atom%	K/atom%	Cl/atom%
C-120	70.13	26.61	0.99	0.60	0.50	0.58
C-150	65.83	31.43	0.75	0.76	0.42	0.80
C-180	66.98	28.98	1.42	1.01	0.44	1.17

**Table 5.2.** Bond compositions of C1s spectra for CDs prepared at different temperatures.

Sample	C=C (%)	C-C (%)	C-O/C-N/C=N (%)	C=O (%)
C-120	6.75	52.96	30.27	10.01
C-150	19.52	42.58	28.65	9.25
C-180	19.76	39.85	31.27	9.13

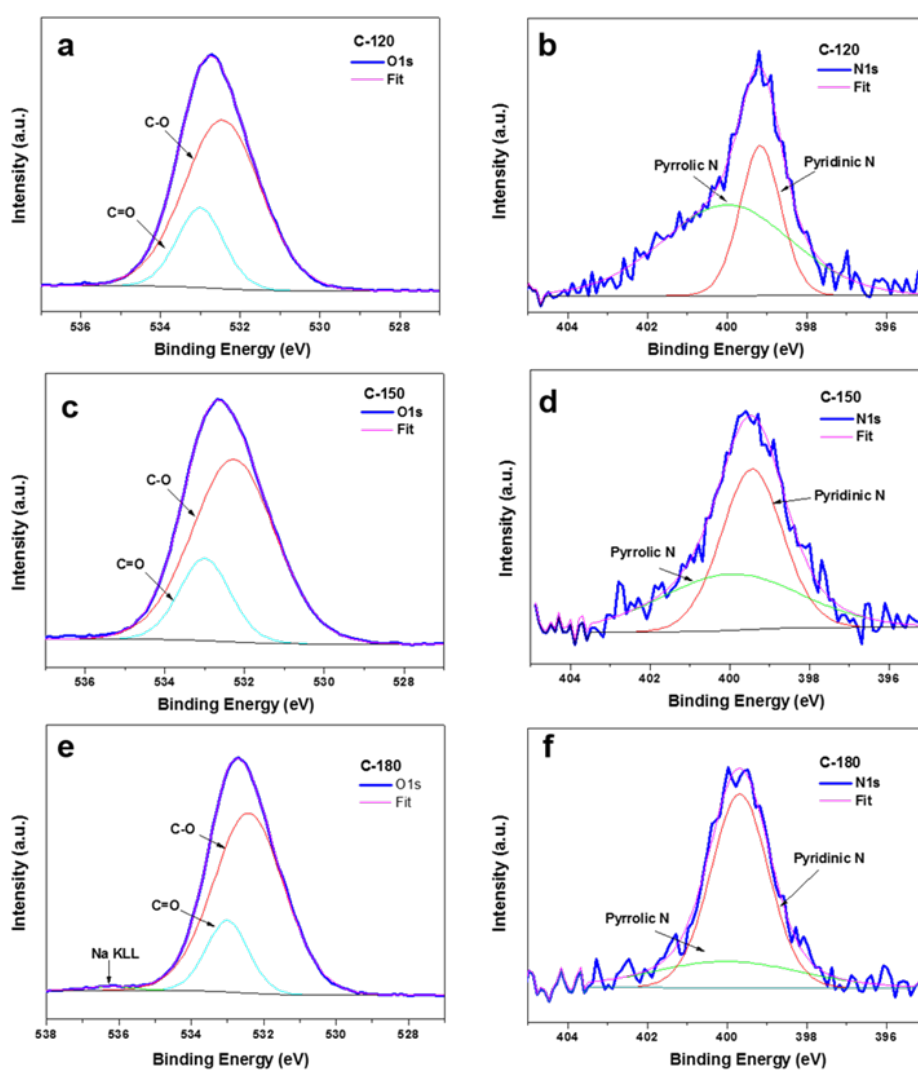


**Figure 5.4.** O<sub>1s</sub> and N<sub>1s</sub> with deconvoluted spectra of the CDs from (a, b) C-120; (c,d) C-150; (e,f) C-180.

### 5.3.2 Optical properties

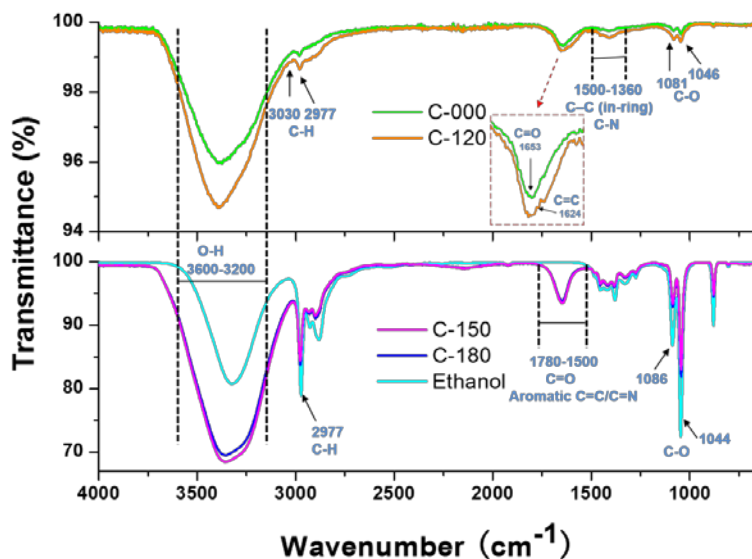


**Figure 5.5.** FTIR spectra of C-000, C-120, C-150, C-180 solution, and an absolute ethanol.

The FTIR spectra of C-000, C-120, C-150, and C-180 alcoholic solutions are shown in Figure 5.5. The broad absorption at a wave number ( $\nu$ ) range of 3200-3600  $\text{cm}^{-1}$  corresponds to the O-H stretching vibration from ethanol. For C-000, the remaining peaks at 2977  $\text{cm}^{-1}$ , 1653  $\text{cm}^{-1}$  and 1360-1500  $\text{cm}^{-1}$  likely indicate the C-H stretching of aliphatic groups, the C=O groups from chlorophyll molecules having conjugation, and the C-C and C-N stretching vibrations in the pyrrole ring of chlorophyll, respectively; while the peaks at 1081  $\text{cm}^{-1}$ , and 1046  $\text{cm}^{-1}$  may arise due to the C-O single bond vibration from chlorophyll or the alcoholic C-OH stretching vibrations.[32, 33] The FTIR pattern of C-120 looks identical to that of C-000, indicating the retainment of the main surface functional groups of dye molecules following autoclave treatment at 120 °C for 2.5 h. A new peak nonetheless appeared at 1624  $\text{cm}^{-1}$ , which is attributed to aromatic C=C stretching, thus implying the formation of CDs.[34] This is further supported by the appearance of the peak at 3030  $\text{cm}^{-1}$  due to the =C-H stretching of aromatics. C-150 and C-180 nonetheless display identical spectra curves to the absolute ethanol one. This indicates that more dye molecules in the extracts decomposed at higher hydrothermal temperatures. In comparison to the ethanol spectrum, intense peaks appear at 1500-1780  $\text{cm}^{-1}$  for both

C-150 and C-180, which represent the stretching vibrations of various C=O groups, the aromatic C=C bending, and the C=N stretching of CDs. Moreover, the O-H stretching peaks of C-150 and C-180 are significantly stronger than that of ethanol, suggesting the presence of large amount of hydroxyl groups on the surface of CDs. These functional groups improve hydrophilicity of CDs, explaining their good solubility in water.

The main pigment compositions of the celery leaf extract are chlorophyll, which includes chlorophyll a and chlorophyll b.[35] The absorption peaks at a wavelength ( $\lambda$ ) of  $\approx 440$  nm and 664 nm on the UV-Vis spectra of C-000 solution (Figure 5.6) match the characteristic absorption data of chlorophyll dye.[36] After hydrothermal treatment, the color of the extract solution changes from original green (C-000) to greenish yellow (C-120), olive-brown (C-150), and dark brown (C-180) at different temperatures (Inset of Figure 5.6). This color change, on one hand, was due to the presence of carbonated hydrocarbons, reflecting the carbonization degree as a function of hydrothermal temperature. Another contributing factor was the conversion of chlorophylls to pheophytins by heat treatment.[21] That C-150 and C-120 have identical UV-Vis patterns to that of C-100 indicates that some pigments like pheophytins and pyropheophytins existed in the two solutions. The photon absorbing intensity of C-120 is stronger than that of C-000 at  $\lambda \approx 490$ -615 nm, but is slightly weaker prior to  $\lambda \approx 490$  nm. In the visible range, the photon absorbing intensity of C-150 is much stronger relative to C-000 and C-120. The C-180 solution shows the highest light absorption property at the entire spectrum region. The absence of sharp absorption peak around  $\lambda \approx 664$  nm for C-180 spectrum implies that most dyes degraded at such high temperature. The expanded absorption range for C-180 is likely ascribed to the increase in the N content in CDs; consistent with the XPS results (Table 5.1).[13]

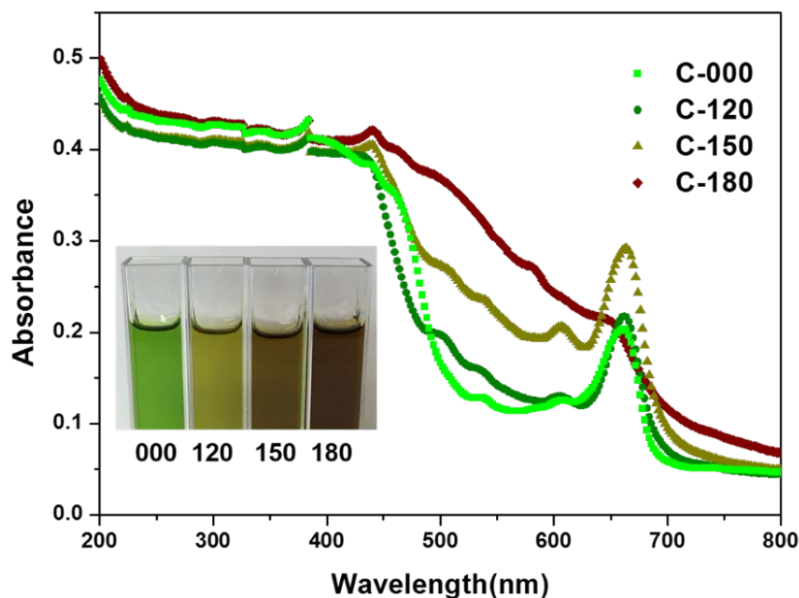


**Figure 5.6.** UV-Vis spectra of C-000, C-120, C-150 and C-180 solution. Insets are the photographs of these solutions under day light.

Photoluminescence (PL) emission spectra of these four solutions were also studied. PL property did not manifest on C-000, C-120, C-150 and C-180 without dilution (Figure 5.7). This is due to the “concentration quenching effect”, in which the average distances between the luminescent centers are narrowed at high concentration, leading to unfavorable energy transfer.[34, 37] Figure 5.8 depicts the PL spectra of the ethanol diluted solution (120  $\mu$ L solution + 4 mL ethanol) excited at 365 nm wavelength. The diluted C-000 gives three emission maxima in the violet region at 428 nm, in the red region at 672 nm, and in the far-red region at 720-740 nm. The red emission of C-000 matches the typical chlorophyll fluorescence emission.[38] The red emission intensity of heat treated solution becomes weaker at higher temperature (Inset of Figure 5.8). This is because of the conversion and decomposition of chlorophyll molecules during heat treatment. However, the emission intensity of C-150 in the red region is slightly higher than that of C-120 (shown more clearly in Figure 5.9), even though more dye molecules were destroyed at higher temperatures. As such, excited electron of dye molecules should be more easily transported to the CDs in C-120 case. The emission maxima in the violet region of the heat treated solutions is centered at 450 nm, which shows a red-shift relative to C-000. This is due

to the introduction of CDs with various surface groups that provides more emissive traps.

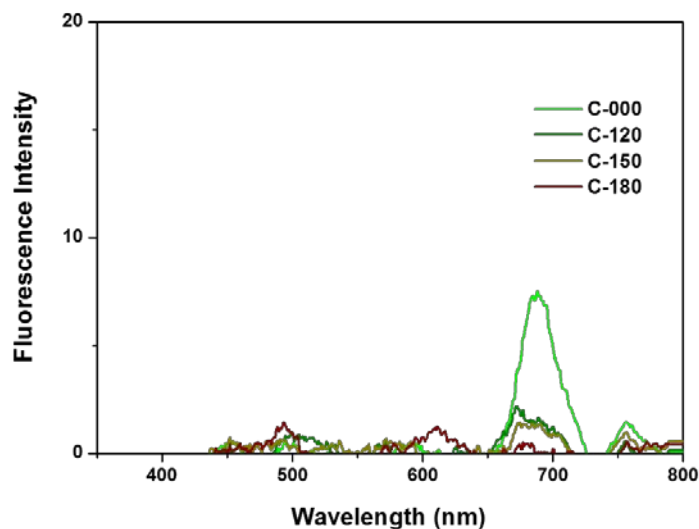


**Figure 5.7.** PL emission spectra of C-000, C-120, C-150 and C-180 without dilution excited at 365nm.

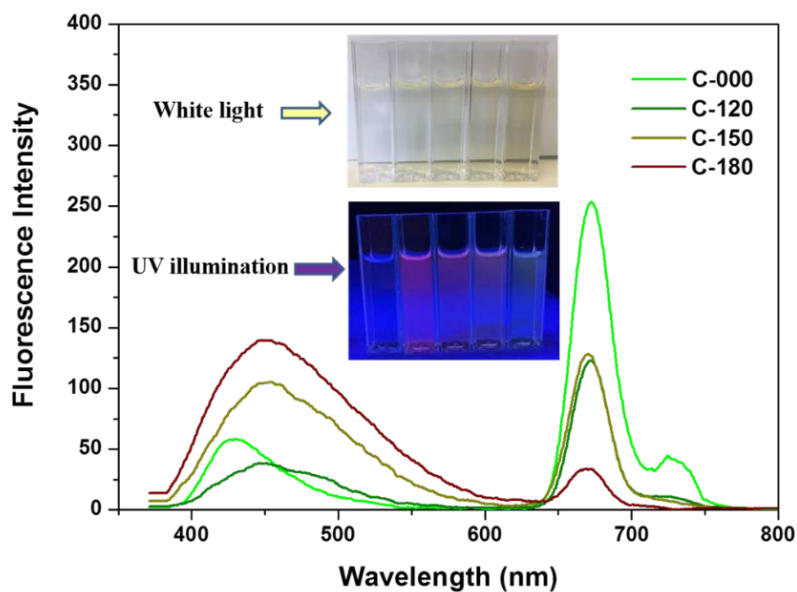


**Figure 5.8.** PL emission spectra of C-000, C-120, C-150, and C-180 diluted with ethanol (120  $\mu$ L sample solution + 4 mL ethanol) excited at 365 nm. Inset shows the diluted solutions (from left to right: ethanol, C-000, C-120, C-150, and C-180) under white light (Top) and 365 nm UV light (Bottom).

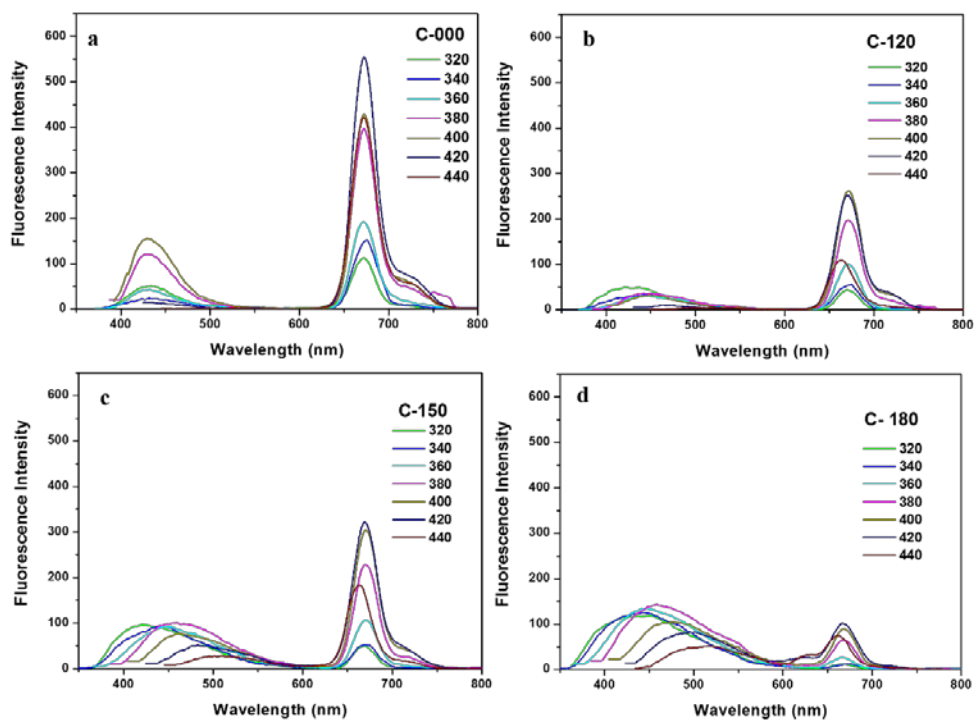


**Figure 5.9.** PL emission spectra of ethanol diluted: (a) C-000; (b) C-120; (c) C-150; and (d) C-180 solutions (120  $\mu$ L sample solution + 4 mL ethanol) with different excitation wavelengths increasing from 320 nm to 440 nm in 20 nm increments.

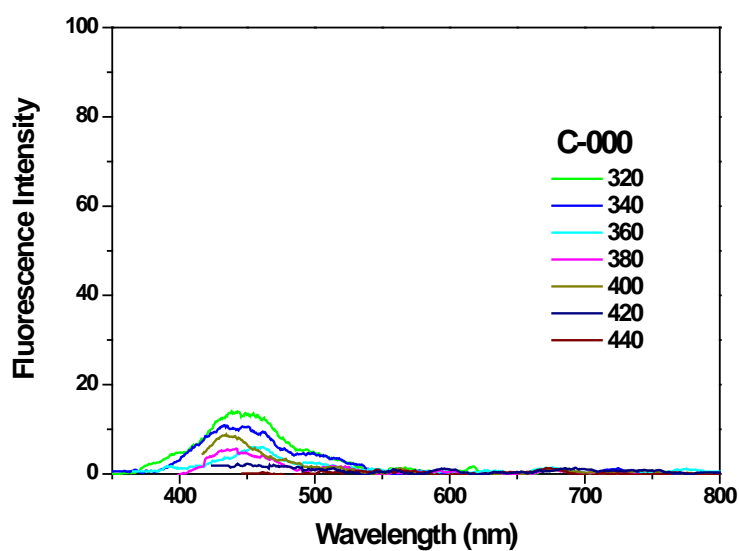


**Figure 5.10.** PL emission spectra of water diluted C-000 solution (120  $\mu$ L sample solution + 4 mL water) with different excitation wavelengths increasing from 320 nm to 440 nm in 20 nm increments.

The PL properties of these ethanol diluted solutions at different excitation

wavelengths ( $\lambda_{\text{ex}}$ ) were also evaluated; the results of which are shown in Figure 5.9. For C-000, the emission intensity varies with  $\lambda_{\text{ex}}$  but the emission wavelength does not shift with the change of  $\lambda_{\text{ex}}$  (Figure 5.9(a)). This is due to the monotonous emissive levels of chlorophyll molecules. In the red region, the emission intensity of C-000 increases with the increase in  $\lambda_{\text{ex}}$  and reaches the highest at  $\lambda_{\text{ex}} = 420$  nm. The trends of the emission intensity variation for the heat treated solutions at red region reproduces that for C-000 since pheophytins or pyropheophytins have similar fluorescence spectra to their corresponding chlorophylls.[21] The main difference between C-000 spectrum and heat treated spectra is higher  $\lambda_{\text{ex}}$  dependence of both wavelength and intensity at short wavelength region where the emission peaks shift to higher wavelengths when the  $\lambda_{\text{ex}}$  increases from 320 to 440 nm (Figure 5.9 (b), (c), (d)). This is an interesting PL feature of CDs which arises due to the presence of different functional surface groups, such as hydroxyl, carboxyl and carbonyl groups, in conjunction with the  $\text{sp}^2$ -hybridized carbon, enabling the presence of various emissive traps between  $\pi$  and  $\pi^*$  state of CDs.[12, 20] The emission is dominated by the particular emissive trap state when the CDs was induced by a light of a specific wavelength. Therefore, the emission wavelengths is  $\lambda_{\text{ex}}$ -dependent since the dominant emissive trap state changes with  $\lambda_{\text{ex}}$ . With the presence of these oxygen containing functional groups on the surface, CDs become highly soluble and colloiddally stable in aqueous or polar organic solvents whereas chlorophyll and its derivatives are insoluble in water and their aqueous solutions has negligible PL properties (Figure 5.10 for water diluted C-000 solution). To isolate the effect of dye molecules, PL spectra of CDs solutions diluted with water are also displayed (Figure 5.11(a), (b), and (c)). The emission intensities of these aqueous CDs solutions are slightly reduced relative to their alcoholic counterparts. The emission intensity clearly increases with increasing hydrothermal temperature. The previous XPS spectra show that this can be ascribed to the percentage increase in C=C bond and pyridinic-N in CDs with temperature rise which leads to the rise in the amount of delocalized electron in the  $\pi$  system.[29, 39] The change in the wave functions of these delocalized electrons may

lead to narrower energy gap between  $\pi$  and  $\pi^*$ . This increases the possibility of electron excitation for the same excitation energy.[29] Moreover, the interaction between the graphitic carbon and CDs in the absence of large CDs aggregates in C-120 (Figure 5.2) also reduces PL intensity.[40] The fluorescence quantum yields (QYs) for these aqueous CDs solutions were calculated to be 0.05% for C-120, 0.11% for C-150, and 0.28% for C-180, respectively (Figure 5.11 (d)). The very low QY may be attributed to the limited carbon source in the extracts and also the influence of the existing dye molecules on the optical density of these solutions.

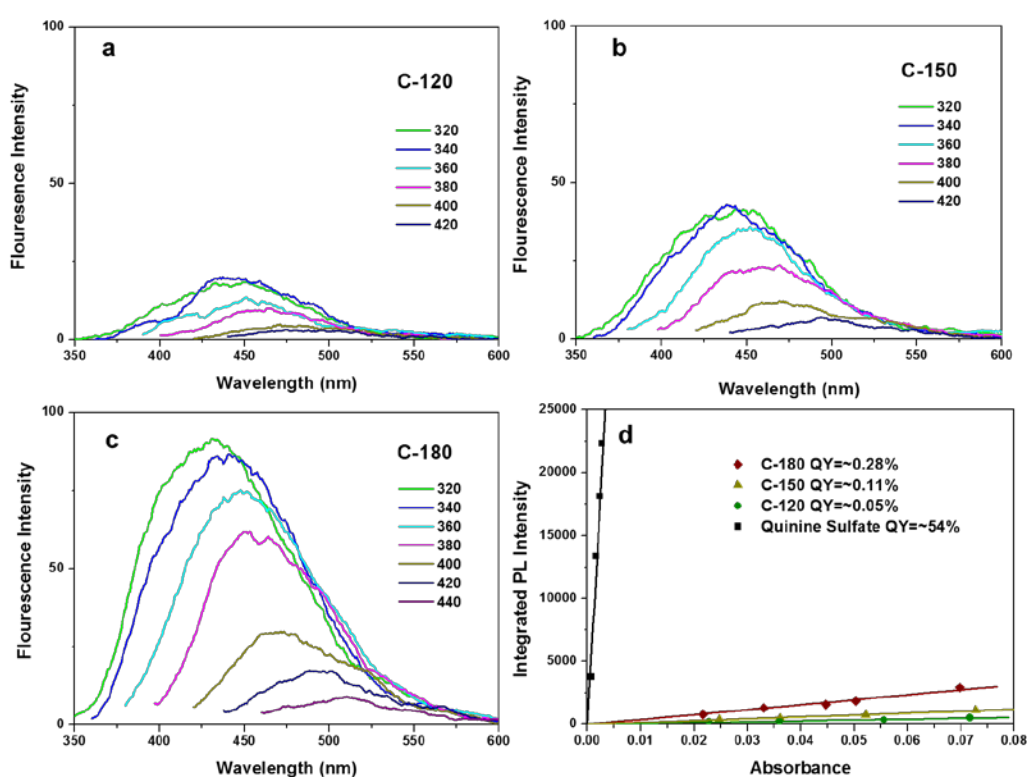


**Figure 5.11.** PL emission spectra of water diluted (a) C-120, (b) C-150 and (c) C-180 solutions (120  $\mu$ L sample solution + 4 mL water) with different excitation wavelengths increasing from 320 nm to 440 nm in 20 nm increments; (d) Integrated PL intensity of CDs with different absorbance.

### 5.3.3 Solar cells performances

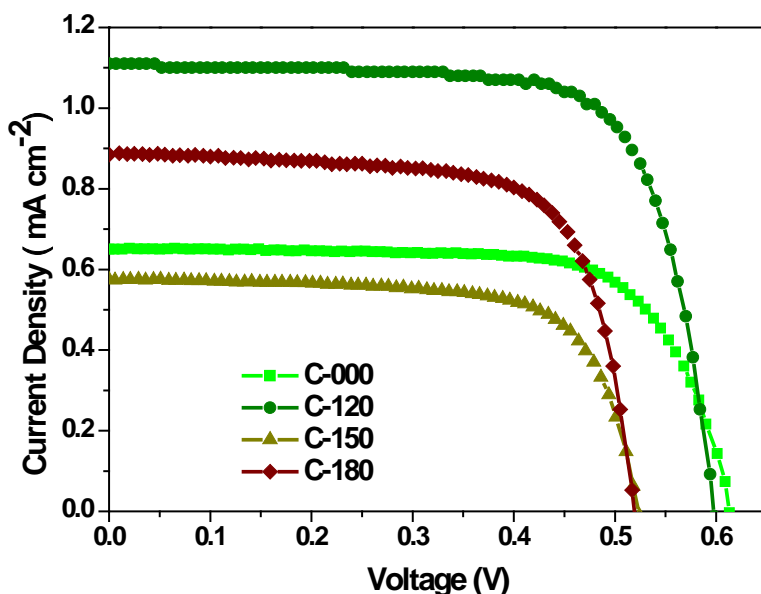


**Figure 5.12.** Photocurrent density-photovoltage ( $J$ - $V$ ) characteristics of  $\text{TiO}_2$  solar cells sensitized with C-000, C-120, C-150, and C-180 solutions measured under an illumination of one sun (AM 1.5G,  $100 \text{ mW cm}^{-2}$ ).

**Table 5.3.** Photovoltaic parameters of  $\text{TiO}_2$  solar cells sensitized with four different solutions measured under AM 1.5 G one sun illumination.

Sensitizer	$J_{sc}$ ( $\text{mA}\cdot\text{cm}^{-2}$ )	$V_{oc}$ (V)	$FF$	$\eta$ (%)
C-000	0.65	0.61	0.72	0.29
C-120	1.11	0.60	0.73	0.48
C-150	0.58	0.52	0.70	0.21
C-180	0.89	0.52	0.71	0.33

As cheap and environment-friendly materials, the four solutions obtained from celery extractive were used as sensitizers for nanocrystalline  $\text{TiO}_2$  based solar cells. The photocurrent density-photovoltage ( $J$ - $V$ ) plots of these dyes and/or CDs sensitized

solar cells are shown in Figure 5.12 while their respective photovoltaic parameters are listed in Table 5.3. The C-120 sensitized cell gave the highest power conversion efficiency (PCE) of 0.48%, which is about 1.7, 2.3, and 1.5 times higher than cells based on C-000, C-150, and C-180, respectively. The enhanced PCE for the C-120 sensitized cell was mainly attributed to its high short circuit current density ( $J_{sc}$ ) despite its slightly lower open circuit voltage ( $V_{oc}$ ) relative to the pure dye (C-000) sensitized cell. The cell based on C-150, on the other hand, displayed the lowest  $J_{sc}$  of  $0.58 \text{ mA}\cdot\text{cm}^{-2}$ . This is mainly since the particle aggregation of CDs in C-150 leads to larger amount of electron-hole recombination sites. Even in the absence of apparent aggregation, the  $J_{sc}$  and  $V_{oc}$  of C-180 sensitized cell are lower than C-120 based cell since almost all dyes decomposed following  $180 \text{ }^\circ\text{C}$  heat treatment. These results imply that C-120 based cell had the best synergistic interaction between dye, CDs, and  $\text{TiO}_2$ , which maximized the photon absorption and electron transfer properties.

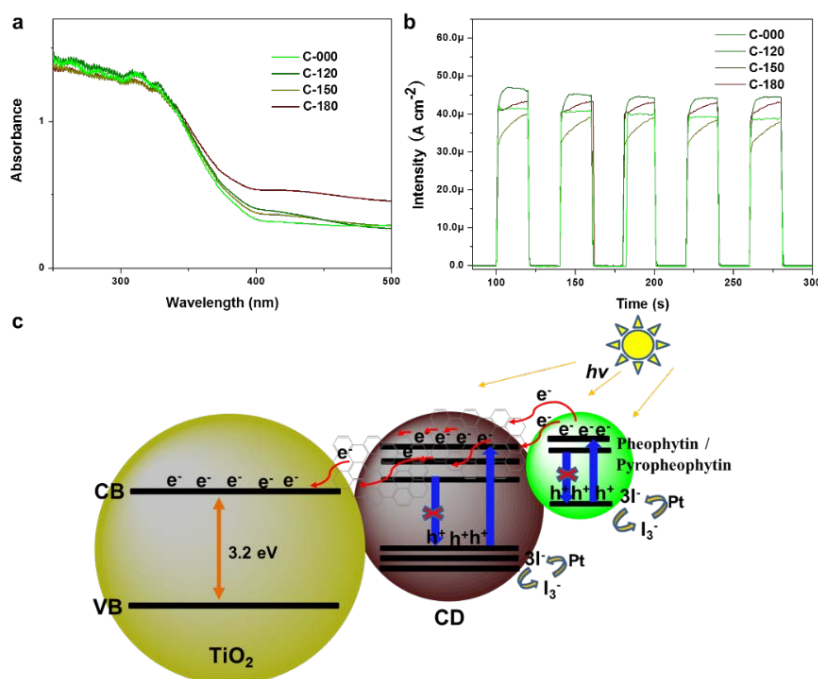


**Figure 5.13.** (a) UV-Vis spectra and (b) Photocurrent density versus time plots for C-000, C-120, C-150, and C-180 sensitized anodes. The results were measured in  $0.5 \text{ M Na}_2\text{SO}_4$  solution under simulated sunlight irradiation ( $100 \text{ mW cm}^{-2}$ ); and (c) Schematic diagram of one of the most possible mechanisms for carriers transfer in C-120 sensitized solar cell.

We further studied the UV-Vis response and the short current response under intermittent illumination of the four sensitized TiO<sub>2</sub> anodes (Figure 5.13). Unlike the UV-Vis spectra for liquid samples, the UV-Vis spectrum for C-120 sensitized anode shows the highest light absorption at the UV region (< 350 nm), corresponding to the highest  $J_{sc}$  of its solar cell. The CDs in C-120 bonded easier with TiO<sub>2</sub> relative to the other two samples (C-150 and C-180) since the strong optical absorption of CDs is mainly centered in the UV region.[7] This enhancement can be attributed to the relatively small particle size of CDs from C-120 and its high percentage of carboxyl C=O bonding (Table 5.2), which improves the interaction of dye/CDs/TiO<sub>2</sub> system by carboxylate fragment anchoring.[41] Consistent with the spectra for liquid samples, the C-180 sensitized anode displays stronger absorption at visible region (> 380 nm) relative to the other three, leading to the second-highest  $J_{sc}$  for its solar cell. The transient short current densities of these four photoanodes is in accord with their solar cell performances, i.e., the density decreases in the order of C-120, C-180, C-000, and C-150. For C-000 based anode, no significant change in the curve shape occurs with the turn-on and turn-off dynamics, which is in agreement a relatively trap-free transport. However, a short-current density rise is observed after turn-on when CDs were introduced into the system. This phenomenon is attributed to the trapping and de-trapping effects, where the initial fast rise can be rationalized in terms of fast free-carrier transport while the slower rise can be associated with the time taken for trapping/de-trapping process to reach steady-state after turn-on.[42] The short-current density rise in the C-150 and C-180 sensitized anodes cases is much slower than that of C-120, indicating that CDs from C-150 and C-180 have a higher trap density due to their more complex surface states or defects as revealed by the previous XPS and PL analysis. In another word, the electron transfer is more efficient in the C-120 sensitized TiO<sub>2</sub> anodes, in which CDs act as an electron transfer bridge in the dye-semiconductor complex given their electron-accepting and electron-donating properties.[15] To confirm this hypothesis, a small quantity of C-180 was added into C-000 (C-000/C-180=5.6:1v/v) as a dye-CD combined sensitizer for solar cell

performance (Figure 5.14). The obtained  $J_{sc}$  of  $0.86 \text{ mA cm}^{-2}$  is close to that of C-180 sensitized cell but is substantially higher than the C-000 based cell. The  $V_{oc}$  of  $0.58 \text{ V}$  nonetheless is improved compared to the C-180 based cell but is still lower than that for C-000 based cell. The PCE of  $0.36\%$  for the combined sensitizer based cell is higher than those for C-000 and C-180 based cells. This means that CDs play an important role on the electron transfer from dye to  $\text{TiO}_2$ . Still, this PCE is lower than the C-120 based cell given the higher amount of trap states for CDs from C-180 relative to those for CDs from C-120. In C-120 case,  $\pi$  state of the graphitic carbon adhered on the CDs could form electronic coupling with the conduction band states of  $\text{TiO}_2$ . [7] This  $\pi$  state can function simultaneously as an electron acceptor to dye and CDs as well as an electron donor to  $\text{TiO}_2$ , thus promoting the electron directional transport and suppressing the recombination of excited electrons and holes. The most possible mechanism for photogenerated electron transfer in C-120 sensitized cell is presented in Figure 5.13(c). The graphitic carbon on CDs serves as an electron transfer intermediate, which can bridge the excited electrons from dye (pheophytins or/and pyropheophytins) and CD itself to  $\text{TiO}_2$ .

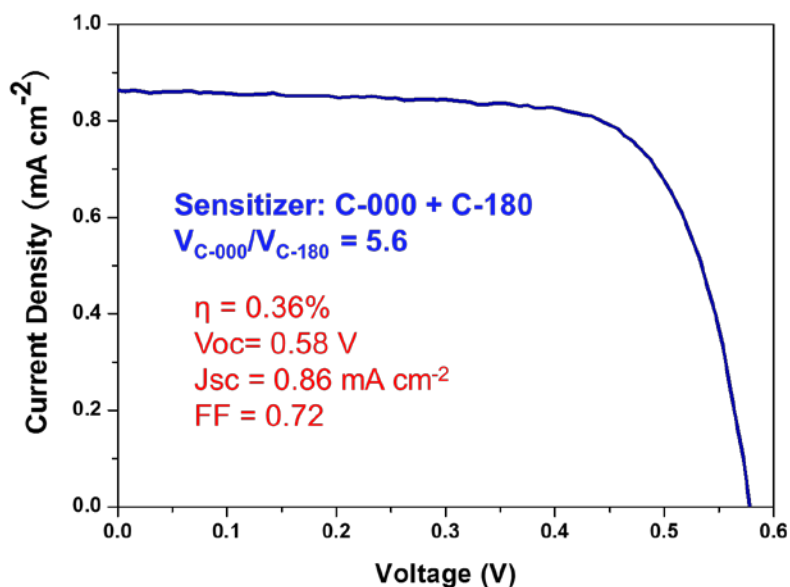


**Figure 5.14.** Photocurrent density-photovoltage ( $J$ - $V$ ) characteristics of  $\text{TiO}_2$  solar cells based on C-000 and C-180 combined sensitizer measured under an illumination of one sun (AM 1.5G,  $100 \text{ mW cm}^{-2}$ ).

## 5.4 Conclusions

Inspired by photosynthetic processes and synthetic methods of CDs, we present a cost-effective and sustainable route to obtain dye-CD complex as sensitizer for the photovoltaic applications *via* a single step hydrothermal treatment of the alcoholic extracts from celery leaves. The particle size, surface states, and optical properties of CDs as well as the surviving amount of dye highly depend on the hydrothermal temperature. The CDs from C-120 have relatively smaller dot size, without aggregation and display lower PL emission intensity relative to the higher temperature counterparts. Three features, i.e., graphitic carbon on the surface, low amount of trap states, and high percentage of carboxyl C=O bonding simultaneously contribute to an effective electron transfer bridge of C-120 CDs. The CDs showed improved interaction between pheophytins/pyropheophytins and TiO<sub>2</sub> and suppressed recombination of photogenerated electrons. By allowing the use of CD as an intermediate and in the presence of high amount of surviving dye molecules, the TiO<sub>2</sub> solar cells sensitized with C-120 achieved the highest PCE of 0.48% relative to those sensitized by original or higher temperature treated extract solutions. This dye/CD/semiconductor system may open a new window to develop highly efficient photoelectric devices in an economic and environmentally benign way.

## References

1. Polman, A., et al., *Photovoltaic materials: Present efficiencies and future challenges*. Science, 2016. **352**(6283): p. 28 pages.
2. Jin, C., et al., *Recent progress in efficient hybrid lead halide perovskite solar cells*. Science and Technology of Advanced Materials, 2015. **16**(3): p. 036004 (14pp).
3. Yan, J. and B.R. Saunders, *Third-generation solar cells: a review and comparison of polymer:fullerene, hybrid polymer and perovskite solar cells*. RSC Advances, 2014. **4**(82): p. 43286-43314.
4. Qin, Y. and Q. Peng, *Ruthenium Sensitizers and Their Applications in Dye-Sensitized Solar Cells*. International Journal of Photoenergy, 2012. **2012**: p. 21 pages.
5. Jun, H.K., M.A. Careem, and A.K. Arof, *Quantum dot-sensitized solar cells—perspective and recent developments: A review of Cd chalcogenide quantum dots as sensitizers*. Renewable and Sustainable Energy Reviews, 2013. **22**: p. 148-167.
6. Zhao, Y. and K. Zhu, *Organic-inorganic hybrid lead halide perovskites for optoelectronic and*

- electronic applications*. Chemical Society Reviews, 2016. **45**(3): p. 655-689.
7. Li, H., et al., *Carbon nanodots: synthesis, properties and applications*. Journal Of Materials Chemistry, 2012. **22**(46): p. 24230-24253.
  8. Girit, Ç.Ö., et al., *Graphene at the Edge: Stability and Dynamics*. Science, 2009. **323**(5922): p. 1705-1708.
  9. Mirtchev, P., et al., *Solution phase synthesis of carbon quantum dots as sensitizers for nanocrystalline TiO2 solar cells*. Journal of Materials Chemistry, 2012. **22**(4): p. 1265-1269.
  10. Gupta, V., et al., *Luminescent Graphene Quantum Dots for Organic Photovoltaic Devices*. Journal Of The American Chemical Society, 2011. **133**(26): p. 9960-9963.
  11. Zhang, Y.-Q., et al., *N-doped carbon quantum dots for TiO2-based photocatalysts and dye-sensitized solar cells*. Nano Energy, 2013. **2**(5): p. 545-552.
  12. Briscoe, J., et al., *Biomass-Derived Carbon Quantum Dot Sensitizers for Solid-State Nanostructured Solar Cells*. Angewandte Chemie International Edition, 2015. **54**(15): p. 4463-4468.
  13. Wang, H., et al., *Nitrogen-Doped Carbon Dots for "green" Quantum Dot Solar Cells*. Nanoscale Research Letters, 2016. **11**:27: p. 6 pages.
  14. Guo, X., et al., *Green Synthesis of Carbon Quantum Dots for Sensitized Solar Cells*. ChemPhotoChem, 2017: p. DOI: 10.1002/cptc.201600038.
  15. Ma, Z., et al., *Bioinspired Photoelectric Conversion System Based on Carbon-Quantum-Dot-Doped Dye-Semiconductor Complex*. Acs Applied Materials & Interfaces, 2013. **5**(11): p. 5080-5084.
  16. Shalini, S., et al., *Review on natural dye sensitized solar cells: Operation, materials and methods*. Renewable and Sustainable Energy Reviews, 2015. **51**: p. 1306-1325.
  17. Li, L.-L. and E.W.-G. Diau, *Porphyrin-sensitized solar cells*. Chemical Society Reviews, 2013. **42**(1): p. 291-304.
  18. Li, H., et al., *Water-Soluble Fluorescent Carbon Quantum Dots and Photocatalyst Design*. Angewandte Chemie International Edition, 2010. **49**(26): p. 4430-4434.
  19. Sahu, S., et al., *Simple one-step synthesis of highly luminescent carbon dots from orange juice: application as excellent bio-imaging agents*. Chemical Communications, 2012. **48**(70): p. 8835-8837.
  20. Lim, S.Y., W. Shen, and Z. Gao, *Carbon quantum dots and their applications*. Chemical Society Reviews, 2015. **44**(1): p. 362-381.
  21. Schwartz, S.J. and T.V. Lorenzo, *Chlorophylls in foods*. Critical Reviews In Food Science And Nutrition, 1990. **29**(1): p. 1-17.
  22. Shen, Z., et al., *Bi-layer photoanode films of hierarchical carbon-doped brookite-rutile TiO2 composite and anatase TiO2 beads for efficient dye-sensitized solar cells*. Electrochimica Acta, 2016. **216**: p. 429-437.
  23. Wang, Y. and A. Hu, *Carbon quantum dots: synthesis, properties and applications*. Journal of Materials Chemistry C, 2014. **2**(34): p. 6921-6939.
  24. Helaly, A.A.-D., et al., *Phytochemical Analysis of Some Celery Accessions*. Journal of Medicinally Active Plants, 2015. **4**(1): p. 1-7.
  25. Markwell, J.P., J.P. Thornber, and R.T. Boggs, *Higher plant chloroplasts: Evidence that all the chlorophyll exists as chlorophyll—protein complexes*. Proceedings of the National Academy of Sciences of the United States of America, 1979. **76**(3): p. 1233-1235.

26. Linehan, K. and H. Doyle, *Solution reduction synthesis of amine terminated carbon quantum dots*. RSC Advances, 2014. **4**(24): p. 12094-12097.
27. Fu, M., et al., *Carbon Dots: A Unique Fluorescent Cocktail of Polycyclic Aromatic Hydrocarbons*. Nano Letters, 2015. **15**(9): p. 6030-6035.
28. Ramanan, V., et al., *Outright Green Synthesis of Fluorescent Carbon Dots from Eutrophic Algal Blooms for In Vitro Imaging*. ACS Sustainable Chemistry & Engineering, 2016. **4**(9): p. 4724-4731.
29. Permatasari, F.A., et al., *Role of C-N Configurations in the Photoluminescence of Graphene Quantum Dots Synthesized by a Hydrothermal Route*. Scientific Reports, 2016. **6**: p. 21042.
30. Fan, X., et al., *Deoxygenation of Exfoliated Graphite Oxide under Alkaline Conditions: A Green Route to Graphene Preparation*. Advanced Materials, 2008. **20**(23): p. 4490-4493.
31. Wang, C., et al., *Simple and green synthesis of nitrogen-, sulfur-, and phosphorus-co-doped carbon dots with tunable luminescence properties and sensing application*. RSC Advances, 2014. **4**(96): p. 54060-54065.
32. Sudip, M., et al., *Green chemistry approach for the synthesis and stabilization of biocompatible gold nanoparticles and their potential applications in cancer therapy*. Nanotechnology, 2012. **23**(45): p. 455103.
33. Sengupta, D., B. Mondal, and K. Mukherjee, *Visible light absorption and photo-sensitizing properties of spinach leaves and beetroot extracted natural dyes*. Spectrochimica Acta Part A: Molecular and Biomolecular Spectroscopy, 2015. **148**: p. 85-92.
34. Wang, J., et al., *Vegetable-extracted carbon dots and their nanocomposites for enhanced photocatalytic H<sub>2</sub> production*. RSC Advances, 2014. **4**(83): p. 44117-44123.
35. Roslon, W., E. Osinska, and J. Gajc-Wolska, *The Influence of Raw Material Stabilization on the Quality of Celery (Apium graveolens L.) Leaves*, in *Vi International Postharvest Symposium*, M. Erkan and U. Aksoy, Editors. 2010. p. 201-208.
36. Lichtenthaler, H.K. and C. Buschmann, *Chlorophylls and Carotenoids: Measurement and Characterization by UV-VIS Spectroscopy*, in *Current Protocols in Food Analytical Chemistry*. 2001, John Wiley & Sons, Inc.
37. Mhlongo, G.H., et al., *Dependence of photoluminescence (PL) emission intensity on Eu<sup>3+</sup> and ZnO concentrations in Y<sub>2</sub>O<sub>3</sub>:Eu<sup>3+</sup> and ZnO:Y<sub>2</sub>O<sub>3</sub>:Eu<sup>3+</sup> nanophosphors*. Optical Materials, 2011. **33**(10): p. 1495-1499.
38. Pedros, R., et al., *Chlorophyll fluorescence emission spectrum inside a leaf*. Photochemical & Photobiological Sciences, 2008. **7**(4): p. 498-502.
39. Tang, L., et al., *Energy-level structure of nitrogen-doped graphene quantum dots*. Journal of Materials Chemistry C, 2013. **1**(32): p. 4908-4915.
40. Hu, C., et al., *Nitrogen-doped carbon dots decorated on graphene: a novel all-carbon hybrid electrocatalyst for enhanced oxygen reduction reaction*. Chemical Communications, 2015. **51**(16): p. 3419-3422.
41. Bai, Y., et al., *Titanium Dioxide Nanomaterials for Photovoltaic Applications*. Chemical Reviews, 2014. **114**(19): p. 10095-10130.
42. Li, Z., et al., *Comparison of the Operation of Polymer/Fullerene, Polymer/Polymer, and Polymer/Nanocrystal Solar Cells: A Transient Photocurrent and Photovoltage Study*. Advanced Functional Materials, 2011. **21**(8): p. 1419-1431.

*Every reasonable effort has been made to acknowledge the owners of copyright material. I would be pleased to hear from any copyright owner who has been omitted or incorrectly acknowledged.*

## **Chapter 6: Carbon-coated three-dimensional WS<sub>2</sub> film consisting of WO<sub>3</sub>@WS<sub>2</sub> core-shell blocks and layered WS<sub>2</sub> nanostructures as counter electrodes for efficient dye-sensitized solar cells**

### **Abstract**

The possibility of using solar energy for electricity generation has inspired intensive enthusiasm on the development of solar cell devices. This work reports the synthesis of a novel counter electrode (CE) composed of WO<sub>x</sub>@WS<sub>2</sub>@carbon core-shell film and compares its electrical performance with other two CEs of WO<sub>x</sub>/carbon film and conventional Pt in the dye-sensitized solar cells (DSSCs). The WO<sub>x</sub>@WS<sub>2</sub>@carbon CE was prepared by a sulfurization treatment of a mesoporous WO<sub>x</sub>/carbon film coated on FTO glass. The well-interconnected three-dimensional (3D) WS<sub>2</sub> structure with coated carbon film provides high electrocatalytic activity and fast reaction kinetics for the reduction of triiodide to iodide due to its sufficient active sites on 3D WS<sub>2</sub> framework containing surface edge-oriented nanosheets and the facile electron transfer and electrolyte diffusion via the continuously carbon layer. Electrochemical performance tests indicate the DSSC device with the counter electrode of WO<sub>x</sub>@WS<sub>2</sub>@carbon core-shell achieved the PCE of 7.71% compared favourably with the values of 6.00% from WO<sub>x</sub>/carbon CE and 7.34% from conventional Pt CE. Such results vividly mirror that the developed WO<sub>x</sub>@WS<sub>2</sub>@carbon core-shell can replace the conventional Pt film, realizing Pt-free counter electrodes for DSSCs.

### **6.1 Introduction**

The solar energy conversion research has attracted wide attention due to the energy crisis and environmental pollution arising from the heavy consumption of non-renewable fossil fuels. The dye-sensitized solar cell (DSSC) is one promising candidate of various photovoltaic conversion devices owing to its low cost, environmental benignity, facile fabrication process, and large design flexibilities.[1, 2]

Platinum (Pt) is the most common counter electrode (CE) material for DSSCs because of its excellent catalytic activity and high electrical conductivity. The DSSCs based on Pt CE have achieved high power conversion efficiency (PCE) exceeding 12%. [3, 4] However, Pt is an expensive noble metal and has weak chemical stability as it can be decomposed to  $PtI_4$  or  $H_2PtI_6$  in the triiodide/iodide ( $I_3^-/I^-$ ) electrolyte. [5, 6] Thus, it is necessary to develop new Pt-free CE materials to reduce the production cost and increase the stability of DSSC performance.

The ideal CE materials for DSSCs should have superior properties to collect electrons, catalyze  $I_3^-$  reduction, and long-term stability as well as being earth-abundant. Tungsten (W)-based compounds, including their oxides, nitrides, carbides and hybrids, have been widely studied as CEs for the DSSC application due to their excellent properties, such as low cost, good stability and notable electrocatalytic activity. [7-15] For W-based oxides, non-stoichiometric tungsten trioxides ( $WO_{3-x}$ , where  $0 < x \leq 1$ ), have better conductivity than tungsten trioxide ( $WO_3$ ), because the carrier concentration in the system of  $WO_3$ - $WO_2$  increases with the decreasing anion coordination numbers. [16] Wu et al. reported a PCE of 7.25% achieved on the DSSC with  $WO_2$  as CE, which is much higher than that of 4.67% based on  $WO_3$  CE. [17]

Similarly, tungsten sulfide ( $WS_2$ ) with an analogous structure of graphite and graphene, [18] is expected to exhibit a good performance in DSSCs due to its high catalytic activity, thermal and chemical stability. Wu et al. have used the pure  $WS_2$  as CE for DSSCs, [19] but the hydrothermal preparation of  $WS_2$  is time-consuming (one week) and not eco-friendly. To compensate for the conductivity of  $WS_2$  film, carbon materials are usually added to fabricate the CE. For instance, carbon-coated  $WS_2$  [20] or the  $WS_2$  composite with  $TiO_2$  (P25) and carbon nanoparticles ( $WS_2/P25/C$ ) [21] was investigated, delivering a PCE of 5.50% or 4.56%, respectively. Moreover, the incorporation of multi-wall carbon nanotubes (MWCNTs) into the  $WS_2$  CE system has also been attempted. [22, 23] An efficiency up to 7.36% was achieved by the DSSC based on  $WS_2/MWCNTs$  CE. [23] Nevertheless, it becomes intractable to control the carbon content in the composite, as too less carbon materials cannot

improve the conductivity while too much addition would cover the active sites of WS<sub>2</sub> and reduce their bonding strength. On the other hand, WS<sub>2</sub> can also be easily obtained through a high temperature sulfurization process from W-based oxides, which can be used to prepare continuous WS<sub>2</sub> film in large area.[24, 25] Hussain et al. fabricated the WS<sub>2</sub> CEs from WO<sub>3</sub> films deposited on fluorine-doped tin oxide (FTO) glass substrate by a sputtering and sulfurization process to be functioned as CE for DSSCs, achieving a PCE around 6.3%.[24] The relatively low efficiency compared with Pt CE (6.64%) can be ascribed to the insufficient active sites for triiodide reduction in the dense film obtained from sputtering. It was found edge-oriented WS<sub>2</sub> nanosheets could maximize the number of active edge sites leading to drastically enhanced catalytic activity toward triiodide reduction. [25]

Here, we present a novel WS<sub>2</sub> electrode prepared by a simple sulfurization of a mesoporous WO<sub>x</sub>/carbon film with rough surfaces coated on FTO Glass substrate, where WO<sub>x</sub> not only provide the tungsten source but also acts as building blocks to scaffold continuous WS<sub>2</sub> layers. In the resultant film electrode, a carbon-coated well-interconnected three-dimensional (3D) WS<sub>2</sub> catalytic network was built up by the interconnected tetragonal WO<sub>3</sub>@WS<sub>2</sub> core-shell blocks with surrounding irregular WS<sub>2</sub> layers, a small amount of WS<sub>2</sub> nanorods and the edge-oriented WS<sub>2</sub> nanosheets on the surface. The synergistic effects of the maximized active edge sites on 3D WS<sub>2</sub> framework's surface, and facile electron transfer and electrolyte diffusion via the continuous carbon matrix lead to drastically enhanced catalytic activity toward I<sub>3</sub><sup>-</sup> reduction in the CE of DSSCs. The DSSC based on this WS<sub>2</sub> CE achieved a PCE of 7.71%, which is superior to the performances of the cells with Pt-based CE (7.34%) and WO<sub>x</sub>/carbon CE (6.00%).

## **6.2 Experimental section**

### **6.2.1 Materials**

Sodium tungstate (Na<sub>2</sub>WO<sub>4</sub>·H<sub>2</sub>O), hydroxylamine hydrochloride (NH<sub>2</sub>OH·HCl),

sulfourea ( $\text{CH}_4\text{N}_2\text{S}$ ), sulfur (S), poly (vinyl alcohol) (PVA, #341584), ethyl cellulose (EC, #46070 and #46080), titanium (IV) bis (ammonium lactato) dihydroxide solution (TALH, 50 wt.% in water), titanium tetrachloride ( $\text{TiCl}_4$ ), terpineol, acetonitrile, tert-butanol, lithium iodide (LiI), lithium perchlorate ( $\text{LiClO}_4$ ), iodine ( $\text{I}_2$ ) and fluorine-doped tin oxide (FTO) glass substrates (TEC7, 2mm, resistance  $\sim 7 \Omega/\text{sq}$ ) were purchased from Sigma-Aldrich. Polyethylene glycol (PEG, 2000) was supplied by Merck while triiodide/iodide ( $\text{I}_3^-/\text{I}^-$ ) electrolyte (MS005615) was purchased from Dyesol.

### 6.2.2 Synthesis of $\text{WO}_x$ green powder

First,  $\text{Na}_2\text{WO}_4 \cdot \text{H}_2\text{O}$  (0.006mol),  $\text{NH}_2\text{OH} \cdot \text{HCl}$  (0.012mol),  $\text{CH}_4\text{N}_2\text{S}$  (0.024 mol) were dissolved in 36 ml deionized water. Then, 0.216g PEG was added into the solution under constant stirring. After complete dissolution, the solution was transferred into a 60 ml Teflon-lined stainless steel autoclave, which was sealed and heated at  $180^\circ\text{C}$  for 24 h in the oven. The obtained precipitates were washed three times with DI water and absolute ethanol, respectively and dried in air at  $60^\circ\text{C}$  for 10 h. The as-prepared powder was then calcined at  $800^\circ\text{C}$  for 1 h with a heating rate of  $5^\circ\text{C}/\text{min}$  in a tube furnace under nitrogen ( $\text{N}_2$ ) protection and the green product obtained is denoted as  $\text{WO}_x$ .

### 6.2.3 Preparation of counter electrodes

A mixture of  $\text{WO}_x$ , terpineol, and EC in the weight ratios of 1:4:0.5 was ball milled with ethanol for 2 h and then subjected to rotary evaporation process at  $40^\circ\text{C}$  to form a viscous paste by removing ethanol. The  $\text{WO}_x$  paste was then applied on FTO glass by using the doctor blade method. After drying at  $125^\circ\text{C}$  for 6 min, the coated FTO glass was sintered in a tube furnace in  $\text{N}_2$  atmosphere at  $500^\circ\text{C}$  for 1 h. The obtained counter electrodes are denoted as  $\text{WO}_x/\text{carbon}$ , which were subjected to the sulfurization process at  $500^\circ\text{C}$  for 1 h in a tube furnace to form new counter electrodes denoted as  $\text{WO}_x@\text{WS}_2@\text{carbon}$ . The schematic diagram of the thermal

vapor sulfurization process is illustrated in Figure 6.1a, where 1g sulfur powder and the WO<sub>x</sub>/carbon electrodes were placed at the upwind low temperature zone and the center of the quartz tube, respectively. The quartz tube was kept in a flowing protective atmosphere of N<sub>2</sub>, with a flow rate of 100 sccm and the heating rate was 5°C/min. The Pt counter electrodes were prepared as described previously.[26]

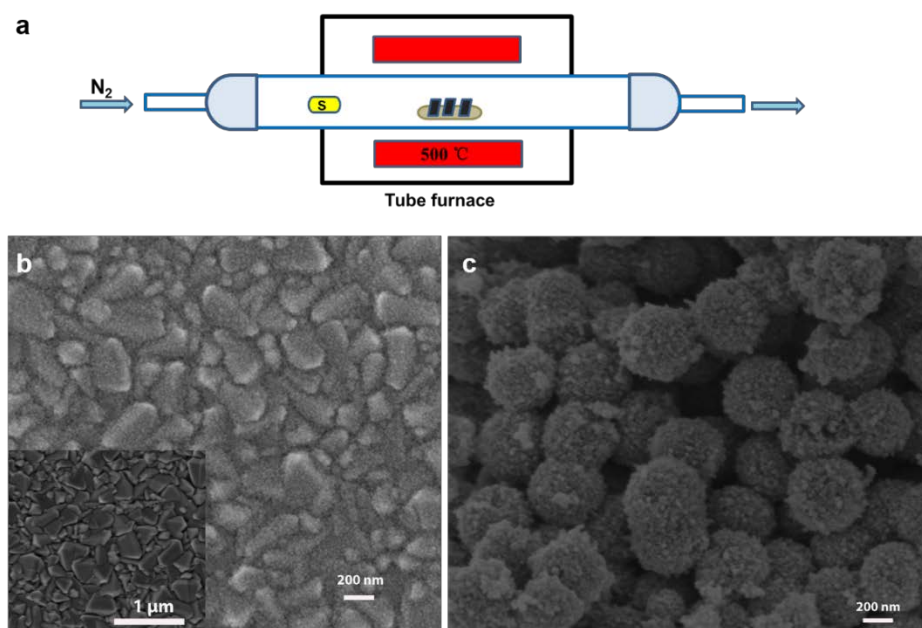


**Figure 6.1.** (a) Schematic diagram for the sulfurization process, and SEM images of (b) the TiO<sub>2</sub> block layer formed on FTO glass with inset–image for the surface of bare FTO glass and (c) TiO<sub>2</sub> beads.

#### 6.2.4 Fabrication of dye-sensitized solar cell

The ultrasonically cleaned FTO glass plates were immersed in a 40 mM aqueous TiCl<sub>4</sub> solution at 70 °C for 30 min and were thoroughly rinsed with water and ethanol. A TALH-PVA aqueous solution (TALH 50 wt.%/PVA 0.75 wt.% = 1: 13.29 v/v) was then spin-coated on to these FTO glasses at 3000 rpm for 30 s, followed by sintering at 500°C for 30 min to form a TiO<sub>2</sub> block layer (Figure 6.1b). A TiO<sub>2</sub> bead paste, where TiO<sub>2</sub> beads, terpineol, and EC in the weight ratios of 1:4:0.5 respectively, was then coated on the FTO glass using the doctor blade method. The TiO<sub>2</sub> beads were synthesized according to our previous report (Figure 6.2c).[26] The resultant film was

then sintered at 325 °C for 5 min, 375 °C for 5 min, 450 °C for 15 min and finally at 500 °C for 15 min. After being re-treated with TiCl<sub>4</sub> solution and re-sintering at 500 °C for 30 min, the TiO<sub>2</sub> films were immersed into 0.5 mM N719 dye solution in acetonitrile/tert-butanol ( $V_{\text{acetonitrile}} : V_{\text{tert-butanol}} = 1:1$ ) solution at room temperature for 24 h. The dye sensitized TiO<sub>2</sub> films were washed with acetonitrile to the loosely physisorbed dye molecules and dried at nitrogen steam. The solar cells were fabricated by injecting I<sub>3</sub><sup>-</sup>/I<sup>-</sup> electrolyte into the void space between the photoanode and the counter electrode.

### 6.2.5 Characterization

The crystal composition and morphology of the samples were characterized by powder X-ray diffractometer (XRD, BrukerD8 Advance with Cu-K $\alpha$  Radiation,  $\lambda = 1.5418 \text{ \AA}$ ), field-emission scanning electron microscopy (FESEM, Zeiss Neon 40EsB) and transmission electron microscopy (TEM, Titan G2 80-200). X-ray photoelectron spectroscopy (XPS) was performed on a Kratos AXIS Ultra DLD machine with a monochromatic Al K $\alpha$  X-ray gun. The Raman spectrum was acquired with a Dilor Labram 1B dispersive Raman spectrometer using a 514.5 nm excitation line. Cyclic voltammetry (CV) was carried out in a three-electrode system in an acetonitrile solution consisting of 0.1 M LiClO<sub>4</sub>, 10nM LiI, and 1 mM I<sub>2</sub> at a scan rate of 10, 20, 50, or 100 mV·s<sup>-1</sup> using an electrochemical workstation (Gamry Reference 3000). In the three-electrode system, a Pt sheet served as a counter electrode and Ag/AgCl as a reference electrode. Electrochemical impedance spectroscopy (EIS) and Tafel curves were conducted using an electrochemical workstation (Zahner Zennium) with a symmetrical dummy cell. EIS was measured under dark with a 0.6 V DC bias voltage and an AC amplitude of 10mV, and the measured frequency ranged from 100 m Hz to 1M Hz. The scan rate for the Tafel curves was 10 mV·s<sup>-1</sup>. The current-voltage characteristics of the solar cells were recorded by the Zahner Zennium system (Zahner Zennium and XPOT) under simulated AM 1.5 G illumination (100 mW·cm<sup>-2</sup>) provided by a solar simulator (TriSOL, OAI).

## 6.3 Results and discussion

### 6.3.1. Morphology and compositions

The SEM images of the as-synthesized green powder are shown in Figure 6.2, where two different structures are observed. The major structure (Figure 6.2a) was formed in prismatic blocks with variable size ranged from 0.2 to 2  $\mu\text{m}$ , while the minor structure (Figure 6.2b) is in the form of nanorods with a diameter of about 30 nm and a length up to 2  $\mu\text{m}$ . Figure S2c shows the XRD pattern of the synthesized powder, in which the main peaks can be well indexed as the tetragonal  $\text{WO}_3$  ( $\alpha\text{-WO}_3$ ) phase (PDF #85-0808) and the peaks of tetragonal  $\text{W}_5\text{O}_{14}$  (PDF #41-0745) are also observed as the minor phase. A small peak at the position of  $14.43^\circ$  is assigned to lattice plane (003) of  $\text{WS}_2$  crystal structure (PDF #35-0651), as some sulfur sourced from sulfourea was remaining in the precursor during the washing process.[27] The uniform lattice fringe of 0.37 nm can be observed on the prismatic structure from the HRTEM image (Figure 6.3), matching well with the (110) of tetragonal phase  $\text{WO}_3$  (PDF #85-0808). The fringes of 0.38 nm are clearly detected in the nanorods (Figure 6.3g&i), which can be assigned to the (001) lattice planes of tetragonal  $\text{W}_5\text{O}_{14}$  (PDF #41-0745). The spots on the fast Fourier transform (FFT) patterns (Inset in Figure 6.3g&j) further confirm the nanorods structure possessing the polycrystalline nature of tetragonal  $\text{W}_5\text{O}_{14}$ . In EDS mapping (Figure 6.4a&b), oxygen (O) and tungsten (W) elements are uniformly distributed in all the particles, while the distribution of carbon (C) mainly focused on the surface of these particles. The C signal on the background originates from the carbon film on the copper TEM grid. The distribution of sulfur (S) elements cannot be confirmed on mapping because of the blurry signal from the background. There is no significant S signal observed on the EDS spectrums (Figure 6.4c, d&e), while strong C, O and W peaks appear in all the spectrums. It is seen that the O and W peaks on the margin area (Figure 6.4d) is relatively weaker compared with the primary body area (Figure 6.4c), further verifying carbon coating on the surface of the particles. In summary, the prismatic crystal structure belongs to tetragonal  $\text{WO}_3$ , a

major component in the synthesized  $\text{WO}_x$  powder, while the nanorod structure belongs to the minor phase of tetragonal  $\text{W}_5\text{O}_{14}$ . All the particles are wrapped by a uniform amorphous carbon layer with a thickness of about 5 nm, as shown in Figure 6.3.

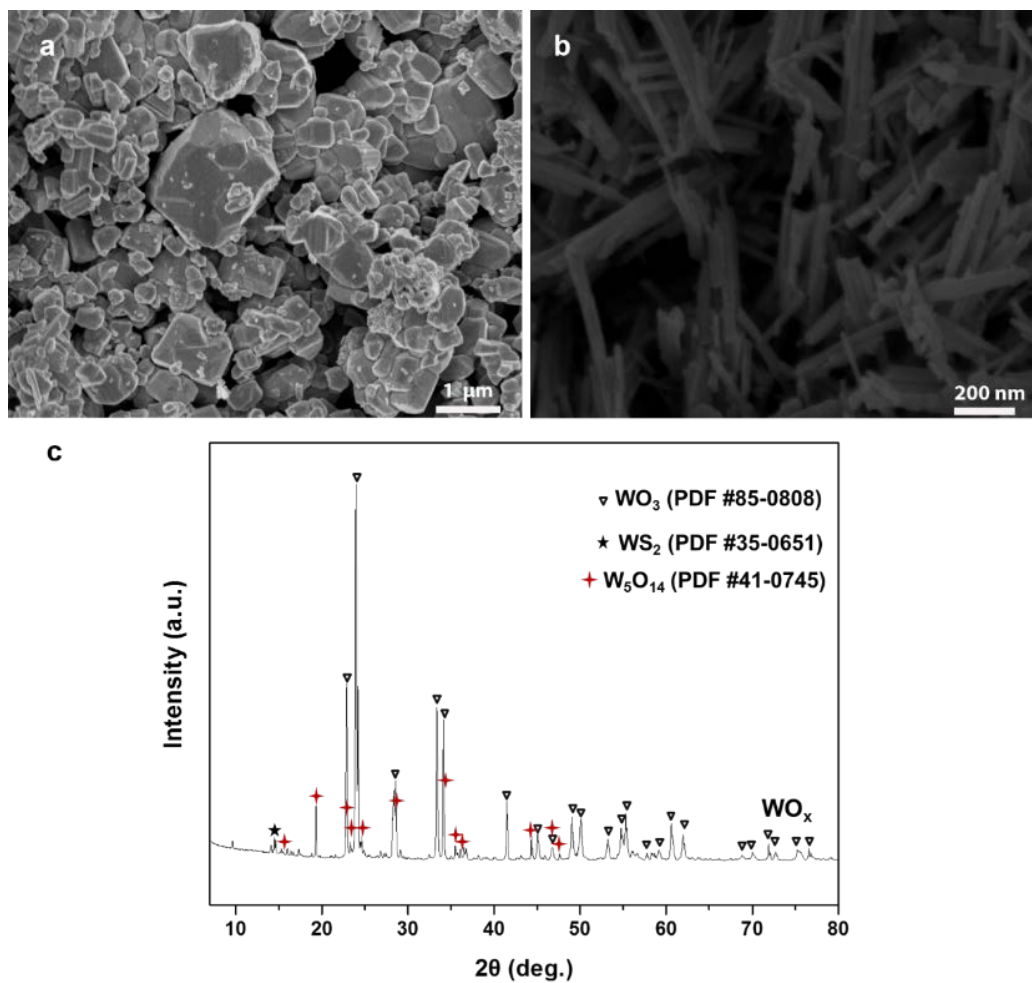


**Figure 6.2.** SEM images of the (a) major structure, (b) minor structure and (c) XRD pattern of the as-synthesized  $\text{WO}_x$  green powder.

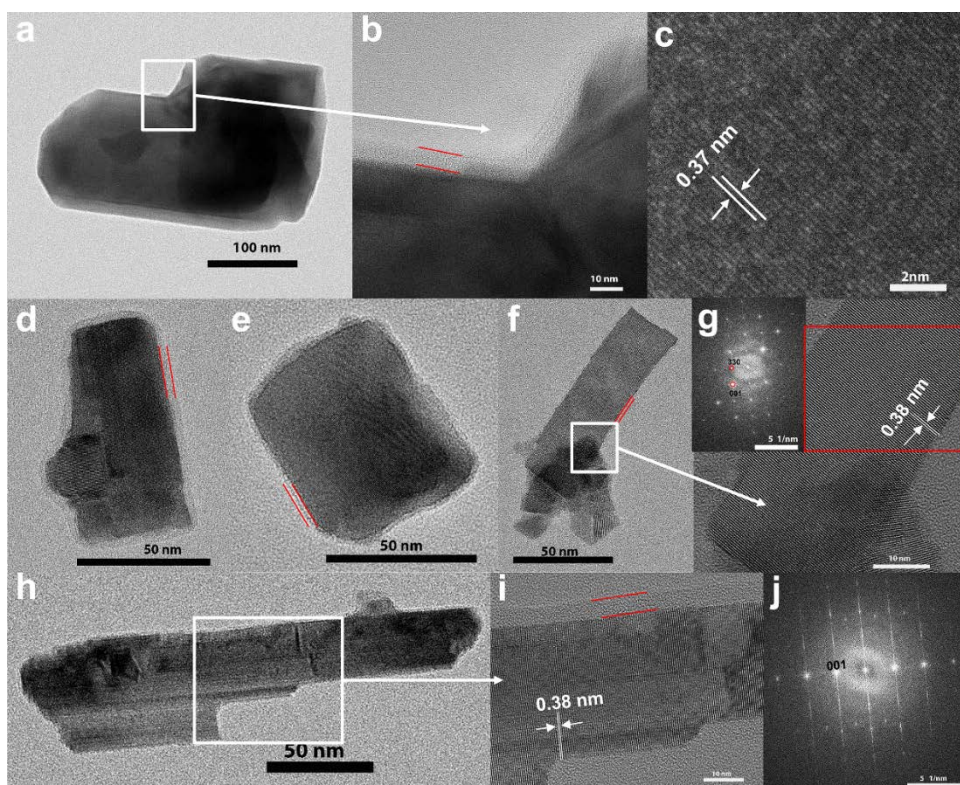


**Figure 6.3.** (a, b, d, e, f and h) TEM image, (c, g and i) HRTEM images (with corresponding Fast Fourier transform (FFT) pattern (from the red square area) at the inset) of particles from the as-synthesized  $\text{WO}_x$  green powder, and (j) FFT pattern from (i).

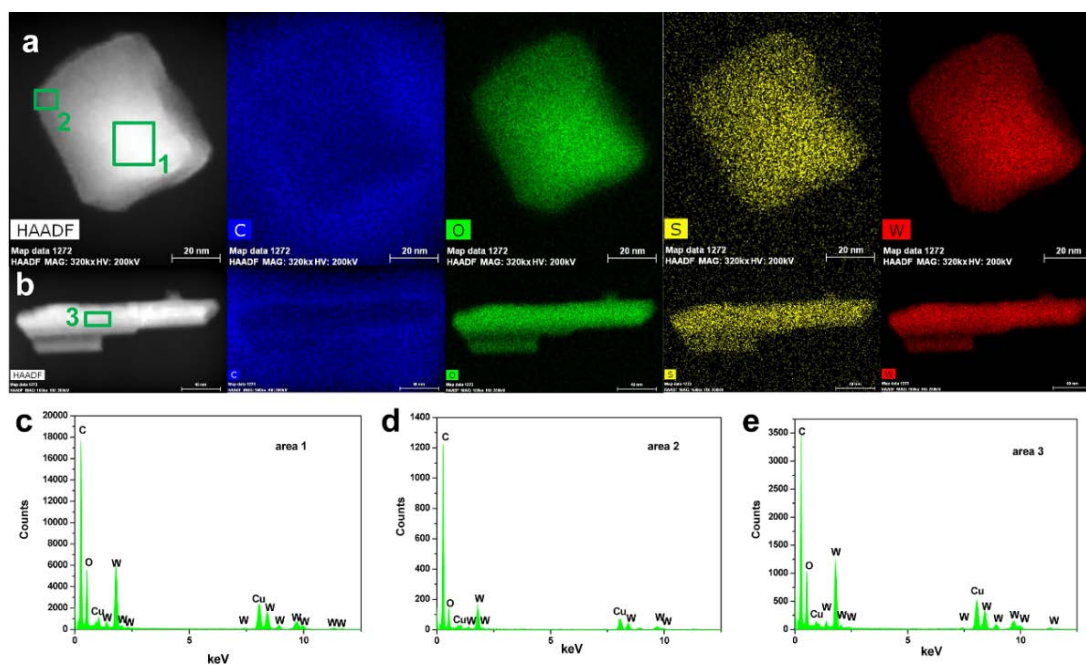


**Figure 6.4.** (a, b) HAADF-EDS image and EDS elemental mapping of particles from the as-synthesized  $\text{WO}_x$  green powder, and (c, d, e) EDS spectrum of selected areas.

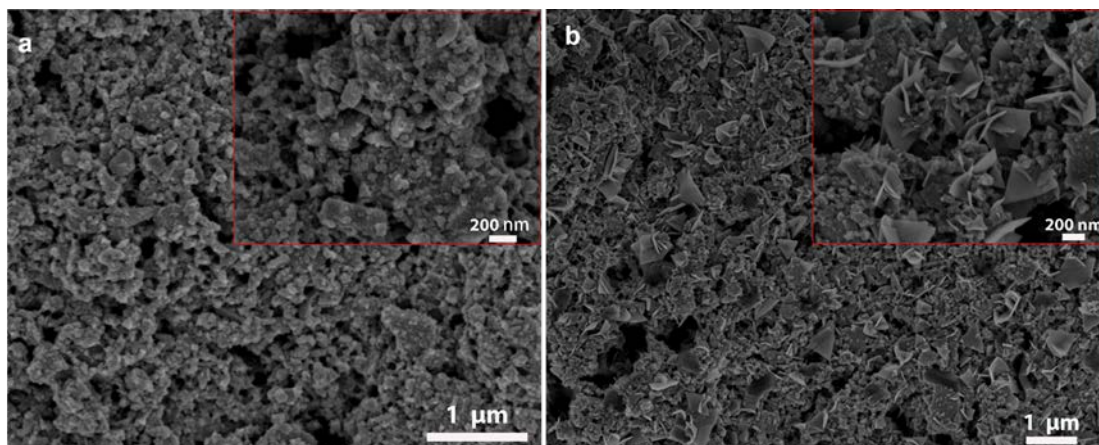


**Figure 6.5** SEM images of counter electrodes (a)  $\text{WO}_x/\text{carbon}$  and (b)  $\text{WO}_x@\text{WS}_2@\text{carbon}$ .

SEM images in Figure 6.5 display the surface morphology of  $\text{WO}_x/\text{carbon}$  and  $\text{WO}_x@\text{WS}_2@\text{carbon}$  counter electrodes (CEs), after the heat treatment of the coated FTO glass. As observed, the mesoporous film with a high porosity and good interconnectivity was obtained in the  $\text{WO}_x/\text{carbon}$  CE (Figure 6.5 a). The particle surface became rough mainly due to the carbon loading from the carbonization of ethyl cellulose during the sintering procedure in  $\text{N}_2$  atmosphere. During the sulfurization at  $500^\circ\text{C}$ ,  $\text{WO}_3$  was partially transferred to  $\text{WS}_2$  resulting in the formation of  $\text{WO}_x@\text{WS}_2@\text{carbon}$  CE. After sulfurization, the oriented nanosheets with submicron size were observed on the surface of the mesoporous structure as shown in Figure 6.5b. Figure 6.6 shows the XRD patterns of the particles peeled off from the  $\text{WO}_x/\text{carbon}$  and  $\text{WO}_x@\text{WS}_2@\text{carbon}$  CE, respectively. In the case of  $\text{WO}_x/\text{carbon}$  CE, an orthorhombic  $\text{WO}_3$  ( $\beta\text{-WO}_3$ , PDF #71-0131) phase appeared with the tetragonal  $\text{WO}_3$  phase, highlighting the fact of the crystallographic transformation of  $\text{WO}_3$  after the heat treatment. This result agrees well with the previous reports.[28, 29] It has been reported that the orthorhombic phase ( $\text{WO}_3$ ) can be formed at above  $330^\circ\text{C}$  but the tetragonal phase tends to arise above  $740^\circ\text{C}$ ; and such phase transformation is partially reversible upon temperature alternation. Noteworthy is that, in this work, both orthorhombic and tetragonal phases have been stably maintained at room temperature, opposite to the previous observation,[30] which can be mainly ascribed to the carbon coating improving their stability. For  $\text{WO}_x@\text{WS}_2@\text{carbon}$  CE,

the main phase is tetragonal  $\text{WO}_3$  (PDF #85-0808) and an intense peak arising at the position of  $14.36^\circ$  is assigned to the (002) lattice plane of  $\text{WS}_2$  (PDF #84-1398), which indicates the original orthorhombic  $\text{WO}_3$  formed in  $\text{WO}_x/\text{carbon}$  CE has been transferred to  $\text{WS}_2$  during the high temperature sulfurization.

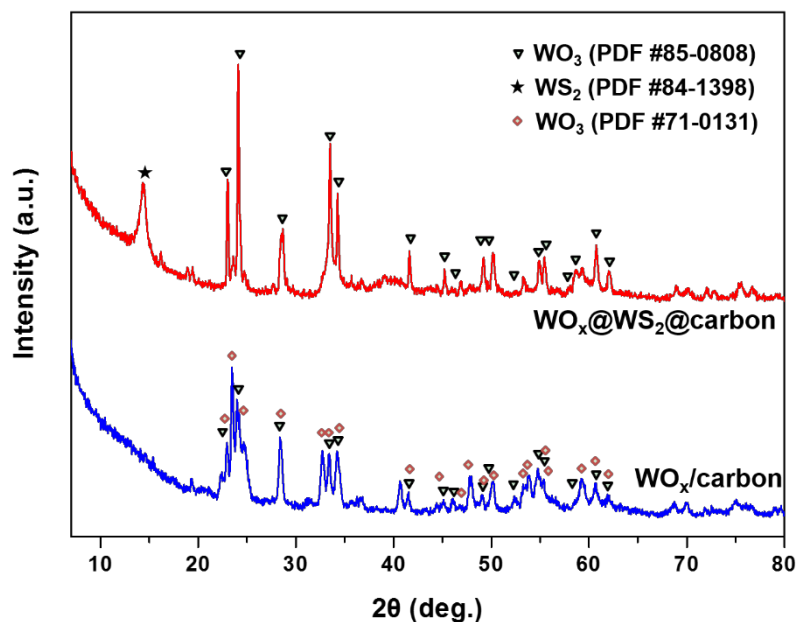


**Figure 6.6** XRD patterns of the powders peeled from  $\text{WO}_x/\text{carbon}$  and  $\text{WO}_x@WS_2@carbon$  electrodes.

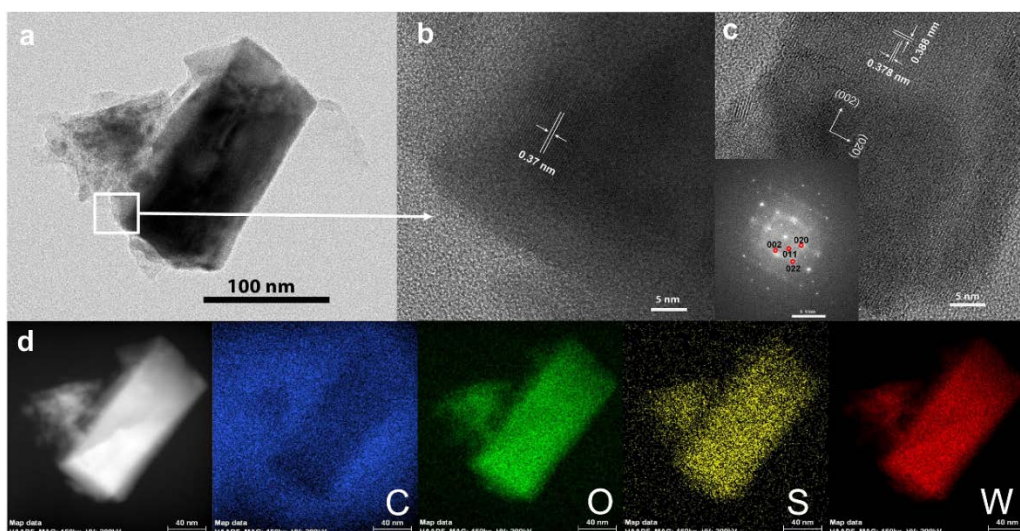


**Figure 6.7.** (a) TEM image, (b and c) HRTEM images (with corresponding Fast Fourier transform (FFT) pattern at the inset), and (d) HAADF STM image and EDS elemental mapping of particles from  $\text{WO}_x/\text{carbon}$  electrode.

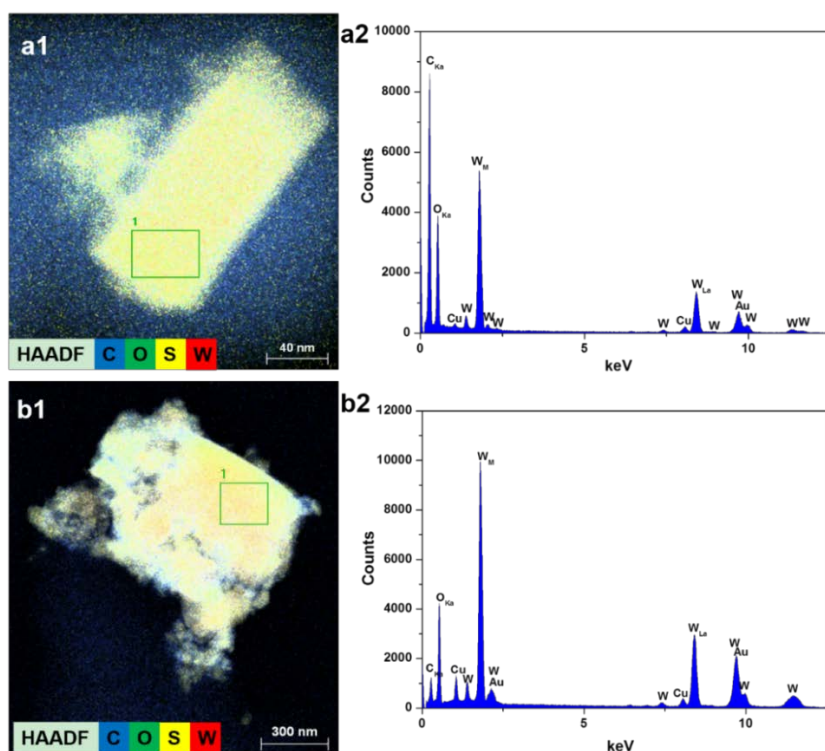


**Figure 6.8.** (a1 and b1) EDS element distribution map of particles from  $\text{WO}_x/\text{carbon}$  electrode and (a2 and b2) EDS spectrum of selected area 1 of particles in a1 and b2.

TEM technique has been used to further identify the elaborate particle structure of the CE composites. The prismatic structure aggregated with smaller nanoparticles is clearly shown in the TEM image of the sample from  $\text{WO}_x/\text{carbon}$  (Figure 6.7a) or  $\text{WO}_x@WS_2@carbon$  (Figure 6.9a). For the sample from  $\text{WO}_x/\text{carbon}$ , the uniform lattice fringe of 0.37 nm can be observed on the primary structure from the HRTEM image (Figure 6.7b), matching well with the (110) of tetragonal phase  $\text{WO}_3$  (PDF #85-0808). Figure 3c is another HRTEM image of one small particle from the marginal area of the prismatic structure. Two perpendicular lattice fringes of 0.388 nm and 0.378 nm are clearly detected, which can be assigned to the (002) and the (020) lattice planes of orthorhombic phase  $\text{WO}_3$  (PDF #71-0131), respectively. The spots on the fast Fourier transform (FFT) patterns (Inset in Figure 6.7c) further confirm the polycrystalline nature of orthorhombic  $\text{WO}_3$ . These results are in agreement with the XRD analysis of the powder from  $\text{WO}_x/\text{carbon}$  CE, which also indicates that small

particles are more likely to be produced during the phase transformation from tetragonal to orthorhombic phase in the sintering process. STEM and the corresponding EDS mapping was further used to investigate the element distribution. Oxygen (O) and tungsten (W) elements are uniformly distributed in all the particles, while the distribution of carbon (C) and sulfur (S) elements cannot be confirmed in Figure 3d because of the blurry signal from the background. The EDS spectrums of particles from  $WO_x$ /carbon electrode are shown in Figure 6.8. The gold (Au) and copper (Cu) signals on the EDS spectrums originate from the gold TEM grid and copper grid holder. The evident C signals are observed on the chosen areas (Figure 6.8), indicating these particles are carbon coated. Compared to the weak S signal, the strong O and W peaks in the EDS spectrum (Figure 6.8) further verifies that the major component of  $WO_x$ /carbon CE is tungsten oxide.

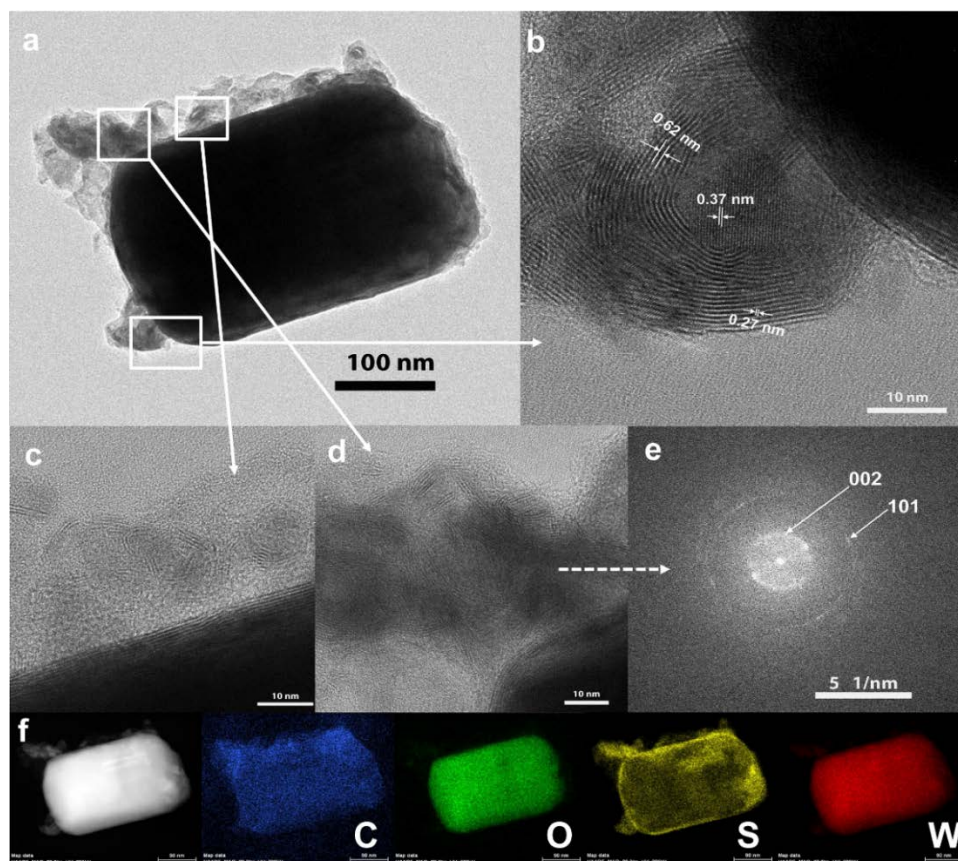


**Figure 6.9.** (a) TEM image, (b, c and d) HRTEM images, (e) Fast Fourier transform (FFT) pattern of (d), and (f) HAADF STM image and EDS elemental mapping of particles from  $WO_x@WS_2$ @carbon electrode.

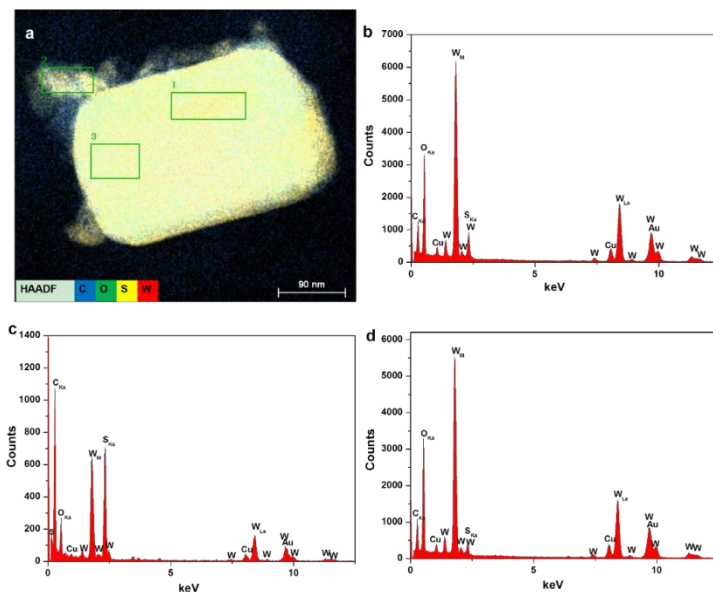


**Figure 6.10.** (a1) EDS element distribution map of particles from  $\text{WO}_x@WS_2@$ carbon electrode and (b, c and d) EDS spectrums of selected area 1, area 2 and area 3.

The HRTEM images of the sample from  $\text{WO}_x@WS_2@$ carbon CE are shown in Figure 6.9b-d. The core-shell structure is observed in Figure 6.9b, where the tetragonal  $\text{WO}_3$  core with the lattice fringe of 0.37 nm is wrapped by a multilayer structure, among which the lattice spacing of 0.62 and 0.27 nm belongs to the interlayer distances of (002) and (101) planes of  $\text{WS}_2$  (PDF #84-1398), respectively. Not only the small particles, but also the primary block displays a core-shell structure of  $\text{WO}_3@WS_2$  (Figure 6.9c). Moreover, some irregularly shaped layer structures surrounding by amorphous carbon are also found in the margin area of the primary particle (Figure 6.9c&d). The corresponding FFT patterns (Figure 6.9e) confirm these layers possess  $\text{WS}_2$  crystal structure. The morphology of  $\text{WS}_2$  is highly dependent on the pristine sample,[31] since sulfur diffused slowly into the core and subsequently transformed the oxide into sulfide during the sulfurization.[32] Thus, small  $\text{WO}_3$  particles can be converted to  $\text{WS}_2$  completely, while big particles would form the  $\text{WO}_3@WS_2$  core-shell structure. For the corresponding EDS mapping (Figure 6.9f), element W is uniformly distributed inside the entire particles, however, O is only distributed in the core of the particle. The distribution of S element is not as dense as O and W in the primary particle but more intensive at the edge and margin area of the main structure,

further supporting the formation of  $\text{WO}_3@WS_2$  core-shell structure was started from the external layer of  $\text{WO}_3$ . The distribution of C on the primary particle from  $\text{WO}_x@WS_2@carbon$  CE is more obvious and uniform than  $\text{WO}_x/carbon$  CE. From the EDS spectrums (Figure 6.10), it is seen that the C peak on the margin area is relatively stronger than other elements compared with that of the primary body, which also can be observed from the HRTEM images (Figure 6.9b-d). The coated carbon layer on  $WS_2$  structure become contiguous and thick (about 10 nm) compared with the particles from the synthesized powder (Figure 6.3). Different to the particles from  $\text{WO}_x/carbon$  CE, S peaks can be observed on all the EDS spectrums from the  $\text{WO}_x@WS_2@carbon$  sample. The S signal in area 1 is stronger than that in area 3 of the main particle (Figure 6.10), while a small nanorod is found adhered at area 1 in the STEM image (Figure 6.9f). This result indicates that the  $W_5O_{14}$  nanorods formed in the synthesis stage of the green powder were also transformed to  $WS_2$  during the sulfurization. Certainly, the chosen margin area has the relatively strongest S signal and the lowest O signal (area 2, Figure 6.10c), as the small tungsten oxide particles could convert to  $WS_2$  more thoroughly than the big blocks.

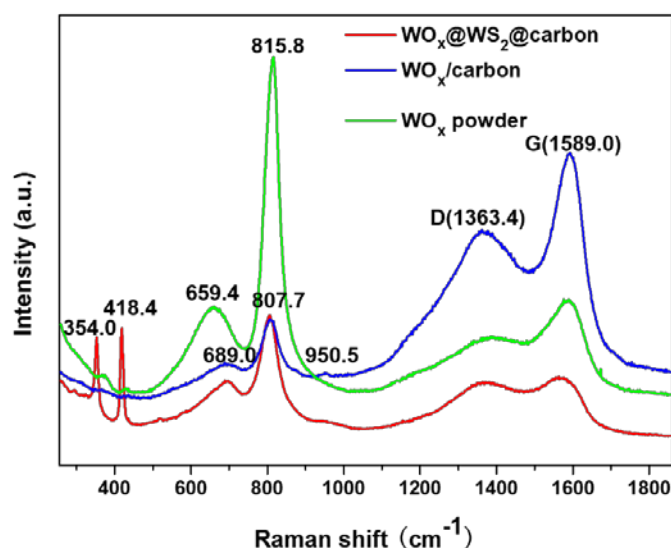


**Figure 6.11.** Raman spectrums of the as-synthesized green  $\text{WO}_x$  powder,  $\text{WO}_x/carbon$  electrode and  $\text{WO}_x@WS_2@carbon$  electrode.

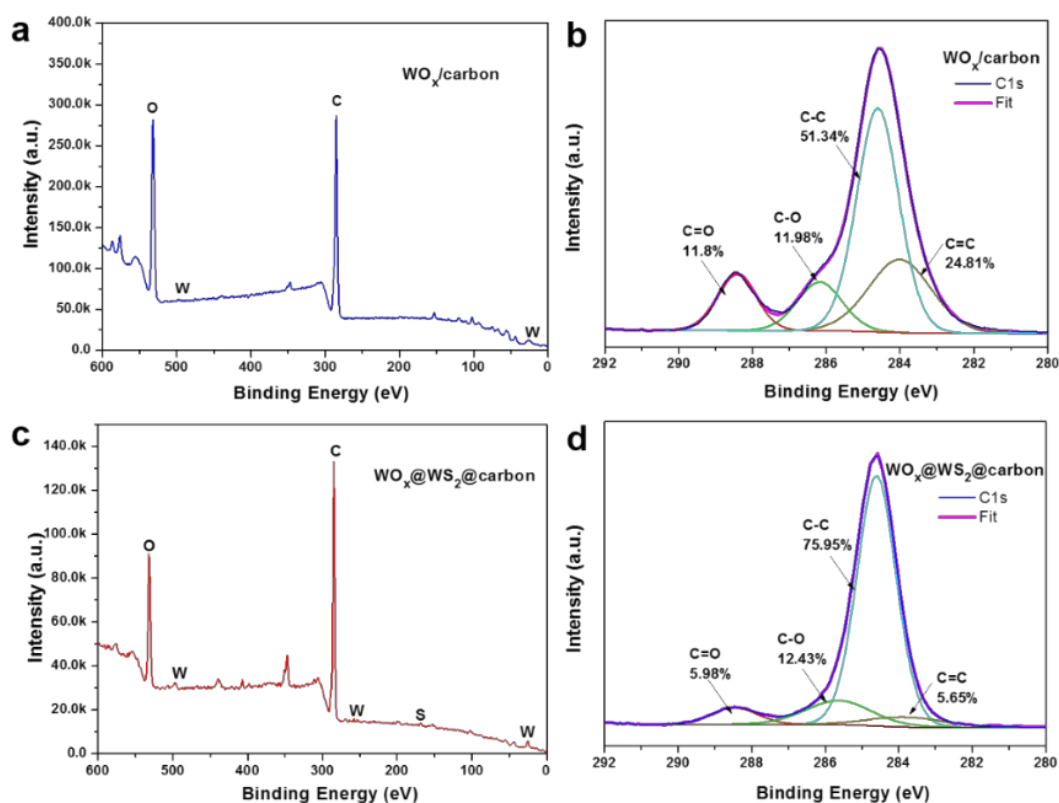


**Figure 6.12.** Survey XPS spectrums of (a)  $\text{WO}_x/\text{carbon}$  and (c)  $\text{WO}_x@WS_2@carbon$  electrode; and C1s and deconvoluted spectrums of (b)  $\text{WO}_x/\text{carbon}$  and (d)  $\text{WO}_x@WS_2@carbon$  electrode.

Figure 6.11 shows Raman spectrum of the synthesized green  $\text{WO}_x$  powder, and the  $\text{WO}_x/\text{carbon}$  and  $\text{WO}_x@WS_2@carbon$  CEs. The spectrum of the synthesized powder is much similar to the Raman spectra of tetragonal  $\text{WO}_3$  reported earlier.[33] The bands at  $815.8$  and  $659.4\text{ cm}^{-1}$  are believed to originate from the stretching modes of O–W–O bonds. The broader peak at  $659.4\text{ cm}^{-1}$  is red-shifted from the corresponding  $714\text{ cm}^{-1}$  line of monoclinic  $\text{WO}_3$ , but it is similar in width and position with the peak observed in  $\alpha\text{-WO}_3$ , existing at a high temperature above  $1000\text{ K}$ .[34] The O–W–O stretching bonds of  $\text{WO}_x/\text{carbon}$  and  $\text{WO}_x@WS_2@carbon$  CEs show lower intensities and shift to  $807.7$  and  $689.0\text{ cm}^{-1}$ , respectively. These changes might relate to the introduction of more carbon into the CEs and the changes in the surface composition of tungsten oxide particles, since the bands position, shape and relative intensities of the Raman spectra of  $\text{WO}_3$  are strongly influenced by the crystallite size and defects in the crystal structure.[35] A small band at  $950.5\text{ cm}^{-1}$  on the spectrum of

WO<sub>x</sub>/carbon CE can be assigned to the stretching mode of W=O bonds of orthorhombic WO<sub>3</sub>,[36] consistent with the analysis of XRD and TEM results. Moreover, the spectrum of WO<sub>x</sub>@WS<sub>2</sub>@carbon CE shows two characteristic WS<sub>2</sub> Raman bands related to the in-plane vibration of W and S atoms at 354.0 cm<sup>-1</sup> and the out-of-plane vibration of S atoms at 418.4 cm<sup>-1</sup>. [24] The two WS<sub>2</sub> bands are also found on the spectrum of the synthesized powder but show lower intensities and a blue shift compared to that of WO<sub>x</sub>@WS<sub>2</sub>@carbon CE, due to the low content of WS<sub>2</sub> in the green powder. The two bands at 1589.0 cm<sup>-1</sup> and 1363.4 cm<sup>-1</sup> are identified as the graphitic sp<sup>2</sup> carbon (G-band) and sp<sup>3</sup>-hybridized carbon (such as structural defects, amorphous carbon, and edge planes) (D-band), respectively.[37, 38] The intensities of both D-band and G-band of WO<sub>x</sub>@WS<sub>2</sub>@carbon CE are much lower than that of the WO<sub>x</sub>/carbon CE, which means the redundant carbon could be removed by the oxygen released during the high temperature sulfurization. The D-band and G-band observed on the spectrum of the synthesized powder due to the surface carbon coating, which echoes with their TEM results. The intensity ratios of D-band to G-band (I<sub>D</sub>/I<sub>G</sub>) of the as-synthesized powder, WO<sub>x</sub>/carbon CE, and WO<sub>x</sub>@WS<sub>2</sub>@carbon CE are 0.78, 0.75 and 0.95, respectively. The highest I<sub>D</sub>/I<sub>G</sub> ratio of WO<sub>x</sub>@WS<sub>2</sub>@carbon CE suggests the interaction between WS<sub>2</sub> and carbon during the sulfurization, which increases the defect density of carbon materials. The high defect density in carbon materials would be beneficial for their electrocatalytic activity.[39] The XPS spectrums of the two CEs also show the similar result, where the percentage area of C=C bond in WO<sub>x</sub>@WS<sub>2</sub>@carbon CE is 5.65% (Figure 6.12d), which is much lower than that of 24.81% in WO<sub>x</sub>/carbon CE (Figure 6.12b). Meanwhile, the weak signals of W and S in the XPS survey spectrums (Figure 6.12a&c) compared with the C signal indicate both WO<sub>3</sub> and WS<sub>2</sub> are well coated by carbon in the two electrodes.

### 6.3.2. Electrochemical properties

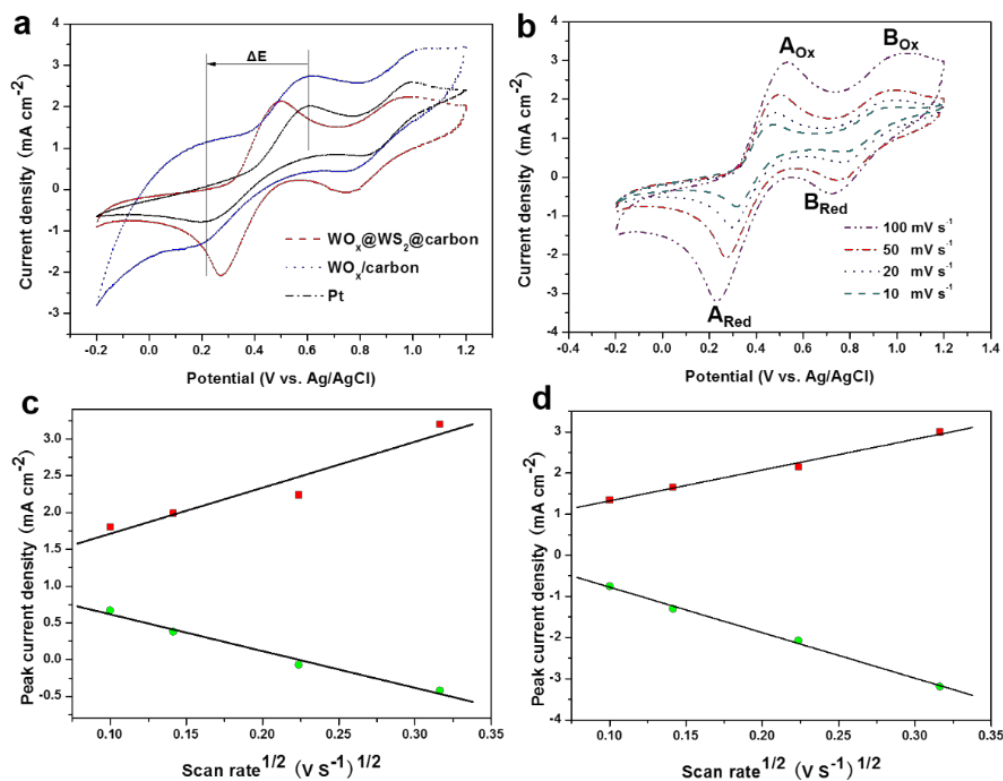


**Figure 6.13.** (a) CV curves of WO<sub>x</sub>/carbon, WO<sub>x</sub>@WS<sub>2</sub>@carbon and Pt electrodes for triiodide/iodide redox couple at scan rates of 50 mV·s<sup>-1</sup>; (b) CV curves of WO<sub>x</sub>@WS<sub>2</sub>@carbon electrode at different scan rates; Relationship between the current densities of anodic (■) and cathodic (●) peaks for (c) redox reaction B and (d) redox reaction A with the square root of scan rate of the WO<sub>x</sub>@WS<sub>2</sub>@carbon electrode.

Cyclic voltammetry (CV) was carried out to evaluate the catalytic activities of the as-prepared WO<sub>x</sub>/carbon, WO<sub>x</sub>@WS<sub>2</sub>@carbon and Pt electrodes, as shown in Figure 6.13. All these electrodes exhibit two typical pairs of oxidation/reduction peaks (A<sub>Ox</sub>/A<sub>Red</sub>, B<sub>Ox</sub>/B<sub>Red</sub>). The A<sub>Ox</sub>/A<sub>Red</sub> pair is assigned to the oxidation and reduction of I<sup>-</sup>/I<sub>3</sub><sup>-</sup>, correlated with the catalytic ability of a CE in DSSCs, whereas the B<sub>Ox</sub>/B<sub>Red</sub> is assigned to the oxidation and reduction of I<sub>3</sub><sup>-</sup>/I<sub>2</sub>. The parameter of peak separation between anodic (A<sub>Ox</sub>) and cathodic (A<sub>Red</sub>) peaks ( $\Delta E$ ) has been widely applied to assess the catalytic activity of a CE, since the standard electrochemical rate constant of a redox reaction is negatively correlated with  $\Delta E$ .<sup>[40]</sup> The measured  $\Delta E$  values of

the different electrodes follow the order of  $\text{WO}_x@WS_2\text{carbon} < \text{Pt} < \text{WO}_x/\text{carbon}$ , indicating that the  $\text{WO}_x@WS_2@carbon$  electrode has the highest catalytic activity for  $\text{I}_3^-$  reduction. In addition, the  $\text{WO}_x@WS_2@carbon$  electrode also has the highest current density at the cathodic peak ( $A_{\text{Red}}$ ), further highlighting its potential as CE for the DSSCs application. Figure 6.13b shows the CV property of the  $\text{WO}_x@WS_2@carbon$  electrode at various scan rates, where the peak current densities increase with the scanning rates. Figure 6.13c&d shows a linear relationship between the peak current densities and the square root of the scanning rates, echoes that the electrode reactions are limited by diffusion for iodide species to reach the  $\text{WO}_x@WS_2@carbon$  CE in the cells.[41]

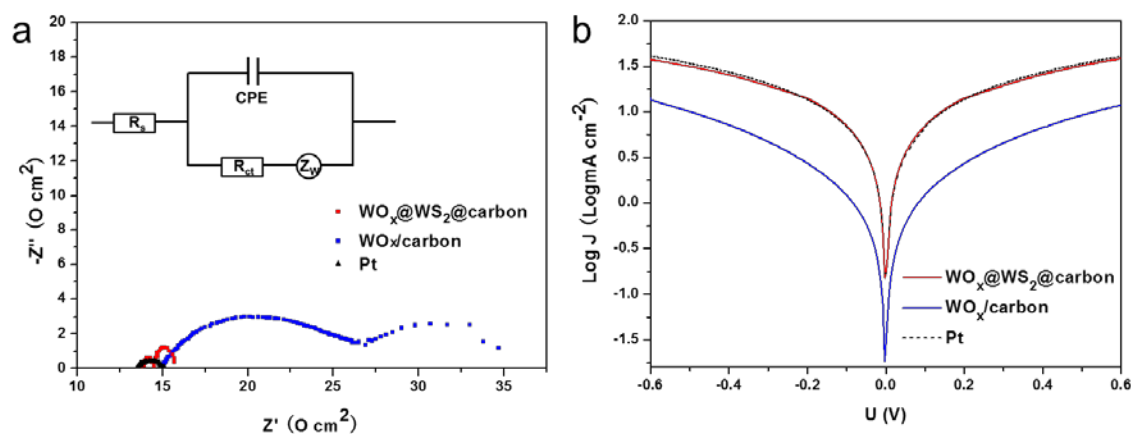


**Figure 6.14.** (a) Nyquist plots and (b) Tafel curves of the symmetrical cells fabricated with two identical  $\text{WO}_x/\text{carbon}$ ,  $\text{WO}_x@WS_2@carbon$  and Pt electrodes.

Electrochemical impedance spectroscopy (EIS) was further performed on symmetrical cells consisting of two identical CEs to investigate the electrochemical reactions occurring at the electrode/electrolyte interface. The obtained Nyquist plots of the three electrodes are presented in Figure 6.14a. The high frequency intercept on the real axis is attributed to a series of resistances ( $R_s$ ) of the cell components, while the left semicircle in the high-frequency range is assigned to the charge transfer resistance ( $R_{ct}$ ) at the electrode/electrolyte interface with the corresponding constant phase angle element (CPE). The right semicircle in the low-frequency range responds to the Nernst diffusion impedance ( $Z_w$ ) of the redox couple transport in the electrolyte. The

Nyquist plots for the three CEs were fitted using the ZSimpWin software with an equivalent circuit diagram (inset of Figure 6.14a) and the corresponding EIS parameters are shown in Table 1. The  $R_s$  value of  $13.69 \Omega \cdot \text{cm}^2$  for  $\text{WO}_x@WS_2@carbon$  CE is smaller than  $\text{WO}_x/carbon$  CE ( $14.88 \Omega \cdot \text{cm}^2$ ) and but close to  $13.52 \Omega \cdot \text{cm}^2$  of Pt CE, which can be attributed to the strong interaction between carbon and  $WS_2$  layers (Figure 6.9) forming a continuously conductive matrix in the  $\text{WO}_x@WS_2@carbon$  electrode. The  $R_{ct}$  of  $\text{WO}_x@WS_2@carbon$  CE is  $0.88 \Omega \cdot \text{cm}^2$ , much smaller than  $12.70 \Omega \cdot \text{cm}^2$  of the  $\text{WO}_x/carbon$  CE and  $1.47 \Omega \cdot \text{cm}^2$  of the Pt CE, indicating the  $\text{WO}_x@WS_2@carbon$  electrode is more efficient in terms of catalytic reduction of  $I_3^-$  at the CE/electrolyte interface. The improvement of the catalytic activity of the  $\text{WO}_x@WS_2@carbon$  CE can be ascribed to the abundant active edge sites on the high-curvature surface of the  $WS_2$  layers, [25] the high defect density of the wrapped carbon and the facile electron transfer via continuous core-shell  $\text{WO}_3@WS_2$  building blocks in the carbon matrix. The  $Z_w$  value of  $8.49 \Omega \cdot \text{cm}^2$  for the redox couple ( $I_3^-/I^-$ ) on the  $\text{WO}_x/carbon$  CE is much bigger than that on the  $\text{WO}_x@WS_2@carbon$  CE ( $1.21 \Omega \cdot \text{cm}^2$ ) and the Pt CE ( $0.20 \Omega \cdot \text{cm}^2$ ). The  $Z_w$  value is known inversely with the diffusion coefficient of triiodide (D), [19] thus large  $Z_w$  is a negative indicator for the  $\text{WO}_x/carbon$  CE in term of catalytic activity. In other words, the redox couple diffusion on the electrode can be improved by the sulfurization of the  $\text{WO}_x/carbon$  because of removal of the surplus carbon by oxidation at high temperatures.

Tafel polarization was employed to further probe the interfacial charge-transfer properties of the  $I_3^-/I^-$  redox couple on the electrode surface. Figure 6.14b exhibits Tafel curves of symmetrical cells based on  $\text{WO}_x/carbon$ ,  $\text{WO}_x@WS_2@carbon$  and Pt CEs, respectively. At Tafel zone (middle potential area), both anodic and cathodic branches of  $\text{WO}_x@WS_2@carbon$  electrode show larger slopes than the  $\text{WO}_x/carbon$ , which are also comparable to the Pt CE. This observation suggests higher exchange current density ( $J_0$ ) generated from the  $\text{WO}_x@WS_2@carbon$  electrode, which is in line with the EIS values in terms of Eqn (1):

$$J_0 = \frac{RT}{nFR_{ct}} \quad (1)$$

Where  $R$ ,  $T$ ,  $F$ ,  $n$  and  $R_{ct}$  are the gas constant, temperature, Faraday constant, the number of electrons involved in the triiodide reduction, and the charge transfer resistance, respectively. At a high potential zone, the limiting diffusion current density ( $J_{lim}$ ) value for the  $WO_x@WS_2@carbon$  electrode is slightly smaller than the Pt CE but much bigger than the  $WO_x/carbon$  electrode. This reflects that the diffusion coefficient in the  $WO_x@WS_2@carbon$  symmetrical cell is comparable to that in the Pt cell according to Eqn (2):

$$D = \frac{l}{2nFC} J_{lim} \quad (2)$$

Where  $D$  is the diffusion coefficient,  $l$  is the distance between the electrodes in a dummy cell, and  $C$  is the  $I_3^-$  concentration. This result matches well with the  $Z_w$  values obtained from the EIS analysis.

### 6.3.3. Photovoltaic performance

Three DSSC devices with  $WO_x/carbon$ ,  $WO_x@WS_2@carbon$  and Pt as CEs were assembled to assess their respective photovoltaic performances under similar operating conditions. Figure 6.15 describes the photocurrent density–voltage (J–V) plots of three devices with the corresponding photovoltaic parameters listed in Table 6.1. The device based on  $WO_x@WS_2@carbon$  CE displayed the highest power conversion efficiency (PCE) of 7.71%, followed by the Pt (PCE 7.34%) and the  $WO_x/carbon$  (PCE 6.00%). The superior PCE from  $WO_x@WS_2@carbon$  against  $WO_x/carbon$  based cell is due to the increase of short-circuit photocurrent ( $J_{sc}$ ), sourced from reason that  $WS_2$  has much better catalytic activity toward the reduction of  $I_3^-$  than  $WO_3$ . The interconnected  $WO_3@WS_2$  core-shell blocks with surrounding irregular  $WS_2$  layers and the edge-oriented  $WS_2$  nanosheets in the  $WO_x@WS_2@carbon$  CE build up an efficient three-dimensional catalytic network and maximize the fraction of exposed active edge sites for the reduction of  $I_3^-$ . Meanwhile, the surface coated carbon with many defect sites provides additional

catalytic activity and a continuously conductive matrix for the efficient electron/electrolyte transport. These synergistic effects resulted in a relatively small  $R_s$  and  $R_{ct}$  as well as in a high diffusion coefficient making the DSSC based on  $WO_x@WS_2@carbon$  CE have a highest fill factor (FF, 69.5%). Thus, the photovoltaic performance of the cells based on the  $WO_x@WS_2@carbon$  CE was further improved even compared with the Pt based cells.

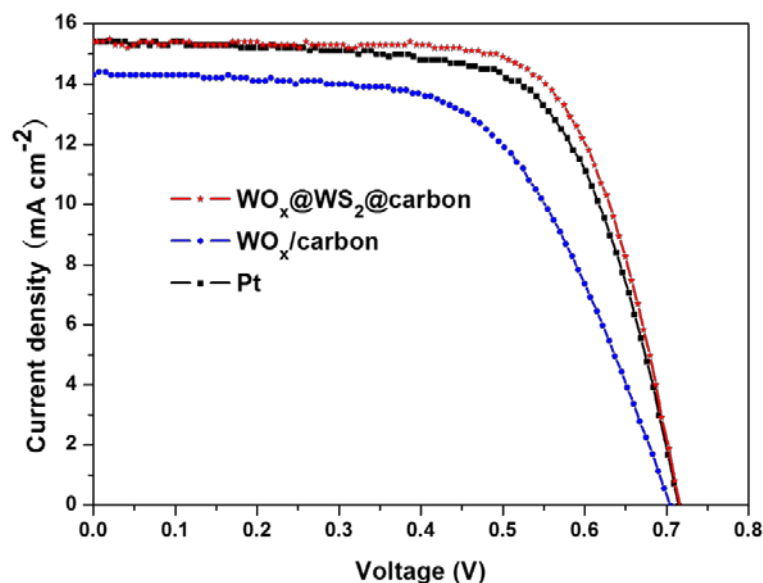


**Figure 6.15.** J-V curves of DSSCs based on the  $WO_x/carbon$ ,  $WO_x@WS_2@carbon$  and Pt counter electrodes measured under an illumination of one sun (AM 1.5G,  $100 \text{ mW}\cdot\text{cm}^{-2}$ ).

**Table 6.1** Photovoltaic Parameters of DSSCs Based on the  $WO_x/carbon$ ,  $WO_x@WS_2@carbon$  and Pt Counter Electrodes and EIS Parameters of the Symmetrical Cells Fabricated with Two Identical  $WO_x/carbon$ ,  $WO_x@WS_2@carbon$  and Pt Electrodes.

Sample	$J_{sc}$ ( $\text{mA}\cdot\text{cm}^{-2}$ )	$V_{oc}$ (V)	FF (%)	$\eta$ (%)	$R_s$ ( $\Omega\cdot\text{cm}^2$ )	$R_{ct}$ ( $\Omega\cdot\text{cm}^2$ )	$Z_w$ ( $\Omega\cdot\text{cm}^2$ )
Pt	15.44	0.715	66.5	7.34	13.52	1.47	0.20
$WO_x/carbon$	14.38	0.705	59.1	6.00	14.88	12.70	8.49
$WO_x@WS_2@carbon$	15.48	0.720	69.5	7.71	13.69	0.88	1.21

## 6.4. Conclusions

A green powder consisted of carbon-coated major tetragonal  $\text{WO}_3$  blocks and tetragonal  $\text{W}_5\text{O}_{14}$  nanorods as well as a small amount of  $\text{WS}_2$  have been synthesized through a hydrothermal and calcination process. The synthesized  $\text{WO}_x$  powder paste with ethyl cellulose was coated onto a FTO glass by the doctor blade method to form a mesoporous electrode named  $\text{WO}_x/\text{carbon}$ , which mainly consists of tetragonal and orthorhombic  $\text{WO}_3$  with carbon. The  $\text{WO}_x@ \text{WS}_2@ \text{carbon}$  electrode was prepared by a rapid sulfurization process of  $\text{WO}_x/\text{carbon}$  at high temperatures. During the sulfurization, the orthorhombic  $\text{WO}_3$  with small particle size was converted to layered  $\text{WS}_2$  structure completely and the inner big tetragonal  $\text{WO}_3$  blocks were transformed to a  $\text{WO}_3@ \text{WS}_2$  core-shell structure. Meanwhile, the redundant carbon was oxidized and removed by the oxygen released during the high temperature sulfurization, which resulted in the continuously conductive carbon matrix and improved the interaction between the carbon and the  $\text{WS}_2$ . The  $\text{W}_5\text{O}_{14}$  nanorods were also transformed to  $\text{WS}_2$  with rod-like structure during sulfurization. Thus, a carbon coated three-dimensional  $\text{WS}_2$  catalytic network was built up in the  $\text{WO}_x@ \text{WS}_2@ \text{carbon}$  electrode by the interconnected  $\text{WO}_3@ \text{WS}_2$  core-shell blocks with surrounding irregular  $\text{WS}_2$  layers, a small amount of  $\text{WS}_2$  nanorods and the superficial edge-oriented  $\text{WS}_2$  nanosheets with high-curvature surface. Owing to its unique catalytic active sites and conductive properties, the  $\text{WO}_x@ \text{WS}_2@ \text{carbon}$  CE exhibits high electrocatalytic activity toward the triiodide reduction in DSSCs. The enhanced DSSC performances in terms of FF and PCE can be evidenced from the lower peak separation between the anodic and cathodic peak ( $\Delta E$ ) in the CV test, the significantly lower charge-transfer resistance ( $R_{ct}$ ) in the EIS analysis, and the higher exchange current density ( $J_0$ ) in the Tafel polarization curves. The DSSC device based on  $\text{WO}_x@ \text{WS}_2@ \text{carbon}$  CE exhibits a PCE of 7.71%, which is superior to that of the cells based on  $\text{WO}_x/\text{carbon}$  (6.00%) and Pt (7.34%) CE. The results show the potential to realize Pt-free counter electrodes for DSSCs.

## References

1. O'Regan, B. and M. Gratzel, *A low-cost, high-efficiency solar cell based on dye-sensitized colloidal TiO<sub>2</sub> films*. Nature, 1991. **353**(6346): p. 737-740.
2. Gong, J., J. Liang, and K. Sumathy, *Review on dye-sensitized solar cells (DSSCs): Fundamental concepts and novel materials*. Renewable and Sustainable Energy Reviews, 2012. **16**(8): p. 5848-5860.
3. Yella, A., et al., *Porphyrin-Sensitized Solar Cells with Cobalt (II/III)-Based Redox Electrolyte Exceed 12 Percent Efficiency*. Science, 2011. **334**(6056): p. 629-634.
4. Kakiage, K., et al., *Highly-efficient dye-sensitized solar cells with collaborative sensitization by silyl-anchor and carboxy-anchor dyes*. Chemical Communications, 2015. **51**(88): p. 15894-15897.
5. Olsen, E., G. Hagen, and S. Eric Lindquist, *Dissolution of platinum in methoxy propionitrile containing LiI/2*. Solar Energy Materials and Solar Cells, 2000. **63**(3): p. 267-273.
6. Kay, A. and M. Grätzel, *Low cost photovoltaic modules based on dye sensitized nanocrystalline titanium dioxide and carbon powder*. Solar Energy Materials and Solar Cells, 1996. **44**(1): p. 99-117.
7. Liu, Y., et al., *Intrinsic Origin of Superior Catalytic Properties of Tungsten-based Catalysts in Dye-sensitized Solar Cells*. Electrochimica Acta, 2017. **242**: p. 390-399.
8. Cheng, L., et al., *Hydrogen-treated commercial WO<sub>3</sub> as an efficient electrocatalyst for triiodide reduction in dye-sensitized solar cells*. Chemical Communications, 2013. **49**(53): p. 5945-5947.
9. Uppachai, P., et al., *A substoichiometric tungsten oxide catalyst provides a sustainable and efficient counter electrode for dye-sensitized solar cells*. Electrochimica Acta, 2014. **145**: p. 27-33.
10. Jeong, I., et al., *Ordered Mesoporous Tungsten Suboxide Counter Electrode for Highly Efficient Iodine-Free Electrolyte-Based Dye-Sensitized Solar Cells*. ChemSusChem, 2013. **6**(2): p. 299-307.
11. Song, D., et al., *NH<sub>3</sub>-treated WO<sub>3</sub> as low-cost and efficient counter electrode for dye-sensitized solar cells*. Nanoscale Research Letters, 2015. **10**(1): p. 16.
12. Vijayakumar, P., et al., *Facile synthesis of tungsten carbide nanorods and its application as counter electrode in dye sensitized solar cells*. Materials Science in Semiconductor Processing, 2015. **39**: p. 292-299.
13. Jang, J.S., et al., *Platinum-free tungsten carbides as an efficient counter electrode for dye sensitized solar cells*. Chemical Communications, 2010. **46**(45): p. 8600-8602.
14. Jeong, I., et al., *Low-cost electrospun WC/C composite nanofiber as a powerful platinum-free counter electrode for dye sensitized solar cell*. Nano Energy, 2014. **9**: p. 392-400.
15. Li, G.R., et al., *Highly Pt-like electrocatalytic activity of transition metal nitrides for dye-sensitized solar cells*. Energy & Environmental Science, 2011. **4**(5): p. 1680-1683.
16. Migas, D.B., V.L. Shaposhnikov, and V.E. Borisenko, *Tungsten oxides. II. The metallic nature of Magneli phases*. Journal of Applied Physics, 2010. **108**(9).
17. Wu, M., et al., *A novel catalyst of WO<sub>2</sub> nanorod for the counter electrode of dye-sensitized solar cells*. Chemical Communications, 2011. **47**(15): p. 4535-4537.

18. Tenne, R., et al., *Polyhedral and cylindrical structures of tungsten disulphide*. Nature, 1992. **360**(6403): p. 444-446.
19. Wu, M., et al., *Economical and effective sulfide catalysts for dye-sensitized solar cells as counter electrodes*. Physical Chemistry Chemical Physics, 2011. **13**(43): p. 19298-19301.
20. Wang, Y., et al., *Dye-sensitized solar cells based on low cost carbon-coated tungsten disulphide counter electrodes*. Electrochimica Acta, 2013. **114**: p. 30-34.
21. Li, S., Z. Chen, and W. Zhang, *Dye-sensitized solar cells based on WS<sub>2</sub> counter electrodes*. Materials Letters, 2012. **72**: p. 22-24.
22. Yue, G., et al., *A counter electrode of multi-wall carbon nanotubes decorated with tungsten sulfide used in dye-sensitized solar cells*. Carbon, 2013. **55**: p. 1-9.
23. Wu, J., et al., *Glucose Aided Preparation of Tungsten Sulfide/Multi-Wall Carbon Nanotube Hybrid and Use as Counter Electrode in Dye-Sensitized Solar Cells*. ACS Applied Materials & Interfaces, 2012. **4**(12): p. 6530-6536.
24. Hussain, S., et al., *Sputtering and sulfurization-combined synthesis of a transparent WS<sub>2</sub> counter electrode and its application to dye-sensitized solar cells*. RSC Advances, 2015. **5**(125): p. 103567-103572.
25. Ahn, S.H. and A. Manthiram, *Edge-Oriented Tungsten Disulfide Catalyst Produced from Mesoporous WO<sub>3</sub> for Highly Efficient Dye-Sensitized Solar Cells*. Advanced Energy Materials, 2016. **6**(3): p. 1501814.
26. Shen, Z., et al., *Bi-layer photoanode films of hierarchical carbon-doped brookite-rutile TiO<sub>2</sub> composite and anatase TiO<sub>2</sub> beads for efficient dye-sensitized solar cells*. Electrochimica Acta, 2016. **216**: p. 429-437.
27. Cao, S., et al., *Hydrothermal synthesis of variety low dimensional WS<sub>2</sub> nanostructures*. Materials Letters, 2014. **129**: p. 205-208.
28. Pokhrel, S., et al., *In situ high temperature X-ray diffraction, transmission electron microscopy and theoretical modeling for the formation of WO<sub>3</sub> crystallites*. CrystEngComm, 2015. **17**(36): p. 6985-6998.
29. Zheng, H., et al., *Nanostructured Tungsten Oxide – Properties, Synthesis, and Applications*. Advanced Functional Materials, 2011. **21**(12): p. 2175-2196.
30. Faudoa-Arzate, A., et al., *HRTEM Microstructural Characterization of  $\beta$ -WO<sub>3</sub> Thin Films Deposited by Reactive RF Magnetron Sputtering*. Materials, 2017. **10**(2): p. 200.
31. Zink, N., et al., *In Situ Heating TEM Study of Onion-like WS<sub>2</sub> and MoS<sub>2</sub> Nanostructures Obtained via MOCVD*. Chemistry of Materials, 2008. **20**(1): p. 65-71.
32. Tenne, R., M. Homyonfer, and Y. Feldman, *Nanoparticles of Layered Compounds with Hollow Cage Structures (Inorganic Fullerene-Like Structures)*. Chemistry of Materials, 1998. **10**(11): p. 3225-3238.
33. Wu, W., et al., *Tetragonal tungsten oxide nanobelts synthesized by chemical vapor deposition*. Journal of Crystal Growth, 2010. **312**(21): p. 3147-3150.
34. Boulova, M. and G. Lucazeau, *Crystallite Nanosize Effect on the Structural Transitions of WO<sub>3</sub> Studied by Raman Spectroscopy*. Journal of Solid State Chemistry, 2002. **167**(2): p. 425-434.
35. Mehmood, F., et al., *Effect of Sn doping on the structural, optical, electrical and anticancer properties of WO<sub>3</sub> nanoplates*. Ceramics International, 2016. **42**(13): p. 14334-14341.
36. Xi, L., et al., *Investigation of hydrogen interaction with Pt-coated tungsten oxide hydrate nanoplates*. Materials Research Express, 2014. **1**(2): p. 025044.

37. Lin, C.-A., et al., *Nitrogen-Doped Graphene/Platinum Counter Electrodes for Dye-Sensitized Solar Cells*. ACS Photonics, 2014. **1**(12): p. 1264-1269.
38. Huo, J., et al., *High performance sponge-like cobalt sulfide/reduced graphene oxide hybrid counter electrode for dye-sensitized solar cells*. Journal of Power Sources, 2015. **293**: p. 570-576.
39. Punckt, C., et al., *Electrochemical Performance of Graphene as Effected by Electrode Porosity and Graphene Functionalization*. Electroanalysis, 2010. **22**(23): p. 2834-2841.
40. Roy-Mayhew, J.D., et al., *Functionalized Graphene as a Catalytic Counter Electrode in Dye-Sensitized Solar Cells*. ACS Nano, 2010. **4**(10): p. 6203-6211.
41. Biallozor, S. and A. Kupniewska, *Study on poly(3,4-ethylenedioxythiophene) behaviour in the I<sup>-</sup>/I<sub>2</sub> solution*. Electrochemistry Communications, 2000. **2**(7): p. 480-486.

*Every reasonable effort has been made to acknowledge the owners of copyright material. I would be pleased to hear from any copyright owner who has been omitted or incorrectly acknowledged.*

## **Chapter 7: Conclusions and Perspectives**

### **7.1 Conclusions**

In this thesis, an overview has been made to summarize the general fabrication methods of carbon-semiconductor hybrid materials (CSHMs) and their recent applications in solar energy conversion including photocatalysis and solar cells. The current synthesis methods of carbon-semiconductor nanocomposites are usually involving the dispersion methods of carbon and semiconductor materials, lacking of precious control in fabrication and thus resulting in low uniformity and quality. Furthermore, the preparation of CSHMs with hierarchical structure is complex involving multiple-step and hazardous chemicals. Such drawbacks are hindering their photocatalytic and photovoltaic performances and restricting their large scale applications. From this perspective, we have tried to use inexpensive sources and facile approaches for the fabrication of different kinds of CSHMs in this thesis. The obtained CSHMs have been employed as the photocatalyst for the degradation of organic pollutants and used as photoanode and counter electrode in dye-sensitized solar cells (DSSCs), all of which have improved the corresponding solar energy-conversion efficiencies.

#### **7.1.1 Green synthesis of carbon- and silver-modified hierarchical ZnO with excellent solar light driven photocatalytic performance**

A series of high-quality ZnO nano/micro-structures enwrapped with a thin carbon layer were synthesized by a green hydrothermal method using yeast mold broth as the source of carbon precursor and the directing agent for ZnO nucleation. By optimizing the reaction parameters, including zinc precursor concentration, broth pH value, and broth content, ZnO@C composites with various sizes and shapes have been produced. After depositing Ag nanoparticles by photo-reduction in the broth, the obtained

ZnO@C–Ag ternary hybrid demonstrated excellent photocatalytic activities towards methylene blue degradation under solar light irradiation.

### **7.1.2 Bi-layer photoanode films of hierarchical carbon-doped brookite-rutile TiO<sub>2</sub> composite and anatase TiO<sub>2</sub> beads for efficient dye-sensitized solar cells**

Surfactants with long alkyl chains commonly used for the synthesis of semiconductor materials can also be converted into carbon after heat treatment resulting in the formation of CSHMs in situ. Carbon-doped hierarchical TiO<sub>2</sub> beads consisting of rutile and brookite nanoparticles were prepared through a hydrothermal treatment of the hexadecylamine directed TiO<sub>2</sub> bead precursor in the presence of 10 wt.% HCl, followed by the calcination at elevated temperatures. These C-TiO<sub>2</sub> beads displayed excellent property for electron transport due to the presence of one-dimensional rutile nanorods and carbon doping. The prepared composite was employed as the top layer above another anatase bead layer with larger surface area in the photoanode of DSSCs, which gave a power conversion efficiency (PCE) of 7.24% exceeding the counterpart DSSCs based on their individual bead-P25 bi-layer films and pure P25 film.

### **7.1.3 Carbon-dot/natural-dye sensitizer for TiO<sub>2</sub> solar cells prepared by a one-step treatment of celery leaf extract**

Dye-carbon dots (CDs) complexes derived from the cost-effective hydrothermal treatment of alcoholic extracts from celery leaves were successfully deposited on TiO<sub>2</sub> film and used as a photoanode for DSSC. It was found the particle size, surface states, and optical properties of CDs as well as the surviving amount of dye highly depend on the hydrothermal temperature, which further influence the solar cell performances. The solar cells sensitized with the complex obtained from 120 °C achieved the highest PCE of 0.48% relative to those sensitized by the original or higher temperature-treated extract solutions. The CDs with smaller particle size, less trap states and more carboxy C=O bonding groups, can work effectively as an

electron transfer bridge between dye and TiO<sub>2</sub> reducing the probability of photo generated charge carrier recombination.

#### **7.1.4 Carbon-coated three-dimensional WS<sub>2</sub> film consisting of WO<sub>3</sub>@WS<sub>2</sub> core-shell blocks and layered WS<sub>2</sub> nanostructures as counter electrodes for efficient dye-sensitized solar cells**

A green WO<sub>x</sub> powder coated with a thin carbon layer has been synthesized through a hydrothermal and calcination process, which was further used to design the Pt-free WO<sub>x</sub>@WS<sub>2</sub>@carbon counter electrode for DSSCs through a rapid sulfurization process. In the three-dimensional WO<sub>x</sub>@WS<sub>2</sub>@carbon electrode, a well-interconnected WS<sub>2</sub> catalytic network consisting of WO<sub>3</sub>@WS<sub>2</sub> core-shell blocks with surrounding irregular WS<sub>2</sub> layers, a small amount of WS<sub>2</sub> nanorods and the edge-oriented WS<sub>2</sub> nanosheets, were enwrapped by a continuous carbon layer. Owing to its unique catalytic active sites and conductive properties, the WO<sub>x</sub>@WS<sub>2</sub>@carbon counter electrode exhibited high electrocatalytic activity toward the triiodide reduction in DSSCs. The device based on WO<sub>x</sub>@WS<sub>2</sub>@carbon counter electrode exhibits a PCE of 7.71%, which was superior to that of the cells based on WO<sub>x</sub>/carbon (6.00%) and Pt (7.34%) electrodes.

## **7.2 Perspectives**

1. The microbe-free biogenic approach presented in Chapter 3 can allow the cheap, large-scale and short-run production of carbon-semiconductor hybrid nanoparticles. However, its mechanisms of action are still not clear. A systematic and detail investigation should be conducted to discover the precise mechanism behind this transformation, and it will definitely make a great contribution for synthesizing other CSHMs via this facile synthesis route.
2. In Chapter 4, the C-TiO<sub>2</sub> composites exhibited excellent electron transport property, which can effectively reduce the photo generated charge recombination when using as

photoanode material in DSSCs. However, its relatively small surface area reduced the amount of dye loading. Thus, this hierarchical structure needs to be further tailored to increase its surface area but still maintain the high electron transport capability.

3. The nature dye/CD/semiconductor system may provide a new route for the development of photoelectric devices in an economic and environment-friendly way. However, the power conversion efficiency still cannot be competitive with the devices based on ruthenium dyes due to the limited light absorption of both nature dye and CDs. The light harvesting ability needs to be further improved. Besides, particle size and functional groups on the surface of CDs would affect the trap states of CDs and their interaction with semiconductor film, which are critical to the solar cell performance. A further study needs to focus on uniformly and precisely controlling particle size and trap states of CDs.

4. Sulfurization is an effective way to prepare sulfide/carbon hybrid film with controllable structures. The obtained  $\text{WO}_x@WS_2@carbon$  film in Chapter 6 demonstrated excellent electrocatalytic activity toward the reduction of triiodide, highlighting the potential to realize Pt-free counter electrodes for DSSCs. The stability test of such counter electrode needs to be further conducted from a practical application point of view.

5. The applications of CSHMs in this thesis are limited in photocatalytic degradation of dyes and DSSCs. It is believed that CSHMs have a wider range of application in regard to solar energy conversion, such as water splitting for hydrogen generation, photocatalytic carbon dioxide reduction, and more efficient perovskite solar cells. In future work, these hybrid materials should be investigated in different fields to explore more possibilities to realize its applications.

## Appendix: Permission of Reproduction from the Copyright Owner



RightsLink®

Home

Account Info

Help



**Title:** Enhanced photocatalytic activity of TiO<sub>2</sub>/carbon@TiO<sub>2</sub> core-shell nanocomposite prepared by two-step hydrothermal method

Logged in as:  
Zhangfeng Shen

LOGOUT

**Author:** Guozhi Zhang, Feng Teng, Changhui Zhao, Lulu Chen, Peng Zhang, Youqing Wang, Chengshi Gong, Zhenxing Zhang, Erqing Xie

**Publication:** Applied Surface Science

**Publisher:** Elsevier

**Date:** 30 August 2014

Copyright © 2014 Elsevier B.V. All rights reserved.

### Order Completed

Thank you for your order.

This Agreement between Zhangfeng Shen ("You") and Elsevier ("Elsevier") consists of your license details and the terms and conditions provided by Elsevier and Copyright Clearance Center.

Your confirmation email will contain your order number for future reference.

### [printable details](#)

License Number	4221670519233
License date	Nov 03, 2017
Licensed Content Publisher	Elsevier
Licensed Content Publication	Applied Surface Science
Licensed Content Title	Enhanced photocatalytic activity of TiO <sub>2</sub> /carbon@TiO <sub>2</sub> core-shell nanocomposite prepared by two-step hydrothermal method
Licensed Content Author	Guozhi Zhang, Feng Teng, Changhui Zhao, Lulu Chen, Peng Zhang, Youqing Wang, Chengshi Gong, Zhenxing Zhang, Erqing Xie
Licensed Content Date	Aug 30, 2014
Licensed Content Volume	311
Licensed Content Issue	n/a
Licensed Content Pages	7
Type of Use	reuse in a thesis/dissertation
Portion	figures/tables/illustrations
Number of figures/tables/illustrations	1
Format	both print and electronic
Are you the author of this Elsevier article?	No
Will you be translating?	No
Original figure numbers	Figure 1
Title of your thesis/dissertation	Engineering Carbon-Semiconductor Hybrid Materials for Photocatalysis and Solar Cells
Expected completion date	Nov 2017
Estimated size (number of pages)	230
Requestor Location	Zhangfeng Shen 10 Lurnea Place, Karawara  Perth, WA 6152



RightsLink®

Home

Account  
Info

Help



ACS Publications  
Most Trusted. Most Cited. Most Read.

**Title:** Soft-Template Simple Synthesis of Ordered Mesoporous Titanium Nitride-Carbon Nanocomposite for High Performance Dye-Sensitized Solar Cell Counter Electrodes

**Author:** Easwaramoorthi Ramasamy, Changshin Jo, Arockiam Anthonyamy, et al

**Publication:** Chemistry of Materials

**Publisher:** American Chemical Society

**Date:** May 1, 2012

Copyright © 2012, American Chemical Society

Logged in as:

Zhangfeng Shen

LOGOUT

#### PERMISSION/LICENSE IS GRANTED FOR YOUR ORDER AT NO CHARGE

This type of permission/license, instead of the standard Terms & Conditions, is sent to you because no fee is being charged for your order. Please note the following:

- Permission is granted for your request in both print and electronic formats, and translations.
- If figures and/or tables were requested, they may be adapted or used in part.
- Please print this page for your records and send a copy of it to your publisher/graduate school.
- Appropriate credit for the requested material should be given as follows: "Reprinted (adapted) with permission from (COMPLETE REFERENCE CITATION). Copyright (YEAR) American Chemical Society." Insert appropriate information in place of the capitalized words.
- One-time permission is granted only for the use specified in your request. No additional uses are granted (such as derivative works or other editions). For any other uses, please submit a new request.

If credit is given to another source for the material you requested, permission must be obtained from that source.

BACK

CLOSE WINDOW

Copyright © 2017 Copyright Clearance Center, Inc. All Rights Reserved. [Privacy statement](#). [Terms and Conditions](#).  
Comments? We would like to hear from you. E-mail us at [customer@copyright.com](mailto:customer@copyright.com)



RightsLink®

Home

Account  
Info

Help



ACS Publications  
Most Trusted. Most Cited. Most Read.

**Title:** New Insight for Enhanced Photocatalytic Activity of TiO<sub>2</sub> by Doping Carbon Nanotubes: A Case Study on Degradation of Benzene and Methyl Orange

**Author:** Yi-Jun Xu, Yangbin Zhuang, Xianzhi Fu

**Publication:** The Journal of Physical Chemistry C

**Publisher:** American Chemical Society

**Date:** Feb 1, 2010

Copyright © 2010, American Chemical Society

Logged in as:  
Zhangfeng Shen

LOGOUT

#### PERMISSION/LICENSE IS GRANTED FOR YOUR ORDER AT NO CHARGE

This type of permission/license, instead of the standard Terms & Conditions, is sent to you because no fee is being charged for your order. Please note the following:

- Permission is granted for your request in both print and electronic formats, and translations.
- If figures and/or tables were requested, they may be adapted or used in part.
- Please print this page for your records and send a copy of it to your publisher/graduate school.
- Appropriate credit for the requested material should be given as follows: "Reprinted (adapted) with permission from (COMPLETE REFERENCE CITATION). Copyright (YEAR) American Chemical Society." Insert appropriate information in place of the capitalized words.
- One-time permission is granted only for the use specified in your request. No additional uses are granted (such as derivative works or other editions). For any other uses, please submit a new request.

If credit is given to another source for the material you requested, permission must be obtained from that source.

BACK

CLOSE WINDOW

Copyright © 2017 Copyright Clearance Center, Inc. All Rights Reserved. [Privacy statement](#). [Terms and Conditions](#). Comments? We would like to hear from you. E-mail us at [customercare@copyright.com](mailto:customercare@copyright.com)



**Title:** A novel composite of TiO<sub>2</sub> nanotubes with remarkably high efficiency for hydrogen production in solar-driven water splitting

**Author:** Caixian Zhao, Hean Luo, Feng Chen, Ping Zhang, Lanhua Yi, Kuiyi You

**Publication:** Energy & Environmental Science

**Publisher:** Royal Society of Chemistry

**Date:** Feb 3, 2014

Copyright © 2014, Royal Society of Chemistry

Logged in as:  
Zhangfeng Shen

LOGOUT

### Order Completed

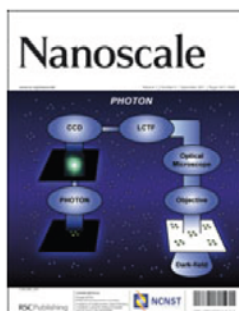
Thank you for your order.

This Agreement between Zhangfeng Shen ("You") and Royal Society of Chemistry ("Royal Society of Chemistry") consists of your license details and the terms and conditions provided by Royal Society of Chemistry and Copyright Clearance Center.

Your confirmation email will contain your order number for future reference.

#### [printable details](#)

License Number	4221690074042
License date	Nov 03, 2017
Licensed Content Publisher	Royal Society of Chemistry
Licensed Content Publication	Energy & Environmental Science
Licensed Content Title	A novel composite of TiO <sub>2</sub> nanotubes with remarkably high efficiency for hydrogen production in solar-driven water splitting
Licensed Content Author	Caixian Zhao, Hean Luo, Feng Chen, Ping Zhang, Lanhua Yi, Kuiyi You
Licensed Content Date	Feb 3, 2014
Licensed Content Volume	7
Licensed Content Issue	5
Type of Use	Thesis/Dissertation
Requestor type	academic/educational
Portion	figures/tables/images
Number of figures/tables/images	1
Distribution quantity	10
Format	print and electronic
Will you be translating?	no
Order reference number	
Title of the thesis/dissertation	Engineering Carbon-Semiconductor Hybrid Materials for Photocatalysis and Solar Cells
Expected completion date	Nov 2017
Estimated size	230
Requestor Location	Zhangfeng Shen 10 Lurnea Place, Karawara  Perth, WA 6152



**Title:** Morphology and crystallinity control of ultrathin TiO<sub>2</sub> layers deposited on carbon nanotubes by temperature-step atomic layer deposition

**Author:** Carlos Guerra-Nuñez, Yucheng Zhang, Meng Li, Vipin Chawla, Rolf Erni, Johann Michler, Hyung Gyu Park, Ivo Utke

**Publication:** Nanoscale

**Publisher:** Royal Society of Chemistry

**Date:** May 11, 2015

Copyright © 2015, Royal Society of Chemistry

Logged in as:  
Zhangfeng Shen

LOGOUT

**Order Completed**

Thank you for your order.

This Agreement between Zhangfeng Shen ("You") and Royal Society of Chemistry ("Royal Society of Chemistry") consists of your license details and the terms and conditions provided by Royal Society of Chemistry and Copyright Clearance Center.

Your confirmation email will contain your order number for future reference.

[printable details](#)

License Number	4221681257312
License date	Nov 03, 2017
Licensed Content Publisher	Royal Society of Chemistry
Licensed Content Publication	Nanoscale
Licensed Content Title	Morphology and crystallinity control of ultrathin TiO <sub>2</sub> layers deposited on carbon nanotubes by temperature-step atomic layer deposition
Licensed Content Author	Carlos Guerra-Nuñez, Yucheng Zhang, Meng Li, Vipin Chawla, Rolf Erni, Johann Michler, Hyung Gyu Park, Ivo Utke
Licensed Content Date	May 11, 2015
Licensed Content Volume	7
Licensed Content Issue	24
Type of Use	Thesis/Dissertation
Requestor type	academic/educational
Portion	figures/tables/images
Number of figures/tables/images	1
Distribution quantity	10
Format	print and electronic
Will you be translating?	no
Order reference number	
Title of the thesis/dissertation	Engineering Carbon-Semiconductor Hybrid Materials for Photocatalysis and Solar Cells
Expected completion date	Nov 2017
Estimated size	230
Requestor Location	Zhangfeng Shen 10 Lurnea Place, Karawara



**Title:** Virus-templated self-assembled single-walled carbon nanotubes for highly efficient electron collection in photovoltaic devices

Logged in as:  
Zhangfeng Shen

LOGOUT

**Author:** Xiangnan Dang, Hyunjung Yi, Moon-Ho Ham, Jifa Qi, Dong Soo Yun et al.

**Publication:** Nature Nanotechnology

**Publisher:** Nature Publishing Group

**Date:** Apr 24, 2011

Copyright © 2011, Rights Managed by Nature Publishing Group

### Order Completed

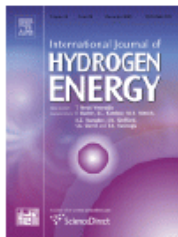
Thank you for your order.

This Agreement between Zhangfeng Shen ("You") and Nature Publishing Group ("Nature Publishing Group") consists of your license details and the terms and conditions provided by Nature Publishing Group and Copyright Clearance Center.

Your confirmation email will contain your order number for future reference.

#### [printable details](#)

License Number	4221690369409
License date	Nov 03, 2017
Licensed Content Publisher	Nature Publishing Group
Licensed Content Publication	Nature Nanotechnology
Licensed Content Title	Virus-templated self-assembled single-walled carbon nanotubes for highly efficient electron collection in photovoltaic devices
Licensed Content Author	Xiangnan Dang, Hyunjung Yi, Moon-Ho Ham, Jifa Qi, Dong Soo Yun et al.
Licensed Content Date	Apr 24, 2011
Licensed Content Volume	6
Licensed Content Issue	6
Type of Use	reuse in a dissertation / thesis
Requestor type	academic/educational
Format	print and electronic
Portion	figures/tables/illustrations
Number of figures/tables/illustrations	1
High-res required	no
Figures	Figure 1
Author of this NPG article	no
Your reference number	
Title of your thesis / dissertation	Engineering Carbon-Semiconductor Hybrid Materials for Photocatalysis and Solar Cells
Expected completion date	Nov 2017
Estimated size (number of pages)	230
Requestor Location	Zhangfeng Shen 10 Lurnea Place, Karawara  Perth, WA 6152



**Title:** Synthesis of reduced graphene oxide-TiO<sub>2</sub> nanoparticle composite systems and its application in hydrogen production

**Author:** Pawan Kumar Dubey, Prashant Tripathi, R.S. Tiwari, A.S.K. Sinha, O.N. Srivastava

**Publication:** International Journal of Hydrogen Energy

**Publisher:** Elsevier

**Date:** 2 October 2014

Copyright © 2014 Hydrogen Energy Publications, LLC.  
Published by Elsevier Ltd. All rights reserved.

Logged in as:  
Zhangfeng Shen

LOGOUT

### Order Completed

Thank you for your order.

This Agreement between Zhangfeng Shen ("You") and Elsevier ("Elsevier") consists of your license details and the terms and conditions provided by Elsevier and Copyright Clearance Center.

Your confirmation email will contain your order number for future reference.

#### [printable details](#)

License Number	4221690616590
License date	Nov 03, 2017
Licensed Content Publisher	Elsevier
Licensed Content Publication	International Journal of Hydrogen Energy
Licensed Content Title	Synthesis of reduced graphene oxide-TiO <sub>2</sub> nanoparticle composite systems and its application in hydrogen production
Licensed Content Author	Pawan Kumar Dubey, Prashant Tripathi, R.S. Tiwari, A.S.K. Sinha, O.N. Srivastava
Licensed Content Date	Oct 2, 2014
Licensed Content Volume	39
Licensed Content Issue	29
Licensed Content Pages	11
Type of Use	reuse in a thesis/dissertation
Portion	figures/tables/illustrations
Number of figures/tables/illustrations	1
Format	both print and electronic
Are you the author of this Elsevier article?	No
Will you be translating?	No
Original figure numbers	Figure 2
Title of your thesis/dissertation	Engineering Carbon-Semiconductor Hybrid Materials for Photocatalysis and Solar Cells
Expected completion date	Nov 2017
Estimated size (number of pages)	230
Requestor Location	Zhangfeng Shen 10 Lurnea Place, Karawara  Perth, WA 6152



RightsLink®

Home

Account Info

Help



Title:

TiO<sub>2</sub>-Graphene  
Nanocomposites for Gas-Phase  
Photocatalytic Degradation of  
Volatile Aromatic Pollutant: Is  
TiO<sub>2</sub>-Graphene Truly Different  
from Other TiO<sub>2</sub>-Carbon  
Composite Materials?

Logged in as:

Zhangfeng Shen

LOGOUT

Author:

Yanhui Zhang, Zi-Rong Tang,  
Xianzhi Fu, et al

Publication: ACS Nano

Publisher: American Chemical Society

Date: Dec 1, 2010

Copyright © 2010, American Chemical Society

#### PERMISSION/LICENSE IS GRANTED FOR YOUR ORDER AT NO CHARGE

This type of permission/license, instead of the standard Terms & Conditions, is sent to you because no fee is being charged for your order. Please note the following:

- Permission is granted for your request in both print and electronic formats, and translations.
- If figures and/or tables were requested, they may be adapted or used in part.
- Please print this page for your records and send a copy of it to your publisher/graduate school.
- Appropriate credit for the requested material should be given as follows: "Reprinted (adapted) with permission from (COMPLETE REFERENCE CITATION). Copyright (YEAR) American Chemical Society." Insert appropriate information in place of the capitalized words.
- One-time permission is granted only for the use specified in your request. No additional uses are granted (such as derivative works or other editions). For any other uses, please submit a new request.

If credit is given to another source for the material you requested, permission must be obtained from that source.

BACK

CLOSE WINDOW

Copyright © 2017 Copyright Clearance Center, Inc. All Rights Reserved. [Privacy statement](#). [Terms and Conditions](#). Comments? We would like to hear from you. E-mail us at [customercare@copyright.com](mailto:customercare@copyright.com)



RightsLink®

Home

Account Info

Help



ACS Publications  
Most Trusted. Most Cited. Most Read.

**Title:** Synthesis of Uniform CdS Nanospheres/Graphene Hybrid Nanocomposites and Their Application as Visible Light Photocatalyst for Selective Reduction of Nitro Organics in Water

**Author:** Zhang Chen, Siqi Liu, Min-Quan Yang, et al

**Publication:** Applied Materials

**Publisher:** American Chemical Society

**Date:** May 1, 2013

Copyright © 2013, American Chemical Society

Logged in as:

Zhangfeng Shen

LOGOUT

#### PERMISSION/LICENSE IS GRANTED FOR YOUR ORDER AT NO CHARGE

This type of permission/license, instead of the standard Terms & Conditions, is sent to you because no fee is being charged for your order. Please note the following:

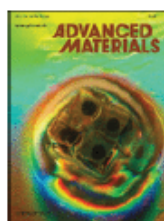
- Permission is granted for your request in both print and electronic formats, and translations.
- If figures and/or tables were requested, they may be adapted or used in part.
- Please print this page for your records and send a copy of it to your publisher/graduate school.
- Appropriate credit for the requested material should be given as follows: "Reprinted (adapted) with permission from (COMPLETE REFERENCE CITATION). Copyright (YEAR) American Chemical Society." Insert appropriate information in place of the capitalized words.
- One-time permission is granted only for the use specified in your request. No additional uses are granted (such as derivative works or other editions). For any other uses, please submit a new request.

If credit is given to another source for the material you requested, permission must be obtained from that source.

BACK

CLOSE WINDOW

Copyright © 2017 Copyright Clearance Center, Inc. All Rights Reserved. [Privacy statement](#). [Terms and Conditions](#).  
Comments? We would like to hear from you. E-mail us at [customercare@copyright.com](mailto:customercare@copyright.com)



**Title:** Convenient Recycling of 3D AgX/Graphene Aerogels (X = Br, Cl) for Efficient Photocatalytic Degradation of Water Pollutants

**Author:** Yingying Fan, Weiguang Ma, Dongxue Han, Shiyu Gan, Xiandui Dong, Li Niu

**Publication:** Advanced Materials

**Publisher:** John Wiley and Sons

**Date:** May 20, 2015

© 2015 WILEY-VCH Verlag GmbH & Co. KGaA, Weinheim

Logged in as:  
Zhangfeng Shen

LOGOUT

### Order Completed

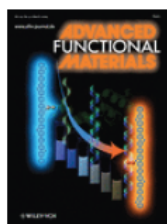
Thank you for your order.

This Agreement between Zhangfeng Shen ("You") and John Wiley and Sons ("John Wiley and Sons") consists of your license details and the terms and conditions provided by John Wiley and Sons and Copyright Clearance Center.

Your confirmation email will contain your order number for future reference.

#### [printable details](#)

License Number	4221700050178
License date	Nov 03, 2017
Licensed Content Publisher	John Wiley and Sons
Licensed Content Publication	Advanced Materials
Licensed Content Title	Convenient Recycling of 3D AgX/Graphene Aerogels (X = Br, Cl) for Efficient Photocatalytic Degradation of Water Pollutants
Licensed Content Author	Yingying Fan, Weiguang Ma, Dongxue Han, Shiyu Gan, Xiandui Dong, Li Niu
Licensed Content Date	May 20, 2015
Licensed Content Pages	7
Type of use	Dissertation/Thesis
Requestor type	University/Academic
Format	Print and electronic
Portion	Figure/table
Number of figures/tables	1
Original Wiley figure/table number(s)	Figure 1
Will you be translating?	No
Title of your thesis / dissertation	Engineering Carbon-Semiconductor Hybrid Materials for Photocatalysis and Solar Cells
Expected completion date	Nov 2017
Expected size (number of pages)	230
Requestor Location	Zhangfeng Shen 10 Lurnea Place, Karawara  Perth, WA 6152 Australia Attn: Zhangfeng Shen



**Title:** Robust Hollow Spheres Consisting of Alternating Titania Nanosheets and Graphene Nanosheets with High Photocatalytic Activity for CO<sub>2</sub> Conversion into Renewable Fuels

Logged in as:  
Zhangfeng Shen

LOGOUT

**Author:** Wenguang Tu, Yong Zhou, Qi Liu, Zhongping Tian, Jun Gao, Xiaoyu Chen, Haitao Zhang, Jianguo Liu, Zhigang Zou

**Publication:** Advanced Functional Materials

**Publisher:** John Wiley and Sons

**Date:** Jan 26, 2012

Copyright © 2012 WILEY-VCH Verlag GmbH & Co. KGaA, Weinheim

### Order Completed

Thank you for your order.

This Agreement between Zhangfeng Shen ("You") and John Wiley and Sons ("John Wiley and Sons") consists of your license details and the terms and conditions provided by John Wiley and Sons and Copyright Clearance Center.

Your confirmation email will contain your order number for future reference.

#### [printable details](#)

License Number	4221700349804
License date	Nov 03, 2017
Licensed Content Publisher	John Wiley and Sons
Licensed Content Publication	Advanced Functional Materials
Licensed Content Title	Robust Hollow Spheres Consisting of Alternating Titania Nanosheets and Graphene Nanosheets with High Photocatalytic Activity for CO <sub>2</sub> Conversion into Renewable Fuels
Licensed Content Author	Wenguang Tu, Yong Zhou, Qi Liu, Zhongping Tian, Jun Gao, Xiaoyu Chen, Haitao Zhang, Jianguo Liu, Zhigang Zou
Licensed Content Date	Jan 26, 2012
Licensed Content Pages	7
Type of use	Dissertation/Thesis
Requestor type	University/Academic
Format	Print and electronic
Portion	Figure/table
Number of figures/tables	2
Original Wiley figure/table number(s)	Figure 1,9
Will you be translating?	No
Title of your thesis / dissertation	Engineering Carbon-Semiconductor Hybrid Materials for Photocatalysis and Solar Cells
Expected completion date	Nov 2017
Expected size (number of pages)	230
Requestor Location	Zhangfeng Shen 10 Lurnea Place, Karawara



RightsLink®

Home

Account  
Info

Help



ACS Publications  
Most Trusted. Most Cited. Most Read.

**Title:** Three-Dimensional Monolayer  
Graphene and TiO<sub>2</sub> Hybrid  
Architectures for High-Efficiency  
Electrochemical Photovoltaic  
Cells

Logged in as:  
Zhangfeng Shen

LOGOUT

**Author:** Dong Hyun Lee, Donghoon  
Song, Yong Soo Kang, et al

**Publication:** The Journal of Physical  
Chemistry C

**Publisher:** American Chemical Society

**Date:** Mar 1, 2015

Copyright © 2015, American Chemical Society

#### PERMISSION/LICENSE IS GRANTED FOR YOUR ORDER AT NO CHARGE

This type of permission/license, instead of the standard Terms & Conditions, is sent to you because no fee is being charged for your order. Please note the following:

- Permission is granted for your request in both print and electronic formats, and translations.
- If figures and/or tables were requested, they may be adapted or used in part.
- Please print this page for your records and send a copy of it to your publisher/graduate school.
- Appropriate credit for the requested material should be given as follows: "Reprinted (adapted) with permission from (COMPLETE REFERENCE CITATION). Copyright (YEAR) American Chemical Society." Insert appropriate information in place of the capitalized words.
- One-time permission is granted only for the use specified in your request. No additional uses are granted (such as derivative works or other editions). For any other uses, please submit a new request.

If credit is given to another source for the material you requested, permission must be obtained from that source.

BACK

CLOSE WINDOW

Copyright © 2017 [Copyright Clearance Center, Inc.](#) All Rights Reserved. [Privacy statement.](#) [Terms and Conditions.](#)  
Comments? We would like to hear from you. E-mail us at [customercare@copyright.com](mailto:customercare@copyright.com)



RightsLink®

Home

Account Info

Help



ACS Publications  
Most Trusted. Most Cited. Most Read.

**Title:** Facile Aerosol Synthesis and Characterization of Ternary Crumpled Graphene-TiO<sub>2</sub>-Magnetite Nanocomposites for Advanced Water Treatment  
**Author:** Yi Jiang, Wei-Ning Wang, Pratim Biswas, et al  
**Publication:** Applied Materials  
**Publisher:** American Chemical Society  
**Date:** Jul 1, 2014  
Copyright © 2014, American Chemical Society

Logged in as:  
Zhangfeng Shen

LOGOUT

#### PERMISSION/LICENSE IS GRANTED FOR YOUR ORDER AT NO CHARGE

This type of permission/license, instead of the standard Terms & Conditions, is sent to you because no fee is being charged for your order. Please note the following:

- Permission is granted for your request in both print and electronic formats, and translations.
- If figures and/or tables were requested, they may be adapted or used in part.
- Please print this page for your records and send a copy of it to your publisher/graduate school.
- Appropriate credit for the requested material should be given as follows: "Reprinted (adapted) with permission from (COMPLETE REFERENCE CITATION). Copyright (YEAR) American Chemical Society." Insert appropriate information in place of the capitalized words.
- One-time permission is granted only for the use specified in your request. No additional uses are granted (such as derivative works or other editions). For any other uses, please submit a new request.

If credit is given to another source for the material you requested, permission must be obtained from that source.

BACK

CLOSE WINDOW

Copyright © 2017 Copyright Clearance Center, Inc. All Rights Reserved. [Privacy statement](#). [Terms and Conditions](#).  
Comments? We would like to hear from you. E-mail us at [customer@copyright.com](mailto:customer@copyright.com)



**Title:** Hierarchical dandelion-flower-like cobalt-phosphide modified CdS/reduced graphene oxide-MoS<sub>2</sub> nanocomposites as a noble-metal-free catalyst for efficient hydrogen evolution from water

**Author:** D. Amaranatha Reddy, Jiha Choi, Seunghee Lee, Yujin Kim, Sangyeob Hong, D. Praveen Kumar, Tae Kyu Kim

**Publication:** Catalysis Science & Technology

**Publisher:** Royal Society of Chemistry

**Date:** May 6, 2016

Copyright © 2016, Royal Society of Chemistry

Logged in as:  
Zhangfeng Shen

LOGOUT

### Order Completed

Thank you for your order.

This Agreement between Zhangfeng Shen ("You") and Royal Society of Chemistry ("Royal Society of Chemistry") consists of your license details and the terms and conditions provided by Royal Society of Chemistry and Copyright Clearance Center.

Your confirmation email will contain your order number for future reference.

#### [printable details](#)

License Number	4221700830012
License date	Nov 03, 2017
Licensed Content Publisher	Royal Society of Chemistry
Licensed Content Publication	Catalysis Science & Technology
Licensed Content Title	Hierarchical dandelion-flower-like cobalt-phosphide modified CdS/reduced graphene oxide-MoS <sub>2</sub> nanocomposites as a noble-metal-free catalyst for efficient hydrogen evolution from water
Licensed Content Author	D. Amaranatha Reddy, Jiha Choi, Seunghee Lee, Yujin Kim, Sangyeob Hong, D. Praveen Kumar, Tae Kyu Kim
Licensed Content Date	May 6, 2016
Licensed Content Volume	6
Licensed Content Issue	16
Type of Use	Thesis/Dissertation
Requestor type	academic/educational
Portion	figures/tables/images
Number of figures/tables/images	1
Distribution quantity	10
Format	print and electronic
Will you be translating?	no
Order reference number	
Title of the thesis/dissertation	Engineering Carbon-Semiconductor Hybrid Materials for Photocatalysis and Solar Cells
Expected completion date	Nov 2017
Estimated size	230
Requestor Location	Zhangfeng Shen



**Title:** Mo-Compound/CNT-Graphene Composites as Efficient Catalytic Electrodes for Quantum-Dot-Sensitized Solar Cells

**Author:** Minsu Seol,Duck Hyun Youn,Jae Young Kim, Ji-Wook Jang,Mingi Choi,Jae Sung Lee,Kijung Yong

**Publication:** Advanced Energy Materials

**Publisher:** John Wiley and Sons

**Date:** Oct 16, 2013

© 2013 WILEY-VCH Verlag GmbH & Co. KGaA, Weinheim

Logged in as:  
Zhangfeng Shen

[LOGOUT](#)

### Order Completed

Thank you for your order.

This Agreement between Zhangfeng Shen ("You") and John Wiley and Sons ("John Wiley and Sons") consists of your license details and the terms and conditions provided by John Wiley and Sons and Copyright Clearance Center.

Your confirmation email will contain your order number for future reference.

#### [printable details](#)

License Number	4221700990189
License date	Nov 03, 2017
Licensed Content Publisher	John Wiley and Sons
Licensed Content Publication	Advanced Energy Materials
Licensed Content Title	Mo-Compound/CNT-Graphene Composites as Efficient Catalytic Electrodes for Quantum-Dot-Sensitized Solar Cells
Licensed Content Author	Minsu Seol,Duck Hyun Youn,Jae Young Kim, Ji-Wook Jang,Mingi Choi,Jae Sung Lee,Kijung Yong
Licensed Content Date	Oct 16, 2013
Licensed Content Pages	1
Type of use	Dissertation/Thesis
Requestor type	University/Academic
Format	Print and electronic
Portion	Figure/table
Number of figures/tables	1
Original Wiley figure/table number(s)	Figure 1
Will you be translating?	No
Title of your thesis / dissertation	Engineering Carbon-Semiconductor Hybrid Materials for Photocatalysis and Solar Cells
Expected completion date	Nov 2017
Expected size (number of pages)	230
Requestor Location	Zhangfeng Shen 10 Lurnea Place, Karawara



**Title:** Charge transfer properties and photoelectrocatalytic activity of TiO<sub>2</sub>/MWCNT hybrid

**Author:** Liao-Chuan Jiang, Wei-De Zhang

**Publication:** Electrochimica Acta

**Publisher:** Elsevier

**Date:** 15 December 2010

Copyright © 2010 Elsevier Ltd. All rights reserved.

Logged in as:  
Zhangfeng Shen

[LOGOUT](#)

### Order Completed

Thank you for your order.

This Agreement between Zhangfeng Shen ("You") and Elsevier ("Elsevier") consists of your license details and the terms and conditions provided by Elsevier and Copyright Clearance Center.

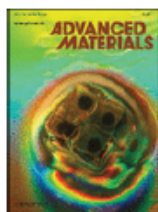
Your confirmation email will contain your order number for future reference.

#### [printable details](#)

License Number	4221701145967
License date	Nov 03, 2017
Licensed Content Publisher	Elsevier
Licensed Content Publication	Electrochimica Acta
Licensed Content Title	Charge transfer properties and photoelectrocatalytic activity of TiO <sub>2</sub> /MWCNT hybrid
Licensed Content Author	Liao-Chuan Jiang, Wei-De Zhang
Licensed Content Date	Dec 15, 2010
Licensed Content Volume	56
Licensed Content Issue	1
Licensed Content Pages	6
Type of Use	reuse in a thesis/dissertation
Portion	figures/tables/illustrations
Number of figures/tables/illustrations	1
Format	both print and electronic
Are you the author of this Elsevier article?	No
Will you be translating?	No
Original figure numbers	Figure 5
Title of your thesis/dissertation	Engineering Carbon-Semiconductor Hybrid Materials for Photocatalysis and Solar Cells
Expected completion date	Nov 2017
Estimated size (number of pages)	230
Requestor Location	Zhangfeng Shen 10 Lurnea Place, Karawara
	Perth, WA 6152 Australia Attn: Zhangfeng Shen
Total	0.00 USD

[ORDER MORE](#) [CLOSE WINDOW](#)

Copyright © 2017 [Copyright Clearance Center, Inc.](#) All Rights Reserved. [Privacy statement.](#) [Terms and Conditions.](#) Comments? We would like to hear from you. E-mail us at [customercare@copyright.com](mailto:customercare@copyright.com)



**Title:** Highly Photoactive, Low Bandgap TiO<sub>2</sub> Nanoparticles Wrapped by Graphene

**Author:** Joon Seok Lee, Kyeong Hwan You, Chan Beum Park

**Publication:** Advanced Materials

**Publisher:** John Wiley and Sons

**Date:** Jan 24, 2012

Logged in as:  
Zhangfeng Shen

LOGOUT

Copyright © 2012 WILEY-VCH Verlag GmbH & Co. KGaA, Weinheim

### Order Completed

Thank you for your order.

This Agreement between Zhangfeng Shen ("You") and John Wiley and Sons ("John Wiley and Sons") consists of your license details and the terms and conditions provided by John Wiley and Sons and Copyright Clearance Center.

Your confirmation email will contain your order number for future reference.

#### [printable details](#)

License Number	4221701345924
License date	Nov 03, 2017
Licensed Content Publisher	John Wiley and Sons
Licensed Content Publication	Advanced Materials
Licensed Content Title	Highly Photoactive, Low Bandgap TiO <sub>2</sub> Nanoparticles Wrapped by Graphene
Licensed Content Author	Joon Seok Lee, Kyeong Hwan You, Chan Beum Park
Licensed Content Date	Jan 24, 2012
Licensed Content Pages	5
Type of use	Dissertation/Thesis
Requestor type	University/Academic
Format	Print and electronic
Portion	Figure/table
Number of figures/tables	2
Original Wiley figure/table number(s)	Figure 1,5
Will you be translating?	No
Title of your thesis / dissertation	Engineering Carbon-Semiconductor Hybrid Materials for Photocatalysis and Solar Cells
Expected completion date	Nov 2017
Expected size (number of pages)	230
Requestor Location	Zhangfeng Shen 10 Lurnea Place, Karawara  Perth, WA 6152 Australia Attn: Zhangfeng Shen
Publisher Tax ID	EU826007151
Billing Type	Invoice
Billing address	Zhangfeng Shen



**Title:** Bare TiO<sub>2</sub> and graphene oxide TiO<sub>2</sub> photocatalysts on the degradation of selected pesticides and influence of the water matrix

Logged in as:  
Zhangfeng Shen

[LOGOUT](#)

**Author:** Marta Cruz, Cristina Gomez, Carlos J. Duran-Valle, Luisa M. Pastrana-Martínez, Joaquim L. Faria, Adrián M.T. Silva, Marisol Faraldos, Ana Bahamonde

**Publication:** Applied Surface Science

**Publisher:** Elsevier

**Date:** 15 September 2017

© 2015 Elsevier B.V. All rights reserved.

### Order Completed

Thank you for your order.

This Agreement between Zhangfeng Shen ("You") and Elsevier ("Elsevier") consists of your license details and the terms and conditions provided by Elsevier and Copyright Clearance Center.

Your confirmation email will contain your order number for future reference.

#### [printable details](#)

License Number	4221701486506
License date	Nov 03, 2017
Licensed Content Publisher	Elsevier
Licensed Content Publication	Applied Surface Science
Licensed Content Title	Bare TiO <sub>2</sub> and graphene oxide TiO <sub>2</sub> photocatalysts on the degradation of selected pesticides and influence of the water matrix
Licensed Content Author	Marta Cruz, Cristina Gomez, Carlos J. Duran-Valle, Luisa M. Pastrana-Martínez, Joaquim L. Faria, Adrián M.T. Silva, Marisol Faraldos, Ana Bahamonde
Licensed Content Date	Sep 15, 2017
Licensed Content Volume	416
Licensed Content Issue	n/a
Licensed Content Pages	9
Type of Use	reuse in a thesis/dissertation
Portion	figures/tables/illustrations
Number of figures/tables/illustrations	1
Format	both print and electronic
Are you the author of this Elsevier article?	No
Will you be translating?	No
Original figure numbers	Figure 11
Title of your thesis/dissertation	Engineering Carbon-Semiconductor Hybrid Materials for Photocatalysis and Solar Cells
Expected completion date	Nov 2017
Estimated size (number of pages)	230
Requestor Location	Zhangfeng Shen 10 Lurnea Place, Karawara



**Title:** Fullerene C70-TiO2 hybrids with enhanced photocatalytic activity under visible light irradiation

**Author:** Shengyao Wang, Changwei Liu, Ke Dai, Peng Cai, Hao Chen, Changjun Yang, Qiaoyun Huang

**Publication:** Journal of Materials Chemistry A

**Publisher:** Royal Society of Chemistry

**Date:** Sep 8, 2015  
Copyright © 2015, Royal Society of Chemistry

Logged in as:  
Zhangfeng Shen

[LOGOUT](#)

### Order Completed

Thank you for your order.

This Agreement between Zhangfeng Shen ("You") and Royal Society of Chemistry ("Royal Society of Chemistry") consists of your license details and the terms and conditions provided by Royal Society of Chemistry and Copyright Clearance Center.

Your confirmation email will contain your order number for future reference.

#### [printable details](#)

License Number	4221710085340
License date	Nov 03, 2017
Licensed Content Publisher	Royal Society of Chemistry
Licensed Content Publication	Journal of Materials Chemistry A
Licensed Content Title	Fullerene C70-TiO2 hybrids with enhanced photocatalytic activity under visible light irradiation
Licensed Content Author	Shengyao Wang, Changwei Liu, Ke Dai, Peng Cai, Hao Chen, Changjun Yang, Qiaoyun Huang
Licensed Content Date	Sep 8, 2015
Licensed Content Volume	3
Licensed Content Issue	42
Type of Use	Thesis/Dissertation
Requestor type	academic/educational
Portion	figures/tables/images
Number of figures/tables/images	1
Distribution quantity	10
Format	print and electronic
Will you be translating?	no
Order reference number	
Title of the thesis/dissertation	Engineering Carbon-Semiconductor Hybrid Materials for Photocatalysis and Solar Cells
Expected completion date	Nov 2017
Estimated size	230
Requestor Location	Zhangfeng Shen 10 Lurnea Place, Karawara  Perth, WA 6152 Australia Attn: Zhangfeng Shen
Billing Type	Invoice



**Title:** Water-Soluble Fluorescent Carbon Quantum Dots and Photocatalyst Design

**Author:** Haitao Li, Xiaodie He, Zhenhui Kang, Hui Huang, Yang Liu, Jinglin Liu, Suoyuan Lian, Chi Him A. Tsang, Xiaobao Yang, Shuit-Tong Lee

Logged in as:  
Zhangfeng Shen

LOGOUT

**Publication:** Angewandte Chemie International Edition

**Publisher:** John Wiley and Sons

**Date:** May 11, 2010

Copyright © 2010 WILEY-VCH Verlag GmbH & Co. KGaA, Weinheim

### Order Completed

Thank you for your order.

This Agreement between Zhangfeng Shen ("You") and John Wiley and Sons ("John Wiley and Sons") consists of your license details and the terms and conditions provided by John Wiley and Sons and Copyright Clearance Center.

Your confirmation email will contain your order number for future reference.

#### [printable details](#)

License Number	4221710260090
License date	Nov 03, 2017
Licensed Content Publisher	John Wiley and Sons
Licensed Content Publication	Angewandte Chemie International Edition
Licensed Content Title	Water-Soluble Fluorescent Carbon Quantum Dots and Photocatalyst Design
Licensed Content Author	Haitao Li, Xiaodie He, Zhenhui Kang, Hui Huang, Yang Liu, Jinglin Liu, Suoyuan Lian, Chi Him A. Tsang, Xiaobao Yang, Shuit-Tong Lee
Licensed Content Date	May 11, 2010
Licensed Content Pages	5
Type of use	Dissertation/Thesis
Requestor type	University/Academic
Format	Print and electronic
Portion	Figure/table
Number of figures/tables	1
Original Wiley figure/table number(s)	Figure 5
Will you be translating?	No
Title of your thesis / dissertation	Engineering Carbon-Semiconductor Hybrid Materials for Photocatalysis and Solar Cells
Expected completion date	Nov 2017
Expected size (number of pages)	230
Requestor Location	Zhangfeng Shen 10 Lurnea Place, Karawara  Perth, WA 6152



**Title:** Carbon quantum dots/Cu<sub>2</sub>O composites with protruding nanostructures and their highly efficient (near) infrared photocatalytic behavior

**Author:** Haitao Li,Ruihua Liu,Yang Liu,Hui Huang,Hang Yu,Hai Ming,Suoyuan Lian,Shuit-Tong Lee,Zhenhui Kang

**Publication:** Journal of Materials Chemistry

**Publisher:** Royal Society of Chemistry

**Date:** Jul 4, 2012

Copyright © 2012, Royal Society of Chemistry

Logged in as:  
Zhangfeng Shen

[LOGOUT](#)

### Order Completed

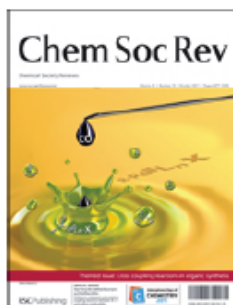
Thank you for your order.

This Agreement between Zhangfeng Shen ("You") and Royal Society of Chemistry ("Royal Society of Chemistry") consists of your license details and the terms and conditions provided by Royal Society of Chemistry and Copyright Clearance Center.

Your confirmation email will contain your order number for future reference.

#### [printable details](#)

License Number	4221710396277
License date	Nov 03, 2017
Licensed Content Publisher	Royal Society of Chemistry
Licensed Content Publication	Journal of Materials Chemistry
Licensed Content Title	Carbon quantum dots/Cu <sub>2</sub> O composites with protruding nanostructures and their highly efficient (near) infrared photocatalytic behavior
Licensed Content Author	Haitao Li,Ruihua Liu,Yang Liu,Hui Huang,Hang Yu,Hai Ming,Suoyuan Lian,Shuit-Tong Lee,Zhenhui Kang
Licensed Content Date	Jul 4, 2012
Licensed Content Volume	22
Licensed Content Issue	34
Type of Use	Thesis/Dissertation
Requestor type	academic/educational
Portion	figures/tables/images
Number of figures/tables/images	1
Distribution quantity	10
Format	print and electronic
Will you be translating?	no
Order reference number	Engineering Carbon-Semiconductor Hybrid Materials for Photocatalysis and Solar Cells
Title of the thesis/dissertation	Engineering Carbon-Semiconductor Hybrid Materials for Photocatalysis and Solar Cells
Expected completion date	Nov 2017
Estimated size	230
Requestor Location	Zhangfeng Shen 10 Lurnea Place, Karawara



**Title:** Heterogeneous photocatalyst materials for water splitting  
**Author:** Akihiko Kudo, Yugo Miseki  
**Publication:** Chemical Society Reviews  
**Publisher:** Royal Society of Chemistry  
**Date:** Nov 18, 2008  
 Copyright © 2008, Royal Society of Chemistry

Logged in as:  
Zhangfeng Shen

LOGOUT

### Order Completed

Thank you for your order.

This Agreement between Zhangfeng Shen ("You") and Royal Society of Chemistry ("Royal Society of Chemistry") consists of your license details and the terms and conditions provided by Royal Society of Chemistry and Copyright Clearance Center.

Your confirmation email will contain your order number for future reference.

#### [printable details](#)

License Number	4221710578727
License date	Nov 03, 2017
Licensed Content Publisher	Royal Society of Chemistry
Licensed Content Publication	Chemical Society Reviews
Licensed Content Title	Heterogeneous photocatalyst materials for water splitting
Licensed Content Author	Akihiko Kudo, Yugo Miseki
Licensed Content Date	Nov 18, 2008
Licensed Content Volume	38
Licensed Content Issue	1
Type of Use	Thesis/Dissertation
Requestor type	academic/educational
Portion	figures/tables/images
Number of figures/tables/images	2
Distribution quantity	10
Format	print and electronic
Will you be translating?	no
Order reference number	
Title of the thesis/dissertation	Engineering Carbon-Semiconductor Hybrid Materials for Photocatalysis and Solar Cells
Expected completion date	Nov 2017
Estimated size	230
Requestor Location	Zhangfeng Shen 10 Lurnea Place, Karawara
	Perth, WA 6152 Australia Attn: Zhangfeng Shen
Billing Type	Invoice



**Title:** Review of one-dimensional and two-dimensional nanostructured materials for hydrogen generation

**Author:** Veluru Jagadeesh Babu, Sessa Vempati, Tamer Uyar, Seeram Ramakrishna

**Publication:** Physical Chemistry Chemical Physics

**Publisher:** Royal Society of Chemistry

**Date:** Nov 28, 2014

Copyright © 2014, Royal Society of Chemistry

Logged in as:  
Zhangfeng Shen

[LOGOUT](#)

### Order Completed

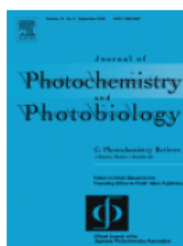
Thank you for your order.

This Agreement between Zhangfeng Shen ("You") and Royal Society of Chemistry ("Royal Society of Chemistry") consists of your license details and the terms and conditions provided by Royal Society of Chemistry and Copyright Clearance Center.

Your confirmation email will contain your order number for future reference.

#### [printable details](#)

License Number	4221710708364
License date	Nov 04, 2017
Licensed Content Publisher	Royal Society of Chemistry
Licensed Content Publication	Physical Chemistry Chemical Physics
Licensed Content Title	Review of one-dimensional and two-dimensional nanostructured materials for hydrogen generation
Licensed Content Author	Veluru Jagadeesh Babu, Sessa Vempati, Tamer Uyar, Seeram Ramakrishna
Licensed Content Date	Nov 28, 2014
Licensed Content Volume	17
Licensed Content Issue	5
Type of Use	Thesis/Dissertation
Requestor type	academic/educational
Portion	figures/tables/images
Number of figures/tables/images	1
Distribution quantity	10
Format	print and electronic
Will you be translating?	no
Order reference number	
Title of the thesis/dissertation	Engineering Carbon-Semiconductor Hybrid Materials for Photocatalysis and Solar Cells
Expected completion date	Nov 2017
Estimated size	230
Requestor Location	Zhangfeng Shen 10 Lurnea Place, Karawara  Perth, WA 6152



**Title:** Recent progress on photocatalytic and photoelectrochemical water splitting under visible light irradiation

**Author:** Ryu Abe

**Publication:** Journal of Photochemistry and Photobiology C: Photochemistry Reviews

**Publisher:** Elsevier

**Date:** December 2010

Logged in as:  
Zhangfeng Shen

LOGOUT

Copyright © 2011 Elsevier B.V. All rights reserved.

### Order Completed

Thank you for your order.

This Agreement between Zhangfeng Shen ("You") and Elsevier ("Elsevier") consists of your license details and the terms and conditions provided by Elsevier and Copyright Clearance Center.

Your confirmation email will contain your order number for future reference.

#### [printable details](#)

License Number	4221710805341
License date	Nov 04, 2017
Licensed Content Publisher	Elsevier
Licensed Content Publication	Journal of Photochemistry and Photobiology C: Photochemistry Reviews
Licensed Content Title	Recent progress on photocatalytic and photoelectrochemical water splitting under visible light irradiation
Licensed Content Author	Ryu Abe
Licensed Content Date	Dec 1, 2010
Licensed Content Volume	11
Licensed Content Issue	4
Licensed Content Pages	31
Type of Use	reuse in a thesis/dissertation
Portion	figures/tables/illustrations
Number of figures/tables/illustrations	1
Format	both print and electronic
Are you the author of this Elsevier article?	No
Will you be translating?	No
Original figure numbers	Figure 2
Title of your thesis/dissertation	Engineering Carbon-Semiconductor Hybrid Materials for Photocatalysis and Solar Cells
Expected completion date	Nov 2017
Estimated size (number of pages)	230
Requestor Location	Zhangfeng Shen 10 Lurnea Place, Karawara  Perth, WA 6152 Australia Attn: Zhangfeng Shen



RightsLink®

Home

Account  
Info

Help



ACS Publications  
Most Trusted. Most Cited. Most Read.

**Title:** A CsPbBr<sub>3</sub> Perovskite Quantum Dot/Graphene Oxide Composite for Photocatalytic CO<sub>2</sub> Reduction

Logged in as:  
Zhangfeng Shen

LOGOUT

**Author:** Yang-Fan Xu, Mu-Zi Yang, Bai-Xue Chen, et al

**Publication:** Journal of the American Chemical Society

**Publisher:** American Chemical Society

**Date:** Apr 1, 2017

Copyright © 2017, American Chemical Society

#### PERMISSION/LICENSE IS GRANTED FOR YOUR ORDER AT NO CHARGE

This type of permission/license, instead of the standard Terms & Conditions, is sent to you because no fee is being charged for your order. Please note the following:

- Permission is granted for your request in both print and electronic formats, and translations.
- If figures and/or tables were requested, they may be adapted or used in part.
- Please print this page for your records and send a copy of it to your publisher/graduate school.
- Appropriate credit for the requested material should be given as follows: "Reprinted (adapted) with permission from (COMPLETE REFERENCE CITATION). Copyright (YEAR) American Chemical Society." Insert appropriate information in place of the capitalized words.
- One-time permission is granted only for the use specified in your request. No additional uses are granted (such as derivative works or other editions). For any other uses, please submit a new request.

If credit is given to another source for the material you requested, permission must be obtained from that source.

BACK

CLOSE WINDOW

Copyright © 2017 [Copyright Clearance Center, Inc.](#) All Rights Reserved. [Privacy statement](#), [Terms and Conditions](#).  
Comments? We would like to hear from you. E-mail us at [customercare@copyright.com](mailto:customercare@copyright.com)



RightsLink®

Home

Account Info

Help



**Title:** Single-Step Preparation of TiO<sub>2</sub>/MWCNT Nanohybrid Materials by Laser Pyrolysis and Application to Efficient Photovoltaic Energy Conversion

Logged in as:  
Zhangfeng Shen

LOGOUT

**Author:** Jin Wang, Yaochen Lin, Mathieu Pinault, et al

**Publication:** Applied Materials

**Publisher:** American Chemical Society

**Date:** Jan 1, 2015

Copyright © 2015, American Chemical Society

#### PERMISSION/LICENSE IS GRANTED FOR YOUR ORDER AT NO CHARGE

This type of permission/license, instead of the standard Terms & Conditions, is sent to you because no fee is being charged for your order. Please note the following:

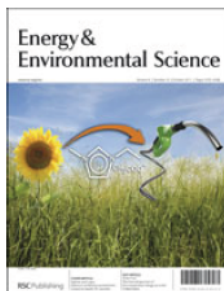
- Permission is granted for your request in both print and electronic formats, and translations.
- If figures and/or tables were requested, they may be adapted or used in part.
- Please print this page for your records and send a copy of it to your publisher/graduate school.
- Appropriate credit for the requested material should be given as follows: "Reprinted (adapted) with permission from (COMPLETE REFERENCE CITATION). Copyright (YEAR) American Chemical Society." Insert appropriate information in place of the capitalized words.
- One-time permission is granted only for the use specified in your request. No additional uses are granted (such as derivative works or other editions). For any other uses, please submit a new request.

If credit is given to another source for the material you requested, permission must be obtained from that source.

BACK

CLOSE WINDOW

Copyright © 2017 [Copyright Clearance Center, Inc.](#) All Rights Reserved. [Privacy statement](#). [Terms and Conditions](#). Comments? We would like to hear from you. E-mail us at [customercare@copyright.com](mailto:customercare@copyright.com)



**Title:** A quasi core-shell nitrogen-doped graphene/cobalt sulfide conductive catalyst for highly efficient dye-sensitized solar cells

**Author:** Enbing Bi, Han Chen, Xudong Yang, Wenqin Peng, Michael Grätzel, Liyuan Han

**Publication:** Energy & Environmental Science

**Publisher:** Royal Society of Chemistry

**Date:** Jun 2, 2014

Copyright © 2014, Royal Society of Chemistry

Logged in as:  
Zhangfeng Shen

LOGOUT

### Review Order

Please review the order details and the associated [terms and conditions](#).

No royalties will be charged for this reuse request although you are required to obtain a license and comply with the license terms and conditions. To obtain the license, click the Accept button below.

Licensed Content Publisher	Royal Society of Chemistry
Licensed Content Publication	Energy & Environmental Science
Licensed Content Title	A quasi core-shell nitrogen-doped graphene/cobalt sulfide conductive catalyst for highly efficient dye-sensitized solar cells
Licensed Content Author	Enbing Bi, Han Chen, Xudong Yang, Wenqin Peng, Michael Grätzel, Liyuan Han
Licensed Content Date	Jun 2, 2014
Licensed Content Volume	7
Licensed Content Issue	8
Type of Use	Thesis/Dissertation
Requestor type	academic/educational
Portion	figures/tables/images
Number of figures/tables/images	3
Distribution quantity	10
Format	print and electronic
Will you be translating?	no
Order reference number	
Title of the thesis/dissertation	Engineering Carbon-Semiconductor Hybrid Materials for Photocatalysis and Solar Cells
Expected completion date	Nov 2017
Estimated size	230
Requestor Location	Zhangfeng Shen 10 Lurnea Place, Karawara  Perth, WA 6152 Australia Attn: Zhangfeng Shen
Total	0.00 USD



**Title:** A fluorescent quenching performance enhancing principle for carbon nanodot-sensitized aqueous solar cells

**Author:** Haimin Zhang, Yun Wang, Porun Liu, Yibing Li, Hua Gui Yang, Taicheng An, Po-Keung Wong, Dan Wang, Zhiyong Tang, Huijun Zhao

**Publication:** Nano Energy

**Publisher:** Elsevier

**Date:** April 2015

Copyright © 2015 Elsevier Ltd. All rights reserved.

Logged in as:  
Zhangfeng Shen

LOGOUT

### Order Completed

Thank you for your order.

This Agreement between Zhangfeng Shen ("You") and Elsevier ("Elsevier") consists of your license details and the terms and conditions provided by Elsevier and Copyright Clearance Center.

Your confirmation email will contain your order number for future reference.

#### [printable details](#)

License Number	4221711330022
License date	Nov 04, 2017
Licensed Content Publisher	Elsevier
Licensed Content Publication	Nano Energy
Licensed Content Title	A fluorescent quenching performance enhancing principle for carbon nanodot-sensitized aqueous solar cells
Licensed Content Author	Haimin Zhang, Yun Wang, Porun Liu, Yibing Li, Hua Gui Yang, Taicheng An, Po-Keung Wong, Dan Wang, Zhiyong Tang, Huijun Zhao
Licensed Content Date	Apr 1, 2015
Licensed Content Volume	13
Licensed Content Issue	n/a
Licensed Content Pages	7
Type of Use	reuse in a thesis/dissertation
Portion	figures/tables/illustrations
Number of figures/tables/illustrations	2
Format	both print and electronic
Are you the author of this Elsevier article?	No
Will you be translating?	No
Original figure numbers	Figure 1,5
Title of your thesis/dissertation	Engineering Carbon-Semiconductor Hybrid Materials for Photocatalysis and Solar Cells
Expected completion date	Nov 2017
Estimated size (number of pages)	230
Requestor Location	Zhangfeng Shen 10 Lurnea Place, Karawara  Perth, WA 6152



RightsLink®

Home

Account Info

Help



ACS Publications  
Most Trusted. Most Cited. Most Read.

**Title:** Simultaneous Top and Bottom Perovskite Interface Engineering by Fullerene Surface Modification of Titanium Dioxide as Electron Transport Layer

Logged in as:  
Zhangfeng Shen

LOGOUT

**Author:** John Ciro, Santiago Mesa, Juan Felipe Montoya, et al

**Publication:** Applied Materials

**Publisher:** American Chemical Society

**Date:** Sep 1, 2017

Copyright © 2017, American Chemical Society

#### PERMISSION/LICENSE IS GRANTED FOR YOUR ORDER AT NO CHARGE

This type of permission/license, instead of the standard Terms & Conditions, is sent to you because no fee is being charged for your order. Please note the following:

- Permission is granted for your request in both print and electronic formats, and translations.
- If figures and/or tables were requested, they may be adapted or used in part.
- Please print this page for your records and send a copy of it to your publisher/graduate school.
- Appropriate credit for the requested material should be given as follows: "Reprinted (adapted) with permission from (COMPLETE REFERENCE CITATION). Copyright (YEAR) American Chemical Society." Insert appropriate information in place of the capitalized words.
- One-time permission is granted only for the use specified in your request. No additional uses are granted (such as derivative works or other editions). For any other uses, please submit a new request.

If credit is given to another source for the material you requested, permission must be obtained from that source.

BACK

CLOSE WINDOW

Copyright © 2017 [Copyright Clearance Center, Inc.](#) All Rights Reserved. [Privacy statement](#). [Terms and Conditions](#).  
Comments? We would like to hear from you. E-mail us at [customer@copyright.com](mailto:customer@copyright.com)



**Title:** Carbon Quantum Dots/TiOx  
Electron Transport Layer Boosts  
Efficiency of Planar  
Heterojunction Perovskite Solar  
Cells to 19%

Logged in as:  
Zhangfeng Shen

LOGOUT

**Author:** Hao Li, Weina Shi, Wenchao  
Huang, et al

**Publication:** Nano Letters

**Publisher:** American Chemical Society

**Date:** Apr 1, 2017

Copyright © 2017, American Chemical Society

#### PERMISSION/LICENSE IS GRANTED FOR YOUR ORDER AT NO CHARGE

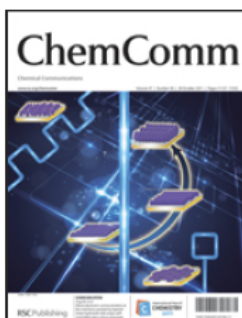
This type of permission/license, instead of the standard Terms & Conditions, is sent to you because no fee is being charged for your order. Please note the following:

- Permission is granted for your request in both print and electronic formats, and translations.
- If figures and/or tables were requested, they may be adapted or used in part.
- Please print this page for your records and send a copy of it to your publisher/graduate school.
- Appropriate credit for the requested material should be given as follows: "Reprinted (adapted) with permission from (COMPLETE REFERENCE CITATION). Copyright (YEAR) American Chemical Society." Insert appropriate information in place of the capitalized words.
- One-time permission is granted only for the use specified in your request. No additional uses are granted (such as derivative works or other editions). For any other uses, please submit a new request.

If credit is given to another source for the material you requested, permission must be obtained from that source.

BACK

CLOSE WINDOW



**Title:** Enhancing the grain size of organic halide perovskites by sulfonate-carbon nanotube incorporation in high performance perovskite solar cells

**Author:** Yong Zhang, Licheng Tan, Qingxia Fu, Lie Chen, Ting Ji, Xiaotian Hu, Yiwang Chen

**Publication:** Chemical Communications (Cambridge)

**Publisher:** Royal Society of Chemistry

**Date:** Mar 1, 2016

Copyright © 2016, Royal Society of Chemistry

Logged in as:  
Zhangfeng Shen

[LOGOUT](#)

### Order Completed

Thank you for your order.

This Agreement between Zhangfeng Shen ("You") and Royal Society of Chemistry ("Royal Society of Chemistry") consists of your license details and the terms and conditions provided by Royal Society of Chemistry and Copyright Clearance Center.

Your confirmation email will contain your order number for future reference.

#### [printable details](#)

License Number	4221720027835
License date	Nov 04, 2017
Licensed Content Publisher	Royal Society of Chemistry
Licensed Content Publication	Chemical Communications (Cambridge)
Licensed Content Title	Enhancing the grain size of organic halide perovskites by sulfonate-carbon nanotube incorporation in high performance perovskite solar cells
Licensed Content Author	Yong Zhang, Licheng Tan, Qingxia Fu, Lie Chen, Ting Ji, Xiaotian Hu, Yiwang Chen
Licensed Content Date	Mar 1, 2016
Licensed Content Volume	52
Licensed Content Issue	33
Type of Use	Thesis/Dissertation
Requestor type	academic/educational
Portion	figures/tables/images
Number of figures/tables/images	1
Distribution quantity	10
Format	print and electronic
Will you be translating?	no
Order reference number	
Title of the thesis/dissertation	Engineering Carbon-Semiconductor Hybrid Materials for Photocatalysis and Solar Cells
Expected completion date	Nov 2017
Estimated size	230
Requestor Location	Zhangfeng Shen 10 Lurnea Place, Karawara



**Title:** Transparent Conductive Oxide-Free Graphene-Based Perovskite Solar Cells with over 17% Efficiency

Logged in as:  
Zhangfeng Shen

[LOGOUT](#)

**Author:** Hyangki Sung, Namyoung Ahn, Min Seok Jang, Jong-Kwon Lee, Heetae Yoon, Nam-Gyu Park, Mansoo Choi

**Publication:** Advanced Energy Materials

**Publisher:** John Wiley and Sons

**Date:** Dec 3, 2015

© 2015 WILEY-VCH Verlag GmbH & Co. KGaA, Weinheim

### Order Completed

Thank you for your order.

This Agreement between Zhangfeng Shen ("You") and John Wiley and Sons ("John Wiley and Sons") consists of your license details and the terms and conditions provided by John Wiley and Sons and Copyright Clearance Center.

Your confirmation email will contain your order number for future reference.

#### [printable details](#)

License Number	4221720178616
License date	Nov 04, 2017
Licensed Content Publisher	John Wiley and Sons
Licensed Content Publication	Advanced Energy Materials
Licensed Content Title	Transparent Conductive Oxide-Free Graphene-Based Perovskite Solar Cells with over 17% Efficiency
Licensed Content Author	Hyangki Sung, Namyoung Ahn, Min Seok Jang, Jong-Kwon Lee, Heetae Yoon, Nam-Gyu Park, Mansoo Choi
Licensed Content Date	Dec 3, 2015
Licensed Content Pages	1
Type of use	Dissertation/Thesis
Requestor type	University/Academic
Format	Print and electronic
Portion	Figure/table
Number of figures/tables	1
Original Wiley figure/table number(s)	Figure 1
Will you be translating?	No
Title of your thesis / dissertation	Engineering Carbon-Semiconductor Hybrid Materials for Photocatalysis and Solar Cells
Expected completion date	Nov 2017
Expected size (number of pages)	230
Requestor Location	Zhangfeng Shen 10 Lurnea Place, Karawara  Perth, WA 6152



RightsLink®

Home

Account Info

Help



ACS Publications  
Most Trusted. Most Cited. Most Read.

**Title:** Green Synthesis of Carbon- and Silver-Modified Hierarchical ZnO with Excellent Solar Light Driven Photocatalytic Performance  
**Author:** Zhangfeng Shen, Ping Liang, Shaobin Wang, et al  
**Publication:** ACS Sustainable Chemistry & Engineering  
**Publisher:** American Chemical Society  
**Date:** May 1, 2015

Logged in as:  
Zhangfeng Shen

LOGOUT

Copyright © 2015, American Chemical Society

#### PERMISSION/LICENSE IS GRANTED FOR YOUR ORDER AT NO CHARGE

This type of permission/license, instead of the standard Terms & Conditions, is sent to you because no fee is being charged for your order. Please note the following:

- Permission is granted for your request in both print and electronic formats, and translations.
- If figures and/or tables were requested, they may be adapted or used in part.
- Please print this page for your records and send a copy of it to your publisher/graduate school.
- Appropriate credit for the requested material should be given as follows: "Reprinted (adapted) with permission from (COMPLETE REFERENCE CITATION). Copyright (YEAR) American Chemical Society." Insert appropriate information in place of the capitalized words.
- One-time permission is granted only for the use specified in your request. No additional uses are granted (such as derivative works or other editions). For any other uses, please submit a new request.

BACK

CLOSE WINDOW

Copyright © 2017 [Copyright Clearance Center, Inc.](#) All Rights Reserved. [Privacy statement](#). [Terms and Conditions](#).  
Comments? We would like to hear from you. E-mail us at [customercare@copyright.com](mailto:customercare@copyright.com)

## permission request

RD

Rights DE <RIGHTS-and-LICENCES@wiley-vch.de>

今天, 16:11

Dear Zhangfeng,

**We hereby grant permission for the requested use expected that due credit is given to the**

If material appears within our work with credit to another source, authorisation from that

Credit must include the following components:

- Journals: Author(s) Name(s): Title of the Article. Name of the Journal. Publication year. Volume

If you also wish to publish your thesis in electronic format, you may use the article according to

### 3. Final Published Version.

Wiley-VCH hereby licenses back to the Contributor the following rights with respect to the

a. [...]

b. Re-use in other publications. The right to re-use the final Contribution or parts thereof if the material constitutes less than half of the total material in such publication. In such case, an

Kind regards

**Heike Weller**

Rights Manager

Rights & Licenses

Wiley-VCH Verlag GmbH & Co. KGaA

Boschstraße 12

69469 Weinheim

Germany

[www.wiley-vch.de](http://www.wiley-vch.de)

T + (49) 6201 606-585

F + (49) 6201 606-332

[rightsDE@wiley.com](mailto:rightsDE@wiley.com)

**WILEY**

...